Exploring Phase-Change Materials for Heat-Storage from First Principles

Dissertation
zur
Erlangung des Doktorgrades (Dr. rer. nat.)
der
Mathematisch-Naturwissenschaftlichen Fakultät
der
Rheinischen Friedrich-Wilhelms-Universität Bonn

vorgelegt von

Stefan Jütten

aus
Aachen

Bonn 2026

Angefertigt mit Genehmigung der Mathematisch-Naturwissenschaftlichen Fakultät der Rheinischen Friedrich-Wilhelms-Universität Bonn

Gutachter/Betreuer:	Prof. Dr. Thomas Bredow
Gutachter:	Prof. Dr. Stefan Grimme
Tag der Promotion:	25.06.2026
Erscheinungsjahr:	2026

Statement of Authorship

I, Stefan Jütten, hereby declare that I am the sole author of this thesis. The ideas and work of others, whether published or unpublished, have been fully acknowledged and referenced in my thesis.

Publications

Parts of this thesis have been published in peer-reviewed journals.

1. S. Jütten, T. Bredow, *First-Principles Investigation of Electronic Properties and Phase Transition of Ti_3O_5*, The Journal of Physical Chemistry C **126** *18* (2022) 7809–7817, DOI: 10.1021/acs.jpcc.2c00572.

2. S. Jütten, T. Bredow, *Doping Effect on the Electronic Structure and Heat-Storage Properties of Ti_3O_5*, The Journal of Physical Chemistry C **127** *22* (2023) 10445–10452, DOI: 10.1021/acs.jpcc.3c01549.

3. S. Jütten, T. Bredow, *Anisotropy of the Pressure Effect in the Ti_3O_5 Phase Transition Process Resolved by Direction-Dependent Interface Propagation*, The Journal of Physical Chemistry C **127** *41* (2023) 20530–20538, DOI: 10.1021/acs.jpcc.3c04986.

4. S. Jütten, T. Bredow, *Effect of Surface Free Energies and Particle Diameter on the Ti_3O_5 $\beta \rightarrow \lambda$ Phase Transition Temperature: A Theoretical Study*, The Journal of Physical Chemistry C **129** *32* (2024) 13402–13409, DOI: 10.1021/acs.jpcc.4c03730.

5. S. Jütten, P. Liu, L. Zuo, X.-Q. Chen, T. Bredow, *Atomistic Mechanisms of Pressure-Induced Phase Transitions in Heat-Storage Material Ti_3O_5*, Physical Review B **113** *9* (2026) 094108, DOI: 10.1103/1wbw-k4n2

Abstract

The transition towards a carbon-neutral energy landscape necessitates the development of efficient thermal energy storage systems to bridge the temporal gap between renewable energy supply and thermal demand. The polymorphic ceramic trititanium pentoxide (Ti_3O_5) has emerged as a promising candidate for latent heat storage, capable of storing thermal energy in a metastable high-temperature phase indefinitely. Here, a comprehensive first-principles investigation of the Ti_3O_5 heat-storage system is presented, ranging from the electronic structure of the bulk material to the complex thermodynamic and kinetic behavior of doped systems, interfaces, surfaces and nanoparticles.

The initial part of this work establishes a robust theoretical framework for describing the open-shell transition metal oxide. It is demonstrated that the meta-GGA functional r^{2}SCAN, augmented with the D3 dispersion correction, provides an accurate description of the structure of Ti_3O_5 polymorphs, superior to standard hybrid functionals. In the bulk, the thermodynamic ground state of the β-phase is identified as an antiferromagnetic semiconductor, while the metastable λ-phase is shown to be a ferromagnetic semiconductor. The transition state is characterized by a rotation of a central Ti-dimer, and predicted r^{2}SCAN-D3 phase transition enthalpy and phase transition temperature are in good agreement with experiment.

Building on this foundation, the modulation of heat-storage properties via aliovalent cation doping (Sc, Al, Mg) is explored. The results reveal that doping lowers the phase transition temperature and enthalpy, primarily through local lattice distortions rather than direct electronic effects. Substitution turns the semiconducting bulk materials into metals, with significant electron density accumulation at the defect site. At low dopant concentration the β-Ti_3O_5 to λ-Ti_3O_5 barrier remains unchanged while the substitution stabilizes the λ-phases relative to β-Ti_3O_5. This provides a theoretical basis for tuning the operational temperature window of the material for specific waste-heat recovery applications.

A central challenge in the theoretical description of Ti_3O_5 has been the discrepancy between calculated and experimental pressures required to induce the phase transition. This thesis resolves this issue by moving beyond bulk models. First, the close degree of lattice matching between β- and λ-phases results in stable optimized phase interfaces along the (100), (010) and (001) grain boundaries between the phases. A more refined picture of the phase transition pathway is obtained by varying the β/λ ratio in large supercell models, revealing a distinct anisotropy in the phase transition pathway involving the (001) interface, which proceeds with a significantly lower barrier as compared to the other considered interfaces, confirming experimental trends. Hydrostatic pressure simulation on these mixed-phase models reveals pressure to destabilize high λ-phase fraction systems, however, these pressures of several GPa still overestimate experimental values by orders of magnitude. Second, the influence of particle size and morphology is quantified. By calculating surface free energies and applying the Wulff construction, it is shown that surface effects stabilize the λ-phase in particles smaller than 43 nm in diameter, providing a thermodynamic explanation for the experimentally observed thermal hysteresis and the persistence of the metastable phase at room temperature. The phase transition temperature is also shown to be influenced by particle size, with nanoparticles exhibiting diameters in the experimentally synthesized regime displaying phase transition temperatures in excellent agreement with experiment.

Finally, the atomistic mechanism of the pressure-induced phase transition is elucidated using machine-learned potentials driven on-the-fly probability enhanced sampling simulations. Simulated annealing simulations reveal a favorable surface reconstruction of the (001) λ-phase surface, which is then subject to repulsive harmonic potentials to model pressure effects. A comprehensive, universal and transferable framework for the translation of the slab compression to a pressure value is introduced. By modeling the uniaxial compression of nanoparticle surfaces rather than hydrostatic bulk compression, the predicted transition threshold of $\approx$700 bar is brought into better agreement with experimental values ($\approx$600 bar). The mechanism is shown to involve a sequential, system size independent nucleation and a resulting layer-by-layer transformation, which is resolved in detail from direct molecular dynamics simulations under pressure at ambient temperatures.

Collectively, this work bridges the gap between quantum-chemical predictions and experimental observations in Ti_3O_5. It establishes a validated computational workflow for the discovery and optimization of phase-change materials, highlighting the critical importance of the correct choice of computational method, uncovering the fundamental effects of cation substitution in the modulation of material properties and the use of realistic models accounting for finite-size effects for accurate predictions of thermodynamic material properties.

Contents

CHAPTER 1

Introduction

1.1 Thermal Energy Usage

The transition towards a carbon-neutral economy is the central challenge of the 21st-century European energy landscape. While significant progress has been made in decarbonizing the electricity sector, the decarbonization of heating and cooling remains a formidable hurdle. Heating and cooling account for approximately 50% of the total final energy consumption in the European Union (EU), making it the single largest energy end-use sector[1–6] (see Fig. 1.1).

Despite the urgent need to mitigate climate change, this sector remains heavily reliant on fossil fuels. The intermittency of renewable energy sources, such as solar and wind, introduces a temporal mismatch between energy supply and thermal energy demand[7–9]. Consequently, the development of efficient heat-storage materials and thermal energy storage systems is not merely a technical optimization but a fundamental prerequisite for a successful energy transition[10,11].

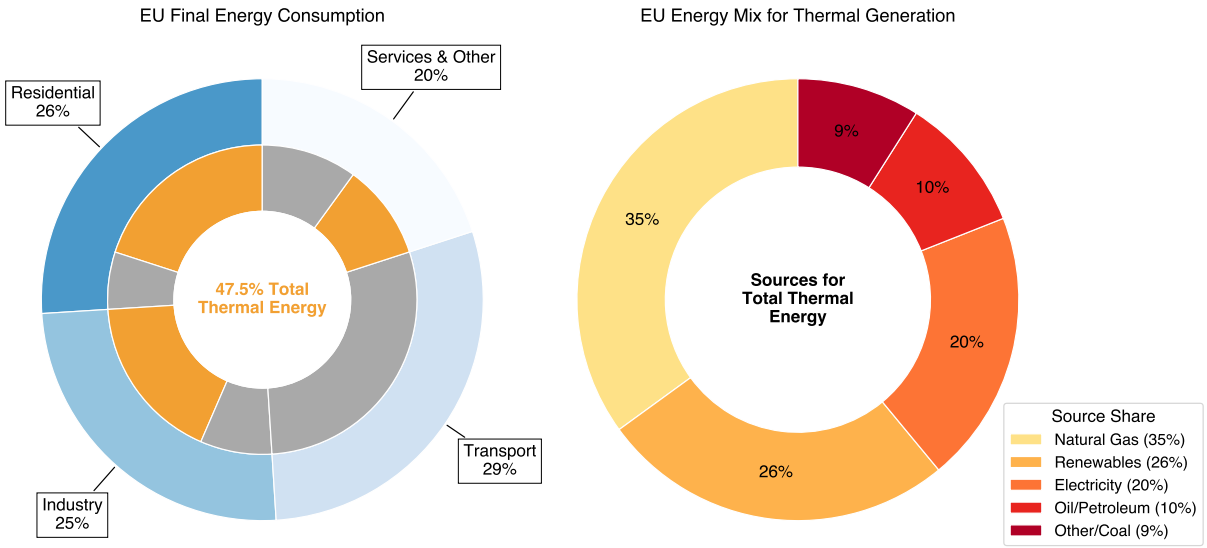

Figure 1.1: Distribution of EU Final Energy Consumption by Sector and Energy Source[3,4,7]. On the left the sectoral breakdown of energy use is shown, with the inner ring highlighting the significant portion (in orange) dedicated to thermal energy. The right chart details the primary energy sources currently used to meet this thermal demand, underscoring the reliance on fossil fuels like natural gas.

1.2 Heat-storage Materials

Thermal energy storage (TES) is critical for matching the intermittent supply of renewable resources with temporal energy demands, particularly for heating and cooling applications[12]. Fundamentally, TES systems are interesting tools for the effective use of energy and therefore CO_2 emission reduction[13–16]. TES systems are broadly classified into sensible and latent heat storage systems.

1.2.1 Sensible & Latent Heat-storage

Thermal energy storage is primarily achieved through sensible and latent heat mechanisms, each suited to different operational requirements. Sensible heat storage (SHS) stores energy by increasing the internal temperature of a material[17], employing diverse media such as water, thermal oils, molten salts, or solid rocks and concrete depending on the required temperature range[18]. Conversely, latent heat storage (LHS) utilizes the energy associated with phase transitions, such as solid–liquid or solid–solid phase changes, to provide high-density heat-storage within a narrow, nearly isothermal temperature window[19,20]. While LHS materials, or Phase Change Materials (PCMs), offer superior energy density, they often require complex management due to lower thermal conductivity and potential stability issues during cycling[21–25]. Table 1.1 summarizes the key differences between the two thermal storage methods.

Table 1.1: Comparison of sensible and latent heat storage approaches[26].

Feature	Sensible Heat Storage (SHS)	Latent Heat Storage (LHS)
Mechanism	Temperature change (ΔT)	Phase transition (ΔH)
Temperature	Variable (wide range)	Nearly Isothermal (narrow range)
Energy Density	Low to Medium	High
Thermal Cond.	Generally High	Generally Low
Complexity	Low (Simple containment)	High (Encapsulation required)
Material Cost	Low (Water, rock, concrete)	Medium to High (Specialized PCMs)
Applications	Domestic heating, solar plants	Electronics cooling, peak shifting

1.2.2 A New Class of Heat-storage Material

The motivation for this work is the idea of a "battery" for thermal energy, i.e. a material that conserves thermal energy and allows the extraction of this stored thermal energy when it is needed (Fig. 1.2). This kind of material could for example find application in the construction of new buildings, where the material would be integrated into cement or roof tiles. During the summer months these elements are exposed to solar radiation, and therefore heat, which could trigger a phase transition in the envisioned material. As a beneficial side effect, the uptake of heat by the material regulates the temperature in the summer, acting like air conditioning. Once the phase transition has taken place, the material would have to persist in this state until the colder seasons (or the night), where the accumulated thermal energy might be utilized. This proposed material would render the use of fossile fuels for energy generation unnecessary and reuse abundant naturally occuring energy sources, effectively bridging the gap in the intermittancy of renewables and seasonal demand patterns. In the following chapter, a material that fulfills these requirements is presented.

Figure 1.2: Proposed use of a heat-storage material integrated into the building materials of a structure, which can undergoes a phase transition during the warmer seasons (left) and releases the accumulated thermal energy on demand in winter (right).

1.2.3 The Trititanium Pentoxide Heat-storage System

The focus of this work is the trititanium pentoxide (Ti_3O_5) ceramic, whose phase change characteristics were first described by Åsbrink and Magnéli in 1959 during their study of phase relations in the titanium-oxygen system[27]. They observed a sharp phase transformation of the thermodynamic ground state, β-Ti_3O_5 in the $C2/m$ space group, to a high-temperature modification of the anosovite type at ≈490 K. When the temperature was allowed to drop below the phase transition temperature, the high-temperature phase reverted back to the ground state in a fully reversible manner.

In 2010 Ohkoshi *et al.* were able to stabilize this high-temperature phase of Ti_3O_5 at ambient conditions by calcinating anatase-TiO_2 nanoparticles under hydrogen at 1200 °C, yielding the higher energy λ-Ti_3O_5 polymorph[28]. The synthesized "flakes" of 2 ± 0.5 µm diameter assembled from 25 ± 15 nm diameter nanocrystals exhibit the same space group ($C2/m$) as β-Ti_3O_5. Proposed applications for this isostructural, first-order phase transition include optical data storage, with the phase transition being induced by nanosecond laser irradiation: black λ-Ti_3O_5 changes to brown β-Ti_3O_5 under irradiation with a 532 nm laser, and the $\beta \rightarrow \lambda$ phase transition is triggered by 410 nm irradiation. Magnetic susceptibility measurements show β-Ti_3O_5 to be a semiconductor with a 0.16 eV band gap and λ-Ti_3O_5 nanoparticles to be metallic. Notably, this form of Ti_3O_5 is the first metal oxide where such a photorewritable property was demonstrated. Pressurizing this form of Ti_3O_5 with 5000 bar induces a λ-Ti_3O_5 to β-Ti_3O_5 phase

transition.

Its potential as a heat-storage system was discovered in 2015 by Tokoro *et al.*[29] (see Fig. 1.3). By sintering rutile-TiO_2 particles under a hydrogen atmosphere at 1117 °C the sample of 4×1 µm particles with a coral-like morphology was obtained, which in turn are composed of aggregates of 200×30 nm rectangular-shaped nanorods. Termed "stripe"-type λ-Ti_3O_5 this material undergoes the $\lambda \rightarrow \beta$-$Ti_3O_5$ phase transition under a reduced pressure of 600 bar. Conversely, the β-Ti_3O_5 phase reverts back to λ-Ti_3O_5 upon heating at 198 °C. A phase transition enthalpy of $\Delta H = 12 \pm 1$ kJ mol^{-1} was measured for the β-Ti_3O_5 to λ-Ti_3O_5 transition.

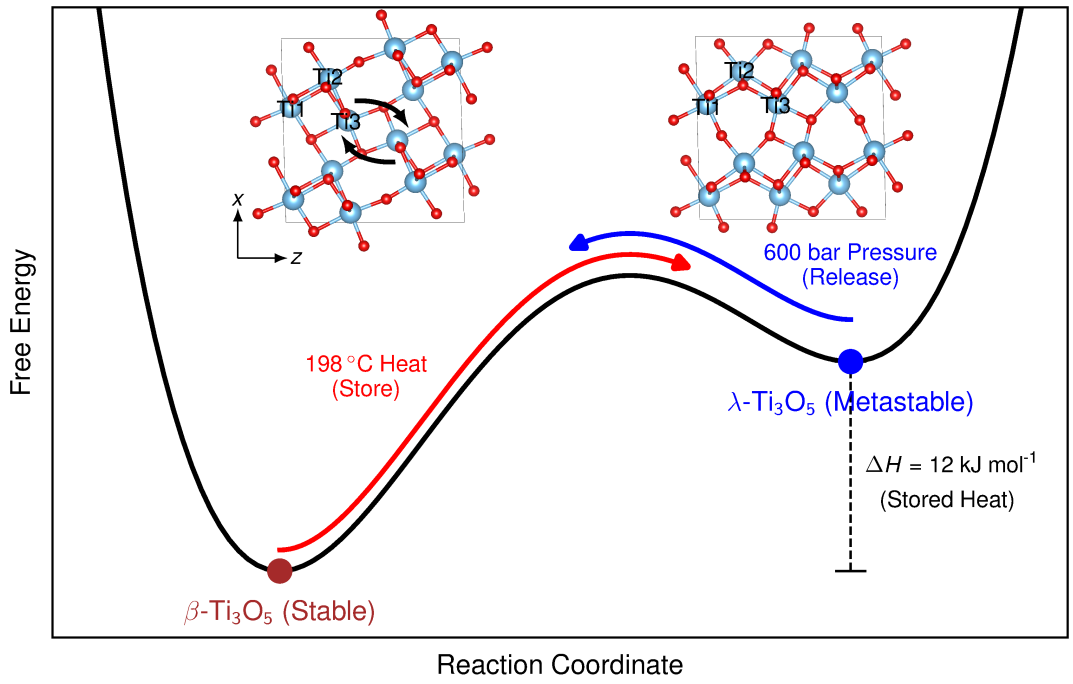

Figure 1.3: Illustration of the β/λ-Ti_3O_5 heat-storage system: upon heating β-Ti_3O_5 transforms into λ-Ti_3O_5, which remains metastable at ambient conditions until pressure is applied to reverse the phase transition. The three symmetry inequivalent Ti atoms in both phases are labeled. The highlighted in-plane rotation of the central Ti3-dimer is the characteristic feature of the phase transition.

Whereas the temperature for the $\beta \rightarrow \lambda$ phase transition remains approximately constant, the pressure threshold for the $\lambda \rightarrow \beta$ transition is markedly particle size and morphology dependent. For instance, "block"-type λ-Ti_3O_5 composed of cubic crystals of ≈ 500 nm size exhibit the lowest pressure threshold of only 70 bar[30]. This material is prepared by sintering rutile-TiO_2 at 1300 °C under a hydrogen atmosphere. At the same time the phase transition enthalpy is increased to $\Delta H = 13.7$ kJ mol^{-1}. An unusually large thermal hysteresis loop is observed in this material, i.e. the material's state depends on its thermal history, causing a $\beta \rightarrow \lambda$ heating transition at 455 K and a $\lambda \rightarrow \beta$ cooling transition at 190 K. Only nanoparticle forms Ti_3O_5 exhibit a thermal hysteresis loop with a lower branch point below ambient temperature, whereas bulk Ti_3O_5 spontaneously reverts back to the thermodynamic β-phase ground state when cooling down and thus does not feature a pressure induced $\lambda \rightarrow \beta$ phase transition.

The range of applications for the heat-storage system can be extended by substituting (or "doping") a small fraction of Ti atoms in the material by another metal. Figure 1.4 provides an overview over all available substituted compounds $M_xTi_{3-x}O_5$ (M = Al[31,32], Mg[33], Sc[34], Zr[35]) that have been experimentally measured with respect to their heat-storage characteristics up to date. It is observed that the heat-storage performance is sensitive to the substituting chemical element, its concentration, as well as the mechanical way of pressure application. Specifically, in $Al_{0.12}Ti_{2.88}O_5$ the pressure application on the polycrystalline sample requires a pressure threshold of 5570 bar, whereas the uniaxial compression on the (001) facet

of a specially prepared "micropillar" lowers the pressure threshold by an order of magnitude[32]. Higher substitution ratios generally lead to reduced phase transition temperatures and reduced phase transition enthalpies, yet higher phase transition pressures. It remains challenging to design a heat-storage material with a phase transition temperature below 100 °C, which captures otherwise wasted heat, with both a high phase transition enthalpy and a low phase transition pressure suitable for practical applications.

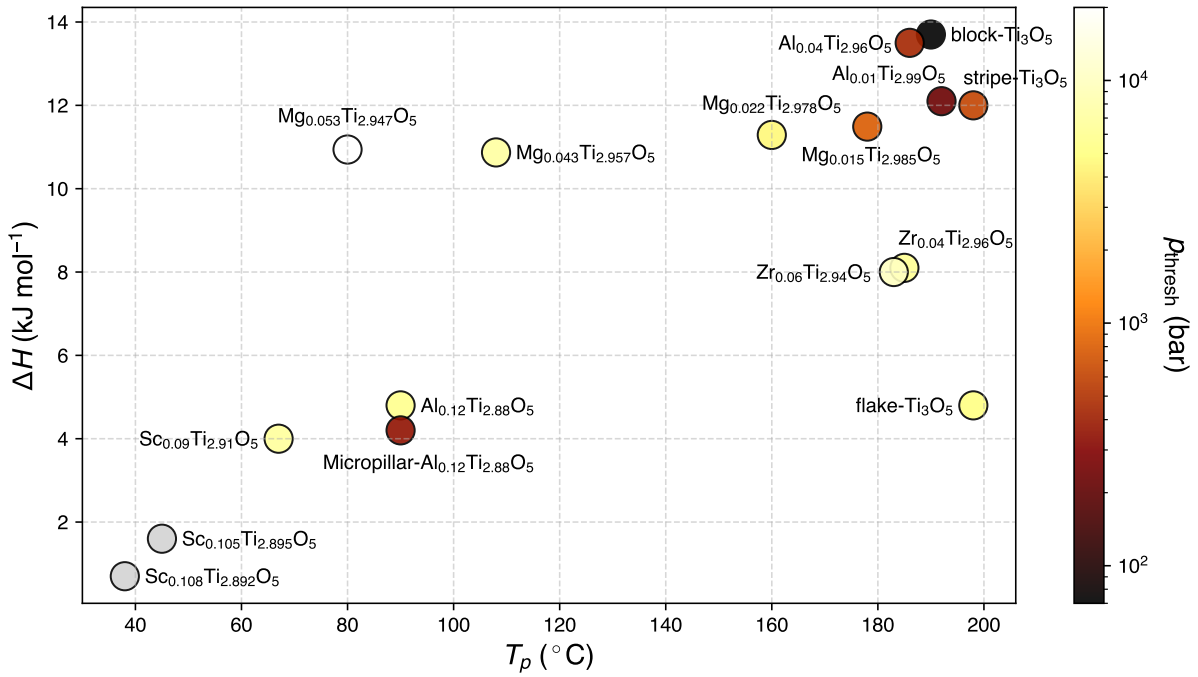

Figure 1.4: Overview of experimental substituted compounds $M_xTi_{3-x}O_5$[31–35] according to their measured phase transition enthalpy ΔH, phase transition temperature T_p and phase transition pressure threshold p_{thresh}. For the two Sc substituted compounds colored in gray no experimental transition pressures are available. "flake"-type[28], "stripe"-type[29] and "block"-type[30] Ti_3O_5 are provided as reference for unsubstituted systems.

Ti_3O_5-based heat-storage systems exhibit several advantageous properties making them ideally suited for long-term heat-storage. Their high volumetric energy storage density of 230 kJ L^{-1} compares favorably to water and eclipses other common organic phase change systems, and is only surpassed by inorganic salt hydrates (300–500 kJ L^{-1})[36]. They are composed of environmentally benign, non-toxic and abundant materials, and their manufacturing process is comparably cheap. The solid–solid phase transition avoids issues associated with liquid phases in traditional solid–liquid PCMs. Its mechanical integrity over extended heating and pressurizing cycles does not compromise the material's properties. Lastly, the defined stoichiometry (as compared to e.g. alloys or amorphous materials) allows for precise tuning (via cation substitution) of the phase transition properties and therefore the operating window of the heat-storage material.

CHAPTER 2

Theoretical Background

In this chapter the fundamental theoretical concepts which were used in the course of this thesis are introduced. After a general overview of electronic structure theory, density functional theory and machine learned interatomic potentials is presented, their extension to solid state quantum chemistry is provided, followed by their application in the determination of thermodynamic functions, determination of reaction pathways, molecular dynamics simulations and enhanced sampling techniques. Note, that atomic units are used throughout.

2.1 Electronic Structure Theory

In quantum chemistry the time-independent, non-relativistic Schrödinger equation[37] is approximated (Eq. 2.1)

$$\hat{H}\Psi = E\Psi \tag{2.1}$$

to obtain the total electronic energy E of a stationary system by applying the Hamilton operator $\hat{H}$ to the wave function Ψ describing the system of interest. In many-body systems the Hamiltonian (Eq. 2.2) is given as the sum of the kinetic energy contributions of electrons $\hat{T}_e$ and nuclei $\hat{T}_n$, and the Coulomb potential between the nuclei $\hat{V}_{nn}$, the electrons $\hat{V}_{ee}$ and between the nuclei and electrons $\hat{V}_{ne}$

$$\hat{H} = \underbrace{-\sum_{A}^{K}\frac{\nabla_A^2}{2M_A}}_{\hat{T}_n} \underbrace{-\sum_{i}^{N}\frac{\nabla_i^2}{2}}_{\hat{T}_e} + \underbrace{\sum_{A}^{K}\sum_{B>A}^{K}\frac{Z_A Z_B}{|\mathbf{R}_A-\mathbf{R}_B|}}_{\hat{V}_{nn}} + \underbrace{\sum_{i}^{N}\sum_{j>i}^{N}\frac{1}{|\mathbf{r}_i-\mathbf{r}_j|}}_{\hat{V}_{ee}} \underbrace{-\sum_{i}^{N}\sum_{A}^{K}\frac{Z_A}{|\mathbf{r}_i-\mathbf{R}_A|}}_{\hat{V}_{ne}} \tag{2.2}$$

where N are the number of electrons at positions $\mathbf{r}$ and K the number of nuclei at positions $\mathbf{R}$ with nuclear charges Z. Due to the large difference in their masses, electronic and nuclear motions can be decoupled within the Born-Oppenheimer approximation[38] (Eq. 2.3) with $\hat{V}_{nn}$ being treated as a constant, simplifying the Hamiltonian

$$\hat{H} = \hat{T}_e + \hat{V}_{ee} + \hat{V}_{ne}. \tag{2.3}$$

To account for the indistinguishability of electrons and antisymmetry requirements[39] of the wavefunction Ψ, a Slater determinant[40] Φ_{SD} (Eq. 2.4) constructed from orthonormal spin orbitals ϕ is used as an approximation

$$\Psi \approx \Phi_{\mathrm{SD}}(1,2,\ldots,N) = \frac{1}{\sqrt{N!}}\begin{vmatrix} \phi_1(1) & \phi_2(1) & \cdots & \phi_N(1) \\ \phi_1(2) & \phi_2(2) & \cdots & \phi_N(2) \\ \vdots & \vdots & \ddots & \vdots \\ \phi_1(N) & \phi_2(N) & \cdots & \phi_N(N) \end{vmatrix}. \tag{2.4}$$

2.2 Density Functional Theory

The workhorse of solid-state quantum chemistry is density functional theory (DFT). Hohenberg and Kohn[41] proved the existence of a direct link between a system's electron density $\rho(\mathbf{r})$ (Eq. 2.5)

$$\rho(\mathbf{r}) = N \int |\Psi(\mathbf{r}, \mathbf{r}_2, \ldots, \mathbf{r}_N)|^2 \, \mathrm{d}\mathbf{r}_2, \ldots, \mathrm{d}\mathbf{r}_N \tag{2.5}$$

and its ground state electronic energy by a (unknown) functional of the electron density. Since the ground state electronic density uniquely defines this energy functional, the electronic structure can be described entirely by $\rho(\mathbf{r})$, circumventing the need for explicit knowledge of the many-electron wavefunction Ψ.

In Kohn-Sham (KS)[42] DFT an auxiliary system of non-interacting electrons is introduced, which are described by KS orbitals ψ_i with occupation number n_i. Importantly, this approach allows for the exact calculation of the kinetic energy. The electron density of the *interacting* system in terms of KS orbitals (Eq. 2.6) is by construction equal to the ground state density of the *non-interacting* system

$$\rho(\mathbf{r}) = \sum_i^N n_i |\psi_i|^2. \tag{2.6}$$

The energy functional $E[\rho]$ of the electron density in KS-DFT (Eq. 2.7) is

$$E[\rho] = T_s[\rho] + V_{ne}[\rho] + J[\rho] + E_{xc}[\rho] \tag{2.7}$$

with T_s being the KS kinetic energy, V_{ne} the nuclear-electron energy, J the Coulomb energy and E_{xc} the exchange-correlation functional. Using KS orbitals in the evaluation of the electronic kinetic energy term T_s (Eq. 2.8) substantially improves upon the purely density based approach, with the orbitals being taken from a single Slater determinant representing a non-interacting system of electrons in the external potential of the nuclei $v(\mathbf{r}) = -\sum_A (Z_A/|\mathbf{r} - \mathbf{R}_A|)$:

$$T_s[\rho] = \sum_i^N n_i \langle \psi_i | -\frac{\nabla^2}{2} | \psi_i \rangle. \tag{2.8}$$

The nuclear-electron potential energy term V_{ne} (Eq. 2.9) is given by

$$V_{ne}[\rho] = \int \rho(\mathbf{r}) v(\mathbf{r}) \, \mathrm{d}\mathbf{r} \tag{2.9}$$

and the Coulomb energy J (Eq. 2.10) by

$$J[\rho] = \frac{1}{2} \int \frac{\rho(\mathbf{r})\rho(\mathbf{r}')}{|\mathbf{r} - \mathbf{r}'|} \, \mathrm{d}\mathbf{r} \, \mathrm{d}\mathbf{r}'. \tag{2.10}$$

While the above terms are closely related to their classical counterparts, KS-DFT incorporates all the unknowns, i.e. many-body effects of the electron-electron interaction and T, into the exchange-correlation functional $E_{xc}[\rho]$ (Eq. 2.11)

$$E_{xc}[\rho] = (T[\rho] - T_s[\rho]) + (E_{ee}[\rho] - J[\rho]), \tag{2.11}$$

where $T[\rho]$ denotes the exact kinetic energy of the *fully interacting* many-electron system and $E_{ee}[\rho]$ the exact expectation value of the full electron-electron interaction in the real *interacting* system. $E_{xc}[\rho]$ is usually partitioned into the exchange term $E_x[\rho]$ and the correlation term $E_c[\rho]$. The former gives rise to the self-interaction error (SIE), which describes the incomplete cancellation of the unphysical self-interaction of an electron with the corresponding Coulomb term. Approximations to the exact $E_{xc}[\rho]$ functional are refered to as density functinoal approximations (DFAs). Perdew ranked different classes of DFAs on rungs according to their level of sophistication, known as "Jacob's Ladder"[43]. Increasing

use of information such as the local density, its gradient or higher derivatives or non-local components in exchange or correlation results in a higher rung on the ladder.

In the local density approximation (LDA) the exchange functional for the uniform electron gas[44] (Eq. 2.12) is used

$$E_x^{\mathrm{LDA}}[\rho] = -\frac{3}{4}\left(\frac{3}{\pi}\right)^{1/3}\int \rho^{4/3}\,\mathrm{d}\mathbf{r}. \tag{2.12}$$

Due to their assumption of uniformly distributed electron density, LDA functionals are suitable for metals, rather than for describing covalent bonds in molecules or polarized bonds in ionic solids. On the next rung, improvements are achieved by additionally including the gradient of the density $\nabla\rho$. These functionals are termed generalized gradient approximation (GGA) functionals, with their most widely known representative being the PBE exchange functional[45] (Eq. 2.13)

$$E_x^{\mathrm{PBE}}[\rho] = -\int \rho^{4/3}\left[\frac{3}{4}\left(\frac{3}{\pi}\right)^{1/3} + \frac{\mu s^2}{1+\mu s^2/\kappa}\right]\mathrm{d}\mathbf{r} \tag{2.13}$$

with μ and κ being functional specific parameters and $s = |\nabla\rho|/(2K_F\rho)$ the reduced density gradient. While adequate for chemical systems in their ground state, reaction barriers or thermochemistry are described insufficiently. To improve upon GGA functionals, on the next rung the second derivative of the electron density is incorporated. Termed meta-GGA functionals, a prominent example which is used throughout this work is the r^{2}SCAN functional[46] (Eq. 2.14):

$$E_x^{\mathrm{r^2SCAN}} = -\frac{3}{4}\left(\frac{3}{\pi}\right)^{1/3}\int \rho^{4/3}\left[g_x(p)\left(h_x^1(p) + f_x(\bar{\alpha})\left[h_x^0 - h_x^1(p)\right]\right)\right]\mathrm{d}\mathbf{r}. \tag{2.14}$$

Here, $\bar{\alpha} = \frac{\tau-\tau_w}{\tau_u+\eta\tau_w}$ is the dimensionless kinetic energy variable, where the von Weizsäcker kinetic energy density $\tau_w = |\nabla\rho|^2/(8\rho)$ and the uniform electron gas kinetic energy is $\tau_u = 3(3\pi^2)^{2/3}$ and η a regularization parameter. The other functions $g_x(p), h_x^0, h_x^1(p)$ are meta-GGA enhancement factors derived from $p = s^2$ and the iso-orbital indicator $\bar{\alpha}$. meta-GGA functionals use most of the available information for semi-local functionals and significantly improve upon GGA functionals by noticeably reducing the SIE. Further improvements on this semi-local approximation are possible by the inclusion of non-local contributions, primarily Fock-exchange, to arrive at the fourth rung of so-called hybrid-functionals. A popular example is the PBE0 functional[47,48], which improves upon the PBE GGA funtional by the admixture of Fock-exchange E_x^{HF} (Eq. 2.15)

$$E_{xc}^{\mathrm{PBE0}} = \frac{1}{4}E_x^{\mathrm{HF}} + \frac{3}{4}E_x^{\mathrm{PBE}} + E_c^{\mathrm{PBE}}. \tag{2.15}$$

Due to the fixed amount of non-local exchange the above is termed a global hybrid functional. Other strategies include varying the amount of non-local exchange for larger inter-electron distances such as in the ωB97X functional[49,50], termed range-separated hybrids. Hybrid functionals improve barrier heights and thermochemistry as compared to semi-local functionals, however, at a significant increase in the computational cost.

Non-local correlation energy, $E_{\mathrm{c}}^{\mathrm{NL}}$, can be introduced into functionals, much like the exchange functional. This is particularly relevant for describing long-range London-dispersion forces in medium-sized or large chemical systems. Most common semi-local functionals, including those up to the fourth rung, lack the ability to model London dispersion explicitly or only manage it partially via fitted parameters[51]. Part of the non-local correlation energy can be recovered by functionals of the fifth rung, termed double-hybrid functionals. Building on hybrid functionals, the wavefunction derived $E_{\mathrm{c}}^{\mathrm{NL}}$ is added in the framework of Møller–Plesset second-order perturbation theory (MP2)[52], further increasing the computational cost.

Alternatively, the dispersion energy can be added to the total KS-DFT energy (Eq. 2.16) as a semi-classical energy correction

$$E_{\mathrm{total}} = E_{\mathrm{KS\text{-}DFT}} + E_{\mathrm{disp}} \tag{2.16}$$

The DFT-D3[53,54] (and the D4 successor[55]) dispersion models have found widespread application due to their favorable balance between accuracy and computational efficiency. In this scheme, the dispersion energy (Eq. 2.17) is given by

$$E_{\text{disp}}^{\text{D3}} = -\sum_{AB}\sum_{n=6,8} s_n \frac{C_n^{AB}}{R_{AB}^n} f_{\text{damp}}^{(n)}(R_{AB}) \tag{2.17}$$

$$-\sum_{ABC} s_9 \frac{C_9^{ABC}\,(3\cos\theta_a\cos\theta_b\cos\theta_c + 1)}{(R_{AB}R_{AC}R_{BC})^3} \times f_{\text{damp}}^{(9)}\left(\bar{R}_{ABC}\right). \tag{2.18}$$

Three body contributions are captured by the Axilrod–Teller–Muto term[56,57] (Eq. 2.18). Divergence at short interatomic distances R_{AB} is muted by the Becke–Johnson (BJ) rational damping function (Eq. 2.19)

$$f_{\text{damp,BJ}}^{(n)}(R_{AB}) = \frac{R_{AB}^n}{R_{AB}^n + \left(a_1 R_0^{AB} + a_2\right)^n} \tag{2.19}$$

with the cut-off radius $R_0^{AB} = \sqrt{C_8^{AB}/C_6^{AB}}$. The dispersion coefficients C_n^{AB} are derived from interpolated electronic polarizabilities based on the local environment of the atom in selected hydrides. These tabulated dispersion coefficients depend on the local chemical environment of each atom resolved by a geometry-derived coordination number. The C_9^{ABC} term is approximated from the C_6 dispersion coefficients. The D4 model extends the calculation of the effective atomic dynamic polarizabilities by atomic charge dependency obtained within a classical electronegativity equilibration (EEQ) scheme. Other parameters (s_6, s_8, s_9, a_1, a_2) are derived empirically and are functional-specific. Inclusion of dispersion effects has proven to be indispensable in the description of non-covalent interactions by DFT.

2.3 Machine-learned Interatomic Potentials

Machine-learned interatomic potentials (MLIPs) represent a paradigm shift in atomistic simulations by bridging the gap between the accuracy of quantum mechanical methods and the efficiency of classical force fields[58]. These potentials are constructed by training flexible regression models, such as neural networks or kernel methods, on high-fidelity reference data (typically DFT generated). By learning the complex, many-body potential energy surface (PES) directly from this quantum mechanical data, MLIPs can predict forces and energies with near-DFT accuracy but at a computational cost several orders of magnitude lower (see Fig. 2.1). This capability extends the scope of simulations to significantly larger systems and longer timescales than are accessible by DFT driven molecular dynamics, without sacrificing the predictive quality of the underlying electronic structure theory[59].

2.3.1 Moment Tensor Potentials

Moment Tensor Potentials (MTPs) are a prominent class of MLIPs that combine *ab initio* accuracy with computational efficiency rivaling traditional force fields. MTPs provide a rigorous, mathematically complete, and systematically improvable framework for describing the PES of complex materials[68].

Similar to other types of MLIPs, the core principle of MTPs is the decomposition of the total potential energy E into a sum of local contributions (Eq. 2.20)

$$E = \sum_i V(\mathbf{r}_i) \tag{2.20}$$

where $\mathbf{r}_i$ represents the local configuration of atom i, which depends on the relative distance vectors $\mathbf{r}_{ij}$ between atom i and neighbors j within a cutoff radius r_{cut} (see Fig. 2.2). The function $V(\mathbf{r}_i)$ is constructed to be invariant under rotations, translations, and permutations of chemically identical atoms.

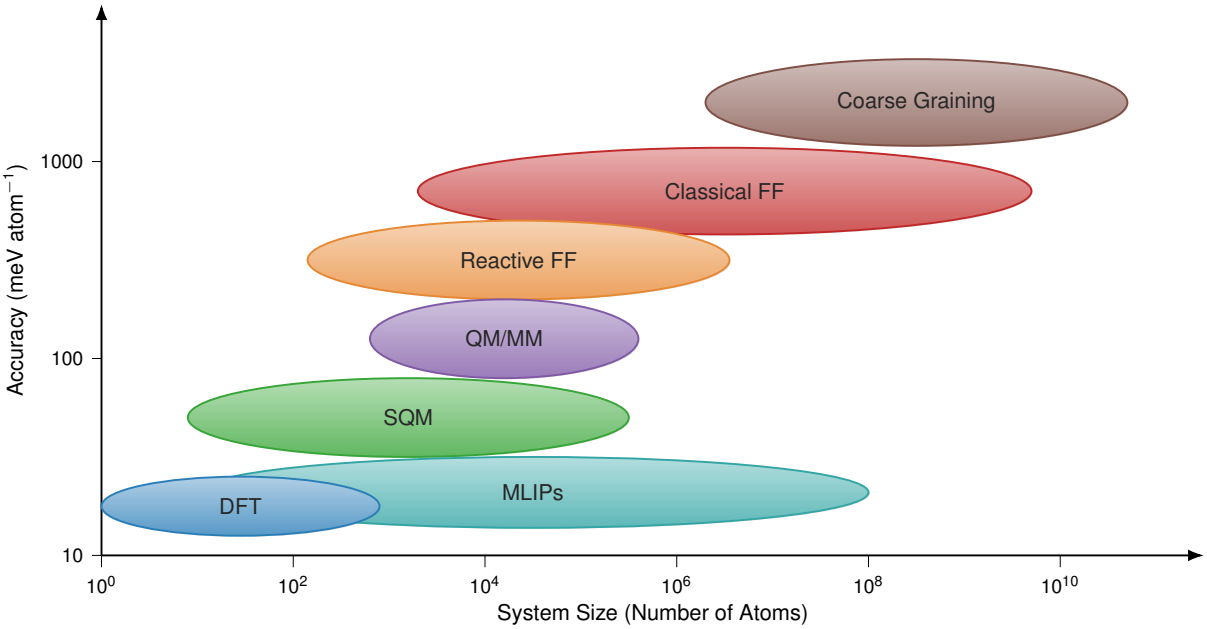

Figure 2.1: Illustration of the trade-off between system size and accuracy (energy mean absolute error relative to high-level quantum mechanical data) for various computational methods[60–67]. Machine-learned potentials bridge the gap to larger system sizes, while retaining the accuracy of the underlying DFT training data.

The primary descriptors in the MTP framework are the *moment tensors* $M_{\mu,\nu}$ (Eq. 2.21) capturing the spatial and chemical distribution of the neighborhood $\mathbf{r}_i$

$$M_{\mu,\nu}(\mathbf{r}_i) = \sum_j f_\mu(|\mathbf{r}_{ij}|, z_i, z_j) \underbrace{\mathbf{r}_{ij} \otimes \mathbf{r}_{ij} \otimes \cdots \otimes \mathbf{r}_{ij}}_{\nu \text{ times}}, \tag{2.21}$$

where ν is the rank of the tensor (representing the degree of angular anisotropy), and f_μ are radial functions that depend on the distance $r_{ij} = |\mathbf{r}_{ij}|$ and the atomic species z_i, z_j (expanded in a basis of Chebyshev polynomials multiplied by a cosine-based cutoff function). As a mechanical interpretation of the moment tensors, consider $\mu = 0$ for $M_{0,0}$ to yield the number of atoms within r_{cut} (their "mass"), $M_{0,1}$ their center of mass, $M_{0,2}$ their tensor of second moments of inertia, or for $\mu > 0$ $M_{\mu,\nu}$ as their weighted moments of inertia.

Because the moment tensors are covariant under rotation, they must be contracted to form scalar-valued basis functions $B_\alpha(\mathbf{r}_i)$. The local energy (Eq. 2.22) is then expressed as a linear combination of these invariants

$$V(\mathbf{r}_i) = \sum_\alpha c_\alpha B_\alpha(\mathbf{r}_i). \tag{2.22}$$

A basis function B_α is formed by the contraction of one or more moment tensors. The general form of this contraction is given by (Eq. 2.23)

$$B_\alpha(\mathbf{r}_i) = \text{contr}\left(\bigotimes_k M_{\mu_k,\nu_k}(\mathbf{r}_i)\right), \tag{2.23}$$

where contr$(\cdot)$ signifies that all Cartesian indices are paired and summed over, resulting in a rank-0 tensor (a scalar), and $\bigotimes$ denotes the tensor product. Simple examples include $B_0(\mathbf{r}_i) = M_{0,0}$ (Radial sum) or $B_1(\mathbf{r}_i) = \sum_a (M_{0,1})_a (M_{0,1})_a = M_{0,1} \cdot M_{0,1}$ (Angular term).

MTPs are characterized by their systematic improvability. Each basis function is assigned a *level* based on its complexity (Eq. 2.24)

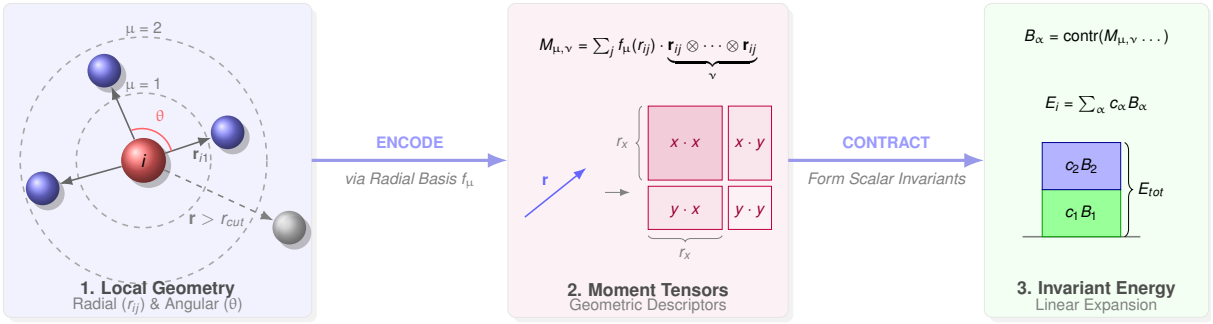

Figure 2.2: Schematic illustration of the MTP formalism: (1) Local Geometry: The atomic environment of a central atom i is defined by relative position vectors $\mathbf{r}_{ij}$ to neighbors j within a cutoff radius r_{cut}. (2) Moment Tensors: The geometry is encoded into descriptors $M_{\mu,\nu}$ (moment tensors). Radial dependence is expanded using basis functions f_μ, while angular information is captured via the outer products of the position vectors. (3) Invariant Energy: These tensors are contracted to form rotationally invariant scalar basis functions B_α. The total energy E is obtained via a linear regression over these basis functions with coefficients c_α.

$$\text{lev}(B_\alpha) = \text{lev}\left(\prod_k M_{\mu_k,\nu_k}\right) = \sum_k (2\mu_k + \nu_k). \tag{2.24}$$

By defining a maximum level lev_{max}, a finite set of basis functions is selected. Increasing lev_{max} allows the potential to represent increasingly complex many-body interactions, ensuring convergence toward the reference *ab initio* data.

A significant advantage of the MTP framework is its compatibility with active learning. Since the potential is linear in the coefficients c_α, the D-optimality criterion[69] can be used to quantify the uncertainty of the model's predictions. During molecular dynamics simulations, an "extrapolation grade" can be calculated, and any configuration exceeding a threshold can be flagged for a subsequent reference calculation to then retrain the potential. This ensures that the MTP remains reliable even when exploring new regions of the configuration space.

MTPs allow for systematic convergence towards the reference method by increasing the polynomial order of the invariant basis B_α and the cutoff radius r_{cut}. Moreover, the linear nature of the fitting problem results in fast training, and the evaluation of the potential and its derivatives (forces and stress) is highly optimized, which is generally up to an order of magnitude faster than comparable deep learning or neural network based methods[59].

As the energy of an atom is derived from its *local* chemical surrounding, long-range interactions are neglected. Using dispersion-corrected DFT reference data captures part of the *non-local* energy, whereas long-range Coulomb interactions or non-local charge transfer require the use of different types of descriptors[70–75]. Furthermore, the dependency on the magnetic moments in the local environment in the MTP context can be resolved by augmenting the function $f_\mu(|\mathbf{r}_{ij}|, s_i, s_j)$ by the spins $s_{i,j}$ of atoms i and j[76], or by the use of other descriptors[77].

2.4 Solid State Quantum Chemistry

The transition from molecular quantum chemistry to the solid state necessitates a fundamental shift in how the boundary conditions of the Schrödinger equation are treated. While isolated molecules are typically treated with vanishing boundary conditions at infinity, crystalline solids are characterized by an orderly, repeating arrangement of atoms. To render the problem computationally tractable, the translational symmetry inherent in the crystal structure is exploited[78].

2.4.1 The Crystal Lattice and Unit Cell

An ideal crystal is constructed by the infinite repetition of a fundamental structural unit in space. The *Bravais lattice* is the set of all points defined by the translation vector $\mathbf{R}$ (Eq. 2.25)

$$\mathbf{R} = \sum_{i=1}^{3} n_i \mathbf{a}_i \tag{2.25}$$

where the n_i are integers, and $\mathbf{a}_i$ are the primitive lattice vectors which span the lattice. These vectors define the geometry of the unit cell.

The *primitive unit cell* is the volume of space which, when translated through all vectors $\mathbf{R}$, fills all space without overlap or voids. It contains exactly one lattice point. However, it is often convenient to use a *conventional unit cell*, which may define a larger volume (and contain multiple lattice points) to preserve the symmetry of the coordinate system[79], and belongs to one of 230 possible space groups.

2.4.2 Born-von Kármàn Boundary Conditions

To treat a macroscopic solid within a quantum mechanical framework without dealing with surface effects or infinite matrices, periodic boundary conditions, specifically the Born-von Kármàn boundary conditions[80], are employed. Consider a finite crystal of volume $V = N_{cell}\Omega_{cell}$, containing $N_1 \times N_2 \times N_3$ unit cells. The wavefunction $\psi(\mathbf{r})$ is enforced to remain invariant under translation through the macroscopic dimensions of the crystal (Eq. 2.26)

$$\psi(\mathbf{r} + N_i \mathbf{a}_i) \overset{!}{=} \psi(\mathbf{r}), \quad i = 1, 2, 3. \tag{2.26}$$

This condition topologically maps the crystal onto a hypertorus, eliminating surface states and allows to treat the system as effectively infinite while maintaining a discrete count of allowed electronic states.

2.4.3 The Reciprocal Lattice

The periodicity of the electron density in real space makes Fourier analysis naturally applicable for solid-state physics. The *reciprocal lattice vectors* $\mathbf{b}_1, \mathbf{b}_2, \mathbf{b}_3$ are defined by the orthogonality relation (Eq. 2.27)

$$\begin{aligned} \mathbf{a}_i \cdot \mathbf{b}_j &= 2\pi\delta_{ij} \\ \mathbf{b}_k &= 2\pi \frac{\mathbf{a}_j \times \mathbf{a}_i}{V} \qquad \text{with} \qquad i, j, k \in 1, 2, 3. \end{aligned} \tag{2.27}$$

The reciprocal lattice is the Fourier transform of the direct lattice. A general lattice vector in reciprocal space is given by $\mathbf{G} = m_1\mathbf{b}_1 + m_2\mathbf{b}_2 + m_3\mathbf{b}_3$ for integers m_i.

The Wigner-Seitz cell of the reciprocal lattice is termed the *First Brillouin Zone* (BZ). This volume is of paramount importance because it contains all unique values of the crystal momentum vector $\mathbf{k}$ (Eq. 2.28)

$$\mathbf{k} = \sum_{i=1}^{3} k_i \mathbf{b}_i \qquad \text{with} \qquad k_i \in \mathbb{R}. \tag{2.28}$$

2.4.4 Bloch's Theorem

The Hamiltonian for a single electron in a perfect crystal contains a potential $V(\mathbf{r})$ that reflects the periodicity of the lattice, such that $V(\mathbf{r} + \mathbf{R}) = V(\mathbf{r})$. Bloch's theorem[81] states that the eigenstates $\psi_{n\mathbf{k}}$ of such a Hamiltonian (Eq. 2.29) can be written as the product of a plane wave and a function $u_{n\mathbf{k}}(\mathbf{r})$ that retains the periodicity of the lattice (Eq. 2.30)

$$\psi_{n\mathbf{k}}(\mathbf{r}) = e^{i\mathbf{k}\cdot\mathbf{r}} u_{n\mathbf{k}}(\mathbf{r}), \tag{2.29}$$

where

$$u_{n\mathbf{k}}(\mathbf{r}+\mathbf{R}) = u_{n\mathbf{k}}(\mathbf{r}). \tag{2.30}$$

Here, n is the band index and $\mathbf{k}$ is the wavevector confined to the first Brillouin zone. The significance of Bloch's theorem is that it reduces the problem of solving the Schrödinger equation for an infinite number of electrons to solving it for a finite number of electrons within a single unit cell, repeated for each $\mathbf{k}$-point in the BZ.

2.4.5 Basis Sets

To solve the Schrödinger equation numerically, the wavefunction must be expanded in a basis set. Given the periodic nature of $u_{n\mathbf{k}}(\mathbf{r})$, it can be expanded in a Fourier series in the reciprocal lattice vectors $\mathbf{G}$ (Eq. 2.31)

$$\psi_{n\mathbf{k}}(\mathbf{r}) = \frac{1}{\sqrt{\Omega}} \sum_{\mathbf{G}}^{\mathbf{G}_{\max}} C_{n\mathbf{k}}(\mathbf{G}) e^{i(\mathbf{k}+\mathbf{G})\cdot\mathbf{r}}. \tag{2.31}$$

Plane waves are computationally efficient (utilizing Fast Fourier Transforms) and unbiased, covering all space with uniform resolution. They are mathematically simple and their convergence is controlled by a single parameter, the kinetic energy cutoff $E_{\text{cut}} = \frac{\hbar^2}{2m}|\mathbf{k}+\mathbf{G}_{\max}|^2$. However, they are extremely inefficient at describing the rapidly oscillating wavefunctions near the atomic nuclei, necessitating the use of pseudopotentials or Projected Augmented Wave (PAW) methods[82].

Alternatively, the crystal wavefunction can be expanded as a linear combination of Bloch sums constructed from localized atomic orbitals ϕ_μ (LCAO ansatz, Eq. 2.32)

$$\psi_{n\mathbf{k}}(\mathbf{r}) = \sum_{\mu} c_{n\mu}(\mathbf{k}) \sum_{\mathbf{R}} e^{i\mathbf{k}\cdot\mathbf{R}} \phi_\mu(\mathbf{r}-\mathbf{R}-\mathbf{r}_\mu), \tag{2.32}$$

where $\mathbf{r}_\mu$ is the position of the atom in the unit cell. This approach, often implemented using Gaussian-type orbitals (GTOs), is intuitive for chemists as it allows for population analysis (e.g., Mulliken charges) and correlates directly with molecular orbital theory. LCAO is generally more efficient for systems with large vacuum regions (such as 2D slabs or porous frameworks) and the evaluation of the Fock exchange fraction in hybrid DFT funcionals, but suffers from basis set superposition error (BSSE) and difficulties in systematic basis set convergence compared to plane waves. Nonetheless, the rev2-POB-type LCAO basis sets[83–88] tailored for solids and fitted to minimize BSSE have emerged as a popular choice.

2.5 Nudged Elastic Band Method

The Nudged Elastic Band (NEB) method serves as a robust approach for identifying the Minimum Energy Path (MEP) between two known equilibrium states on a potential energy surface. In the context of solid-state transitions, such as atomic diffusion or surface catalysis, the MEP represents the most energetically favorable route, where every point along the path is at an energy minimum with respect to all degrees of freedom perpendicular to the path. The highest energy point along this trajectory is defined as the first-order saddle point, which corresponds to the transition state (TS) of the process.

The fundamental algorithm involves the discretization of the transition path into a series of intermediate configurations, or images, which are connected by virtual springs to form an elastic band. The NEB method employs a "nudging" technique that decouples the potential and spring forces (S). The total force acting on each image is partitioned (Eq. 2.33) by projecting the components onto the local tangent vector $\hat{\tau}$ of the path

$$\mathbf{F}_i = \mathbf{F}_i^{V\perp} + \mathbf{F}_i^{S\parallel}. \tag{2.33}$$

The force is restricted to its perpendicular component (Eq. 2.34) by subtracting the parallel projection from the full gradient, ensuring the band is pushed toward the MEP without affecting the spacing of the images

$$\mathbf{F}_i^{V\perp} = -\nabla V(\mathbf{R}_i) + (\nabla V(\mathbf{R}_i) \cdot \hat{\tau}_i)\,\hat{\tau}_i. \tag{2.34}$$

Conversely, the spring force is restricted to its parallel component (Eq. 2.35) by using the relative distance between neighboring images, which maintains the distribution of images along the path without pulling them off the MEP

$$\mathbf{F}_i^{S\parallel} = k\,(|\mathbf{R}_{i+1} - \mathbf{R}_i| - |\mathbf{R}_i - \mathbf{R}_{i-1}|)\,\hat{\tau}_i, \tag{2.35}$$

where k is the spring constant.

A significant enhancement to this methodology is the Climbing Image NEB (CI-NEB) variation. Whereas in conventional NEB, the images only provide a discrete approximation of the path, and the actual saddle point may fall between images, the CI-NEB modification identifies the image with the highest energy and modifies its force by removing the spring components entirely and inverting the potential gradient along the path tangent. This allows the specific image to move uphill along the MEP to converge precisely on the maximum energy point.

In solid-state NEB, where the transition can involve a change in the crystal symmetry or volume, the lattice vectors are incorporated into the configuration space, allowing the unit cell dimensions to relax alongside the internal atomic coordinates, thereby providing a comprehensive description of the structural transformation.

2.6 Statistical Thermodynamics

The relation of the electronic energy E obtained from quantum chemical calculations to experiment is achieved by the fundamental thermodynamic functions enthalpy H, entropy S and the free energy G (Eq. 2.36)

$$G(T) = H(T) + TS(T). \tag{2.36}$$

In an often sufficient attempt the harmonic approximation is employed to calculate them by means of frequency calculations. Although enthalpy and entropy contain translational, rotational and vibrational contributions, only the latter are considered for solids (Eq. 2.37–2.38)

$$H_{\text{vib}} = E + \sum_i \frac{1}{2} h\nu_i + \sum_i \frac{h\nu_i}{\exp\left(\frac{h\nu_i}{k_B T} - 1\right)} + pV \tag{2.37}$$

$$S_{\text{vib}} = \frac{1}{T}\left(\sum_i \frac{1}{2} h\nu_i + \sum_i \frac{h\nu_i}{\exp\left(\frac{h\nu_i}{k_B T} - 1\right)}\right) + k_B \ln\left(\frac{\exp\left(\frac{h\nu_i}{2k_B T}\right)}{1 - \exp\left(-\frac{h\nu_i}{k_B T}\right)}\right). \tag{2.38}$$

Here, p denotes the pressure, V the volume, k_B the Boltzmann constant, h Planck's constant and ν_i the vibrational modes of the system.

2.7 Molecular Dynamics Simulations

Molecular dynamics (MD) simulations provide a deterministic temporal evolution of a system of interacting particles. By numerically solving Newton's equations of motion, MD allows for the exploration of the phase space of a system, thereby bridging the gap between microscopic details and macroscopic observables through the formalism of statistical mechanics[89]. The fundamental assumption underlying these simulations is the ergodic hypothesis, which postulates that over a sufficiently long time trajectory,

the time average of a physical property equals its ensemble average. This equivalence enables the calculation of thermodynamic properties, transport coefficients, and structural information directly from the trajectory of atomic coordinates and momenta.

Employing the Born-Oppenheimer approximation, atoms are treated as point masses moving on a potential energy surface determined by the electronic structure. The motion of a system of N particles is governed by Newton's second law, which for particle i with mass m_i and coordinates $\mathbf{r}_i$ is given by (Eq. 2.39)

$$m_i \frac{d^2\mathbf{r}_i}{dt^2} = \mathbf{F}_i(\mathbf{r}_1, \ldots, \mathbf{r}_N) = -\nabla_i V(\mathbf{r}_1, \ldots, \mathbf{r}_N). \tag{2.39}$$

Here, $\mathbf{F}_i$ represents the force acting on particle i, derived from the gradient of the potential energy function V, which is usually approximated by force fields, quantum chemical methods, or MLIPs. Due to the long-ranged nature of electrostatic forces, their treatment often involves lattice sum methods such as Particle Mesh Ewald to accurately capture interactions across periodic boundaries without excessive computational cost[90]. To propagate the system forward in time, these continuous differential equations are discretized into small time steps Δt, typically on the order of femtoseconds (10^{-15} s) to resolve the fastest atomic vibrations. Integration algorithms such as the Verlet or Velocity Verlet schemes[91,92] are commonly employed due to their structure-preserving nature, time-reversibility, and conservation of phase space volume, which are critical for maintaining energy stability over long simulation timescales.

Solving Newton's equations of motion naturally conserves the total energy, resulting in a microcanonical (NVE) ensemble, where the number of particles, the volume and energy remain constant. However, most experimental measurements are conducted under conditions of constant temperature and pressure. To mimic these conditions, MD simulations utilize specific algorithms to couple the system to external heat and pressure baths, generating the canonical (NVT) or isothermal-isobaric (NPT) ensembles.

Temperature control is achieved through thermostats. Simple methods like velocity rescaling provide crude control, while more rigorous approaches such as the Nosé-Hoover thermostat introduce an additional dynamic variable to the system's Hamiltonian[93,94]. This extended system approach mimics a thermal reservoir, allowing energy to flow dynamically into and out of the system to maintain the target average temperature while preserving the correct canonical velocity distribution. Similarly, pressure control is implemented via barostats, such as the Parrinello-Rahman algorithm[95], which allows the simulation box volume to fluctuate in response to the internal pressure virial and the external target pressure.

2.8 On-the-fly Probability Enhanced Sampling

Many processes such as phase transitions or biological processes occur on time scales longer than those accessible to MD simulations. Enhanced sampling methods are essential in MD simulations to surmount high free-energy barriers that confine trajectories to local minima, thereby impeding the exploration of rare events. Established approaches, such as umbrella sampling[96] and metadynamics[97], employ collective variables (CV) and history dependent external bias potentials to promote barrier crossing, yet they often necessitate intricate parameterization reliant on prior system knowledge.

The On-the-Fly Probability Enhanced Sampling (OPES) method[98–100], unifies CV-based biasing and expanded ensemble techniques within a probabilistic framework. OPES facilitates sampling from a prescribed target distribution $p_{tg}(\mathbf{x})$ while permitting reweighting to unbiased statistics. By adaptively estimating probabilities or free energies during the simulation, OPES minimizes manual intervention and extends applicability to intricate atomistic systems.

A physical system, such as the atoms in a material, is described by its configuration $\mathbf{x}$. In a canonical ensemble, the probability density $p(\mathbf{x})$ (Eq. 2.40) is given by the Boltzmann distribution

$$p(\mathbf{x}) = \frac{e^{-\beta U(\mathbf{x})}}{Z} \qquad \text{with} \qquad Z = \int d\mathbf{x}\, e^{-\beta U(\mathbf{x})}, \tag{2.40}$$

where $U(\mathbf{x})$ is the potential energy, $\beta = 1/(k_B T)$ is the inverse temperature (k_B is the Boltzmann constant and T is the temperature), and Z is the partition function.

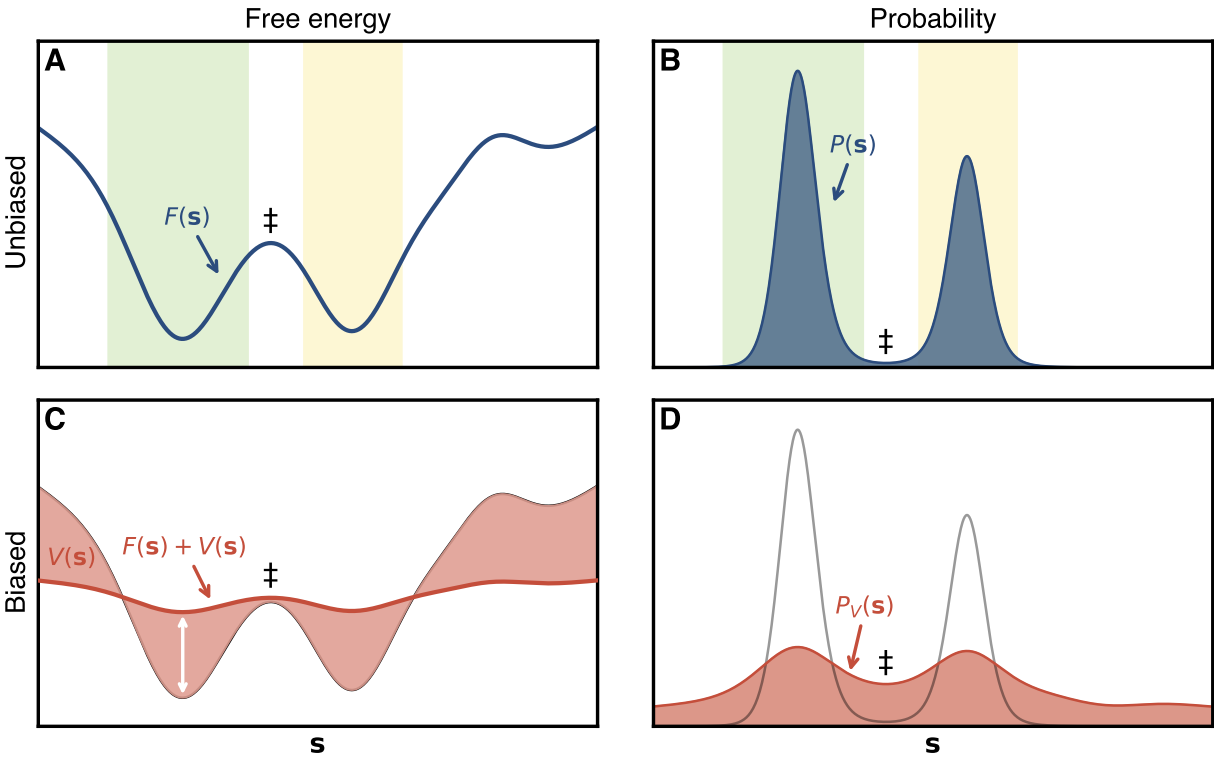

Figure 2.3: Schematic visualization of the relationship between free energy (A, C) and probability distribution (B, D) along a collective variable $\mathbf{s}$. Top row (Unbiased): (A) The natural free energy $F(\mathbf{s})$ (blue line) exhibits distinct metastable states (green and yellow shaded regions) separated by a transition barrier (‡). (B) The corresponding unbiased probability distribution $P(\mathbf{s})$ is strongly localized within these basins, resulting in rare sampling of the transition region. Bottom row (Biased): (C) A bias potential $V(\mathbf{s})$ (red filled region) is applied, acting to fill the free energy wells. The resulting effective free energy surface, $F(\mathbf{s}) + V(\mathbf{s})$ (red line), has significantly lowered barriers. (D) Consequently, the biased probability distribution $P_V(\mathbf{s})$ is broadened, enhancing the sampling of the transition state region and facilitating transitions between metastable states.

The high-dimensional configuration space $\mathbf{x}$ is projected onto a few collective variables (CVs) $\mathbf{s}(\mathbf{x})$. The marginal probability density along $\mathbf{s}$ (see Fig. 2.3) is obtained by integrating $p(\mathbf{x})$ over all configurations $\mathbf{x}$ that yield a specific value $\mathbf{s}$ (Eq. 2.41)

$$p(\mathbf{s}) = \int d\mathbf{x}\, \delta(\mathbf{s} - \mathbf{s}(\mathbf{x}))p(\mathbf{x}). \tag{2.41}$$

The Helmholtz free energy surface (FES) $F(\mathbf{s})$ is directly related to $p(\mathbf{s})$ (Eq. 2.42)

$$F(\mathbf{s}) = -\frac{1}{\beta} \ln p(\mathbf{s}). \tag{2.42}$$

The FES is essential for identifying metastable states (local minima, see Fig. 2.3A) and transition barriers.

Enhanced sampling methods like metadynamics [97] seek to increase the probability to encounter rare configurations corresponding to e.g. transition states by introducing an external bias potential $V(\mathbf{s}(\mathbf{x}))$ along the CVs to decrease these barriers (Fig. 2.3C). The simulation is performed under the modified potential $U(\mathbf{x}) + V(\mathbf{s}(\mathbf{x}))$. The resulting biased distribution $p_V(\mathbf{x})$ (Eq. 2.43) is

$$p_V(\mathbf{x}) = \frac{e^{-\beta(U(\mathbf{x})+V(\mathbf{s}(\mathbf{x})))}}{Z_V} \qquad \text{with} \qquad Z_V = \int d\mathbf{x}\, e^{-\beta(U(\mathbf{x})+V(\mathbf{s}(\mathbf{x})))} \tag{2.43}$$

This biased distribution (Fig. 2.3D) is related to the unbiased one by $p_V(\mathbf{x}) \propto p(\mathbf{x})e^{-\beta V(\mathbf{s}(\mathbf{x}))}$.

OPES augments the potential energy $U(\mathbf{x})$ with a time-dependent bias $V(\mathbf{x}, t)$ to enforce the target distribution $p_{tg}(\mathbf{x})$, diverging from the canonical Boltzmann distribution $P(\mathbf{x})$, where the bias required to perfectly match the target distribution (Eq. 2.44) is

$$V(\mathbf{x}) = -\frac{1}{\beta} \ln \frac{p_{tg}(\mathbf{x})}{P(\mathbf{x})}. \tag{2.44}$$

This compensates the free energy landscape to align with p_{tg}, yielding uniform sampling in targeted regions. The target is a well-tempered marginal (Eq. 2.45)[101]:

$$p_{WT}(\mathbf{s}) \propto [P(\mathbf{s})]^{1/\gamma}, \quad \gamma > 1, \tag{2.45}$$

where γ governs flattening intensity ($\gamma \to \infty$ implies flat sampling).

At iteration n, the bias is (Eq. 2.46)

$$V_n(\mathbf{s}) = \left(1 - \frac{1}{\gamma}\right) \frac{1}{\beta} \ln \left(\frac{P_n(\mathbf{s}) + \varepsilon/Z_n}{\varepsilon/Z_n + 1/\gamma} \right), \tag{2.46}$$

with ε a small number employed to avert singularities.

OPES dynamically approximates p_{tg} or $P_n(\mathbf{s})$ through reweighted kernel density estimation, augmented by regularization against divergences and kernel merging for computational efficiency[98]. The iterative construction counters undersampling, yielding rapid convergence to the target distribution and precise free-energy profiles[98].

To compute the ensemble average of a generic quantity $\langle O(\mathbf{x}) \rangle$ (Eq. 2.47) under the original, unbiased distribution $p(\mathbf{x})$

$$\langle O(\mathbf{x}) \rangle = \int d\mathbf{x}\, O(\mathbf{x}) p(\mathbf{x}) \tag{2.47}$$

a reweighting procedure must be performed. By algebraic manipulation, the unbiased average can be expressed as a ratio of averages over the biased distribution $p_V(\mathbf{x})$ (Eq. 2.48)

$$\langle O(\mathbf{x}) \rangle = \frac{\langle O(\mathbf{x}) e^{\beta V(\mathbf{s}(\mathbf{x}))} \rangle_V}{\langle e^{\beta V(\mathbf{s}(\mathbf{x}))} \rangle_V} \tag{2.48}$$

where $\langle \cdot \rangle_V$ denotes the average with respect to $p_V(\mathbf{x})$.

In practice, this is estimated using a discrete summation over the n_k samples $\mathbf{x}_k$ obtained during the MD trajectory. This leads to the formulation as a weighted time average (Eq. 2.49)

$$\langle O(\mathbf{x}) \rangle \approx \sum_{k=1}^{n_k} O(\mathbf{x}_k) w(\mathbf{x}_k) \qquad \text{with} \qquad w(\mathbf{x}_k) = \frac{e^{\beta V(\mathbf{s}(\mathbf{x}_k))}}{\sum_{j=1}^{n_k} e^{\beta V(\mathbf{s}(\mathbf{x}_j))}} \tag{2.49}$$

where $w(\mathbf{x}_k)$ denotes the normalized weight for the k-th configuration. This weight corrects the sampling bias, recovering the properties of the original distribution in the limit of a large number of samples.

By substituting the delta function $\delta(\mathbf{s} - \mathbf{s}(\mathbf{x}))$ for the observable $O(\mathbf{x})$, the estimation of the unbiased probability density along the CV is (Eq. 2.50)

$$p(\mathbf{s}) \approx \sum_{k=1}^{n_k} \delta(\mathbf{s} - \mathbf{s}(\mathbf{x}_k)) w(\mathbf{x}_k) \tag{2.50}$$

This estimate of $p(\mathbf{s})$ is then used to compute the FES via $F(\mathbf{s}) = -\frac{1}{\beta} \ln p(\mathbf{s})$.

CHAPTER 3

First-Principles Investigation of Electronic Properties and Phase Transition of Ti_3O_5

Stefan Jütten,[†] Thomas Bredow[†]

Received: January 24, 2022
Published online: April 27, 2022

Reprinted in Appendix A with permission[§] from
S. Jütten, T. Bredow, *First-Principles Investigation of Electronic Properties and Phase Transition of Ti_3O_5*, The Journal of Physical Chemistry C **126** *18* (2022) 7809–7817, DOI: 10.1021/acs.jpcc.2c00572

Own contributions

- Conceptualization of the study
- Performing all calculations
- Interpretation of the results
- Writing of the manuscript

[†]Mulliken Center for Theoretical Chemistry, University of Bonn, Beringstr. 4, 53115 Bonn, Germany
[§]Permission requests to reuse material from this chapter should be directed to the American Chemical Society.

The theoretical description of the promising heat-storage material trititanium pentoxide (Ti_3O_5)[28,29], and the concomitant prediction of its phase change properties, is challenging due to its open-shell nature, with formally two unpaired Ti d-electrons per formula unit Ti_3O_5. Theoretical studies up to this point employed LSDA and GGA methods, often in conjunction with empirical Hubbard U corrections[102], inadequately addressed the electronic ground state, did not explicitly treat dispersion effects, and could not reliably predict thermodynamic properties like the phase transition temperature (T_p) and enthalpy (ΔH)[103–107].

This work provides a comprehensive, parameter-free description using hybrid DFAs and the meta-GGA r^{2}SCAN[46] functional augmented with D3 dispersion correction[53,54]. However, for more exact descriptions of the electronic structure the M06-D3[108] hybrid functional was selected after extensive functional tests. Spin configurations were systematically explored on the M06-D3 level, identifying symmetry-inequivalent antiferromagnetic (AFM) and ferromagnetic (FM) states. Thermodynamic properties were derived from harmonic frequency calculations in appropriate supercells, while the phase transition mechanism was probed via solid-state nudged elastic band (ss-NEB)[109] calculations.

It was found that the β-phase exhibits an AFM ground state with antiparallel spins on symmetry equivalent Ti sites and a fundamental band gap of 1.3 eV, while the λ-phase is FM with spin accumulation on Ti2 sites and a 0.7 eV indirect band gap, contradicting earlier metallic predictions but aligning with recent conductivity measurements[110]. Lattice parameters closely matched experimental data, with the $C2/m$ space group monoclinic angle β showing strong electronic state dependence. Benchmarking various commonly used hybrid functionals (e.g., B3LYP[111,112], B3PW[111,113,114], PBE0[47], PW1PW[115], B97H[49,116], HSE06[45,117], ωB97-X[49,50], M06) against r^{2}SCAN showed that dispersion correction is essential for correct relative phase stabilities; without it, most functionals erroneously stabilized the λ-phase. r^{2}SCAN-D3 outperformed hybrids in accuracy for geometries (mean absolute relative deviations $< 1\%$ for lattice parameters) and energetics ($\Delta E = 10.6$ kJ mol^{-1}), at significantly lower computational cost, making it suitable for high-throughput screening. Band structure and density of states (DOS) analyses at the M06-D3 level highlighted differences between the two phases: the β-phase features low-dispersion Ti d_{z^2} and d_{xz} valence bands separated from O p-states by 2.7 eV, while the λ-phase shows higher dispersion in Ti d_{yz} bands, correlating with enhanced conductivity.

Thermodynamic predictions using r^{2}SCAN-D3 yielded $T_p = 525$ K (overestimating experiment by 55 K) and $\Delta H = 9.5$ kJ mol^{-1} (underestimating by ≈ 2.5 kJ mol^{-1}), attributed to the neglect of anharmonicities and surface effects, besides the inaccuracy of the functional/basisset combination. The ss-NEB reaction path identified a single transition state (TS) with barriers of 26 kJ mol^{-1} ($\beta \rightarrow$TS) and 16 kJ mol^{-1} ($\lambda \rightarrow$TS), characterized by rotation of the central Ti3-Ti3′ dimer in the ac-plane and an imaginary mode at $i73$ cm^{-1}. The TS adopts a metallic AFM ground state at M06-D3 level. Structural evolution along the path (decreasing the β angle to 90.3°, volume expansion to 371 Å^3) semiquantitatively matched time-resolved X-ray diffraction data from irradiation-induced transitions.

In conclusion, r^{2}SCAN-D3 was demonstrated to be optimally suited for describing the structure, thermodynamics, and phase transition properties of Ti_3O_5. The findings underscore the critical role of dispersion effects in the accurate description of structures and thermodynamics. Large energy differences of different electronic states of the same polymorph highlight that selecting the correct state is imperative for quantitative prediction of energy differences between phases. The method is recommended for the study of similar heat-storage or phase change materials, along with its application in the study of defective Ti_3O_5.

CHAPTER 4

Doping Effect on the Electronic Structure and Heat-Storage Properties of Ti_3O_5

Stefan Jütten,[†] Thomas Bredow[†]

Received: March 07, 2023
Published online: May 25, 2023

Reprinted in Appendix B with permission[§] from
S. Jütten, T. Bredow, *Doping Effect on the Electronic Structure and Heat-Storage Properties of Ti_3O_5*, The Journal of Physical Chemistry C **127** *22* (2023) 10445–10452, DOI: 10.1021/acs.jpcc.3c01549

Own contributions

- Conceptualization of the study
- Performing all calculations
- Interpretation of the results
- Writing of the manuscript

[†]Mulliken Center for Theoretical Chemistry, University of Bonn, Beringstr. 4, 53115 Bonn, Germany
[§]Permission requests to reuse material from this chapter should be directed to the American Chemical Society.

The substitution of titanium atoms in Ti_3O_5 by aliovalent metals such as scandium, aluminum, and magnesium modifies the heat-storage properties, specifically the enthalpy and temperature T_p of the $\beta \rightarrow \lambda$ phase transition, thereby expanding applications in waste heat capture and utilization. Compared against Ti_3O_5, both the phase transition enthalpy and phase transition temperature change as a dopant is introduced, for instance T_p decreases from ≈200 °C to 67 °C for $Sc_{0.09}Ti_{2.91}O_5$ (ΔH = 75 kJ L^{-1}[134] as compared to ΔH = 230 kJ L^{-1} for Ti_3O_5[29]), to 140 °C for $Al_{0.06}Ti_{2.94}O_5$ (ΔH = 2 kJ mol^{-1})[118] and to 80 °C for $Mg_{0.053}Ti_{2.947}O_5$ (ΔH = 142 kJ L^{-1}[133]). The vast parameter space of dopant elements and dopant concentration poses challenges to computational studies due to small energy differences, necessitating reliable computational predictions to screen potential materials prior to synthesis. To analyze these effects theoretically, electronic ground states were calculated using the M06-D3 hybrid functional[108], while structural optimizations and thermodynamic properties were determined using the dispersion-corrected r^2SCAN meta-GGA functional[119].

From a conceptual point of view the first challenge to be overcome is modeling the correct dopant concentration as used in the experiment. Using only a single substitution per cell, a tradeoff between the size of the employed supercell expansion and the accuracy of that model makes the description of low-concentration dopants challenging. Systematic variations in the substitution position between the irreducible Ti1, Ti2 and Ti3 sites show that higher dopant concentrations lead to larger lattice distortions, and vice versa, when the r^2SCAN-D3 method was used for the optimization.

To investigate the electronic structure modulation caused by the substitution, the most stable configuration of the β- and λ-phases was calculated using the M06-D3. The hybrid functional's better ability to localize spin densities at the Ti atoms compared to semilocal functionals was exploited to show the antiferromagnetic spin configurations remain the preferred state for cation substituted β-phases, whereas ferromagnetic spin configurations are favored in λ-phases. At r^2SCAN-D3 level the Ti2 site is preferred for Sc and Al, and Ti1 for Mg substitutions in β-type structures, with no clear trends observed in the λ-phase. However, as a general trend, the energy differences in $M_xTi_{3-x}O_5$ between the substitution Ti sites decrease as x decreases (M06-D3 exhibits larger differences, but the same overall trend). Both methods agree on the preferred substitution positions for λ-structures, with the agreement being less pronounced in the β-phase. It is observed that doping leads to an increased metallic character in all substituted compounds $M_xTi_{3-x}O_5$ of both the β- and λ-phases. Through re-substitution analysis, it was demonstrated that this modulation of the electronic structure is primarily caused by local distortions induced by the dopant, rather than by the electronic nature of the substituting element itself. The analysis of charge density differences in the β-phase reveals an accumulation of charge density at the defect site, which is redistributed from the neighboring Ti3 d_{xz}-orbitals. In the λ-phase, only an overall increase in delocalized charge density is observed.

Furthermore, heat-storage properties were predicted for those dopant concentrations of Sc, Al, and Mg that match the experimental compounds most closely. The calculated phase transition enthalpies were found to be in good agreement with experimental values, correctly reproducing the trend of decreased ΔH upon doping. Similar to phase pure Ti_3O_5 an overestimation of the T_p is noted, for example by 90 K for the Sc-substituted compound. It is notable that the $G(T)$ slope across the substituted compounds barely changes, which can be explained by deviations in entropy differences $\Delta S(T)$ as compared to experimental reference entropies. An further attempt to improve the predictions by including the configurational entropy for the dopant position resulted in negligible changes.

The mechanism of the phase transition was studied using the solid-state nudged elastic band method[109]. The results indicate that at low concentrations the substitution primarily affects the relative thermodynamic stability of the phases rather than the transition barrier height. The transition state structure is almost unaffected by doping, exhibiting only minor distortions. The barrier height is only lowered for high dopant concentrations, however, here the λ-phase is stabilized over the β-phase and becomes the thermodynamic ground state of the heat-storage system, rendering it useless for practical applications.

Inaccuracies in the predicted phase transition temperatures are attributed to potential anharmonic effects, which are too costly to include in frequency calculations, or surface effects present in experimental nanocrystalline samples[120] that are not captured in bulk calculations, and finally the DFT method itself.

CHAPTER 5

Anisotropy of the Pressure Effect in the Ti_3O_5 Phase Transition Process Resolved by Direction-Dependent Interface Propagation

Stefan Jütten,[†] Thomas Bredow[†]

Received: July 25, 2023
Published online: October 04, 2023

Reprinted in Appendix C with permission[§] from
S. Jütten, T. Bredow, *Anisotropy of the Pressure Effect in the Ti_3O_5 Phase Transition Process Resolved by Direction-Dependent Interface Propagation*, The Journal of Physical Chemistry C **127** *41* (2023) 20530–20538, DOI: 10.1021/acs.jpcc.3c04986

Own contributions

- Conceptualization of the study
- Performing all calculations
- Interpretation of the results
- Writing of the manuscript

[†]Mulliken Center for Theoretical Chemistry, University of Bonn, Beringstr. 4, 53115 Bonn, Germany
[§]Permission requests to reuse material from this chapter should be directed to the American Chemical Society.

Phase transitions in materials crystallizing in anisotropic unit cells may in principle proceed via different pathways. The interphase region, where the emerging phase is in direct contact with the existing phase, is generally distinct for every possible combination of lattice planes. For the isostructural phase transition (both β- and λ-phase crystallize in the $C2/m$ space group) in Ti_3O_5 it was experimentally shown that the phase transition pathway is governed by a selection rule, allowing photoinduced phase transitions in single crystals of Ti_3O_5 only when a laser pulse is applied on the ab plane[121]. Here, the directionality of the general phase transition process in Ti_3O_5 is studied involving the bc, ac and ab interfaces (i.e. the (100)/(100), (010)/(010) and (001)/(001) β/λ interfaces, respectively), and the effect of pressure on bulk and interface properites is compared.

The quasi-harmonic approximation (QHA) that is frequently applied to study phase transitions in solids is used to establish a pressure–volume relation for β-Ti_3O_5 and λ-Ti_3O_5. QHA extends the harmonic model by introducing a volume dependence to phonon frequencies, thereby capturing the effects of anharmonicity, such as thermal expansion, to accurately determine the Gibbs free energy and locate the thermodynamic boundaries of pressure- or temperature-induced phase transitions in crystalline solids. At the intersection of both curves, at a volume of ≈362 Å, the predicted pressure on λ-Ti_3O_5 is 3.9 GPa, largely overestimating the experimental reference value for the heat-storage material of 600 bar (0.06 GPa)[29]. Optimization of bulk unit cells of β-Ti_3O_5, the transition state (TS) of the phase transition, and λ-Ti_3O_5 under hydrostatic pressure of up to 2 GPa reveals virtually unchanged free energy differences between the phases ($\Delta G^{\lambda-\beta}$), the TS and the λ-phase ($\Delta G^{\mathrm{TS}-\lambda}$), and the TS and β-Ti_3O_5 ($\Delta G^{\mathrm{TS}-\beta}$) up to the maximum pressure, i.e. pressure equally destabilizes all phases by similar amounts and cannot account for any pressure effect. It is therefore concluded, that the conventional QHA approach cannot explain the experimentally observed pressure effect.

To improve upon the conventional model, large supercell models incorporating β/λ interfaces perpendicular to the (100), (010), and (001) directions are utilized to simulate phase propagation and volume changes realistically. Large computational models must be employed to capture the physically important region of interest and to minimize artificial interactions between periodic images of the phase boundaries. Such models (> 6000 atoms) are inaccessable by DFT methods, thus a machine learned force field as implemented in VASP[122–124] fitted on r^{2}SCAN-D3 reference data for bulk λ- and β-Ti_3O_5 is employed in the full optimizations of the interface structures. Starting from a pure λ-phase supercell, a fraction of the atoms are converted to the β-phase, simulating the emergence and spread of the new phase, until the whole supercell is converted to the β-phase. The optimized interface regions for the bc, ac and ab interfaces display distinct motifs related to the anisotropy of the underlying cell and partly adopt the TS structure. Moreover, interface models demonstrate significant anisotropy in the energy profile of their respective phase transition pathways: λ-Ti_3O_5 → TS activation energy barriers are ≈16 kJ mol^{-1} along (100) and ≈27 kJ mol^{-1} along (010), but negligible (≈1 kJ mol^{-1}) along (001). Pressure destabilizes high λ-fraction structures, eliminating the barrier along (001) at ≈10.9 GPa, enabling spontaneous transformation.

Phonon density of states analysis show softening of low-frequency acoustic modes under pressure, distorting λ-Ti_3O_5 toward the transition state structure, facilitating conversion.

The fact that the possible phase transformation pathways along different directions in the crystal differ substantially with respect to energetic barriers confirms the experimentally established anisotropy of the strain associated with the phase transition[125] as well as the experimental selection rule for the photoinduced phase transition[121]. Different stacking in the phase interface region of the crystal present during the phase transition rationalizes these observations. The results suggest that considering bulk models for the estimation of phase transition pressures is insufficient, and certain facets of nanoparticles, for example the (001) facet of λ-Ti_3O_5, might be considered for more quantitative pressure predictions.

CHAPTER 6

Effect of Surface Free Energies and Particle Diameter on the Ti_3O_5 $\beta \rightarrow \lambda$ Phase Transition Temperature: A Theoretical Study

Stefan Jütten,[†] Thomas Bredow[†]

Received: June 04, 2024
Published online: August 07, 2024

Reprinted in Appendix D with permission[§] from
S. Jütten, T. Bredow, *Effect of Surface Free Energies and Particle Diameter on the Ti_3O_5 $\beta \rightarrow \lambda$ Phase Transition Temperature: A Theoretical Study*, The Journal of Physical Chemistry C **129** *32* (2024) 13402–13409, DOI: 10.1021/acs.jpcc.4c03730

Own contributions

- Conceptualization of the study
- Performing all calculations
- Interpretation of the results
- Writing of the manuscript

[†]Mulliken Center for Theoretical Chemistry, University of Bonn, Beringstr. 4, 53115 Bonn, Germany
[§]Permission requests to reuse material from this chapter should be directed to the American Chemical Society.

A crucial feature of the Ti_3O_5 heat-storage system is the persistence of the λ-phase over long time frames, until an external stimulus is applied. This is disfavored from a thermodynamic viewpoint, since after cooling down to ambient temperatures the β-phase is the thermodynamic ground state of crystalline Ti_3O_5. However, heat-storage grade Ti_3O_5 is synthetically obtained as a powder of nanoparticles[28–30,120,126–130] with diameters ranging from 8 ± 2 nm[126] to 400 nm[30], often agglomerating into coral-like microparticles. Here it is observed that smaller particles adopt the λ-structure, while larger ones favor the β-phase[120], indicating surface contributions to relative phase stability. Thus, the quantification of these surface effects on nanoparticles and the influence of the surface energy corrected free energy of these nanoparticles on the phase transition temperature are studied here using the established r^{2}SCAN-D3 method.

Structures of slab models of low-index surface terminations of both phases were optimized and systematically enlarged until the surface energy E^{surf} as a function of the stoichiometric layers converged. λ-phase surfaces of a certain facet are always lower in surface energy and therefore more stable as compared to their β-phase counterparts. Nanoparticle morphologies are predicted based on the Gibbs–Wulff theorem[131], comparing favorably to available experimental STM images of λ-phase particles[29].

Properties of heat-storage materials change under increased temperature, motivating the study of the temperature-dependence of surface free energies $G^{\text{surf}}(T)$ and thus the evolution of the morphology of nanoparticles during the heat-storage process. Surface free energies generally decrease uniformly with increasing temperature (except for the (100) facet), and while the deviation from electronic surface energies E^{surf} is at most -0.09 J m^{-2} at 300 K, the difference increases to -0.43 J m^{-2} at 600 K. Temperature dependent changes of G^{surf} are reflected in the predicted nanoparticle morphology: the share of the (100) facet in both β- and λ-phase particles is notably increased, which results in an elongation of the particle along the c-axis.

Free energies of bulk models are routinely calculated in the harmonic approximation and overestimate the experimental phase transition temperature of 470 K by at least 55 K[132]. In order to quantify the temperature-dependent stabilization of λ-Ti_3O_5 with respect to β-Ti_3O_5, the conventional approach is extended to incorporate surface effects in the calculation of the relative phase stability of nanoparticles of a given diameter. As a prerequisite, the weighted surface free energies of Wulff constructions of the nanoparticles $\overline{G}_{\text{Wulff}}(T)$ is introduced. Here, the free energy difference $\Delta\overline{G}^{\lambda-\beta}_{\text{Wulff}}$ is -0.36 J m^{-2} at 300 K, with λ-phase particles becoming increasingly stabilized with respect to β-phase particles as the temperature increases. Multiplying $\Delta\overline{G}^{\lambda-\beta}_{\text{Wulff}}$ with the molar surface area $A_{\text{mol}}(d)$ for a particle with diameter d (taken from experiment[127]) yields the stabilizing contribution to the free energy balance $\Delta G^{\text{stabil.}}_{\text{surf}}(d)$. Using a thermodynamic model by Navrotsky[133], nanoparticles are approximated as spherical with only the outer 5 Å shell contributing significantly to the surface (the averaged interlayer distance of 4 Å is used here). The overall free energy difference is then given as the surface fraction of the nanoparticle $x_{\text{surf}}(d)$ multiplied by the surface stabilization $\Delta G^{\text{stabil.}}_{\text{surf}}(d)$ for the surface contribution, and $(1 - x_{\text{surf}}(d))\Delta G^{\lambda-\beta}_{\text{bulk}}$ for the bulk contribution.

Surface effects contribute to the overall free energy difference between the particles below diameters of $\approx$ 200 nm. At $T \geq 300$ K the equilibrium structure of Ti_3O_5 nanoparticles with a diameter below 43 nm is λ-Ti_3O_5, explaining the experimentally observed thermal hysteresis. Spherical λ-Ti_3O_5 particles are obtained (depending on synthesis conditions) with diameters of 25 ± 15[28], 57 ± 0.3[130], 30–50[127], 8 ± 2–36 ± 15[126], 40[128] and 22 ± 8[129] nm at ambient conditions, comparing favorably to the predicted stability regime below 43 nm.

In summary, the stability of β-Ti_3O_5 and λ-Ti_3O_5 surfaces was calculated on the basis of their free surface energies. Their temperature dependence changes the shape of nanoparticles, modeled by Wulff-constructions, during the heat-storage process. The proposed model predicts nanoparticles with $d < 43$ nm to be trapped in the λ-phase after cooling down in the heat-storage process, since their thermodynamic stability prevents the $\lambda \rightarrow \beta$ phase transition. Moreover, the $\beta \rightarrow \lambda$ phase transition temperature T_p is predicted to be equal to the experimental reference value of 470 K for particles of diameters of 80–90 nm. However, for the experimental reference particles with $d = 70$ nm, the model prediction underestimates T_p by 22 K, which could be explained by particle agglomeration during heating.

CHAPTER 7

Atomistic Mechanisms of Pressure-Induced Phase Transitions in Heat-Storage Material Ti_3O_5

Stefan Jütten,[†] Peitao Liu,[‡] Liang Zuo,[*] Xing-Qi Chen,[‡] Thomas Bredow[†]

Received: November 05, 2025
Published online: March 16, 2026

Reprinted in Appendix E with permission[§] from
S. Jütten, P. Liu, L. Zuo, X.-Q. Chen, T. Bredow, *Atomistic Mechanisms of Pressure-Induced Phase Transitions in Heat-Storage Material Ti_3O_5*, Physical Review B **113** *9* (2026) 094108, DOI: 10.1103/1wbw-k4n2

Own contributions

- Conceptualization of the study
- Performing DFT reference calculations
- Performing NEB, MD and OPES simulations
- Developed theoretical framework for pressure–compression relationship, carried out all numerical simulations
- Interpretation of the results
- Writing of the manuscript

[†]Mulliken Center for Theoretical Chemistry, University of Bonn, Beringstr. 4, 53115 Bonn, Germany
[‡]Shenyang National Laboratory for Materials Science, Institute of Metal Research, Chinese Academy of Sciences, Shenyang 110016, China
[*]Key Laboratory for Anisotropy and Texture of Materials (Ministry of Education), School of Materials Science and Engineering, Northeastern University, Shenyang 110819, China
[§]Permission requests to reuse material from this chapter should be directed to the American Physical Society.

Predicting the pressure threshold for phase transition in materials is challenging and usually relies on shrinking the lattice vectors of the unit cell, or by employing the quasi-harmonic approximation. These approaches yield phase transition pressures of 3–4 GPa for the $\lambda \rightarrow \beta$ phase transition in Ti_3O_5[134,135], severely overestimating the experimental value of ≈600 bar[29] (0.06 GPa) measured for nanoparticles. Based on our previous findings on the anisotropy of the $\lambda \rightarrow \beta$ phase transition pathway preferably involving the (001) phase interface[134] and recent experimental observations that nanoparticles aligned along their z-axis exhibited a phase transition threshold of only 35–40 bar[32], the uniaxial application of pressure on the (001) facet of a λ-Ti_3O_5 nanoparticle is modeled here.

A moment tensor potential (MTP)[136,137] based on r^{2}SCAN-D3[46,119] reference data was trained with structures covering the entire phase space of the phase transition. This enables molecular dynamics (MD) simulation and enhanced sampling simulations using On-the-fly Probability Enhanced Sampling (OPES)[98–100] simulations over extended time frames.

Optimized surfaces cut from the bulk do not necessarily resemble the surfaces under *operando* conditions. Simulated annealing simulations reveal a surface reconstruction of the λ-Ti_3O_5 surface, where the terminal Ti atom is migrated into the slab and an oxygen atom is exposed above it on the outer surface layer, resulting in a decrease of the surface energy by -0.4 J m^{-2}.

The mechanism of the phase transition is probed by climbing image nudged elastic band (CI-NEB)[138] simulations. Starting with the transformation of the subsurface layer, the mechanism proceeds with the sequential transformation of the neighboring layers in a layer-by-layer process, as previously observed in the bulk[135]. Investigating the size effect of the surface model on the activation energy of the phase transition reveals that the $\lambda \rightarrow$ TS activation barrier is constant at $\Delta E^{\ddagger} = 0.23$ eV with increasing cell size, highlighting multiple independent nucleation events.

Direct MD simulations at 300 K under increasing slab compression were performed to probe the dynamics of the phase transition. External pressure was modeled by repulsive harmonic potentials placed at a given position above the slab. A $\lambda \rightarrow \beta$ transition of the subsurface layer was observed at a slab compression of 3.8 Åin c direction, and additional compressions by 0.6 Å each sequentially transformed the opposing subsurface layer, and finally the central layer of the slab. Analyzing the dynamics of the phase transition reveals an intra-layer nucleation event, which initially transforms one slice of the current layer. Thereafter, the neighboring layers are transformed following the same mechanism, until the whole layer has transitioned to β-phase.

Applying a bias potential $V(\mathbf{s}(\mathbf{x}))$ (see Section 2.8) to the phase transition mode, i.e. the rotation of a Ti3-Ti3 dimer, during OPES simulations yields the free energy surface. Under the critical compression threshold of 3.8 Å the free activation energy of the $\lambda \rightarrow \beta$ phase transition $\Delta G^{\ddagger}$ is significantly lowered from 0.16 eV to 0.05 eV in the subsurface layer of the slab, and from 0.24 eV to 0.11 eV in the inner slab layers. To convert the compression of the slab to the corresponding pressure, the classic expression $p = F/A$ of a force acting on the surface area A is utilized, where the mean force F acting normal to the surface is obtained by the derivative of the harmonic potential, which compresses the slab. Here, the external potential's force constant is a free parameter, which must be chosen by convergence tests.

When the bias is applied to the central dimer of the slab, the free energy difference ΔG between the λ- and β-phase is sensitive already to small slab compressions. At a compression of 0.6 Å corresponding to a pressure of ≈ 700 bar, ΔG vanishes, in close agreement with the experimentally measured 600 bar[29].

In summary it was shown that the selective application of pressure, modeled by repulsive harmonic potentials compressing the (001) λ-Ti_3O_5 slab model, predicts a pressure threshold for the $\lambda \rightarrow \beta$ phase transition in Ti_3O_5 of ≈ 700 bar, close to the experimental value of 600 bar. Identifying the correct surface termination for pressure application significantly improves upon conventional bulk models and emphasizes the need to consider surfaces of nanoparticles in describing the pressure effect in anisotropic materials. The proposed prediction of pressure from the forces applied normal to the surface is generally applicable and solely relies on prior convergence test for the force constant of the harmonic potential. The proposed workflow is suggested to be applied, among other phase change materials, in the study of the pressure effect of doped Ti_3O_5.

CHAPTER 8

Summary and Outlook

The central objective of this thesis was to develop a comprehensive theoretical understanding of the Ti_3O_5 heat-storage system, utilizing first-principles methods to resolve the interplay between electronic structure, thermodynamics, and external stimuli. The research trajectory evolved from establishing fundamental bulk properties to addressing complex phenomena such as doping, interface anisotropy, and finite-size effects, ultimately resolving long-standing discrepancies between theoretical predictions and experimental realities. This work represents a systematic computational investigation that bridges the gap between idealized bulk calculations and the experimentally observed behavior of nanoscale materials under realistic operating conditions.

The initial investigation benchmarked various density functional approximations to identify a reliable method for the open-shell Ti_3O_5 system. The meta-GGA functional r^2SCAN-D3 was established as the method of choice, offering a balanced description of phase stabilities, magnetic coupling, and structural parameters at a computational cost significantly lower than hybrid functionals. This methodological choice proved critical, as it enabled the extensive calculations performed throughout this work while maintaining a high degree of accuracy. The close agreement with experiment was again verified by modeling the entire reaction pathway of the $\beta \rightarrow \lambda$ phase transition, where the characteristic rotation of a Ti3 dimer was identified as the transition state mode connecting β- and λ-phase during the concerted phase transformation. Crucially, the inclusion of London dispersion corrections was found to be indispensable for correctly predicting the relative stability of the β- and λ-phases. Without dispersion corrections, the energetic ordering of the two phases was reversed, demonstrating that dispersion interactions play a decisive role in determining the thermodynamic landscape of Ti_3O_5. While nanoparticles of the λ-phase are metallic, the electronic analysis characterized the bulk λ-phase as a ferromagnetic semiconductor, a finding supported by recent conductivity measurements for the bulk and thin films.

The modification of heat-storage properties through cation substitution (Sc, Al, Mg) was systematically explored across a range of concentrations and substitution sites. The calculations successfully reproduced the experimental trend of decreasing phase transition enthalpies and temperatures upon doping, with quantitative agreement achieved for the concentration dependence of the transition temperature. Electronic structure analysis revealed that these property changes are driven by local lattice distortions induced by the dopant, which destabilize the ground state (β-phase) relative to the metastable λ-phase. This structural control mechanism allows for the predictive screening of dopants to tailor the material's operating temperature, opening pathways toward application-specific optimization. The computational framework presented here has the potential to enable the rapid evaluation of dopant elements before costly experimental syntheses, and the identified structure-property relationships provide design rules for targeted property engineering. Beyond the specific dopants investigated, the methodology established a general protocol for assessing substitutional defects in phase-change materials, including the treatment of charge compensation, local relaxation effects, and the coupling between electronic and structural degrees of freedom.

Investigating the kinetic pathways of the phase transition revealed a pronounced directionality that had been overlooked in previous theoretical treatments. By simulating the propagation of the β/λ phase interface along multiple crystallographic directions, it was shown that the activation barrier is highly dependent on the crystallographic orientation along which the phase transition proceeds, with the (001) direction exhibiting the lowest activation barrier among all sampled directions. This anisotropy explains the experimentally observed selection rules for photo-induced transitions, where laser excitation preferentially induces the transition in crystals oriented with their (001) planes perpendicular to the beam direction. The microscopic origin of this directional preference lies in the arrangement of Ti3 dimers within the crystal structure: along the (001) direction, these dimers are aligned such that cooperative rotation can occur with minimal disruption to the surrounding lattice, whereas transitions along other directions require the breaking and reformation of multiple Ti–O bonds. This insight highlights the limitations of isotropic bulk models in describing the dynamics of phase transitions in low-symmetry monoclinic crystals and underscores the necessity of explicitly considering interfacial effects in modeling phase transitions.

A major contribution of this work is the resolution of the thermal hysteresis phenomenon, which was previously conjectured to arise from nanoparticle properties. By calculating temperature-dependent surface free energies for all low-index facets and constructing Wulff shapes as a function of temperature, a thermodynamic crossover point was identified. λ-Ti_3O_5 nanoparticles below a critical diameter ($\approx$ 43 nm) are thermodynamically stabilized with respect to the β-phase by their overall free surface energy, preventing the reversion to the thermodynamically more favorable β-phase even when the bulk free energy difference would favor the transition. Particles with smaller diameters are predicted to transform from β- to the λ-phase at lower phase transition temperatures, with the magnitude of the temperature shift correlating inversely with particle diameter, in quantitative agreement with experimental observations. The model predicts that particles synthesized at the typical experimental scale (30–50 nm) transform at temperatures 20–30 K below the bulk transition temperature, consistent with experimental X-ray powder diffraction measurements.

This model provides a quantitative link between synthesis conditions (particle size) and storage performance (stability duration), enabling rational design of nanostructured heat-storage materials. Moreover, the framework developed here—combining surface thermodynamics with Wulff construction—is broadly applicable to other nanoscale phase-change materials where surface effects compete with bulk driving forces.

The following study addressed the "pressure gap"—the order-of-magnitude difference between theoretically predicted bulk transition pressures (10^4 bar) and experimental values (10^2 bar). By employing machine-learned interatomic potentials trained on high-level DFT data to simulate large-scale slab compression, combined with enhanced sampling techniques (OPES), the transition mechanism was identified as a surface-nucleated process. This represents a paradigm shift in understanding pressure-induced phase transitions in nanomaterials: the transition does not occur uniformly throughout the material but initiates at specific surface sites where the local atomic environment facilitates the structural rearrangement. The application of uniaxial pressure on specific facets lowers the free energy barrier significantly, accurately predicting the experimental pressure threshold of $\approx$ 600 bar and demonstrating that the sensitivity to pressure is an intrinsic feature of the nanoparticle surface rather than the bulk lattice. A universally applicable framework of quantifying the compression of a material's surface into a pressure value was proposed, linking calculation and experiment.

The findings of this thesis open several avenues for future research, ranging from methodological extensions to application-oriented material design. Future work should employ the here proposed methodological advancements to investigate the intricate interplay between the substituting element species, their accurate concentration, and resulting phase transition temperature, enthalpies and pressures. Specifically, the combined effect of multiple dopants (co-doping) remains unexplored. The established workflow combining MLIPs and OPES is ideally suited to explore the high-dimensional parameter space of doped surfaces under stress, potentially identifying synergistic combinations that outperform single-element

doping strategies.

The current models focused on isolated nanoparticles or single interfaces, whereas in practical heat-storage units, particles agglomerate, forming complex networks with grain boundaries that mediate stress transfer and heat flow. The inter-particle grain boundaries and the mechanics of sintering during repeated heating cycles has experimentally been shown to critically influence the heat-storage properties of a material. Understanding how the phase transition propagates across grain boundaries and whether grain boundary character (high-angle vs. low-angle, coherent vs. incoherent) affects the kinetics represents an important next step. Future more efficient machine-learned potentials extending the range of application to the dynamics of these mesoscopic systems should be employed here.

From a fundamental perspective, the coupling between the phase transition and other external stimuli—particularly electric fields and electromagnetic radiation beyond simple photothermal effects—deserves investigation. Ultrafast laser spectroscopy experiments have hinted at photoinduced phase transitions occurring on sub-picosecond timescales, far faster than can be explained by thermal mechanisms alone, suggesting direct electronic excitation pathways that remain to be theoretically characterized.

The methodological framework established here—hybrid functionals like M06-D3 for electronic structure, r^{2}SCAN-D3 for structures and energies, Wulff construction for finite-size thermodynamics, and MLIP-driven enhanced sampling for rare events—is highly transferable to other material systems. It should be applied to screen other transition metal oxides that exhibit metal-insulator transitions with potential thermal storage applications. The goal would be to identify new classes of phase-change materials that operate at different temperature ranges, specifically lower temperatures suitable for domestic heating (40–80 °C) or higher temperatures for industrial process heat (300–500 °C). The computational screening protocol developed here could evaluate candidate materials in silico before experimental synthesis, dramatically accelerating the materials discovery pipeline.

Beyond titanium oxides, the methodological advances regarding surface-mediated phase transitions have implications for catalysis, where analogous surface transformations under reactive atmospheres control catalyst activation and deactivation. The combination of surface thermodynamics, kinetic barriers, and particle size effects explored here provides a template for understanding restructuring phenomena in supported metal oxide catalysts.

Finally, moving towards the motivating vision of "thermal batteries" integrated into construction materials, theoretical models should investigate the interaction between Ti_3O_5 nanoparticles and potential matrices, such as cementitious materials or polymers. Understanding the chemical compatibility and mechanical stress transfer at the matrix-particle interface will be crucial for the successful deployment of these materials in the built environment. Multiscale modeling approaches that couple atomistic descriptions of the particle-matrix interface with continuum mechanics of the composite material will be necessary.

The work presented in this thesis demonstrates that modern computational materials science, combining accurate and robust electronic structure methods with machine learning and advanced sampling techniques, can explain experimentally unresolved observations and guide the rational design of functional materials.

Acknowledgements

At this point I would like to thank everybody who made this thesis possible and supported me along the way. First and foremost, I sincerely thank Prof. Dr. Thomas Bredow for welcoming me into his working group and offering me the opportunity to work on this interesting project. I was able to learn a lot from him and valued the time he took out of his busy schedule every week to meet with me and brainstorm about possible avenues to further my research progress. His permissiveness to let me explore alternative approaches, and patience amid my occasional stubbornness, both personally and scientifically enriched my time under his supervision.

I also want to express my gratitude to Prof. Dr. Stefan Grimme for giving me the opportunity to work on my Bachelor's and Master's thesis in his working group and for agreeing to be the second referee to this thesis. Moreover, I thank Prof. Dr. Sigurd Höger and PD Dr. Elisabeth Soergel for agreeing to evaluate my thesis as part of my doctoral committee.

During the initial three years of my studies I was honored to be part of the International Max Planck Research School on Reactive Structure Analysis for Chemical Reactions (IMPRS-RECHARGE), where I was fortunate to be part of a diverse cohort of motivated students from the partnering universities and could participate in various events, which further refined my personal and scientific profile, in addition to providing funding for my studies. Here, I want to thank Prof. Dr. Martin Muhler and Prof. Dr. Alexander Auer for providing valuable input during our Thesis Advisory Committee meetings. Moreover, I want to thank my colleagues from Bonn Berenike Stahl, Henrik Niemöller and Tom Frömbgen, and my entire cohort for the joint experience.

I want to thank Dr. Benjamin Grimm for our scientific and wordly discussions as well as our friendly chess matches in the top floor of the institute. Furthermore, I am thankful to former and present members of the Bredow working group, in particular Ritu Tomar and Hirshita Malik, whose participation in our group meetings broadened my understanding of other cultures and whose presence I thoroughly enjoyed during my time in the working group.

During my Bachelor's and Master's thesis I had the opportunity to work alongside exceptional colleagues who provided valuable input for my work, including but not limited to, Sebastian Dohm, Eike Caldeweyher and Sebastian Ehlert.

I thank Jens Mekelburger for helping with technical issues I encountered during my studies.

I am deeply grateful to Dr. Peitao Liu for his invaluable collaboration on one of the more demanding phases of this research. His expertise and guidance turned a significant challenge into a profound learning opportunity. In this context I would like to express my gratitude to the staff at the Hochschulrechenzentrum for their generous allocation of resources on the Marvin HPC cluster, which was essential to the computational demands of this work.

Lastly, I want to thank my family for their unconditional and generous support during this time and my girlfriend Simin You for her love and for being my greatest source of motivation.

Bibliography

[1] Eurostat, *Shedding light on energy in the EU: A guided tour of energy statistics*, https://ec.europa.eu/eurostat/web/interactive-publications/energy-2023, 2023, DOI: 10.2785/8045944.

[2] B. V. Mathiesen, H. Lund, D. Connolly, H. Wenzel, P. A. Østergaard, B. Möller, S. Nielsen, I. Ridjan, P. Karnøe, K. Sperling, and F. Hvelplund, *Smart Energy Systems for coherent 100% renewable energy and transport solutions*, Appl. Energy **145**, 139–154 (2015), DOI: 10.1016/j.apenergy.2015.01.075.

[3] Eurostat, *Energy consumption in households*, https://ec.europa.eu/eurostat/statistics-explained/index.php?title=Energy_consumption_in_households, Accessed on 25 Nov 2025. Data retrieved for year 2023, 2024.

[4] Eurostat, *Final energy consumption in industry - detailed statistics*, https://ec.europa.eu/eurostat/statistics-explained/index.php?title=Final_energy_consumption_in_industry_-_detailed_statistics, Accessed on 25 Nov 2025, 2024.

[5] T. Naegler, S. Simon, M. Klein, and H. C. Gils, *Quantification of the European industrial heat demand by branch and temperature level*, Int. J. Energy Res. **39**, 2019–2030 (2015), DOI: 10.1002/er.3436.

[6] A. Colmenar-Santos, E. Rosales-Asensio, D. Borge-Diez, and J.-J. Blanes-Peiró, *District heating and cogeneration in the EU-28: Current situation, potential and proposed energy strategy for its generalisation*, Renew. Sustain. Energy Rev. **62**, 621–639 (2016), DOI: 10.1016/j.rser.2016.05.004.

[7] Eurostat, *Renewable energy statistics*, https://ec.europa.eu/eurostat/statistics-explained/index.php?title=Renewable_energy_statistics, Accessed on 25 Nov 2025. Share of energy from renewable sources for heating and cooling, 2024.

[8] K. Pielichowska and K. Pielichowski, *Phase change materials for thermal energy storage*, Prog. Mater. Sci. **65**, 67–123 (2014), DOI: 10.1016/j.pmatsci.2014.03.005.

[9] H. Zhang, J. Baeyens, G. Cáceres, J. Degrève, and Y. Lv, *Thermal energy storage: Recent developments and practical aspects*, Prog. Energy Combust. Sci. **53**, 1–40 (2016), DOI: 10.1016/j.pecs.2015.10.003.

[10] Odyssee-Mure, *Heating energy consumption by energy source*, https://www.odyssee-mure.eu/publications/efficiency-by-sector/households/heating-energy-consumption-by-energy-sources.html, Accessed on 25 Nov 2025. Sectoral Profile - Households, 2024.

[11] I. E. Agency, *Energy Efficiency 2023*, https://www.iea.org/reports/energy-efficiency-2023, Accessed on 25 Nov 2025. IEA Report, Paris, 2023.

[12] I. Sarbu, in *Advances in Building Services Engineering: Studies, Researches and Applications* (Springer, 2021), pp. 559–627, DOI: 10.1007/978-3-030-64781-0_7.

[13] D. Lindley, *The energy should always work twice*, Nature **458**, 138–141 (2009), DOI: 10.1038/458138a.

[14] E. Cartlidge, *Saving for a Rainy Day*, Science **334**, 922–924 (2011), DOI: 10.1126/science.334.6058.922.

[15] A. S. Rattner and S. Garimella, *Energy harvesting, reuse and upgrade to reduce primary energy usage in the USA*, Energy **36**, 6172–6183 (2011), DOI: 10.1016/j.energy.2011.07.047.

[16] D. B. Gingerich and M. S. Mauter, *Quantity, quality, and availability of waste heat from United States thermal power generation*, Environ. Sci. Technol. **49**, 8297–8306 (2015), DOI: 10.1021/es5060989.

[17] I. Gur, K. Sawyer, and R. Prasher, *Searching for a Better Thermal Battery*, Science **335**, 1454–1455 (2012), DOI: 10.1126/science.1218761.

[18] D. Butler, *Solar power: California's latest gold rush.*, Nature **450**, 768–768 (2007), DOI: 10.1038/450768a.

[19] A. Sharma, V. V. Tyagi, C. R. Chen, and D. Buddhi, *Review on thermal energy storage with phase change materials and applications*, Renew. Sustain. Energy Rev. **13**, 318–345 (2009), DOI: 10.1016/j.rser.2007.10.005.

[20] M. Farid, A. M. Khudhair, S. A. K. Razack, and S. Al-Hallaj, *A review on phase change energy storage: materials and applications*, Energy Convers. Manag., 4–23 (2021), DOI: 10.1016/j.enconman.2003.09.015.

[21] Q. Cao and P. Liu, *Hyperbranched polyurethane as novel solid–solid phase change material for thermal energy storage*, Eur. Polym. J. **42**, 2931–2939 (2006), DOI: 10.1016/j.eurpolymj.2006.07.020.

[22] D. Benson, R. Burrows, and J. Webb, *Solid state phase transitions in pentaerythritol and related polyhydric alcohols*, Sol. Energ. Mater. **13**, 133–152 (1986), DOI: 10.1016/0165-1633(86)90040-7.

[23] M. Barrio, D. López, J. L. Tamarit, P. Negrier, and Y. Haget, *Molecular interactions and packing in molecular alloys between nonisomorphous plastic phases*, J. Solid State Chem. **124**, 29–38 (1996), DOI: 10.1006/jssc.1996.0203.

[24] V. Busico, C. Carfagna, V. Salerno, M. Vacatello, and F. Fittipaldi, *The layer perovskites as thermal energy storage systems*, Sol. Energy **24**, 575–579 (1980), DOI: 10.1016/0038-092X(80)90356-4.

[25] W. Li, D. Zhang, T. Zhang, T. Wang, D. Ruan, D. Xing, and H. Li, *Study of solid–solid phase change of $(n\text{-}C_nH_{2n+1}NH_3)_2MCl_4$ for thermal energy storage*, Thermochim. Acta **326**, 183–186 (1999), DOI: 10.1016/S0040-6031(98)00497-3.

[26] G. Van Den Branden, M. Hesius, and W. D'haeseleer, *Comparison of heat storage systems employing sensible and latent heat*, Int. J. Energy Res. **23**, 605–624 (1999), DOI: 10.1002/(SICI)1099-114X(19990610)23:7<605::AID-ER496>3.0.CO;2-7.

[27] S. Åsbrink and A. Magnéli, *Crystal structure studies on trititanium pentoxide, Ti_3O_5*, Acta Cryst. **12**, 575–581 (1959), DOI: 10.1107/S0365110X59001694.

[28] S.-i. Ohkoshi, Y. Tsunobuchi, T. Matsuda, K. Hashimoto, A. Namai, F. Hakoe, and H. Tokoro, *Synthesis of a metal oxide with a room-temperature photoreversible phase transition*, Nat. Chem. **2**, 539–545 (2010), DOI: 10.1038/nchem.670.

[29] H. Tokoro, M. Yoshikiyo, K. Imoto, A. Namai, T. Nasu, K. Nakagawa, N. Ozaki, F. Hakoe, K. Tanaka, K. Chiba, et al., *External stimulation-controllable heat-storage ceramics*, Nat. Comm. **6**, 7037 (2015), DOI: 10.1038/ncomms8037.

[30] S.-i. Ohkoshi, H. Tokoro, K. Nakagawa, M. Yoshikiyo, F. Jia, and A. Namai, *Low-pressure-responsive heat-storage ceramics for automobiles*, Sci. Rep. **9**, 13203 (2019), DOI: 10.1038/s41598-019-49690-0.

[31] F. Jia, M. Yoshikiyo, R. Makuta, K. Kawakami, H. Tokoro, and S.-i. Ohkoshi, *Observation of a Pressure Effect on an Al-substituted λ-Ti_3O_5 Heat-storage Material*, Chem. Lett. **52**, 748–751 (2023), DOI: 10.1246/cl.230244.

[32] P. Zhao, G. Li, X. Xiong, P. Cheng, Z. Pang, C. Sun, H. Cheng, C. Shi, X. Yu, Q. Xu, et al., *Sub-minute synthesis and modulation of β/λ-$M_xTi_{3-x}O_5$ ceramics towards accessible heat storage*, Nat. Commun. **16**, 2443 (2025), DOI: 10.1038/s41467-025-57604-0.

[33] S.-i. Ohkoshi, F. Jia, M. Yoshikiyo, K. Imoto, H. Tokoro, K. Nakagawa, Y. Maeno, A. Namai, R. Harada, K. Hattori, et al., *Pressure effect on long-term heat storage ceramics based on Mg-substituted λ-Ti_3O_5*, Mater. Adv. **3**, 4824–4830 (2022), DOI: 10.1039/D2MA00278G.

[34] Y. Nakamura, Y. Sakai, M. Azuma, and S.-i. Ohkoshi, *Long-term heat-storage ceramics absorbing thermal energy from hot water*, Sci. Adv. **6**, eaaz5264 (2020), DOI: 10.1126/sciadv.aaz5264.

[35] T. Otake, L. Wang, F. Jia, M. Yoshikiyo, K. Kawakami, A. Namai, H. Tokoro, and S.-i. Ohkoshi, *Long-term heat-storage ceramics based on Zr-Substituted λ-Ti_3O_5*, Eur. J. Inorg. Chem. **27**, e202400047 (2024), DOI: 10.1002/ejic.202400047.

[36] M. Kenisarin and K. Mahkamov, *Salt hydrates as latent heat storage materials: Thermophysical properties and costs*, Sol. Energ. Mat. Sol. Cells **145**, 255–286 (2016), DOI: 10.1016/j.solmat.2015.10.029.

[37] E. Schrödinger, *Quantisierung als Eigenwertproblem*, Ann. Phys. **385**, 437–490 (1926), DOI: 10.1002/andp.19263840404.

[38] M. Born and R. Oppenheimer, *Zur Quantentheorie der Molekeln*, Ann. Phys. **389**, 457–484 (1927), DOI: 10.1002/andp.19273892002.

[39] W. Pauli, *Über den Zusammenhang des Abschlusses der Elektronengruppen im Atom mit der Komplexstruktur der Spektren*, Z. Phys. **31**, 765–783 (1925), DOI: 10.1007/BF02980631.

[40] J. C. Slater, *The theory of complex spectra*, Phys. Rev. **34**, 1293 (1929), DOI: 10.1103/PhysRev.34.1293.

[41] P. Hohenberg and W. Kohn, *Inhomogeneous electron gas*, Phys. Rev. **136**, B864 (1964), DOI: 10.1103/PhysRev.136.B864.

[42] W. Kohn and L. J. Sham, *Self-consistent equations including exchange and correlation effects*, Phys. Rev. **140**, A1133 (1965), DOI: 10.1103/PhysRev.140.A1133.

[43] J. P. Perdew and K. Schmidt, "Jacob's ladder of density functional approximations for the exchange-correlation energy", in AIP conference proceedings, Vol. 577, 1 (American Institute of Physics, 2001), pp. 1–20, DOI: 10.1063/1.1390175.

[44] P. A. Dirac, "Note on exchange phenomena in the Thomas atom", in Mathematical proceedings of the Cambridge philosophical society, Vol. 26, 3 (Cambridge University Press, 1930), pp. 376–385, DOI: 10.1017/S0305004100016108.

[45] J. P. Perdew, K. Burke, and M. Ernzerhof, *Generalized gradient approximation made simple*, Phys. Rev. Lett. **77**, 3865 (1996), DOI: 10.1103/PhysRevLett.77.3865.

[46] J. W. Furness, A. D. Kaplan, J. Ning, J. P. Perdew, and J. Sun, *Accurate and numerically efficient r2SCAN meta-generalized gradient approximation*, J. Phys. Chem. Lett. **11**, 8208–8215 (2020), DOI: 10.1021/acs.jpclett.0c02405.

[47] C. Adamo and V. Barone, *Toward reliable density functional methods without adjustable parameters: The PBE0 model*, J. Chem. Phys. **110**, 6158–6170 (1999), DOI: 10.1063/1.478522.

[48] M. Ernzerhof and G. E. Scuseria, *Assessment of the Perdew–Burke–Ernzerhof exchange-correlation functional*, J. Chem. Phys. **110**, 5029–5036 (1999), DOI: 10.1063/1.478401.

[49] A. D. Becke, *Density-functional thermochemistry. V. Systematic optimization of exchange-correlation functionals*, J. Chem. Phys. **107**, 8554–8560 (1997), DOI: 10.1063/1.475007.

[50] J.-D. Chai and M. Head-Gordon, *Long-range corrected hybrid density functionals with damped atom–atom dispersion corrections*, Phys. Chem. Chem. Phys. **10**, 6615–6620 (2008), DOI: 10.1039/b810189b.

[51] S. Grimme, A. Hansen, J. G. Brandenburg, and C. Bannwarth, *Dispersion-corrected mean-field electronic structure methods*, Chem. Rev. **116**, 5105–5154 (2016), DOI: 10.1021/acs.chemrev.5b00533.

[52] C. Møller and M. S. Plesset, *Note on an approximation treatment for many-electron systems*, Phys. Rev. **46**, 618 (1934), DOI: 10.1103/PhysRev.46.618.

[53] S. Grimme, J. Antony, S. Ehrlich, and H. Krieg, *A consistent and accurate ab initio parametrization of density functional dispersion correction (DFT-D) for the 94 elements H-Pu*, J. Chem. Phys. **132**, DOI: 10.1063/1.3382344 (2010), DOI: 10.1063/1.3382344.

[54] S. Grimme, S. Ehrlich, and L. Goerigk, *Effect of the damping function in dispersion corrected density functional theory*, J. Comput. Chem. **32**, 1456–1465 (2011), DOI: 10.1002/jcc.21759.

[55] E. Caldeweyher, S. Ehlert, A. Hansen, H. Neugebauer, S. Spicher, C. Bannwarth, and S. Grimme, *A generally applicable atomic-charge dependent London dispersion correction*, J. Chem. Phys. **150**, DOI: 10.1063/1.5090222 (2019), DOI: 10.1063/1.5090222.

[56] B. Axilrod and E. Teller, *Interaction of the van der Waals type between three atoms*, J. Chem. Phys. **11**, 299–300 (1943), DOI: 10.1063/1.1723844.

[57] Y. Muto, "Force between nonpolar molecules", in Proc. Phys. Math. Soc. Jpn, Vol. 17 (1943), pp. 629–631.

[58] V. L. Deringer, M. A. Caro, and G. Csányi, *Machine learning interatomic potentials as emerging tools for materials science*, Adv. Mater. **31**, 1902765 (2019), DOI: 10.1002/adma.201902765.

[59] Y. Zuo, C. Chen, X. Li, Z. Deng, Y. Chen, J. Behler, G. Csányi, A. V. Shapeev, A. P. Thompson, M. A. Wood, et al., *Performance and cost assessment of machine learning interatomic potentials*, J. Phys. Chem. A **124**, 731–745 (2020), DOI: 10.1021/acs.jpca.9b08723.

[60] D. Marx and J. Hutter, *Ab initio molecular dynamics: Theory and Implementation*, Mod. Methods Algorithms Quantum Chem. **1**, 301–449 (2000).

[61] V. Bolnykh et al., *Extreme Scalability of DFT-Based QM/MM MD Simulations Using MiMiC*, J. Chem. Theory Comput. **15**, 5601–5613 (2019), DOI: 10.1021/acs.jctc.9b00424.

[62] C. Bannwarth, E. Caldeweyher, S. Ehlert, A. Hansen, P. Pracht, J. Seibert, S. Spicher, and S. Grimme, *Extended tight-binding quantum chemistry methods*, Wiley Interdiscip. Rev. Comput. Mol. Sci. **11**, e1493 (2021), DOI: 10.1002/wcms.1493.

[63] A. Buccheri, R. Li, J. E. Deustua, S. M. Moosavi, P. J. Bygrave, and F. R. Manby, *Periodic GFN1-xTB Tight Binding: A Generalized Ewald Partitioning Scheme for the Klopman–Ohno Function*, J. Chem. Theory Comput. **21**, 1615–1625 (2025), DOI: 10.1021/acs.jctc.4c01234.

[64] I. Batatia, P. Benner, Y. Chiang, A. M. Elena, D. P. Kovács, J. Riebesell, X. R. Advincula, M. Asta, M. Avaylon, W. J. Baldwin, et al., *A foundation model for atomistic materials chemistry*, J. Chem. Phys. **163**, DOI: 10.1063/5.0297006 (2025), DOI: 10.1063/5.0297006.

[65] A. C. T. van Duin, S. Dasgupta, F. Lorant, and W. A. Goddard, *ReaxFF: A Reactive Force Field for Hydrocarbons*, J. Phys. Chem. A **105**, 9396–9409 (2001), DOI: 10.1021/jp004368u.

[66] J. L. Klepeis, K. Lindorff-Larsen, R. O. Dror, and D. E. Shaw, *Long-timescale molecular dynamics simulations of protein structure and function*, Curr. Opin. Struct. Biol. **19**, 120–127 (2009), DOI: 10.1016/j.sbi.2009.03.004.

[67] S. J. Marrink and D. P. Tieleman, *Perspective on the Martini model*, Chem. Soc. Rev. **42**, 6801–6822 (2013), DOI: 10.1039/c3cs60093a.

[68] A. V. Shapeev, *Moment Tensor Potentials: a systematic construction of symmetry-adapted polynomial basis for the energy of atomistic systems*, Multiscale Model. Simul. **14**, 202–232 (2016), DOI: 10.1137/15M1043315.

[69] E. V. Podryabinkin and A. V. Shapeev, *Active learning of linearly parametrized interatomic potentials*, Comput. Mater. Sci. **140**, 171–180 (2017), DOI: 10.1016/j.commatsci.2017.08.031.

[70] A. Grisafi and M. Ceriotti, *Incorporating long-range physics in atomic-scale machine learning*, J. Chem. Phys. **151**, DOI: 10.1063/1.5128375 (2019), DOI: 10.1063/1.5128375.

[71] T. W. Ko, J. A. Finkler, S. Goedecker, and J. Behler, *General-purpose machine learning potentials capturing nonlocal charge transfer*, Acc. Chem. Res. **54**, 808–817 (2021), DOI: 10.1021/acs.accounts.0c00689.

[72] D. M. Anstine and O. Isayev, *Machine learning interatomic potentials and long-range physics*, J. Phys. Chem. A **127**, 2417–2431 (2023), DOI: 10.1021/acs.jpca.2c06778.

[73] D. S. King, D. Kim, P. Zhong, and B. Cheng, *Machine learning of charges and long-range interactions from energies and forces*, Nat. Commun. **16**, 8763 (2025), DOI: 10.1038/s41467-025-63852-x.

[74] J. Thomas, W. Baldwin, G. Csanyi, and C. Ortner, *Self-consistent Coulomb interactions for machine learning interatomic potentials*, Nonlinearity **38**, 095024 (2025), DOI: 10.1088/1361-6544/ae0402.

[75] Y. Ji, J. Liang, and Z. Xu, *Machine-learning interatomic potentials for long-range systems*, Phys. Rev. Lett. **135**, 178001 (2025), DOI: 10.1103/ssp9-7s81.

[76] I. Novikov, B. Grabowski, F. Körmann, and A. Shapeev, *Magnetic Moment Tensor Potentials for collinear spin-polarized materials reproduce different magnetic states of bcc Fe*, npj Comput. Mater. **8**, 13 (2022), DOI: 10.1038/s41524-022-00696-9.

[77] M. Eckhoff and J. Behler, *High-dimensional neural network potentials for magnetic systems using spin-dependent atom-centered symmetry functions*, npj Comput. Mater. **7**, 170 (2021), DOI: 10.1038/s41524-021-00636-z.

[78] C. Kittel and P. McEuen, *Introduction to solid state physics* (John Wiley & Sons, 2018).

[79] N. W. Ashcroft and N. D. Mermin, *Solid State Physics* (Saunders College Publishing, Philadelphia, 1976), DOI: 10.1002/piuz.19780090109.

[80] M. Born and T. von Kármàn, *Über Schwingungen in Raumgittern*, Phys. Z. **13**, 297–309 (1912).

[81] F. Bloch, *Über die Quantenmechanik der Elektronen in Kristallgittern*, Z. Phys. **52**, 555–600 (1928), DOI: 10.1007/BF01339455.

[82] G. Kresse and D. Joubert, *From ultrasoft pseudopotentials to the projector augmented-wave method*, Phys. Rev. B **59**, 1758–1775 (1999), DOI: 10.1103/PhysRevB.59.1758.

[83] M. F. Peintinger, D. V. Oliveira, and T. Bredow, *Consistent Gaussian basis sets of triple-zeta valence with polarization quality for solid-state calculations*, J. Comput. Chem. **34**, 451–459 (2013), DOI: 10.1002/jcc.23153.

[84] J. Laun, D. Vilela Oliveira, and T. Bredow, *Consistent gaussian basis sets of double-and triple-zeta valence with polarization quality of the fifth period for solid-state calculations*, J. Comput. Chem. **39**, 1285–1290 (2018), DOI: 10.1002/jcc.25195.

[85] D. Vilela Oliveira, J. Laun, M. F. Peintinger, and T. Bredow, *BSSE-correction scheme for consistent gaussian basis sets of double-and triple-zeta valence with polarization quality for solid-state calculations*, J. Comput. Chem. **40**, 2364–2376 (2019), DOI: 10.1002/jcc.26013.

[86] J. Laun and T. Bredow, *BSSE-corrected consistent Gaussian basis sets of triple-zeta valence with polarization quality of the sixth period for solid-state calculations*, J. Comput. Chem. **42**, 1064–1072 (2021), DOI: 10.1002/jcc.26521.

[87] J. Laun and T. Bredow, *BSSE-corrected consistent Gaussian basis sets of triple-zeta valence with polarization quality of the fifth period for solid-state calculations*, J. Comput. Chem. **43**, 839–846 (2022), DOI: 10.1002/jcc.26839.

[88] L. M. Seidler, J. Laun, and T. Bredow, *BSSE-corrected consistent Gaussian basis sets of triple-zeta valence quality of the lanthanides La-Lu for solid-state calculations*, J. Comput. Chem. **44**, 1418–1425 (2023), DOI: 10.1002/jcc.27097.

[89] B. J. Alder and T. E. Wainwright, *Studies in Molecular Dynamics. I. General Method*, J. Chem. Phys. **31**, 459–466 (1959), DOI: 10.1063/1.1730376.

[90] T. Darden, D. York, and L. Pedersen, *Particle mesh Ewald: An $N \cdot \log(N)$ method for Ewald sums in large systems*, J. Chem. Phys. **98**, 10089–10092 (1993), DOI: 10.1063/1.464397.

[91] L. Verlet, *Computer "Experiments" on Classical Fluids. I. Thermodynamical Properties of Lennard-Jones Molecules*, Phys. Rev. **159**, 98–103 (1967), DOI: 10.1103/PhysRev.159.98.

[92] W. C. Swope, H. C. Andersen, P. H. Berens, and K. R. Wilson, *A computer simulation method for the calculation of equilibrium constants for the formation of physical clusters of molecules: Application to small water clusters*, J. Chem. Phys. **76**, 637–649 (1982), DOI: 10.1063/1.442716.

[93] S. Nosé, *A unified formulation of the constant temperature molecular dynamics methods*, J. Chem. Phys. **81**, 511–519 (1984), DOI: 10.1063/1.447334.

[94] W. G. Hoover, *Canonical dynamics: Equilibrium phase-space distributions*, Phys. Rev. A **31**, 1695–1697 (1985), DOI: 10.1103/PhysRevA.31.1695.

[95] M. Parrinello and A. Rahman, *Polymorphic transitions in single crystals: A new molecular dynamics method*, J. Appl. Phys. **52**, 7182–7190 (1981), DOI: 10.1063/1.328693.

[96] G. M. Torrie and J. P. Valleau, *Nonphysical sampling distributions in Monte Carlo free-energy estimation: Umbrella sampling*, J. Comput. Phys. **23**, 187–199 (1977), DOI: 10.1016/0021-9991(77)90121-8.

[97] A. Laio and M. Parrinello, *Escaping free-energy minima*, Proc. Natl. Acad. Sci. **99**, 12562–12566 (2002), DOI: 10.1073/pnas.202427399.

[98] M. Invernizzi and M. Parrinello, *Rethinking metadynamics: from bias potentials to probability distributions*, J. Phys. Chem. Lett. **11**, 2731–2736 (2020), DOI: 10.1021/acs.jpclett.0c00497.

[99] M. Invernizzi, P. M. Piaggi, and M. Parrinello, *Unified approach to enhanced sampling*, Phys. Rev. X **10**, 041034 (2020), DOI: 10.1103/PhysRevX.10.041034.

[100] M. Invernizzi and M. Parrinello, *Exploration vs convergence speed in adaptive-bias enhanced sampling*, J. Chem. Theory Comput. **18**, 3988–3996 (2022), DOI: 10.1021/acs.jctc.2c00152.

[101] A. Barducci, G. Bussi, and M. Parrinello, *Well-tempered metadynamics: a smoothly converging and tunable free-energy method*, Phys. Rev. Lett. **100**, 020603 (2008), DOI: 10.1103/PhysRevLett.100.020603.

[102] V. I. Anisimov, J. Zaanen, and O. K. Andersen, *Band theory and Mott insulators: Hubbard U instead of Stoner I*, Phys. Rev. B **44**, 943 (1991), DOI: 10.1103/PhysRevB.44.943.

[103] R. Liu and J.-X. Shang, *First-principles study of thermal properties and phase transition between β-Ti_3O_5 and λ-Ti_3O_5*, Model. Simul. Mater. Sci. Eng. **20**, 035020 (2012), DOI: 10.1016/j.commatsci.2013.08.001.

[104] R. Liu, J.-X. Shang, and F.-H. Wang, *Electronic, magnetic and optical properties of β-Ti3O5 and λ-Ti3O5: A density functional study*, Comput. Mater. Sci. **81**, 158–162 (2014), DOI: 10.1016/j.commatsci.2013.08.001.

[105] X. Fu, W. Chen, Z. Jiang, B. Yang, X. Zhao, and L. Zuo, *First-principles investigation on elastic, electronic, and optical properties of Ti_3O_5*, Acta Phys. Sin **68**, 207301 (2019), DOI: 10.7498/aps.68.20190664.

[106] X.-K. Fu, B. Yang, W.-Q. Chen, Z.-S. Jiang, Z.-B. Li, H.-L. Yan, X. Zhao, and L. Zuo, *Evidence for bandwidth-control metal-insulator transition in Ti3O5*, Comput. Mater. Sci. **173**, 109435 (2020), DOI: 10.1016/j.commatsci.2019.109435.

[107] X. Fu, X. Hao, W. Chen, B. Yang, X. Zhao, and L. Zuo, *Influences of hole/electron-lattice coupling on phase transition between λ-Ti3O5 and β-Ti3O5*, J. Phys. Condens. Matter **32**, 46LT01 (2020), DOI: 10.1088/1361-648X/abacae.

[108] Y. Zhao and D. G. Truhlar, *The M06 suite of density functionals for main group thermochemistry, thermochemical kinetics, noncovalent interactions, excited states, and transition elements: two new functionals and systematic testing of four M06-class functionals and 12 other functionals*, Theor. Chem. Acc. **120**, 215–241 (2008), DOI: 10.1007/s00214-007-0310-x.

[109] D. Sheppard, P. Xiao, W. Chemelewski, D. D. Johnson, and G. Henkelman, *A generalized solid-state nudged elastic band method*, J. Chem. Phys. **136**, DOI: 10.1063/1.3684549 (2012), DOI: 10.1063/1.3684549.

[110] K. Yoshimatsu and H. Kumigashira, *Direct Synthesis of Metastable λ-Phase Ti3O5 Films on LaAlO3 (110) Substrates at High Temperatures*, Cryst. Growth Des. **22**, 703–710 (2021), DOI: 10.1021/acs.cgd.1c01214.

[111] A. D. Becke, *Density-functional thermochemistry. I. The effect of the exchange-only gradient correction*, J. Chem. Phys. **96**, 2155–2160 (1992), DOI: 10.1063/1.462066.

[112] S. H. Vosko, L. Wilk, and M. Nusair, *Accurate spin-dependent electron liquid correlation energies for local spin density calculations: a critical analysis*, Can. J. Phys. **58**, 1200–1211 (1980), DOI: 10.1139/p80-159.

[113] J. P. Perdew and Y. Wang, *Pair-distribution function and its coupling-constant average for the spin-polarized electron gas*, Phys. Rev. B **46**, 12947 (1992), DOI: 10.1103/PhysRevB.46.12947.

[114] J. P. Perdew and W. Yue, *Accurate and simple density functional for the electronic exchange energy: Generalized gradient approximation*, Phys. Rev. B **33**, 8800 (1986), DOI: 10.1103/PhysRevB.33.8800.

[115] T. Bredow and A. R. Gerson, *Effect of exchange and correlation on bulk properties of MgO, NiO, and CoO*, Phys. Rev. B **61**, 5194 (2000), DOI: 10.1103/PhysRevB.61.5194.

[116] F. A. Hamprecht, A. J. Cohen, D. J. Tozer, and N. C. Handy, *Development and assessment of new exchange-correlation functionals*, J. Chem. Phys. **109**, 6264–6271 (1998), DOI: 10.1063/1.477267.

[117] A. V. Krukau, O. A. Vydrov, A. F. Izmaylov, and G. E. Scuseria, *Influence of the exchange screening parameter on the performance of screened hybrid functionals*, J. Chem. Phys. **125**, DOI: 10.1063/1.2404663 (2006), DOI: 10.1063/1.2404663.

[118] Z. Shen, Q. Shi, W. Huang, B. Huang, M. Wang, J. Gao, Y. Shi, and T. Lu, *Stabilization of microcrystal λ-Ti_3O_5 at room temperature by aluminum-ion doping*, Appl. Phys. Lett. **111**, 191902 (2017), DOI: 10.1063/1.5010684.

[119] S. Ehlert, U. Huniar, J. Ning, J. W. Furness, J. Sun, A. D. Kaplan, J. P. Perdew, and J. G. Brandenburg, *r2SCAN-D4: Dispersion corrected meta-generalized gradient approximation for general chemical applications*, J. Chem. Phys. **154**, DOI: 10.1063/5.0041008 (2021), DOI: 10.1063/5.0041008.

[120] R. Makiura, Y. Takabayashi, A. N. Fitch, H. Tokoro, S.-i. Ohkoshi, and K. Prassides, *Nanoscale Effects on the Stability of the λ-Ti3O5 Polymorph*, Chem. – Asian J. **6**, 1886–1890 (2011), DOI: 10.1002/asia.201100125.

[121] T. Saiki, T. Yoshida, K. Akimoto, D. Indo, M. Arizono, T. Okuda, and T. Katsufuji, *Selection rule for the photoinduced phase transition dominated by anisotropy of strain in Ti_3O_5*, Phys. Rev. B **105**, 075134 (2022), DOI: 10.1103/PhysRevB.105.075134.

[122] R. Jinnouchi, J. Lahnsteiner, F. Karsai, G. Kresse, and M. Bokdam, *Phase transitions of hybrid perovskites simulated by machine-learning force fields trained on the fly with Bayesian inference*, Phys. Rev. Lett. **122**, 225701 (2019), DOI: 10.1103/PhysRevLett.122.225701.

[123] R. Jinnouchi, F. Karsai, and G. Kresse, *On-the-fly machine learning force field generation: Application to melting points*, Phys. Rev. B **100**, 014105 (2019), DOI: 10.1103/PhysRevB.100.014105.

[124] R. Jinnouchi, F. Karsai, C. Verdi, R. Asahi, and G. Kresse, *Descriptors representing two-and three-body atomic distributions and their effects on the accuracy of machine-learned inter-atomic potentials*, J. Chem. Phys. **152**, DOI: 10.1063/5.0009491 (2020), DOI: 10.1063/5.0009491.

[125] C. Mariette, M. Lorenc, H. Cailleau, E. Collet, L. Guérin, A. Volte, E. Trzop, R. Bertoni, X. Dong, B. Lépine, et al., *Strain wave pathway to semiconductor-to-metal transition revealed by time-resolved X-ray powder diffraction*, Nat. Commun. **12**, 1239 (2021), DOI: 10.1038/s41467-021-21316-y.

[126] T. Nasu, H. Tokoro, K. Tanaka, F. Hakoe, A. Namai, and S. Ohkoshi, "Sol–gel synthesis of nanosized λ-Ti_3O_5 crystals", in IOP Conf. Ser.: Mater. Sci. Eng. Vol. 54, 1 (IOP Publishing, 2014), p. 012008, DOI: 10.1088/1757-899X/54/1/012008.

[127] G. Chai, W. Huang, Q. Shi, S. Zheng, and D. Wei, *Preparation and characterization of λ-Ti_3O_5 by carbothermal reduction of TiO_2*, J. Alloys. Compd. **621**, 404–410 (2015), DOI: 10.1016/j.jallcom.2014.10.011.

[128] Y. Cai, Q. Shi, M. Wang, X. Lv, Y. Cheng, and W. Huang, *Synthesis of nanoscale λ-Ti_3O_5 via a PEG assisted sol-gel method*, J. Alloys Compd. **848**, 156585 (2020), DOI: 10.1016/j.jallcom.2020.156585.

[129] Y. Araki, S. Ohkoshi, and H. Tokoro, *Synthesis of λ-Ti_3O_5 nanocrystals using a block copolymer*, Mater. Today Energy **18**, 100525 (2020), DOI: 10.1016/j.mtener.2020.100525.

[130] T. Kubota, R. Seiki, A. Fujisawa, A. F. Fadilla, F. Jia, S.-i. Ohkoshi, and H. Tokoro, *Synthesis of heat storage ceramic λ-Ti_3O_5 using titanium chloride as the starting material*, Mater. Adv. **5**, 3832–3837 (2024), DOI: 10.1039/D3MA01162C.

[131] G. Wulff, *On the question of speed of growth and dissolution of crystal surfaces*, Z. Kristallogr.–Cryst. Mater. **34**, 449 (1901).

[132] S. Jütten and T. Bredow, *First-principles investigation of electronic properties and phase transition of Ti_3O_5*, J. Phys. Chem. C **126**, 7809–7817 (2022), DOI: 10.1021/acs.jpcc.2c00572.

[133] A. Navrotsky, *Nanoscale effects on thermodynamics and phase equilibria in oxide systems*, ChemPhysChem **12**, 2207–2215 (2011), DOI: 10.1002/cphc.201100129.

[134] S. Jütten and T. Bredow, *Anisotropy of the pressure effect in the Ti3O5 phase transition process resolved by direction-dependent interface propagation*, J. Phys. Chem. C **127**, 20530–20538 (2023), DOI: 10.1021/acs.jpcc.3c04986.

[135] M. Liu, J. Wang, J. Hu, P. Liu, H. Niu, X. Yan, J. Li, H. Yan, B. Yang, Y. Sun, et al., *Layer-by-layer phase transformation in Ti3O5 revealed by machine-learning molecular dynamics simulations*, Nat. Commun. **15**, 3079 (2024), DOI: 10.1038/s41467-024-47422-1.

[136] A. V. Shapeev, *Moment tensor potentials: a class of systematically improvable interatomic potentials*, Multiscale Model Simul. **14**, 1153–1173 (2016), DOI: 10.1137/15M1054183.

[137] J. Wang, P. Liu, H. Zhu, M. Liu, H. Ma, Y. Chen, Y. Sun, and X.-Q. Chen, *Efficient moment tensor machine-learning interatomic potential for accurate description of defects in Ni-Al Alloys*, Phys. Rev. Mater. **9**, 053805 (2025), DOI: 10.1103/PhysRevMaterials.9.053805.

[138] G. A. Henkelman, B. P. Uberuaga, and H. Jónsson, *A climbing image nudged elastic band method for finding saddle points and minimum energy paths*, J. Chem. Phys. **113**, 9901–9904 (2000), DOI: 10.1063/1.1329672.

APPENDIX A

First-Principles Investigation of Electronic Properties and Phase Transition of Ti_3O_5

THE JOURNAL OF PHYSICAL CHEMISTRY C
A JOURNAL OF THE AMERICAN CHEMICAL SOCIETY

pubs.acs.org/JPCC

Article

First-Principles Investigation of Electronic Properties and Phase Transition of Ti_3O_5

Stefan Jütten and Thomas Bredow*

Cite This: *J. Phys. Chem. C* 2022, 126, 7809−7817

Read Online

ACCESS | Metrics & More | Article Recommendations | Supporting Information

ABSTRACT: Heat storage materials preserving large amounts of thermal energy over long time frames enable the storage of waste energy from thermal energy generation or excess energy generated by intermittent and renewable sources. Trititanium pentoxide, Ti_3O_5, has emerged as a promising material with a high energy storage density and the capability of releasing the stored energy on demand, for example, by the application of pressure. During the release, the higher energy λ polymorph undergoes an isostructural phase transition to the lower energy β polymorph. Accurate predictions of the heat storage properties of the two polymorphs using first-principles methods are not yet available. Using hybrid density functionals and the recently proposed r^{2}SCAN meta-generalized gradient approximation functional augmented by the D3 dispersion correction, we offer a comprehensive description of the electronic ground state of this material. We find that r^{2}SCAN-D3 provides a similar accuracy for structural and thermodynamic properties compared to hybrid functionals at an order of magnitude reduced computational cost. Inclusion of the dispersion interaction is essential to obtain correct energy differences between the two phases. The r^{2}SCAN-D3 method is applied to the investigation of the reaction mechanism of the phase transition, resulting in full characterization of the transition state. We highlight the good performance of the r^{2}SCAN-D3 functional by predicting the phase transition temperature and phase transition enthalpy of the heat storage system and recommend this method for high-throughput investigations of heat storage materials.

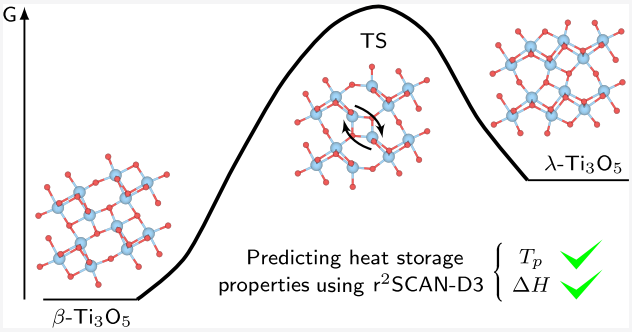

INTRODUCTION

Trititanium pentoxide Ti_3O_5 has emerged as a promising material with applications in heat storage and optical data storage.[1,2] The reversible first-order phase transition from the lower energy β polymorph to the higher energy λ polymorph can be induced by heat, irradiation, or electric current. Due to hysteresis phenomena, the higher energy phase does not spontaneously revert back to the ground state of the system but persists as a thermodynamically metastable state. A release of the energy stored in the system, that is, the transformation of λ-Ti_3O_5 to β-Ti_3O_5, can be triggered on demand, for example, by the application of pressure.

It was recently shown that substituting 3% of the Ti atoms by Sc atoms alters the heat storage properties of this compound, extending its range of application to capture, for example, waste heat from thermal power generation.[3] Substitutions with 2% Al and <1% Mg have also been reported.[4,5]

Previous theoretical approaches employ local spin density approximation (LSDA) and generalized gradient approximation (GGA) methods in combination with empirical Hubbard U corrections and often focus on optical properties.[6] They neither investigate the correct electronic ground state of this spin-polarized system nor apply dispersion corrections to their methods. Thus, important features of the phase transition, such as the phase transition temperature T_p, were not accurately described.[3,7−10]

Here, we offer a comprehensive overview of the electronic ground states of β- and λ-Ti_3O_5 and describe the transition state (TS) of the phase transition. Our approach does not rely on empirical parameters and thus can be routinely employed to treat this class of materials. In this context, we propose the accurate and efficient r^{2}SCAN-D3 functional for the calculation of solid-state structures and thermodynamics. It is shown that r^{2}SCAN-D3 provides comparable or higher accuracy for the relative phase stability of β- and λ-Ti_3O_5 compared to the standard hybrid functionals B3PW, B3LYP, PBE0, PW1PW, B97H, HSE06, ωB97X, and M06 at a much lower computational cost. For the calculation of electronic properties, we recommend the M06-D3 functional.

Received: January 24, 2022
Revised: March 29, 2022
Published: April 27, 2022

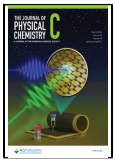

COMPUTATIONAL DETAILS

Due to the efficient implementation of the Fock exchange, all hybrid density functional theory (DFT) calculations were performed using the CRYSTAL17 v1.0.2 program.[11] The improved description of open-shell transition metal compounds by hybrid density functionals in comparison to GGA and meta-GGA functionals is established in the literature.[12,13] We employ the optimized pob-TZVP-rev2 basis set.[14] Symmetry inequivalent spin configurations were determined using the CONFCOUNT keyword.[15,16] Structural relaxations utilizing the global hybrid functionals B3PW,[17−19] B3LYP,[17,20] PBE0,[21] PW1PW,[22] B97H,[23,24] and M06[25] and the range-separated hybrid functionals HSE06[26,27] and ωB97X[23,28] were performed in internal redundant coordinates and converged to a gradient RMS below 3×10^{-4} a.u. Due to its good results in the description of transition metal-containing systems and overall thermodynamics,[12] as well as its high amount of the Fock exchange, the M06 functional was used to determine the spin configuration of the open-shell oxides.

Recently, the r^{2}SCAN functional was proposed by Furness et al.[29] In particular, combined with dispersion correction, it has shown excellent performance for the calculation of structural and energetic properties.[30,31] Since the r^{2}SCAN functional is not implemented in the CRYSTAL17 program, calculations employing this functional were performed using the Vienna *ab initio* simulation package (VASP) v6.2.1.[32,33] The projector-augmented wave (PAW) method[34,35] with a plane wave basis set was used with plane wave cutoff energies set to 600 eV. The thermodynamic target properties are well-converged at this cutoff energy. Structures were considered converged if the norm of all forces was below 10^{-5} eV/Å. Partial band occupations are determined using Gaussian smearing with a width of σ. For every system, convergence tests of the total electronic energy with respect to σ were performed.

We performed single-point hybrid calculations on the primitive cells using the CRYSTAL and VASP codes, which revealed a 2 orders of magnitude speedup of the CRYSTAL calculations performed in the Gaussian basis.

In all CRYSTAL calculations, the recommended integral truncation tolerances for hybrid functionals of 10^{-7}, 10^{-7}, 10^{-7}, 10^{-14}, and 10^{-42} were applied. Integral evaluations in the reciprocal space utilized Γ-centered Monkhorst−Pack meshes with a spacing of 0.2 Å^{-1} between k-points, except for frequency calculations, where the spacing between k-points was increased to 0.4 Å^{-1}. A comparison of frequencies computed with both k-point densities showed deviations of below 1 cm^{-1}. However, in the calculation of thermodynamic properties, the electronic energies were computed with the denser k-point meshes in order to improve numerical precision.

Self-consistent field (SCF) convergence thresholds of 10^{-8} eV (VASP) and 10^{-8} a.u. (CRYSTAL) and large integration grids were used throughout. All energies and net magnetizations presented in this work refer to one formula unit of Ti_3O_5.

Long-ranged dispersion interactions are known to be crucial in the description of not only molecules and molecular aggregates but also strongly and weakly bound solids.[36,37] Therefore, dispersion interactions are treated in the efficient and accurate DFT-D3(BJ) scheme,[38] where Becke−Johnson (BJ) damping in the short-ranged regime is used due to its established superior performance as compared with that of its zero-damped counterpart.[39] Three-body dispersion terms were included in all CRYSTAL calculations but are neglected by default in VASP.

Band structure calculations are sampled between suggested high-symmetry points in the first Brillouin zone of the $C2/m$ space group.[40] Solid-state nudged elastic band (ss-NEB) calculations were conducted in the climbing image mode.[41] Every image was converged until the acting forces were below 10^{-3} eV/Å.[41]

For the visualization of atomic structures, the VESTA program was used.[42] The visualization of vibrational modes was performed using the PDielec program.[43]

RESULTS AND DISCUSSION

Electronic Ground State. In order to investigate the electronic ground state of both polymorphs, all symmetry-inequivalent spin configurations in the primitive cell of β-Ti_3O_5 and λ-Ti_3O_5 (Figure 1) were identified. Antiferromagnetic spin states as well as the ferromagnetic and closed-shell spin states were optimized at the M06-D3 level of theory.

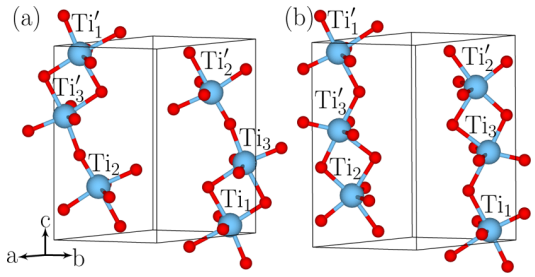

Figure 1. Primitive unit cells of β-Ti_3O_5 (a) and λ-Ti_3O_5 (b). Atoms generated by symmetry are labeled with superscripts.

We compare the energies of all spin configurations relative to the electronic ground state, Mulliken populations of the Ti atoms, fundamental band gaps, and optimized lattice parameters in Table 1. In the initial guess of the SCF procedures, the six Ti atoms of the unit cell were assigned spin-up (α) or spin-down (β) spin configurations, respectively. If not mentioned otherwise, the final spin configuration corresponds to the initial guess.

For the β-phase, an antiferromagnetic electronic ground state is found within the broken-symmetry approximation applied in this study. The spin configuration characterizing the electronic ground state is made up of pairs of symmetry-equivalent atoms (e.g., Ti_1 and Ti_1') with antiparallel spins. All initial spin configurations converge to the same electronic state, which we therefore identify as the electronic ground state of β-Ti_3O_5. Mulliken spin densities on these pairs of titanium atoms are equal in absolute values, with particularly high values on Ti_1 and Ti_3 sites. In accordance with the experiment, a semi-conducting state is obtained with a band gap of 1.3 eV for both spin-up and spin-down spin channels. Experimental lattice vector lengths[1] are best reproduced in the electronic ground state; however, the unique monoclinic angle β is overestimated by 0.23°. Here, the closed-shell state produces the value closest to the experiment (91.53°) with 91.51°, which represents the energetically closest state to the electronic ground state among all other investigated states.

In general, we note that among the optimized geometric parameters of both phases, the monoclinic angle β exhibits the strongest dependency on the electronic state.

https://doi.org/10.1021/acs.jpcc.2c00572
J. Phys. Chem. C 2022, 126, 7809−7817

Table 1. Comparison of All Considered Optimized Electronic Ground States for the Primitive Cell of β- and λ-Ti_3O_5 at the M06-D3 Level of Theory[a]

spin config.	E^{rel}	Mulliken populations						Mag.	band gap		lattice vectors			β
		Ti_1	Ti_1'	Ti_2	Ti_2'	Ti_3	Ti_3'		α	β	a	b	c	
β-Ti_3O_5									0.2[b]		9.75[c]	3.80[c]	9.44[c]	91.53[c]
closed shell	4	0.0	0.0	0.0	0.0	0.0	0.0	0.0	0.99		9.63	3.79	9.44	91.51
$\alpha\,\alpha\,\alpha\,\alpha\,\alpha\,\alpha$	22	1.1	1.1	0.5	0.5	0.7	0.7	4.0	*		9.61	3.87	9.41	91.76
$\alpha\,\alpha\,\alpha\,\beta\,\beta\,\beta$	21	1.0	1.0	0.5	−0.5	−0.1	−0.7	1.1	*		9.64	3.87	9.38	91.92
$\alpha\,\alpha\,\beta\,\beta\,\alpha\,\beta$	8	1.0	1.0	0.2	−0.1	0.5	−0.4	2.0	1.19	1.67	9.61	3.83	9.42	91.92
$\alpha\,\beta\,\alpha\,\alpha\,\beta\,\beta$	14	0.4	−0.4	0.5	0.5	−0.5	−0.4	0.0	*		9.74	3.83	9.39	91.19
$\alpha\,\beta\,\alpha\,\beta\,\alpha\,\beta$	0	0.7	−0.7	−0.2	0.2	−0.5	0.5	0.0	1.33	1.33	9.72	3.79	9.48	91.76
$\alpha\,\beta\,\alpha\,\beta\,\beta\,\alpha$	0	0.7	−0.7	−0.2	0.2	−0.5	0.5	0.0	1.33	1.33	9.72	3.79	9.48	91.75
$\alpha\,\beta\,\beta\,\alpha\,\alpha\,\beta$	0	0.7	−0.7	−0.2	0.2	−0.5	0.5	0.0	1.33	1.33	9.72	3.79	9.48	91.76
$\alpha\,\beta\,\beta\,\alpha\,\beta\,\alpha$	0	0.7	−0.7	−0.2	0.2	−0.5	0.5	0.0	1.33	1.33	9.72	3.79	9.48	91.76
$\alpha\,\beta\,\beta\,\beta\,\alpha\,\alpha$	17	0.4	−0.4	−0.5	−0.1	0.4	0.7	0.5	*		9.71	3.83	9.42	91.46
$\beta\,\beta\,\alpha\,\alpha\,\alpha\,\beta$	8	−1.0	−1.0	0.1	−0.2	0.4	−0.5	−2.0	1.67	1.19	9.61	3.83	9.42	91.92
$\beta\,\beta\,\alpha\,\beta\,\alpha\,\alpha$	21	−1.0	−1.0	0.5	−0.5	0.7	0.1	−1.1	*		9.64	3.87	9.38	91.92
λ-Ti_3O_5										*[b]	9.83[c]	3.79[c]	9.97[c]	91.29[c]
closed shell	37	0.0	0.0	0.0	0.0	0.0	0.0	0.0	*		9.50	3.80	9.99	90.60
$\alpha\,\alpha\,\alpha\,\alpha\,\alpha\,\alpha$	0	0.6	0.6	1.0	1.0	0.6	0.6	4.0	0.74	6.08	9.82	3.80	9.96	91.68
$\alpha\,\alpha\,\alpha\,\beta\,\beta\,\beta$	0	0.3	0.8	1.0	−1.0	−0.9	−0.2	0.0	1.34	1.16	9.84	3.81	9.95	91.46
$\alpha\,\alpha\,\beta\,\beta\,\alpha\,\beta$	16	0.0	0.0	−0.5	−1.0	0.5	0.0	−0.9	*		9.70	3.77	10.02	91.81
$\alpha\,\beta\,\alpha\,\alpha\,\beta\,\beta$	12	0.9	−0.9	1.0	0.5	0.0	−0.5	0.9	*		9.81	3.79	10.00	90.50
$\alpha\,\beta\,\alpha\,\beta\,\alpha\,\beta$	7	0.9	−0.9	0.9	−0.9	0.2	−0.2	0.0	1.07	1.07	9.80	3.79	10.04	89.91
$\alpha\,\beta\,\alpha\,\beta\,\beta\,\alpha$	20	0.9	−0.9	0.6	−0.6	−0.4	0.4	0.0	*		9.78	3.78	10.00	91.14
$\alpha\,\beta\,\beta\,\alpha\,\alpha\,\beta$	22	0.8	−0.8	−0.6	0.6	0.5	−0.5	0.0	*		9.80	3.78	9.99	91.07
$\alpha\,\beta\,\beta\,\alpha\,\beta\,\alpha$	12	0.9	−0.9	−0.9	0.9	−0.1	0.1	0.0	1.25	1.25	9.81	3.79	10.04	90.08
$\alpha\,\beta\,\beta\,\beta\,\alpha\,\alpha$	12	0.9	−0.9	−0.5	−1.0	0.5	0.0	−0.9	*		9.81	3.79	10.00	90.50
$\beta\,\beta\,\alpha\,\alpha\,\alpha\,\beta$	16	0.0	0.0	1.0	0.5	0.0	−0.5	0.9	*		9.70	3.77	10.02	91.81
$\beta\,\beta\,\alpha\,\beta\,\alpha\,\alpha$	0	−0.8	−0.3	0.9	−1.0	0.2	0.9	0.0	1.16	1.34	9.84	3.81	9.95	91.46

[a]Closed-shell, ferromagnetic, and all symmetry-inequivalent anti-ferromagnetic spin configurations are compared with respect to their energy relative to the electronic ground state (E^{rel}/kJ mol^{-1}), Mulliken populations (in units of e) of the irreducible and symmetry-equivalent (superscript ′) titanium atoms, net magnetization (in units of e), electronic band gap (in eV) or metallic character (*), optimized lattice vector lengths (Å), and unique monoclinic angle β (°). Experimental values for comparison are obtained from refs 44 and 1. [b]Reference 44. [c]Reference 1.

Table 2. Electronic Ground States of β- and λ-Ti_3O_5 after Optimization Using the r^{2}SCAN-D3 Functional[a]

polymorph	Mulliken populations						Mag.	lattice vectors			β
	Ti_1	Ti_1'	Ti_2	Ti_2'	Ti_3	Ti_3'		a	b	c	
β-Ti_3O_5	0.2	0.2	0.2	0.2	0.1	0.1	1.0	9.70	3.85	9.28	91.07
λ-Ti_3O_5	0.6	0.6	0.7	0.7	0.5	0.5	1.5	9.81	3.81	9.93	91.21

[a]Atomic net populations and net magnetization (in units of e), optimized lattice vectors (in Å), and monoclinic angle β (in °) are given.

For the λ-phase, a ferromagnetic electronic ground state is calculated. It is characterized by a marked accumulation of spin density on Ti_2 sites, although all spin densities are increased compared to that of the β-phase. The net magnetization confirms temperature-dependent magnetization measurements of the phase transition, where a distinct increase in the magnetization of titanium atoms was noticed after the phase transition temperature, that is, for the λ-phase.[45,46] Earlier publications suggest a metallic electronic ground for λ-Ti_3O_5.[1,2] At variance, we obtain a semi-conducting state with an electronic band gap of ≈0.7 eV, which is in line with more recent electrical conductivity measurements on λ-Ti_3O_5 thin films.[47] Though four initial spin configurations all converge to the same electronic state in the β-phase, this is not observed in the λ-phase. Here, however, three initial spin configurations converge to three energetically degenerate but electronically distinct states.

Due to the small energy differences between the spin configurations, it must be noted that an accurate description of the electronic ground state is only possible using multi-determinantal approaches or quantum Monte Carlo simulations.[48] However, these methods are too demanding to study Ti_3O_5.

We observe several equivalent solutions among the listed symmetry-inequivalent states. The inversion of electron spins during the SCF field procedure reduces the number of distinct electronic ground states from 12 to 7 for the β-phase and from 12 to 8 for the λ-phase.

The spins are in general less localized using the r^{2}SCAN-D3 functional[30] due to its meta-GGA nature. At variance with the M06-D3 results, we identified the ferromagnetic spin configuration as the magnetic ground state for both phases. Therefore, all calculations using this functional were carried out with an initial ferromagnetic spin configuration. We note that all other initial spin configurations converge to the same antiferromagnetic electronic state, which is less stable by 0.5 kJ mol^{-1} with respect to the ferromagnetic state. Both phases converge to metallic states with r^{2}SCAN. Bader net

https://doi.org/10.1021/acs.jpcc.2c00572
J. Phys. Chem. C 2022, 126, 7809−7817

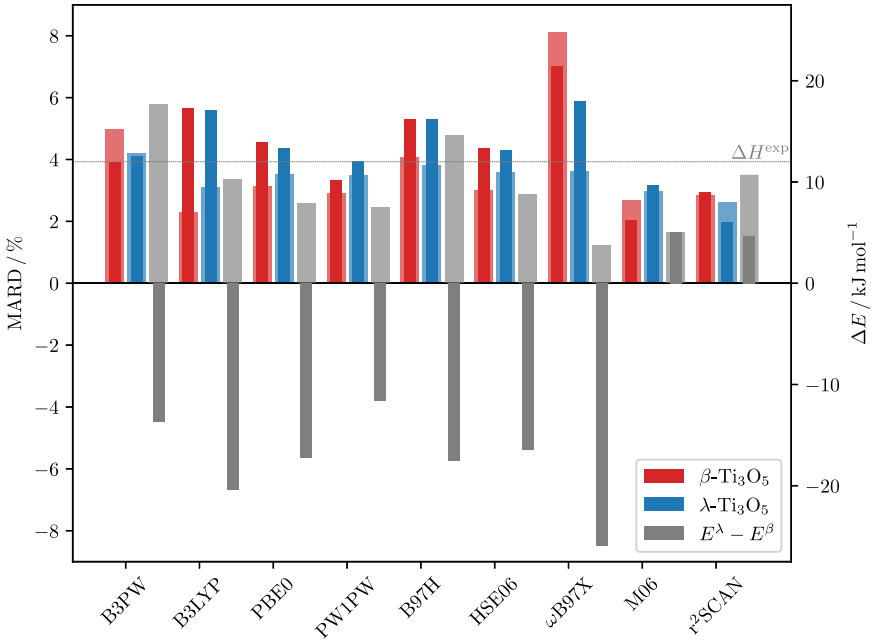

Figure 2. Comparison of MARDs of optimized lattice parameters of both phases and phase energy differences ΔE (kJ mol^{-1}) for a selection of density functionals. Wider low opacity bars indicate dispersion-corrected results. The experimental enthalpy difference ΔH^{exp} is shown as a reference.

populations, net magnetizations, and optimized lattice parameters are shown in Table 2.

The β-phase optimized lattice vectors lack the high accuracy observed using the M06-D3 hybrid functional, whereas the λ-phase lattice vectors show only small deviations from the experiment. Notably, the c lattice vector in the β-phase deviates from the experiment, along with the monoclinic angle β. For the latter, a qualitatively wrong trend is found, where the monoclinic angle of the λ-phase is greater than that of the β-phase, which contradicts the experimental data. In the λ-phase, a similar accumulation of spin density at the Ti_2 sites is observed, as seen in our hybrid functional results.

Assessment of Selected Density Functionals. The electronic ground states obtained using M06-D3 were used to evaluate a selection of standard density functionals with an emphasis on geometric parameters and thermodynamics (Figure 2). All optimized structures are provided in Supporting Information Tables S1−S9, and dispersion-corrected results are given in Supporting Information Tables S10−S18.

As a quality measure for calculated structures, we adopt the sum of the mean absolute relative differences (MARDs) of optimized lattice parameters and atomic positions with respect to the experiment. Here, the deviation of atomic positions from experimental data contributes the most, with MARDs of about 2% for the β-phase and 3% for the λ-phase, when dispersion interaction is included. Considering that the powder diffraction at ambient temperatures was used in the generation of our reference data, this is to be expected. In contrast, lattice parameters are accurately reproduced with MARDs well below 1% for all dispersion-corrected functionals. Dispersion correction in general improves the calculated geometries. Only the M06 results are almost unaffected by the dispersion correction, owing to its extensive parameterization. Similarly, only minor improvements of optimized geometries are observed upon application of a dispersion correction for the r^{2}SCAN functional. The overall best geometries are obtained using the M06-D3 and B3LYP-D3 hybrid functionals and the r^{2}SCAN-D3 meta-GGA functional. In contrast to ref 13, we observe higher accuracies for B3LYP-D3 than for PBE0-D3.

In phase transition materials, the enthalpy difference $\Delta H = H^{\lambda} - H^{\beta}$ is a crucial parameter since it reflects the energy storage capability of the system. As a widely accepted approximation, we use the phase energy difference $\Delta E = E^{\lambda} - E^{\beta}$ to gauge the description of thermodynamic properties of each functional. The majority of assessed functionals yield qualitatively wrong negative values for this quantity without dispersion correction, that is, they predict the λ-phase to be more stable than the β-phase. This erroneous stabilization of the λ-phase ranges from −10 to −25 kJ mol^{-1}. The notable exceptions are the M06 functional with ΔE = 5.1 kJ mol^{-1} and the r^{2}SCAN functional with ΔE = 4.7 kJ mol^{-1}.

The application of dispersion correction leads to qualitatively correct relative phase stabilities using all methods. With a ΔE of 10.6 kJ mol^{-1}, the r^{2}SCAN-D3 functional is the most accurate, eclipsing the best performing hybrid functional B3LYP-D3 with ΔE = 10.2 kJ mol^{-1} by 0.4 kJ mol^{-1}. An assessment of the evaluated dispersion-corrected hybrid DFT methods and the r^{2}SCAN-D3 meta-GGA functional corroborates their comparable accuracy observed in ref 30.

The profound effect of dispersion interactions on the thermodynamics of this system suggests that long-ranged interactions play a fundamental role in the phase transition.

The band gaps obtained from the optimized structures with each functional are provided in Supporting Information Table S19. All hybrid functionals yield band gaps greater than 1.09 eV for the β-phase and greater than 0.23 eV for the λ-phase, with the exception of the B97H-D3 functional, which yields a metallic state for the λ-phase. The ωB97X-D3 functional with band gaps of 6.18 eV for the β-phase and 4.33 eV for the λ-phase is an outlier and not suited to model this material, as previously shown with the highest MARDs in structural optimizations. The r^{2}SCAN-D3 method yields metallic states

https://doi.org/10.1021/acs.jpcc.2c00572
J. Phys. Chem. C 2022, 126, 7809−7817

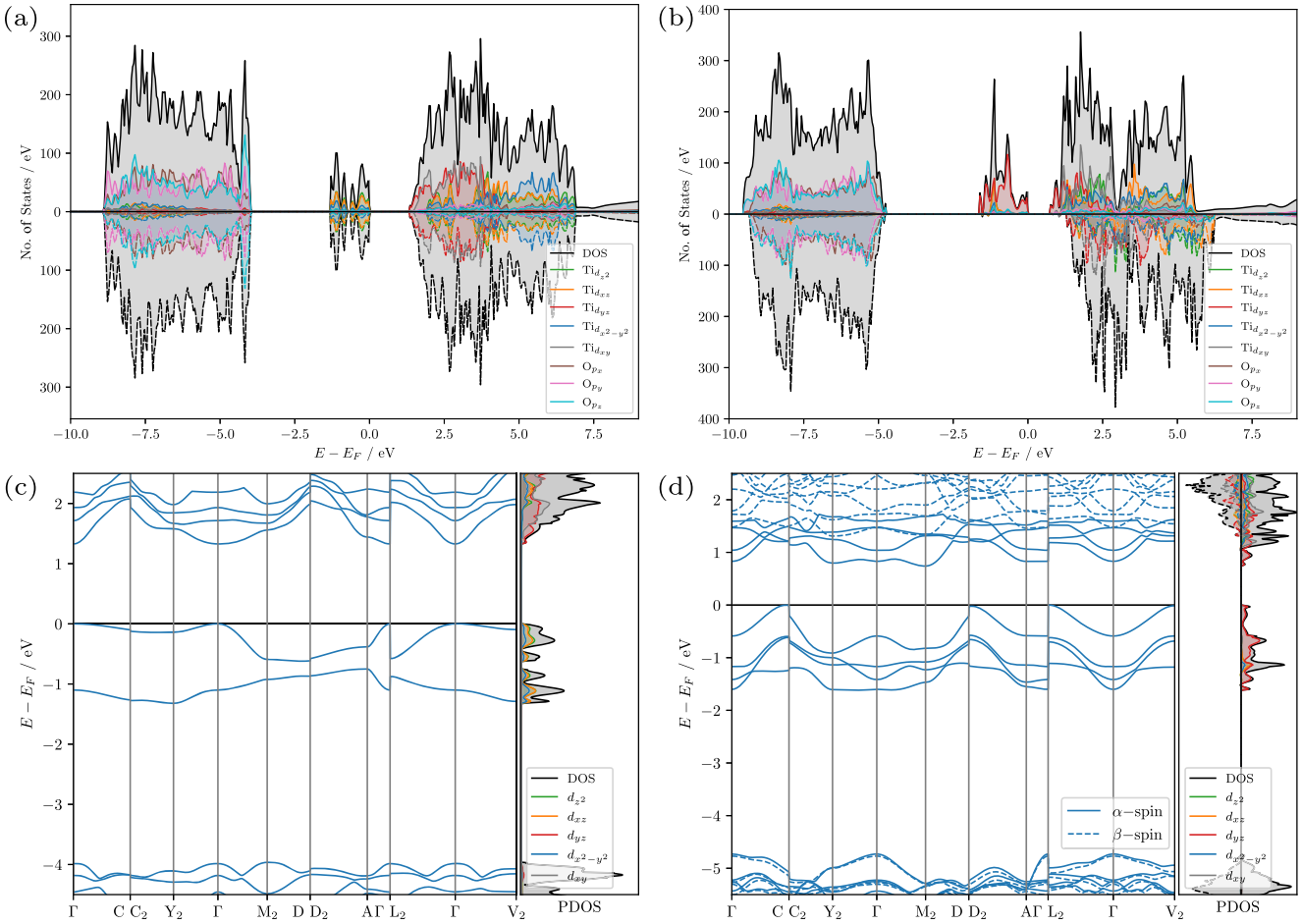

Figure 3. DOS of β-Ti_3O_5 (a) and λ-Ti_3O_5 (b) with projections onto valence orbitals of Ti and O and band structures of β-Ti_3O_5 (c) and λ-Ti_3O_5 (d).

for both phases due to the inherent artificial charge delocalization of the meta-GGA functional.

Band Structure and Density of States. We present the electronic band structure of the electronic ground states of β-Ti_3O_5 and λ-Ti_3O_5 calculated at the M06-D3 level of theory along with the corresponding density of states (DOS) in Figure 3. Here, we focus on the ferromagnetic state of the λ-phase because it is nearly free from spin contamination. Electron spins are resolved separately in each case, and projections of oxygen p-AOs and titanium d-AOs on the total DOS are provided.

In the DOS of the β-phase, the oxygen valence states are separated by 2.7 eV from the titanium valence states, which are located just below the Fermi level (E_F). For this semiconducting phase, a direct band gap of 1.3 eV is obtained, which most published DOSs calculated using Hubbard parameters U are unable to attain (even with $U > 5$ eV) and instead predict a metallic state.[8] There is no difference in the number of states occupied with spin-up (α) and spin-down (β) electrons.

By contrast, in the ferromagnetic λ-phase, titanium valence states exist only for α-electrons, which are separated by 3.1 eV with respect to the oxygen valence states. They exhibit an indirect band gap of 0.7 eV.

The two bands below E_F corresponding to Ti valence states of β-Ti_3O_5 exhibit low band dispersion. Here, the number of states involving d_z^2 and d_{xz} orbitals are similar, mainly resulting from orbitals centered at the Ti_1 and Ti_3 sites. States involving d_{yz} and d_{xy} orbitals do not contribute to these bands; however, both orbitals contribute the most to the virtual bands.

In the band structure of the λ-phase, we obtain four bands below the Fermi level, which display a considerably stronger band dispersion. We correlate this with the experimentally observed enhanced electrical conductivity of the λ-phase, compared with that of the β-phase. We note that these four bands are associated with α-spin electrons and that the band gap of the α-electrons is reduced compared with that of the β-phase. All four bands are composed of states primarily dominated by Ti d_{yz} orbitals. Here, the first band below the Fermi level results exclusively from the contributions of Ti_3 d_{yz}-orbitals. The three energetically lower lying bands result from states involving Ti_2 d_{yz}-orbitals.

Heat Storage Properties. We apply the r^{2}SCAN-D3 functional for the prediction of heat storage properties, in particular, the phase transition temperature T_p and the phase transition enthalpy ΔH. T_p is defined as the temperature at which a 1:1 ratio of both phases is observed, and ΔH has been obtained from differential scanning calorimetry measurements.[1,3] In our theoretical approach, we obtain both properties from frequency calculations in the harmonic approximation. In this framework, a phase transition will occur when the free energy of λ-Ti_3O_5 becomes lower than the free energy of β-Ti_3O_5. Therefore, we define T_p as the temperature at which $\Delta G = 0$. We approximate the phase

https://doi.org/10.1021/acs.jpcc.2c00572
J. Phys. Chem. C 2022, 126, 7809−7817

transition enthalpy as the difference between the enthalpies of both phases, evaluated at T_p, that is, $\Delta H(T_p) = H^{\lambda}(T_p) - H^{\beta}(T_p)$.

In Figure 4, we display our results of frequency calculations carried out in the 1 × 3 × 1 supercell expansion of the

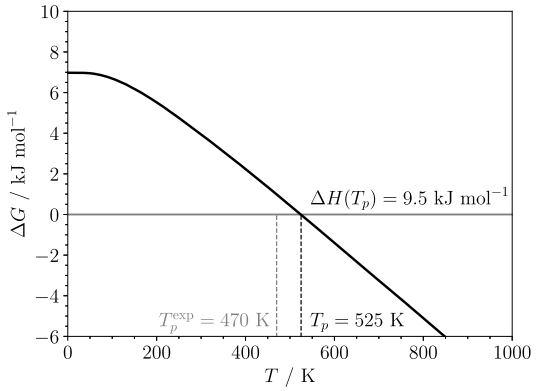

Figure 4. Free energy difference between both phases of Ti_3O_5 as a function of temperature at the r^{2}SCAN-D3 level of theory.

conventional cell, resulting in T_p = 525 K and ΔH = 9.5 kJ mol^{-1}. We note that this expansion leads to cells with similar dimensions in *a*, *b*, and *c* directions (e.g., 9.83 Å × 11.36 Å × 9.97 Å for λ-Ti_3O_5). These supercells are considered converged with respect to the lowest wavenumbers obtained for primitive cells, conventional cells, and 1 × 2 × 1 supercell expansions. Our calculated ΔH slightly underestimates the experimental value of ΔH^{exp} = 12 ± 1 kJ mol^{-1} but is well within chemical accuracy. Our obtained T_p overestimates the experimental value of T_p^{exp} = 470 K by 55 K.

The prediction of phase transition temperatures is highly sensitive with respect to the difference of electronic energies ΔE between the phases. For instance, we observed a >50 K increase of T_p for every 1 kJ mol^{-1} increase of ΔE. It is therefore essential to apply a carefully tested accurate method. We emphasize that in the presented approach, no scaling factor was applied to the frequencies obtained from the electronic structure method. We expect further improvement of these predictions by including surface free energy differences in our approach since microparticles with a high surface-to-bulk ratio were used in the experiments. Anharmonic corrections to vibrational frequencies have been shown to improve thermodynamic properties of related titanium oxides;[49] however, their contribution was not studied in this case due to the focus on a reliable yet efficient screening approach.

Reaction Mechanism. We studied the mechanism of the phase transition using the ss-NEB method at the r^{2}SCAN-D3 level of theory and compared our obtained results to the experimental data. The reference experiments recorded lattice deformations during the irradiation-induced phase transition on the picosecond timescale using powder X-ray diffraction.[50] We attempt to correlate the temporal evolution of the phase transition with our calculated reaction mechanism.

We present the energy relative to β-Ti_3O_5 as a function of the reaction coordinate in Figure 5a. A single TS with a barrier of $\Delta H^{TS-\beta}$ = 26 kJ mol^{-1} relative to the β-phase and $\Delta H^{TS-\lambda}$ = 16 kJ mol^{-1} to the λ-phase was obtained.

We compare the experimental time-resolved structural changes during the phase transition with our optimized images along the reaction path in Figure 5b. The calculated monoclinic angle β decreases from 91.1° (β-phase) to 90.3° (TS) and again increases to 91.2° (λ-phase). Immediately after irradiation, the experimentally recorded value for β is 91.1°, which decreases at a slower pace toward a plateau of 90.5° in

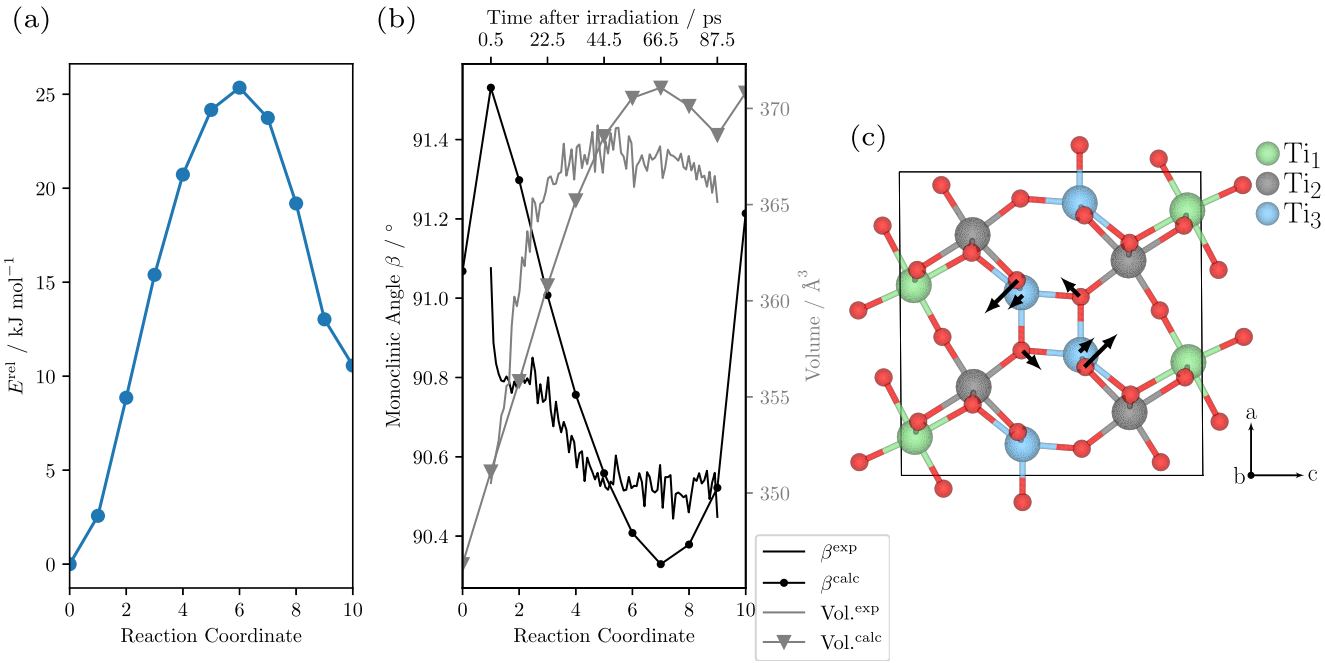

Figure 5. Energy relative to the β-Ti_3O_5 phase along the $\beta \rightarrow \lambda$-$Ti_3O_5$ reaction path (a), comparison of the monoclinic angle and volume of the optimized images to the experiment (b) [Reprinted with permission from C. Mariette et al. Strain wave pathway to semiconductor-to-metal transition revealed by time-resolved X-ray powder diffraction. *Nat. Commun.* **2021**, *12*, 1−11. Copyright 2021, The Author(s)], and the structure of the TS with the acting forces of the associated mode are indicated by arrows (c).

https://doi.org/10.1021/acs.jpcc.2c00572
J. Phys. Chem. C 2022, 126, 7809−7817

Table 3. Comparison of Structural and Electronic Properties of the Optimized Ti_3O_5 TS with Experimental Data of the α-Ti_3O_5 Structure[a]

			Mulliken populations							lattice vectors			
method	Spin conf.	$\Delta H^{TS-\beta}$	Ti_1	Ti_1'	Ti_2	Ti_2'	Ti_3	Ti_3'	Mag.	a	b	c	β
									α-Ti_3O_5 exp[b]	9.85	3.80	9.99	90.00
M06-D3	AFM	25	0.6	−0.6	0.5	−0.5	0.5	−0.5	0.0	9.84	3.78	9.91	90.55
M06-D3	FM	26	0.8	0.8	0.8	0.8	0.6	0.6	4.0	9.84	3.83	9.90	90.02
r^{2}SCAN-D3	AFM	29	0.0	0.0	0.5	−0.5	0.4	−0.4	0.2	9.84	3.79	9.95	90.38
r^{2}SCAN-D3	FM	26	0.0	0.0	0.5	0.5	0.6	0.6	2.0	9.86	3.79	9.93	90.40

[a]The activation barrier $\Delta H^{TS-\beta}$ is given in kilojoules per mole, Mulliken populations and net magnetizations are given in units of electron charge units, lattice vectors are given in angstroms, and the monoclinic angle β is given in degrees. For both methods, the ferromagnetic and antiferromagnetic spin configurations are compared. [b]Reference.[51]

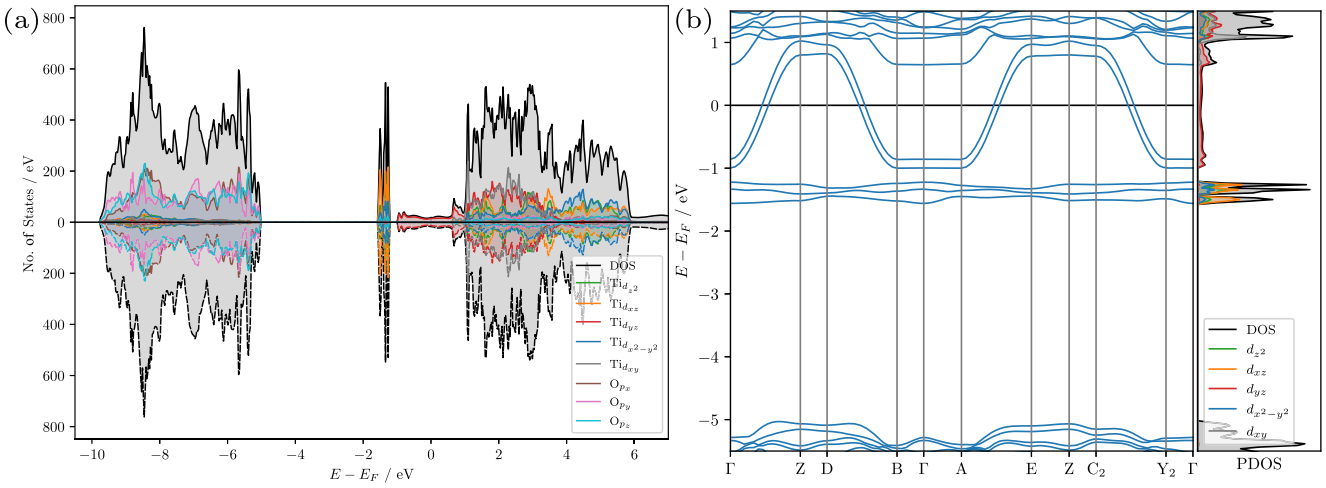

Figure 6. DOS (a) with projections of valence orbitals of Ti and O and band structure (b) of the TS, calculated at the M06-D3 level of theory.

the TS (87 ps after irradiation). The calculated volume increases linearly from 346 Å^3 in β-Ti_3O_5 to 371 Å^3 in the TS. This is followed by a slight decrease in the volume of 2 Å^3, before an expansion toward the λ-Ti_3O_5 unit cell volume. Experimentally, the volume increases from 351 to 369 Å^3 and then decreases to 365 Å^3.

Our calculated structural parameters reproduce the qualitative progression of the phase transition as recorded experimentally. Calculated angles are slightly overestimated in the initial period of the phase transition and slightly underestimated near the TS. Similarly, our calculated volume near the TS and λ-phase is slightly overestimated. Overall, a semiquantitative agreement of the calculated phase transition mechanism and experiment is obtained.

We confirmed the presence of a TS by performing a frequency calculation, which resulted in a single imaginary mode with a corresponding frequency of i73 cm^{-1}. We indicate forces acting on the atoms of the TS structure in Figure 5c and provide visualizations of this mode in the Supporting Information, as well as the TS structure (at the r^{2}SCAN-D3 and M06-D3 levels) in Supporting Information Tables S20 and S21. The TS mode is characterized by a rotation of the central Ti_3−Ti_3' dimer and surrounding oxygen atoms in the crystallographic *ac*-plane.

According to the experimentalists, an estimate of the upper bound for the energy transfer to the system is given by 53 kJ mol^{-1} (0.55 eV).[50] Due to the ca. 30 kJ mol^{-1} difference between our results and this estimate, we investigated the impact of using hybrid DFT methods to estimate this energy barrier. We optimized the TS using the M06-D3 method to adequately compare the TS's electronic properties with β- and λ-Ti_3O_5. The obtained energy barrier of 26 kJ mol^{-1} confirms our r^{2}SCAN-D3 result. Thus, we established a lower threshold for the phase transition energy and suggest that the higher energy barriers observed in experimental phase transitions are caused due to the crystal morphology, surface energy differences, and overall experimental conditions.

We provide the optimized structural parameters of the TS in Table 3 and compare our results with the experimental structure of α-Ti_3O_5 (space group *Cmcm*)[51] as ref 50 suggests a distortion toward the α-phase following irradiation. A symmetry analysis reveals that the TS adopts the *Pm* space group. Comparing the TS structure with α-Ti_3O_5, we observe a slightly distorted monoclinic angle and a shortened *c* lattice vector. Our r^{2}SCAN-D3 optimized structure of λ-Ti_3O_5 converges to the same value for *c* and differs from the TS structure with a slightly shorter *a* lattice vector and a decrease in the monoclinic angle β.

All spin configurations and used methods predict the TS to be a metal. At the r^{2}SCAN-D3 level, the ferromagnetic spin configuration is stabilized by 5 kJ mol^{-1} compared with the antiferromagnetic state. At the M06-D3 level, the antiferromagnetic spin configuration is stabilized by 23 kJ mol^{-1} with respect to the ferromagnetic configuration and thus forms the electronic ground state of the TS. This electronic ground state was used to calculate the DOS and electronic band structure of the TS (Figure 6). The titanium valence states are separated from the oxygen valence states by 3.4 eV. Many titanium

https://doi.org/10.1021/acs.jpcc.2c00572
J. Phys. Chem. C 2022, 126, 7809−7817

valence states with energies of ca. −1.5 eV give rise to three flat bands. Of those, the lowest energy band mostly results from Ti_3 d_{xz} orbitals, whereas the d_{xz} contributions to the two higher energy flat bands result from Ti_1 centered orbitals. All d_z^2 and $d_{x^2-y^2}$ states associated with these three flat bands arise from Ti_1 sites. The two bands exhibiting strong band dispersion and crossing E_F are associated entirely with Ti_2 d_{yz} orbitals.

CONCLUSIONS

Through an assessment of various hybrid and meta-GGA functionals, we identified the r^{2}SCAN-D3 method as being optimally suited for the calculation of energetic and structural properties of two Ti_3O_5 polymorphs. Thermodynamic functions are calculated with harmonic phonon frequencies for converged supercells. Inclusion of the London dispersion is crucial to obtain the correct energy difference between the β and λ phases. The approach does not rely on empirical parameters, with its accuracy comparing favorably with respect to hybrid DFT methods, though at significantly reduced computational costs. Our predicted phase transition enthalpy and phase transition temperature are in good agreement with the experiment.

We explored the phase transition mechanism and assessed our predictions of geometries along the reaction pathway to the experiment, which yields very reasonable results. We characterized the structural and electronic properties of the TS during the phase transition and specify the relevant vibrational mode.

We systematically explored the spin configuration giving rise to the electronic ground state of the β and λ polymorphs using the meta-GGA hybrid method M06-D3 and arrive at an antiferromagnetic state for β-Ti_3O_5 and a ferromagnetic state for λ-Ti_3O_5. We predict the latter phase to be a semiconductor, in contrast to previous theoretical and earlier experimental approaches but in accordance with more recent experiments. With the same approach, we predict the TS of the phase transition to be a metal.

The thermodynamic properties of heat storage systems could be applied in mean field models to improve the prediction of thermal hysteresis phenomena from the first-principles investigation.[3,52]

The treatment of defects and their impact on the heat storage properties will be studied in the future.

ASSOCIATED CONTENT

Supporting Information

The Supporting Information is available free of charge at https://pubs.acs.org/doi/10.1021/acs.jpcc.2c00572.

Optimized structures with all assessed functionals, band gaps obtained using all assessed functionals, and optimized structure of the TS, with front and side view animations of the TS mode (PDF)

AUTHOR INFORMATION

Corresponding Author

Thomas Bredow − *Mulliken Center for Theoretical Chemistry, Bonn 53115, Germany*; Email: bredow@thch.uni-bonn.de

Author

Stefan Jütten − *Mulliken Center for Theoretical Chemistry, Bonn 53115, Germany; Max Planck Institute for Chemical Energy Conversion, Mühlheim an der Ruhr 45470, Germany*; orcid.org/0000-0001-8756-7963

Complete contact information is available at: https://pubs.acs.org/10.1021/acs.jpcc.2c00572

Notes

The authors declare no competing financial interest.

ACKNOWLEDGMENTS

This work was supported by the International Max Planck Research School on Reactive Structure Analysis for Chemical Reactions (IMPRS-RECHARGE). We thank the Leibniz University Hannover IT Services (LUIS) for providing computational resources. The authors gratefully acknowledge the granted access to the bonna cluster hosted by the University of Bonn.

REFERENCES

(1) Tokoro, H.; Yoshikiyo, M.; Imoto, K.; Namai, A.; Nasu, T.; Nakagawa, K.; Ozaki, N.; Hakoe, F.; Tanaka, K.; Chiba, K.; et al. External stimulation-controllable heat-storage ceramics. *Nat. Commun.* **2015**, *6*, 7037.

(2) Ohkoshi, S.-i.; Tsunobuchi, Y.; Matsuda, T.; Hashimoto, K.; Namai, A.; Hakoe, F.; Tokoro, H. Synthesis of a metal oxide with a room-temperature photoreversible phase transition. *Nat. Chem.* **2010**, *2*, 539−545.

(3) Nakamura, Y.; Sakai, Y.; Azuma, M.; Ohkoshi, S.-i. Long-term heat-storage ceramics absorbing thermal energy from hot water. *Sci. Adv.* **2020**, *6*, No. eaaz5264.

(4) Shen, Z.; Shi, Q.; Huang, W.; Huang, B.; Wang, M.; Gao, J.; Shi, Y.; Lu, T. Stabilization of microcrystal λ-Ti_3O_5 at room temperature by aluminum-ion doping. *Appl. Phys. Lett.* **2017**, *111*, 191902.

(5) Wang, M.; Huang, W.; Shen, Z.; Gao, J.; Shi, Y.; Lu, T.; Shi, Q. Phase evolution and formation of λ phase in Ti_3O_5 induced by magnesium doping. *J. Alloys Compd.* **2019**, *774*, 1189−1194.

(6) Fu, X.-K.; Chen, W.-Q.; Jiang, Z.-S.; Yang, B.; Zhao, X.; Zuo, L. First-principles investigation on elastic, electronic, and optical properties of Ti_3O_5. *Acta Phys. Sin.* **2019**, *68*, 207301.

(7) Liu, R.; Shang, J.-X. First-principles study of thermal properties and phase transition between β-Ti_3O_5 and λ-Ti_3O_5. *Modell. Simul. Mater. Sci. Eng.* **2012**, *20*, 035020.

(8) Liu, R.; Shang, J.-X.; Wang, F.-H. Electronic, magnetic and optical properties of β-Ti_3O_5 and λ-Ti_3O_5: A density functional study. *Comput. Mater. Sci.* **2014**, *81*, 158−162.

(9) Fu, X.-K.; Yang, B.; Chen, W.-Q.; Jiang, Z.-S.; Li, Z.-B.; Yan, H.-L.; Zhao, X.; Zuo, L. Evidence for bandwidth-control metal-insulator transition in Ti_3O_5. *Comput. Mater. Sci.* **2020**, *173*, 109435.

(10) Fu, X.; Hao, X.; Chen, W.; Yang, B.; Zhao, X.; Zuo, L. Influences of hole/electron-lattice coupling on phase transition between λ-Ti_3O_5 and β-Ti_3O_5. *J. Phys. Condens. Matter* **2020**, *32*, 46LT01.

(11) Dovesi, R.; Erba, A.; Orlando, R.; Zicovich-Wilson, C.; Civalleri, B.; Maschio, L.; Rérat, M.; Casassa, S.; Baima, J.; Salustro, S.; et al. Quantum-mechanical condensed matter simulations with CRYSTAL. *Wiley Interdiscip. Rev.: Comput. Mol. Sci.* **2018**, *8*, No. e1360.

(12) Cramer, C. J.; Truhlar, D. G. Density functional theory for transition metals and transition metal chemistry. *Phys. Chem. Chem. Phys.* **2009**, *11*, 10757−10816.

(13) Tran, F.; Stelzl, J.; Blaha, P. Rungs 1 to 4 of DFT Jacob's ladder: Extensive test on the lattice constant, bulk modulus, and cohesive energy of solids. *J. Chem. Phys.* **2016**, *144*, 204120.

(14) Vilela Oliveira, D.; Laun, J.; Peintinger, M. F.; Bredow, T. BSSE-correction scheme for consistent gaussian basis sets of double- and triple-zeta valence with polarization quality for solid-state calculations. *J. Comput. Chem.* **2019**, *40*, 2364−2376.

(15) Mustapha, S.; D'Arco, P.; De La Pierre, M.; Noël, Y.; Ferrabone, M.; Dovesi, R. On the use of symmetry in configurational analysis for the simulation of disordered solids. *J. Phys. Condens. Matter* **2013**, *25*, 105401.
(16) D'Arco, P.; Mustapha, S.; Ferrabone, M.; Noël, Y.; De La Pierre, M.; Dovesi, R. Symmetry and random sampling of symmetry independent configurations for the simulation of disordered solids. *J. Phys. Condens. Matter* **2013**, *25*, 355401.
(17) Becke, A. D. Density-functional thermochemistry. I. The effect of the exchange-only gradient correction. *J. Chem. Phys.* **1992**, *96*, 2155−2160.
(18) Perdew, J. P.; Wang, Y. Pair-distribution function and its coupling-constant average for the spin-polarized electron gas. *Phys. Rev. B: Condens. Matter Mater. Phys.* **1992**, *46*, 12947.
(19) Perdew, J. P.; Yue, W. Accurate and simple density functional for the electronic exchange energy: Generalized gradient approximation. *Phys. Rev. B: Condens. Matter Mater. Phys.* **1986**, *33*, 8800.
(20) Vosko, S. H.; Wilk, L.; Nusair, M. Accurate spin-dependent electron liquid correlation energies for local spin density calculations: a critical analysis. *Can. J. Phys.* **1980**, *58*, 1200−1211.
(21) Adamo, C.; Barone, V. Toward reliable density functional methods without adjustable parameters: The PBE0 model. *J. Chem. Phys.* **1999**, *110*, 6158−6170.
(22) Bredow, T.; Gerson, A. R. Effect of exchange and correlation on bulk properties of MgO, NiO, and CoO. *Phys. Rev. B: Condens. Matter Mater. Phys.* **2000**, *61*, 5194.
(23) Becke, A. D. Density-functional thermochemistry. V. Systematic optimization of exchange-correlation functionals. *J. Chem. Phys.* **1997**, *107*, 8554−8560.
(24) Hamprecht, F. A.; Cohen, A. J.; Tozer, D. J.; Handy, N. C. Development and assessment of new exchange-correlation functionals. *J. Chem. Phys.* **1998**, *109*, 6264−6271.
(25) Zhao, Y.; Truhlar, D. G. The M06 suite of density functionals for main group thermochemistry, thermochemical kinetics, noncovalent interactions, excited states, and transition elements: two new functionals and systematic testing of four M06-class functionals and 12 other functionals. *Theor. Chem. Acc.* **2008**, *120*, 215−241.
(26) Krukau, A. V.; Vydrov, O. A.; Izmaylov, A. F.; Scuseria, G. E. Influence of the exchange screening parameter on the performance of screened hybrid functionals. *J. Chem. Phys.* **2006**, *125*, 224106.
(27) Perdew, J. P.; Burke, K.; Ernzerhof, M. Generalized gradient approximation made simple. *Phys. Rev. Lett.* **1996**, *77*, 3865.
(28) Chai, J.-D.; Head-Gordon, M. Long-range corrected hybrid density functionals with damped atom−atom dispersion corrections. *Phys. Chem. Chem. Phys.* **2008**, *10*, 6615−6620.
(29) Furness, J. W.; Kaplan, A. D.; Ning, J.; Perdew, J. P.; Sun, J. Accurate and Numerically Efficient r2SCAN Meta-Generalized Gradient Approximation. *J. Phys. Chem. Lett.* **2020**, *11*, 8208−8215 PMID: 32876454.
(30) Ehlert, S.; Huniar, U.; Ning, J.; Furness, J. W.; Sun, J.; Kaplan, A. D.; Perdew, J. P.; Brandenburg, J. G. r2SCAN-D4: Dispersion corrected meta-generalized gradient approximation for general chemical applications. *J. Chem. Phys.* **2021**, *154*, 061101.
(31) Grimme, S.; Hansen, A.; Ehlert, S.; Mewes, J.-M. r2SCAN-3c: A "Swiss army knife" composite electronic-structure method. *J. Chem. Phys.* **2021**, *154*, 064103.
(32) Kresse, G.; Furthmüller, J. Efficient iterative schemes for ab initio total-energy calculations using a plane-wave basis set. *Phys. Rev. B: Condens. Matter Mater. Phys.* **1996**, *54*, 11169.
(33) Kresse, G.; Furthmüller, J. Efficiency of ab-initio total energy calculations for metals and semiconductors using a plane-wave basis set. *Comput. Mater. Sci.* **1996**, *6*, 15−50.
(34) Blöchl, P. E. Projector augmented-wave method. *Phys. Rev. B* **1994**, *50*, 17953.
(35) Kresse, G.; Joubert, D. From ultrasoft pseudopotentials to the projector augmented-wave method. *Phys. Rev. B* **1999**, *59*, 1758.
(36) Grimme, S.; Hansen, A.; Brandenburg, J. G.; Bannwarth, C. Dispersion-corrected mean-field electronic structure methods. *Chem. Rev.* **2016**, *116*, 5105−5154.
(37) Tran, F.; Kalantari, L.; Traoré, B.; Rocquefelte, X.; Blaha, P. Nonlocal van der Waals functionals for solids: Choosing an appropriate one. *Phys. Rev. Mater.* **2019**, *3*, 063602.
(38) Grimme, S.; Antony, J.; Ehrlich, S.; Krieg, H. A consistent and accurate ab initio parametrization of density functional dispersion correction (DFT-D) for the 94 elements H-Pu. *J. Chem. Phys.* **2010**, *132*, 154104.
(39) Grimme, S.; Ehrlich, S.; Goerigk, L. Effect of the damping function in dispersion corrected density functional theory. *J. Comput. Chem.* **2011**, *32*, 1456−1465.
(40) Hinuma, Y.; Pizzi, G.; Kumagai, Y.; Oba, F.; Tanaka, I. Band structure diagram paths based on crystallography. *Comput. Mater. Sci.* **2017**, *128*, 140−184.
(41) Sheppard, D.; Xiao, P.; Chemelewski, W.; Johnson, D. D.; Henkelman, G. A generalized solid-state nudged elastic band method. *J. Chem. Phys.* **2012**, *136*, 074103.
(42) Momma, K.; Izumi, F. VESTA: a three-dimensional visualization system for electronic and structural analysis. *J. Appl. Crystallogr.* **2008**, *41*, 653−658.
(43) Kendrick, J.; Burnett, A. D. PDielec: The calculation of infrared and terahertz absorption for powdered crystals. *J. Comput. Chem.* **2016**, *37*, 1491−1504.
(44) Kobayashi, K.; Taguchi, M.; Kobata, M.; Tanaka, K.; Tokoro, H.; Daimon, H.; Okane, T.; Yamagami, H.; Ikenaga, E.; Ohkoshi, S.-i. Electronic structure and correlation in $\beta - Ti_3O_5$ and $\lambda - Ti_3O_5$ studied by hard X-ray photoelectron spectroscopy. *Phys. Rev. B: Condens. Matter Mater. Phys.* **2017**, *95*, 085133.
(45) Ohkoshi, S.-i.; Tokoro, H.; Nakagawa, K.; Yoshikiyo, M.; Jia, F.; Namai, A. Low-pressure-responsive heat-storage ceramics for automobiles. *Sci. Rep.* **2019**, *9*, 13203.
(46) Araki, Y.; Ohkoshi, S.; Tokoro, H. Synthesis of λ-Ti_3O_5 nanocrystals using a block copolymer. *Mater. Today Energy* **2020**, *18*, 100525.
(47) Yoshimatsu, K.; Kumigashira, H. Direct Synthesis of Metastable λ-Phase Ti_3O_5 Films on $LaAlO_3$ (110) Substrates at High Temperatures. *Cryst. Growth Des.* **2022**, *22*, 703−710.
(48) Kylänpää, I.; Balachandran, J.; Ganesh, P.; Heinonen, O.; Kent, P. R. C.; Krogel, J. T. Accuracy of ab initio electron correlation and electron densities in vanadium dioxide. *Phys. Rev. Mater.* **2017**, *1*, 065408.
(49) Trail, J.; Monserrat, B.; López Ríos, P.; Maezono, R.; Needs, R. J. Quantum Monte Carlo study of the energetics of the rutile, anatase, brookite, and columbite TiO_2 polymorphs. *Phys. Rev. B: Condens. Matter Mater. Phys.* **2017**, *95*, 121108.
(50) Mariette, C.; Lorenc, M.; Cailleau, H.; Collet, E.; Guérin, L.; Volte, A.; Trzop, E.; Bertoni, R.; Dong, X.; Lépine, B.; et al. Strain wave pathway to semiconductor-to-metal transition revealed by time-resolved X-ray powder diffraction. *Nat. Commun.* **2021**, *12*, 1239.
(51) Onoda, M.; Ogawa, Y.; Taki, K. Phase transitions and the doping effect in Ti_3O_5. *J. Phys. Condens. Matter* **1998**, *10*, 7003.
(52) Tokoro, H.; Namai, A.; Yoshikiyo, M.; Fujiwara, R.; Chiba, K.; Ohkoshi, S.-i. Theoretical prediction of a charge-transfer phase transition. *Sci. Rep.* **2018**, *8*, 63.

https://doi.org/10.1021/acs.jpcc.2c00572
J. Phys. Chem. C 2022, 126, 7809−7817

APPENDIX B

Doping Effect on the Electronic Structure and Heat-Storage Properties of Ti_3O_5

THE JOURNAL OF PHYSICAL CHEMISTRY C
A JOURNAL OF THE AMERICAN CHEMICAL SOCIETY

pubs.acs.org/JPCC

Article

Doping Effect on the Electronic Structure and Heat-Storage Properties of Ti_3O_5

Stefan Jütten* and Thomas Bredow*

Cite This: *J. Phys. Chem. C* 2023, 127, 10445−10452

Read Online

ACCESS | Metrics & More | Article Recommendations | Supporting Information

ABSTRACT: It is known that substitution of a small fraction of Ti atoms in Ti_3O_5 by aliovalent metal atoms alters its heat-storage properties, i.e., $\beta \rightarrow \lambda$ phase-transition enthalpy and temperature, and extends its range of application to, for example, the capture and utilization of waste heat. Heat-storage properties vary depending on the substituting element and its concentration. The exploration of the vast space of possible combinations of these quantities is challenging due to the small energy differences under consideration. Thus, computational approaches which reliably predict heat-storage properties of such defective systems can aid in the screening of potential material candidates for subsequent synthesis. Substituted compounds $M_xTi_{3-x}O_5$ with trivalent M = Sc, Al, and Mg have been reported in the literature. Here we present the first thorough study of the doping effect on the electronic structure and the heat-storage properties of Ti_3O_5 from first principles. Electronic ground states were calculated for all Ti−M substitution positions using the M06 hybrid functional. Doping leads to increased metallic character in both phases, which primarily results from a change in atomic positions and not from the substituting element itself. We applied the r^{2}SCAN-D3 method to the study of heat-storage properties of those materials and found good agreement in phase-transition enthalpies with experimentally recorded data. Calculated phase-transition entropies show larger deviations from experiment. The phase-transition mechanism is studied as a function of the defect concentration by calculating the minimum-energy path. Doping primarily changes the relative energy of both phases and leaves the activation barrier virtually unchanged. Our results suggest that heat-storage systems of this kind are efficient only for M concentrations below 4 atom %.

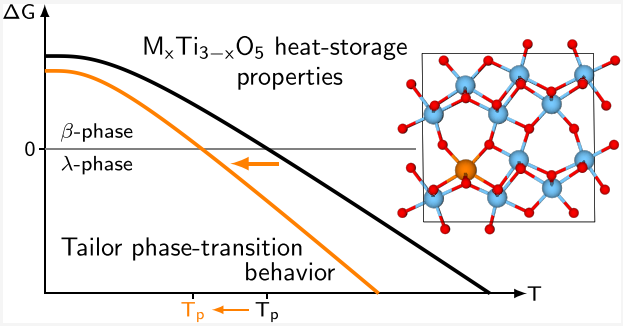

INTRODUCTION

Latent heat-storage materials find application in the capture and utilization of thermal energy and are of interest in waste heat utilization, space and water heating, building applications, and renewable energy generation.[1−3] Commonly, materials used for these applications involve a physical phase change, which can be operationally challenging. In contrast, the Ti_3O_5 ceramic has emerged as a heat-storage material that undergoes a thermally induced solid−solid phase change from the more stable β-phase to the thermodynamically less stable λ-phase, which can be triggered by the application of heat, irradiation, and electric current.[4] The first-order $\beta \rightarrow \lambda$ phase transition occurs at a phase-transition temperature of T_p = 470 K, and a further transformation to the α-phase is observed above 530 K.[5] Application of 600 bar of pressure to the λ-phase triggers the back transition to the β-phase.[4] The phase-transition enthalpy (ΔH) is 12 ± 1 kJ mol^{-1}, which is close to the heat capacity of water.[4] At ambient pressure, nanocrystalline λ-Ti_3O_5 does not spontaneously transform back to the more stable β-Ti_3O_5 polymorph but instead is trapped in the metastable state, resulting in a pronounced thermal hysteresis loop.[6]

Substitutions of a small fraction of the Ti atoms in Ti_3O_5 by other elements M are reported in the literature.[7−13] However, the heat-storage properties of nanocrystalline samples were studied only for M = Sc,[14] Al,[15] and Mg.[16] All substitutions reduce T_p as the amount of the substituted element increases and eventually to below room temperature. Therefore, compounds $M_xTi_{3-x}O_5$ can be used as heat-storage materials targeted for waste-heat utilization only if the amount of dopant is sufficiently small to ensure that T_p > 298 K.

A substitution of 3% of Ti atoms by Sc results in a reduction of T_p from 470 to 340 K and decreases ΔH from 12 to 4 kJ mol^{-1}.[14] This allows for the storage of the thermal energy of hot water. Doping with 2 atom % Al further lowers ΔH to ≈2 ± 1 kJ mol^{-1} and T_p by 57 K.[15] Even lower substitution levels are expected to yield heat-storage properties closer to those of the parent compound Ti_3O_5. Accordingly, Mg substitutions of 1.7 atom % retain a high phase-transition enthalpy of ΔH = 11.5 kJ mol^{-1}

Received: March 7, 2023
Revised: May 9, 2023
Published: May 25, 2023

https://doi.org/10.1021/acs.jpcc.3c01549
J. Phys. Chem. C 2023, 127, 10445−10452

Table 1. Stoichiometry of the Supercell Models with the Corresponding Concentration of Dopant Atom M and the Resulting Space Group and Monoclinic (mon) or Triclinic (tri) Crystal System[a]

Compound	M, atom %	Space group	Crystal system	Z	Expansion	Lattice parameters		
						a	b	c
$M_{0.5}Ti_{2.5}O_5$	16.7	C/m	mon.	2	$1 \times 1 \times 1^p$	5.27	5.27	9.97
$M_{0.25}Ti_{2.75}O_5$	8.3	C/m	mon.	4	$1 \times 1 \times 1^c$	9.83	3.79	9.97
$M_{0.125}Ti_{2.875}O_5$	4.2	P_1	tri.	8	$1 \times 2 \times 1^c$	9.83	7.58	9.97
$M_{0.083}Ti_{2.917}O_5$	2.8	P_1	tri.	12	$1 \times 3 \times 1^c$	9.83	11.36	9.97
$M_{0.0624}Ti_{2.9376}O_5$	2.1	P_1	tri.	16	$2 \times 2 \times 2^p$	10.54	10.54	19.94
$M_{0.05}Ti_{2.95}O_5$	1.7	P_1	tri.	20	$1 \times 5 \times 1^c$	9.77	18.98	9.94

[a]The number of formula units Z in the expansion of the primitive (superscript p) or conventional (superscript c) unit cell is indicated. The lattice parameters a, b, and c (in Å, referring to λ-$M_xTi_{3-x}O_5$) correspond to unsubstituted Ti_3O_5.

and still lower the phase-transition temperature by 117 K to T_p = 353 K.

Developing new heat-storage materials of this kind requires the synthesis of a large number of potential candidate materials, which is costly and cumbersome. Thus, reliable predictions of heat-storage properties with theoretical methods could enable a knowledge-based approach in which only certain prescreened candidates have to be synthesized.

Theoretical methods employed for screening various dopant elements and concentrations must accurately predict the energy difference $\Delta E = E^{\lambda} - E^{\beta}$ between the β and λ phases, which is the principal theoretical benchmark for evaluating the heat-storage potential of a given compound. Moreover, they also must yield appreciable entropy differences for substituted systems to recover experimental trends in the phase-transition temperature, for which free energies have to be computed.

In this study, we initially calculate the electronic structure modulation upon Ti/M substitution using the hybrid density functional M06-D3.[17] We find that the observed changes in the electronic structure depend only on the lattice distortion caused by the dopant atom and not the dopant itself. Then, we apply the r^{2}SCAN-D3 method, which was previously found to yield accurate geometries and heat-storage properties for Ti_3O_5,[18] to the prediction of heat-storage properties of $M_xTi_{3-x}O_5$. The phase-transition behavior of $M_xTi_{3-x}O_5$ as a function of the dopant concentration x was studied by calculating the minimum-energy path of the phase transformation with the solid-state nudged elastic band (ss-NEB) method. It was observed that the substitution mostly affects the thermodynamics of the system but does not appreciably alter the phase-transition mechanism itself.

COMPUTATIONAL DETAILS

All structural relaxations and phonon calculations were performed with the Vienna *Ab Initio* Simulation Package (VASP) v6.2.1,[19,20] where the projector augmented wave (PAW) method[21,22] with a 600 eV plane wave cutoff energy and standard PAW potentials was used. We considered structures to be converged if the norm of all forces was below 1×10^{-4} eV/Å. We employed the r^{2}SCAN meta-GGA functional[23] augmented by the DFT-D3(BJ) dispersion correction,[24,25] which has been identified as an accurate method for the calculation of structural and thermodynamic properties.[18,26−28] Partial band occupations were treated by Gaussian smearing, where for each system the width σ was carefully converged with respect to the total electronic energy. The tetrahedron method with Blöchl corrections[29] was employed for more accurate final total electronic energies in systems where statistical thermodynamics was applied after frequency calculations.

Experimentally it was determined that the λ-phase is Pauli paramagnetic and the β-phase exhibits a much lower magnetization.[30] We previously investigated the electronic ground states of both phases by assuming different magnetic configurations[18] and concluded that β is close to nonmagnetic (small positive and negative spin densities, denoted as antiferromagnetic by us) and λ can be simplified as ferromagnetic, since the individual Ti atoms have positive but nonequal spin densities. We observed that the antiferromagnetic state is also obtained for the β-phase if the SCF procedure is started with a ferromagnetic spin setting by using the r^{2}SCAN-D3 method. Therefore, ferromagnetic initial spin configurations were used for all subsequent calculations.

Our calculations of electronic properties employed hybrid DFT, which provides an improved description of open-shell transition-metal compounds.[31,32] We chose the M06-D3 method due to its good performance for transition-metal-containing systems.[31] The CRYSTAL17 v1.0.2 program[33] was used for the hybrid DFT calculations since the evaluation of Fock exchange with Gaussian-type basis functions used in this program is computationally more efficient compared to a plane-wave basis.[34] We employed the optimized pob-TZVP-rev2 basis sets.[35] Three-body dispersion terms were included in all CRYSTAL D3 calculations but are neglected by default in VASP.

SCF convergence thresholds of 10^{-8} eV (VASP) and 10^{-8} au (CRYSTAL) and dense integration grids (XXLGRID) were used throughout. All energies presented in this work refer to one formula unit, Ti_3O_5 or $M_xTi_{3-x}O_5$. In all CRYSTAL calculations, the recommended integral truncation tolerances for hybrid functionals of 10^{-7}, 10^{-7}, 10^{-7}, 10^{-14}, and 10^{-42} were applied. Integral evaluations in reciprocal space utilized Γ-centered Monkhorst−Pack meshes with a spacing of 0.2 Å^{-1} between k points. This spacing was increased to 0.4 Å^{-1} for the calculation of vibrational frequencies with the r^{2}SCAN-D3 method in order to reduce the computational effort in the frequency calculations of defective systems, where no exploitation of symmetry was possible. A comparison of frequencies computed with both k-point densities shows only small deviations of a few cm^{-1}. Since electronic energies are more affected by the chosen k-point density, we used those electronic energies obtained with denser meshes in the calculation of thermodynamic properties.

RESULTS AND DISCUSSION

Substitutions. In order to vary the M concentration, we built several Ti_3O_5 supercells as shown in Table 1. A single M/Ti substitution in the $1 \times 3 \times 1$ expansion of the conventional unit

https://doi.org/10.1021/acs.jpcc.3c01549
J. Phys. Chem. C 2023, 127, 10445−10452

cell is our model for the experimentally synthesized 3 atom % Sc substituted crystals.[14] 2 atom % Al-substituted Ti_3O_5[15] is modeled by a 2 × 2 × 2 supercell, and the compound is doped with 1.7 atom % Mg[16] with a 1 × 5 × 1 supercell. It has to be mentioned that all supercells are neutral since we considered only the exchange of neutral Ti and M atoms.

Substitutions in the primitive and conventional unit cells of the monoclinic $C2/m$ crystal remove the $C2$ symmetry operation and result in the monoclinic C/m space group. Models with $M < 0.25$ do not exhibit any nonprimitive symmetry operations and are therefore classified as space group P_1 in the triclinic crystal system. Figures of all model systems can be found in the Supporting Information.

High dopant concentrations of 16.7 and 8.3% are known to stabilize the λ-phase and even the α-phase, respectively.[13,15] However, we performed all calculations starting from the experimental β and λ crystal structures of Ti_3O_5. This approach enables us to perform consistent comparisons and identify trends as a function of the dopant concentration for the substituted systems.

Substitutions with Sc, Al, and Mg in all three irreducible Ti sites of Ti_3O_5 were considered.[4] We fully optimized the β- and λ-phases of all of the shown compounds using r^{2}SCAN-D3. The optimized lattice vectors and monoclinic angles are provided in the Supporting Information Table S1. Comparisons of optimized structures with the corresponding experimental structures are provided in Supporting Information Table S2, which underscores our previous asessment[18] that the deviation of optimized λ-phase lattice vector lengths and monoclinic angles from experiment is smaller (∼±0.5%) than for β-phases (∼±1%). Increasing x generally results in a more severe distortion of the lattice. We performed single-point calculations on the r^{2}SCAN-D3 optimized structures with the M06-D3 method to obtain higher-quality electronic structures and compared trends with our r^{2}SCAN-D3 results. In the M06-D3 calculations, we considered antiferromagnetic and ferromagnetic spin configurations. As described above for r^{2}SCAN-D3, antiferromagnetic spin configurations are more stable for β-phases and ferromagnetic spin configurations are favored for λ-phases. The energies of the respective electronic ground states relative to the most stable substitution site are given in Table 2.

According to the r^{2}SCAN-D3 results, the Ti2 site is preferred for M = Sc and Al, and Ti1 is preferred for M = Mg in the β-type structures. The λ-type structures show a less clear trend. At the lowest concentration, the Ti3 site is most stable for all three metals. As a general trend, we observe decreasing energy differences between substitution sites with decreasing x. In most cases, the M06-D3 method yields larger energy differences than the r^{2}SCAN-D3 method, possible due to the larger spin localization obtained at the hybrid DFT level. With only one exception, the preferred substitution positions with both methods are in agreement for the λ structures. For the β phase, agreement between the methods is less pronounced. However, the energy differences of a few kJ mol^{-1} are within the expected error range of DFT methods. In the following, the minimum-energy structures obtained with r^{2}SCAN-D3 will be used for further analysis.

Electronic Structure. We present the electronic structure of Sc-substituted Ti_3O_5 calculated with M06-D3/pob-TZVP-rev2 in Figure 1. Corresponding figures for Al and Mg substitutions are provided in the Supporting Information. They do not differ substantially, and our following discussion of the Sc substitution applies.

Table 2. Comparison of the Relative Energies (in kJ mol^{-1}) among Cation Substitutions in the Three Irreducible Ti Sites of Ti_3O_5 Calculated with r^{2}SCAN-D3[a]

	r^{2}SCAN-D3			M06-D3		
Compound	Pos. 1	Pos. 2	Pos. 3	Pos. 1	Pos. 2	Pos. 3
β-$Sc_{0.5}Ti_{2.5}O_5$	3.8	0.0	2.2	13.5	6.8	0.0
β-$Sc_{0.25}Ti_{2.75}O_5$	2.0	0.0	3.1	1.4	0.0	0.4
β-$Sc_{0.125}Ti_{2.875}O_5$	1.0	0.0	1.4	2.2	0.0	0.2
β-$Sc_{0.083}Ti_{2.917}O_5$	0.8	0.0	1.0	2.0	4.0	0.0
β-$Al_{0.5}Ti_{2.5}O_5$	7.7	0.0	10.3	20.2	0.0	15.6
β-$Al_{0.25}Ti_{2.75}O_5$	3.7	0.0	6.3	13.8	0.0	8.0
β-$Al_{0.125}Ti_{2.875}O_5$	1.7	0.0	3.2	7.9	0.0	4.2
β-$Al_{0.0624}Ti_{2.9376}O_5$	0.4	0.0	1.3	2.7	0.0	2.4
β-$Mg_{0.5}Ti_{2.5}O_5$	0.0	12.9	17.9	0.0	9.9	29.4
β-$Mg_{0.25}Ti_{2.75}O_5$	0.0	3.9	8.1	0.0	2.4	6.6
β-$Mg_{0.125}Ti_{2.875}O_5$	0.0	1.3	5.0	0.2	0.0	2.9
β-$Mg_{0.05}Ti_{2.95}O_5$	0.0	0.5	2.1	3.1	1.5	0.0
λ-$Sc_{0.5}Ti_{2.5}O_5$	4.0	0.0	9.2	6.5	0.0	16.2
λ-$Sc_{0.25}Ti_{2.75}O_5$	0.4	0.0	0.3	0.6	0.0	3.1
λ-$Sc_{0.125}Ti_{2.875}O_5$	1.6	0.0	4.7	2.2	0.0	6.9
λ-$Sc_{0.083}Ti_{2.917}O_5$	1.6	0.4	0.0	2.5	0.0	0.4
λ-$Al_{0.5}Ti_{2.5}O_5$	0.0	2.2	0.0	0.0	6.8	0.0
λ-$Al_{0.25}Ti_{2.75}O_5$	1.3	1.4	0.0	10.1	2.9	0.0
λ-$Al_{0.125}Ti_{2.875}O_5$	1.0	0.0	2.5	3.3	0.0	4.5
λ-$Al_{0.0624}Ti_{2.9376}O_5$	0.6	3.3	0.0	1.3	4.8	0.0
λ-$Mg_{0.5}Ti_{2.5}O_5$	7.7	0.0	7.4	12.1	0.0	8.4
λ-$Mg_{0.25}Ti_{2.75}O_5$	6.6	0.0	0.4	9.8	0.0	1.8
λ-$Mg_{0.125}Ti_{2.875}O_5$	0.0	0.0	2.8	0.0	0.0	22.2
λ-$Mg_{0.05}Ti_{2.95}O_5$	0.2	0.7	0.0	2.4	3.2	0.0

[a]M06-D3 energy differences refer to single-point calculations of the r^{2}SCAN-D3 optimized structures.

Upon substitution of a Ti atom by Sc, Al, or Mg, the 2-fold rotation axis and mirror plane symmetry operations vanish. The increased degrees of freedom in the optimization of atomic positions are reflected in the spread of states over a continuous energy interval instead of the clustering of states at particular energies as seen in the Ti_3O_5 references. All substituted compounds $M_xTi_{3-x}O_5$ exhibit metallic character as a result of the cation doping, caused by the emergence of states near the Fermi level (E_F). In the following, we discuss the Ti 3d states located in the energy range of up to 2 eV below E_F. In substituted β-Ti_3O_5 compounds, there are two groups of defect states, centered at −1.7 eV below E_F and near the Fermi level. The former has large contributions from the d_{z^2}, d_{xz}, and $d_{x^2-y^2}$ states. In the latter, the contribution of d_{yz} states decreases with decreasing x while the weights of d_{z^2} and d_{xz} states increase. In substituted λ-Ti_3O_5, d_{yz} states dominate below E_F.

As expected, the differences between substituted systems and Ti_3O_5 become less pronounced with decreasing x. States associated with M are between −6 and −7 eV and do not hybridize with the Ti 3d states.

To examine the doping effect in more detail, we performed calculations on the optimized doped structures, with Ti resubstituted into the dopant position (Supporting Information figures). This approach allows for a distinction between changes in the electronic structure caused by the structural distortion on the one hand and by the dopant element on the other hand. Surprisingly, the differences between doped and Ti-resubstituted DOS are not significant, although the number of valence electrons is different. This means that the observed changes in

https://doi.org/10.1021/acs.jpcc.3c01549
J. Phys. Chem. C 2023, 127, 10445−10452

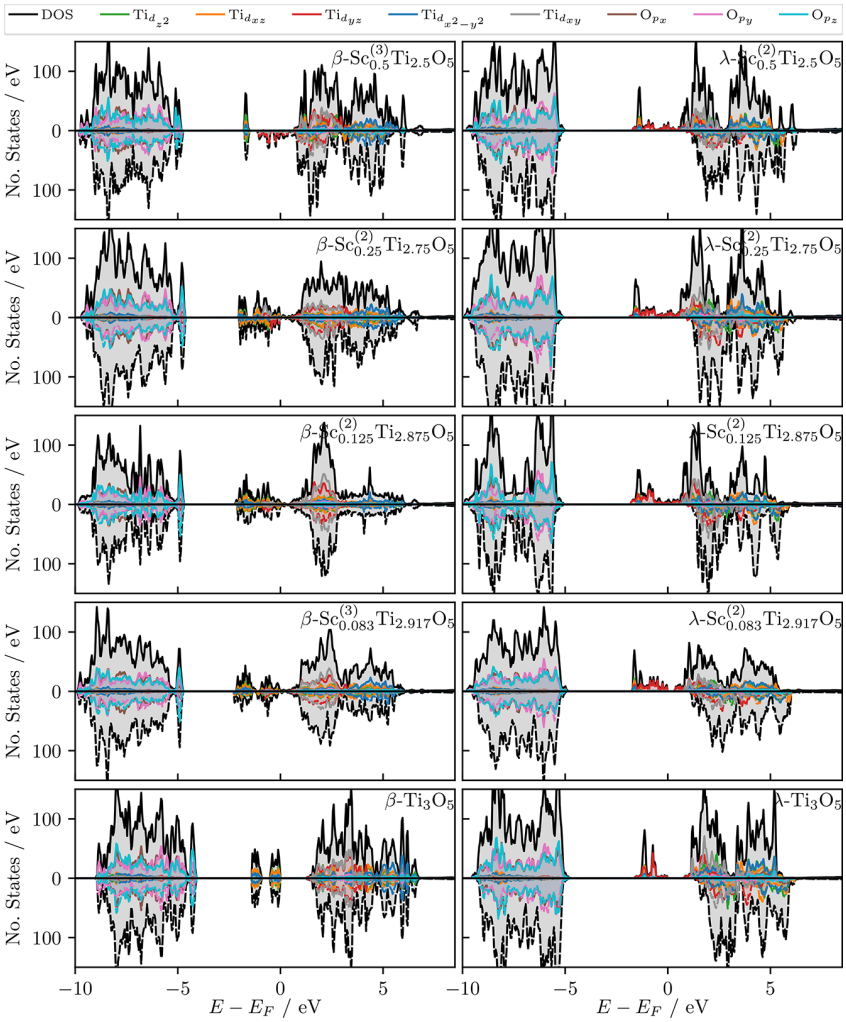

Figure 1. Density of states of Sc-substituted Ti_3O_5 as a function of dopant concentration (M06-D3/pob-TZVP-rev2 results); Ti and O valence states are projected onto the total DOS. The DOS of Ti_3O_5 is shown as a reference. Sc superscripts indicate the Ti substitution site.

the electronic structure are mainly due to structural distortion and are not a consequence of electron holes in the valence band introduced by the trivalent metals, although these two processes have completely different physical origins.

In the next step, we analyze the electron density difference between Ti-resubstituted $Sc_{0.083}Ti_{2.917}O_5$ phases and the respective Sc-substituted phases, $\Delta\rho = \rho^{Sc_xTi_{3-x}O_5} - \rho^{Ti_3O_5}$ (Figure 2).

First, we notice a significant accumulation of charge density at the defect site, where formally Ti^{4+} is substituted by Sc^{3+}. In the β-phase, this electron density is redistributed from nearby Ti3 d_{xz} orbitals. Local electronic effects caused by the defect are less pronounced in the λ-phase, where only an overall increase in delocalized charge density can be identified. The electron density along the bonds between the defect and the six octahedrally coordinated O atoms is reduced in both phases. In turn, the electron density at these O atoms increases. In the β-phase, doping leads to a notable loss of electron density in Ti3 d_{xz} orbitals. At the same time, electron density increases around the displaced O1, which connects the central Ti3 dimer. We correlate the decreased electronic charge density in Ti3 d_{xz} orbitals with the reduced number of d_{xz} states below E_F in the Ti-resubstituted DOS compared to its Sc-substituted counterpart. Moreover, we notice an increase in delocalized electron density in the area above and below the defect.

In the λ-phase, we generally observe less pronounced differences between the charge densities, except for an overall increase in delocalized electron density as a result of the doping. This corroborates our previous observation that cation doping increases the metallic character.

Prediction of Heat-Storage Properties. A Ti_3O_5-based heat-storage system undergoes a thermally induced phase change from the more stable β-phase to the thermodynamically less stable λ-phase. At the phase-transition temperature T_p, the free energies of both polymorphs are equal, i.e., $\Delta G(T_p) = 0$. The enthalpy difference ΔH at that temperature is equivalent to the thermal energy that can be stored. Enthalpy and free-energy differences are calculated with r^{2}SCAN-D3 for the respective most-stable M sites discussed above (Figure 3), where our previous results for phase-pure Ti_3O_5[18] are provided as a reference.

Doping results in lower phase-transition enthalpies and, correspondingly, lower phase-transition temperatures. The zero-point energy difference between both phases is decreased by ~4 kJ mol^{-1}, irrespective of the substituting element. Our ΔH predictions correctly reproduce experimental trends. For Mg-substituted Ti_3O_5, measured ΔH decreases by 0.5 kJ mol^{-1},[16]

https://doi.org/10.1021/acs.jpcc.3c01549
J. Phys. Chem. C 2023, 127, 10445−10452

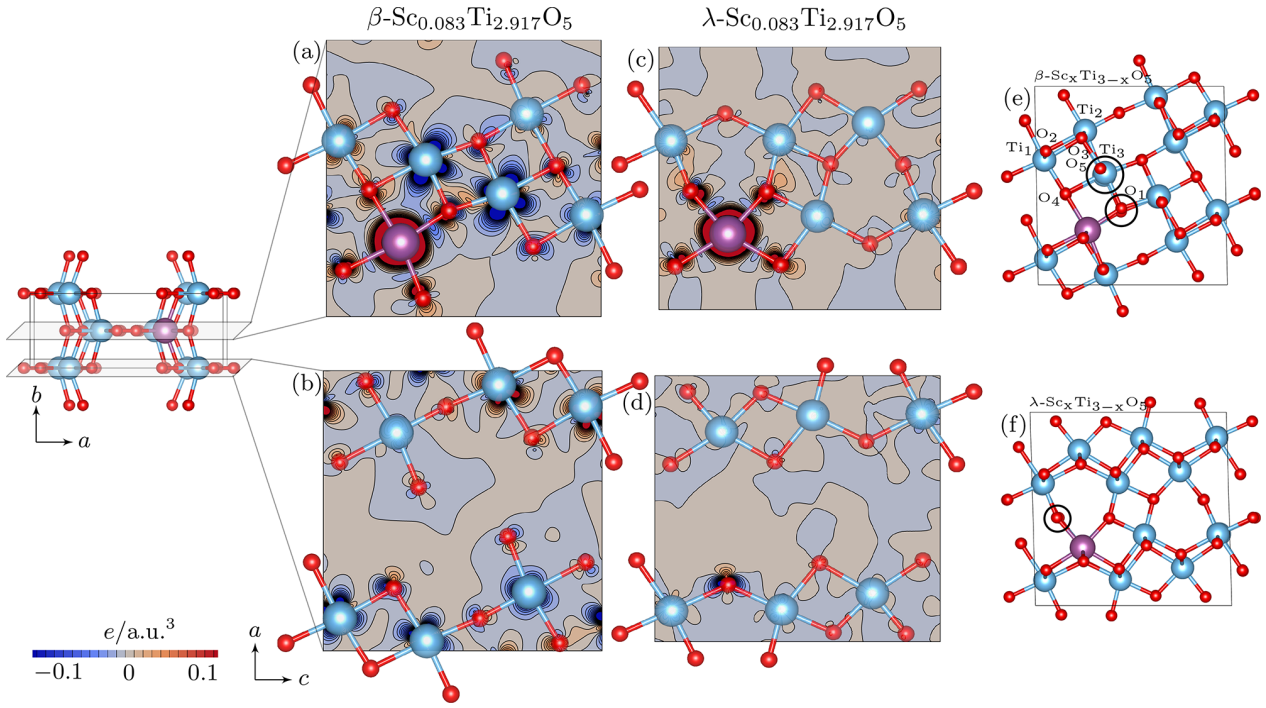

Figure 2. Electron density difference plots of (a, b) β-$Sc_{0.083}Ti_{2.917}O_5$ and (c, d) λ-$Sc_{0.083}Ti_{2.917}O_5$, with the Sc atom on a Ti2 site. Density differences are shown for the two planes along the crystallographic b axis. Structural distortions caused by the defect in the β-phase (e) and λ-phase (f) are highlighted in overlays of the substituted structure (front) and the respective Ti_3O_5 structure (background).

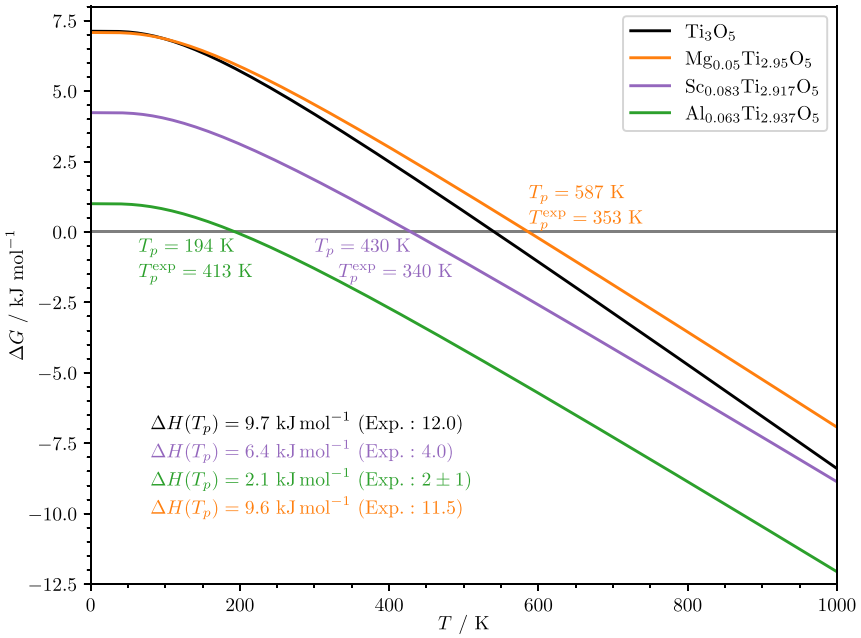

Figure 3. Free-energy difference ($\Delta G = G^{\lambda} - G^{\beta}$) plots of Sc-, Al-, and Mg-substituted Ti_3O_5 as a function of temperature and the predicted phase-transition temperatures T_p and phase-transition enthalpies $\Delta H(T_p)$ obtained from r^{2}SCAN-D3 frequency calculations, compared to experimental results.

which is close to the computed difference, 0.1 kJ mol^{-1}. For Al substitutions, similarly good agreement with an experimental ΔH of 2 ± 1 kJ mol^{-1}[15] (calcd 2.1 kJ mol^{-1}) is obtained. Note that we assigned an uncertainty of ±1 kJ mol^{-1} to this ΔH value since the experimental ratio between the phases is not known. However, ΔH for Sc-substituted systems is overestimated by 2.4 kJ mol^{-1}. For a discussion of possible reasons, see below.

Our predicted T_p, except for M = Al, overestimate the experimental values, similar to that obtained previously for pure Ti_3O_5.[18] For M = Al, the calculated T_p is ∼200 K lower than the measured value.[15] The Al sample was synthesized using carbothermal reduction, which left carbon traces in the sample that were seen in XPS spectra. These carbon impurities may significantly affect the value of T_p, while our theoretical result

https://doi.org/10.1021/acs.jpcc.3c01549
J. Phys. Chem. C 2023, 127, 10445−10452

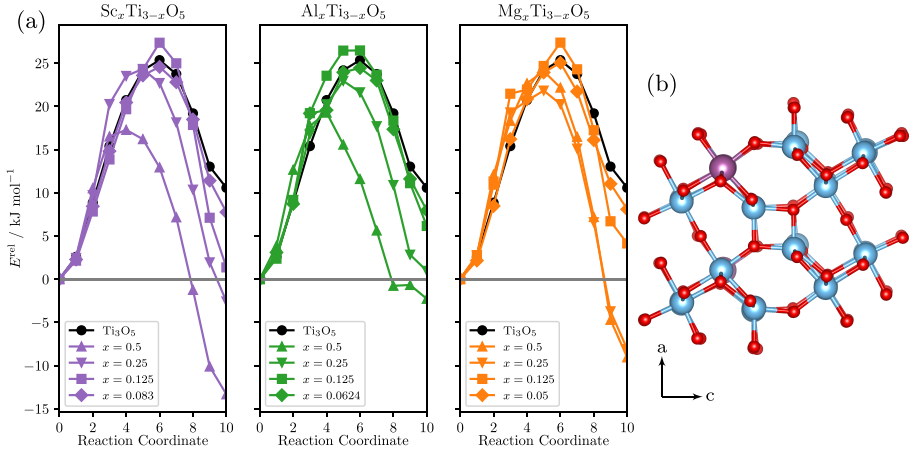

Figure 4. (a) Prediction of the reaction mechanism of the phase transition with the solid-state NEB method on the r^{2}SCAN-D3 level of theory for compounds with varying dopant concentrations x. Image 0 corresponds to β-phases and image 10 corresponds to λ-phases. All energies are given in kJ mol^{-1} relative to the respective β-phase. (b) Overlay for the structural comparison of Sc-substituted transition states: $x = 0.5$ in the background (lower opacity), $x = 0.083$ in the front.

refers to pure compounds. In Sc-substituted systems, T_p is overestimated by 90 K in accordance with an ΔH value that is too large. For M = Mg, we even obtain a higher value of T_p than that for Ti_3O_5 itself.

Inaccurate predictions of T_p are attributed to a lack of sensitivity of the calculated frequencies to the dopant element or its concentration, which is evident from the similar slopes of $\Delta G(T)$ in Figure 3. This may be due to anharmonic effects that are not taken into account in the present results due to high computational demand. The steeper slope of $\Delta G(T)(Ti_3O_5)$ indicates that the entropy of the pure λ-phase is larger than that of the pure β-phase. This trend is also observed in the substituted systems. For further analysis, we provide plots of $\Delta H(T)$ and $\Delta S(T)$ in the Supporting Information. The entropy differences at the phase-transition temperature are obtained as $\Delta S^{Sc}(T_p) = S^{\lambda,Sc} - S^{\beta,Sc} = 14.8$ J mol^{-1} K^{-1} (exp. 12 J mol^{-1} K^{-1}), $\Delta S^{Al}(T_p) = 10.7$ J mol^{-1}K^{-1} (no exp. value available), and $\Delta S^{Mg}(T_p) = 16.4$ J mol^{-1}K^{-1} (exp. 28 J mol^{-1} K^{-1}). In Ti_3O_5, we obtain the highest value of $\Delta S(T_p) = 17.9$ J mol^{-1}K^{-1} (no exp. value available). The difference between calculated and measured entropy is responsible for the deviations obtained for T_p (M = Mg) but cannot explain the deviation for M = Sc.

We attempted to improve our free-energy results by adding a configurational entropy correction

$$\Delta S^{conf} = -R \sum_{i=1,2,3} p_i \ln p_i \quad (1)$$

with $p_i \propto e^{-\beta \Delta E}$ by taking into account our calculated energy differences ΔE among the three symmetry-inequivalent substitution sites i in Ti_3O_5 (Table 2). However, this approach led to negligible changes.

We also carefully investigated the influence of the PAW approximation by varying the PAW pseudopotential for Ti and O and the density of the k-point grid. However, this also did not improve the results.

An alternative explanation for the discrepancies between theory and experiment is that experimental samples are powders consisting of micro- and nanocrystallites, while the calculations correspond to the infinite bulk. Therefore surface effects may change the thermodynamic stability of the two phases. This will be accounted for in a forthcoming study.

Doping Effect on the Phase Transition. In the next step, we study the atomistic mechanism of the phase change by performing solid-state NEB[36] calculations along the reaction pathway. Hereby it is assumed that the phase transformation takes place simultaneously in all regions of the crystal. This method is used to find saddle points and minimum-energy paths between known reactants and products by optimizing intermediate images along the reaction path. This path is described by a reaction coordinate as a linear combination of changes in interatomic distances and lattice vectors. The approach optimizes both atomic positions and lattice vectors and is hence applicable to the modeling of a phase transition, where the volume of both phases differs. Images are constrained to maintain equal distances between each other by adding spring forces along the band. Thus, each image along the path is optimized, and the energetically favored reaction path is obtained. The transition state (TS) in the climbing image formalism is obtained by removing the spring forces along the band and inverting the true force along the band experienced by this image but minimizing the energy in all other directions. Therefore, the energy of the TS image is ensured to be the maximum along the reaction path.

We considered varying substituent concentrations x for each dopant element M = Sc, Al, and Mg in $M_xTi_{3-x}O_5$ (Figure 4(a)). In these calculations, only Ti2 was substituted in both polymorphs to ensure comparability between initial and final structures.

A strong dependence of the activation energy and relative phase stability on x is observed in all cases. Only small dopant concentrations ($x \leq 0.125$) yield β-phases that are more stable than the respective λ-phase. Thus, compounds with $x > 0.125$ are not suitable as heat-storage systems of this kind, as these concentrations stabilize λ-phases under ambient conditions. These trends confirm experimental observations for Sc[14] and Al[37] substitutions; however, they are less pronounced in calculations for M = Al.

Activation barriers for the phase transition are similar to those of Ti_3O_5 at the lowest dopant concentrations, which is to be expected. Only Mg-substituted systems retain higher activation barriers and do not exhibit a notable shift. For higher concentrations, we observe a shift of the potential energy maxima to the β-phase. Figure 4 illustrates that the main

https://doi.org/10.1021/acs.jpcc.3c01549
J. Phys. Chem. C 2023, 127, 10445−10452

difference between the TS structures with low (in the foreground) and high (in the background) dopant concentrations is the stronger displacement of the second-nearest-neighbor Ti3 and O1 connected to Ti3 for larger x. Since the rotation of the central Ti3−Ti3 dimer is the main atomic movement along the $\beta \rightarrow \lambda$ transition, we conclude that this rotation is hindered for larger x so that the TS structure becomes similar to the β structure.

CONCLUSIONS

The doping effect on the electronic structure and heat-storage properties of $M_xTi_{3-x}O_5$, M = Mg, Al, and Sc, was studied by density functional theory. While the structural perturbations caused by doping are confined to the near surroundings of the defect, doping leads to an overall delocalization of charge density in both phases, which increases their metallic character. The changes in the density of states caused by the different number of valence electrons in M and Ti and by the structural distortion after substitution cannot be distinguished. This effect is more pronounced in the λ-phase. We obtain phase-transition enthalpies in agreement with experiment, whereas phase-transition temperatures are subject to larger deviations. Possible reasons for this discrepancy were discussed. Doping with up to 4 atom % M was found to primarily change the relative energy of β- and λ-phases and to have a minor effect on the structure of transition states and barrier heights. The activation barriers are, however, significantly lower for high dopant concentrations. Above 4 atom % M/Ti substitution, the λ-phase becomes more stable than the β-phase. Our results suggest doping to be an efficient strategy to modify the thermodynamic stability of the phases. The development of heat-storage materials using Ti_3O_5 as a template should focus on substitution levels below 4 atom %.

ASSOCIATED CONTENT

Supporting Information

The Supporting Information is available free of charge at https://pubs.acs.org/doi/10.1021/acs.jpcc.3c01549.

Tabulated lattice vectors and monoclinic angles of optimized substituted structures with respect to substitution site and dopant concentration (PDF)

Comparison of lattice vectors and monoclinic angles of optimized substituted structures to available experimental structures; figures of all structures used to model substitutions; projected density of states as a function of substituent concentration and with defect resubstituted by titanium atoms; enthalpy and entropy difference plots as a function of temperature; and archive containing optimized transition state structures in POSCAR format (ZIP)

AUTHOR INFORMATION

Corresponding Authors

Stefan Jütten − *Mulliken Center for Theoretical Chemistry, 53115 Bonn, Germany; Max Planck Institute for Chemical Energy Conversion, 45470 Mülheim an der Ruhr, Germany;* orcid.org/0000-0001-8756-7963; Email: juetten@thch.uni-bonn.de

Thomas Bredow − *Mulliken Center for Theoretical Chemistry, 53115 Bonn, Germany*; Email: bredow@thch.uni-bonn.de

Complete contact information is available at: https://pubs.acs.org/10.1021/acs.jpcc.3c01549

Notes

The authors declare no competing financial interest.

ACKNOWLEDGMENTS

This work is supported by the International Max Planck Research School on Reactive Structure Analysis for Chemical Reactions (IMPRS-RECHARGE). We thank the Leibniz University Hannover IT Services (LUIS) for providing computational resources. The authors gratefully acknowledge the access granted to the bonna cluster hosted by the University of Bonn.

REFERENCES

(1) Bauer, T.; Steinmann, W.-D.; Laing, D.; Tamme, R. Thermal energy storage materials and systems. *Annu. rev. heat transf.* **2012**, *15*, 131−177.

(2) Tatsidjodoung, P.; Le Pierrès, N.; Luo, L. A review of potential materials for thermal energy storage in building applications. *Renew. Sustain. Energy Rev.* **2013**, *18*, 327−349.

(3) Alva, G.; Liu, L.; Huang, X.; Fang, G. Thermal energy storage materials and systems for solar energy applications. *Renew. Sustain. Energy Rev.* **2017**, *68*, 693−706.

(4) Tokoro, H.; Yoshikiyo, M.; Imoto, K.; Namai, A.; Nasu, T.; Nakagawa, K.; Ozaki, N.; Hakoe, F.; Tanaka, K.; Chiba, K.; et al. External stimulation-controllable heat-storage ceramics. *Nat. Commun.* **2015**, *6*, 7037.

(5) Ohkoshi, S.-i.; Tsunobuchi, Y.; Matsuda, T.; Hashimoto, K.; Namai, A.; Hakoe, F.; Tokoro, H. Synthesis of a metal oxide with a room-temperature photoreversible phase transition. *Nat. Chem.* **2010**, *2*, 539−545.

(6) Makiura, R.; Takabayashi, Y.; Fitch, A. N.; Tokoro, H.; Ohkoshi, S.-i.; Prassides, K. Nanoscale Effects on the Stability of the λ-Ti_3O_5 Polymorph. *Chem.—Asian J.* **2011**, *6*, 1886−1890.

(7) Åsbrink, S.; Magnéli, A. Crystal structure studies on trititanium pentoxide, Ti_3O_5. *Acta Crystallogr.* **1959**, *12*, 575−581.

(8) Shveikin, G. P.; Kellerman, D. G.; Gorshkov, V. S.; Perelyaev, V. A. Magnetic Properties of Ti_3O_5 with Chromium Additions. *Z. Anorg. Allg. Chem.* **1987**, *544*, 21−27.

(9) Onoda, M.; Ogawa, Y.; Taki, K. Phase transitions and the doping effect in Ti_3O_5. *J. Condens. Matter Phys.* **1998**, *10*, 7003.

(10) Müller-Buschbaum, H.; Werthmann, U. Magnetische Eigenschaften von $Ti_{3-x}M_xO_5$-Phasen (M = V^{3+}, Cr^{3+}, Nb^{4+}). *Z. Anorg. Allg. Chem.* **1987**, *545*, 134−142.

(11) Müller-Buschbaum, H.; Bluhm, K. Weitere magnetische Untersuchungen an $Ti_{3-x}M_xO_5$-Phasen (M = Al^{3+}, Fe^{2+}, Mn^{2+}, Mg^{2+}) mit einem Beitrag über $CrTi_2O_5$. *Z. Anorg. Allg. Chem.* **1988**, *558*, 28−34.

(12) Fu, X.; Chen, W.; Hao, X.; Zhang, Z.; Tang, R.; Yang, B.; Zhao, X.; Zuo, L. Preparing high purity λ-Ti_3O_5 and Li/λ-Ti_3O_5 as high-performance electromagnetic wave absorbers. *J. Mater. Chem. C* **2021**, *9*, 7976−7981.

(13) Wang, M.; Huang, W.; Shen, Z.; Gao, J.; Shi, Y.; Lu, T.; Shi, Q. Phase evolution and formation of λ phase in Ti_3O_5 induced by magnesium doping. *J. Alloys Compd.* **2019**, *774*, 1189−1194.

(14) Nakamura, Y.; Sakai, Y.; Azuma, M.; Ohkoshi, S.-i. Long-term heat-storage ceramics absorbing thermal energy from hot water. *Sci. Adv.* **2020**, *6*, No. eaaz5264.

(15) Shen, Z.; Shi, Q.; Huang, W.; Huang, B.; Wang, M.; Gao, J.; Shi, Y.; Lu, T. Stabilization of microcrystal λ-Ti_3O_5 at room temperature by aluminum-ion doping. *Appl. Phys. Lett.* **2017**, *111*, 191902.

(16) Ohkoshi, S.-i.; Jia, F.; Yoshikiyo, M.; Imoto, K.; Tokoro, H.; Nakagawa, K.; Maeno, Y.; Namai, A.; Harada, R.; Hattori, K.; et al. Pressure effect on long-term heat storage ceramics based on Mg-substituted λ-Ti_3O_5. *Mater. Adv.* **2022**, *3*, 4824−4830.

(17) Zhao, Y.; Truhlar, D. G. The M06 suite of density functionals for main group thermochemistry, thermochemical kinetics, noncovalent interactions, excited states, and transition elements: two new

functionals and systematic testing of four M06-class functionals and 12 other functionals. *Theor. Chem. Acc.* **2008**, *120*, 215−241.
(18) Jütten, S.; Bredow, T. First-Principles Investigation of Electronic Properties and Phase Transition of Ti_3O_5. *J. Phys. Chem. C* **2022**, *126*, 7809−7817.
(19) Kresse, G.; Furthmüller, J. Efficient iterative schemes for ab initio total-energy calculations using a plane-wave basis set. *Phys. Rev. B* **1996**, *54*, 11169.
(20) Kresse, G.; Furthmüller, J. Efficiency of ab-initio total energy calculations for metals and semiconductors using a plane-wave basis set. *Comput. Mater. Sci.* **1996**, *6*, 15−50.
(21) Blöchl, P. E. Projector augmented-wave method. *Phys. Rev. B* **1994**, *50*, 17953.
(22) Kresse, G.; Joubert, D. From ultrasoft pseudopotentials to the projector augmented-wave method. *Phys. Rev. B* **1999**, *59*, 1758.
(23) Furness, J. W.; Kaplan, A. D.; Ning, J.; Perdew, J. P.; Sun, J. Accurate and Numerically Efficient r2SCAN Meta-Generalized Gradient Approximation. *J. Phys. Chem. Lett.* **2020**, *11*, 8208−8215.
(24) Grimme, S.; Antony, J.; Ehrlich, S.; Krieg, H. A consistent and accurate ab initio parametrization of density functional dispersion correction (DFT-D) for the 94 elements H-Pu. *J. Chem. Phys.* **2010**, *132*, 154104.
(25) Grimme, S.; Ehrlich, S.; Goerigk, L. Effect of the damping function in dispersion corrected density functional theory. *J. Comput. Chem.* **2011**, *32*, 1456−1465.
(26) Ehlert, S.; Huniar, U.; Ning, J.; Furness, J. W.; Sun, J.; Kaplan, A. D.; Perdew, J. P.; Brandenburg, J. G. r2SCAN-D4: Dispersion corrected meta-generalized gradient approximation for general chemical applications. *J. Chem. Phys.* **2021**, *154*, 061101.
(27) Grimme, S.; Hansen, A.; Ehlert, S.; Mewes, J.-M. r2SCAN-3c: A "Swiss army knife" composite electronic-structure method. *J. Chem. Phys.* **2021**, *154*, 064103.
(28) Kingsbury, R.; Gupta, A. S.; Bartel, C. J.; Munro, J. M.; Dwaraknath, S.; Horton, M.; Persson, K. A. Performance comparison of r^2SCAN and SCAN metaGGA density functionals for solid materials via an automated, high-throughput computational workflow. *Phys. Rev. Mater.* **2022**, *6*, 013801.
(29) Blöchl, P. E.; Jepsen, O.; Andersen, O. K. Improved tetrahedron method for Brillouin-zone integrations. *Phys. Rev. B* **1994**, *49*, 16223−16233.
(30) Ohkoshi, S.-i.; Tokoro, H.; Nakagawa, K.; Yoshikiyo, M.; Jia, F.; Namai, A. Low-pressure-responsive heat-storage ceramics for automobiles. *Sci. Rep.* **2019**, *9*, 13203.
(31) Cramer, C. J.; Truhlar, D. G. Density functional theory for transition metals and transition metal chemistry. *Phys. Chem. Chem. Phys.* **2009**, *11*, 10757−10816.
(32) Tran, F.; Stelzl, J.; Blaha, P. Rungs 1 to 4 of DFT Jacob's ladder: Extensive test on the lattice constant, bulk modulus, and cohesive energy of solids. *J. Chem. Phys.* **2016**, *144*, 204120.
(33) Dovesi, R.; Erba, A.; Orlando, R.; Zicovich-Wilson, C.; Civalleri, B.; Maschio, L.; Rérat, M.; Casassa, S.; Baima, J.; Salustro, S.; et al. Quantum-mechanical condensed matter simulations with CRYSTAL. *WIREs Comput. Mol. Sci.* **2018**, *8*, No. e1360.
(34) Marsman, M.; Paier, J.; Stroppa, A.; Kresse, G. Hybrid functionals applied to extended systems. *J. Phys.: Condens. Matter* **2008**, *20*, 064201.
(35) Vilela Oliveira, D.; Laun, J.; Peintinger, M. F.; Bredow, T. BSSE-correction scheme for consistent gaussian basis sets of double-and triple-zeta valence with polarization quality for solid-state calculations. *J. Comput. Chem.* **2019**, *40*, 2364−2376.
(36) Sheppard, D.; Xiao, P.; Chemelewski, W.; Johnson, D. D.; Henkelman, G. A generalized solid-state nudged elastic band method. *J. Chem. Phys.* **2012**, *136*, 074103.
(37) Saiki, T.; Yoshida, T.; Akimoto, K.; Indo, D.; Arizono, M.; Okuda, T.; Katsufuji, T. Selection rule for the photoinduced phase transition dominated by anisotropy of strain in Ti_3O_5. *Phys. Rev. B* **2022**, *105*, 075134.

https://doi.org/10.1021/acs.jpcc.3c01549
J. Phys. Chem. C 2023, 127, 10445−10452

APPENDIX C

Anisotropy of the Pressure Effect in the Ti_3O_5 Phase Transition Process Resolved by Direction-Dependent Interface Propagation

THE JOURNAL OF PHYSICAL CHEMISTRY C
A JOURNAL OF THE AMERICAN CHEMICAL SOCIETY

pubs.acs.org/JPCC

Article

Anisotropy of the Pressure Effect in the Ti_3O_5 Phase Transition Process Resolved by Direction-Dependent Interface Propagation

Stefan Jütten* and Thomas Bredow*

Cite This: *J. Phys. Chem. C* 2023, 127, 20530–20538

Read Online

ACCESS | Metrics & More | Article Recommendations | Supporting Information

ABSTRACT: Transformation of the metastable λ-phase to the stable β-phase of Ti_3O_5 is triggered by external pressure, irradiation, or electric current. Recent investigations of the photoinduced phase transition revealed a selection rule according to which the photoinduced phase transformation only proceeds when the pump pulse is applied to the *ab* plane. In the present study, possible reasons for this phenomenon are investigated theoretically. We calculate the relative free energy of the β-phase, transition state, and λ-phase under external pressure at the density functional theory (DFT) level. In light of the experimentally proposed selection rule, we investigate the phase transition process in more detail by considering the pressure-dependent formation and propagation of a β-phase front in λ-Ti_3O_5 in a large supercell. This mixed-phase model inherently features an interface region, which connects both phases. We investigate several lattice planes as possible interfaces and their energetic contribution to the phase transition process. Compared to traditional solid-state nudged elastic band calculations, this approach offers a more realistic model of the phase transition by incorporating the gradual conversion of the phases with differing ratios of β:λ-phase fractions and volume change. These simulations featuring extended supercells necessitate the use of machine learned potentials, which, in our case, employ r^{2}SCAN-D3 as a reference method. Our approach reveals significant anisotropy in the energetic pathways and confirms that phase transitions in Ti_3O_5 involving the *ab* interface are energetically favored, which offers a rationalization of the experimental findings. We analyze exemplary acoustic-like phonon modes and find that the pressure effect on the phase transition is rooted in the softening of these modes, which distort the λ structure toward the transition state.

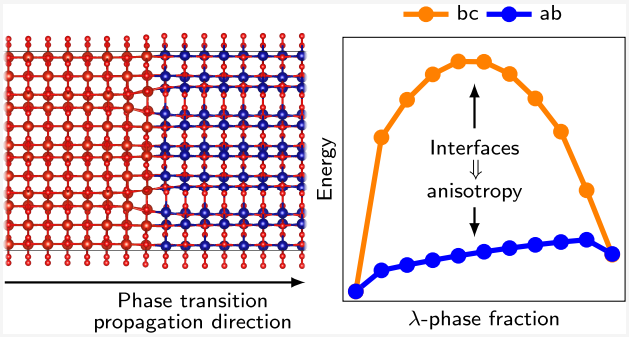

INTRODUCTION

Solid−solid phase change materials can be used, for example, in data storage[1] or as heat-storage materials.[2] The phase transition process is governed by spatial and temporal changes of the phases relative to each other. There is general consensus that a phase transition is ignited by a nucleation event in some region of the crystal and is propagated by elastic waves traveling through the material.[3,4] The phase transition might be initiated in the bulk material, at crystallite surfaces, or within grain boundaries. These factors influence the speed of the transition process and energetic barriers that need to be overcome.

Regardless of where the phase transition is initiated, in all phase transitions the newly emerging phase and the present phase are in contact at an interface region. At the interface, the currently predominating phase is transformed to the emerging phase, which requires additional energy. Interfaces in solids play a role, e.g., in protonic ceramic devices,[5] charge transfer kinetics,[6] or ion transport at electrodes.[7] Considering interface effects is of particular importance in nanoparticles, for instance, the nucleation in a nanocrystalline powder may proceed via particle−particle contacts.[8] Moreover, the variety of possible combinations of interfaces for nanoparticle contacts can influence the heat flow between them.[9] Interface energies might even influence the stability of polymorphs of a material.[10]

Only a few experimental measurements of interface energies[11] and the interface structures[12] have been reported.

The calculation of interface energies from first principles is possible and provides insight at atomistic resolution of processes at interfaces propagating through the bulk.[13,14] In theoretical models, it has to be taken into account that the space groups of the phases may differ and that their interface might be heterogeneous (for example, a (100)/(110) interface). Ref 13 details an approach tailored to interfaces consisting of two phases of a material, which crystallize in different space groups. Thus, it is possible to optimize them using only the symmetry-allowed forces for each space group. However, for the

Received: July 25, 2023
Revised: September 14, 2023
Published: October 4, 2023

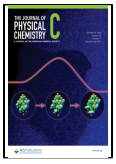

isostructural β/λ-Ti_3O_5 interface with both phases in the $C2/m$ space group, this strategy cannot be applied. The computational models must be large enough to capture the physically important region of interest. Due to extremely high computational demand, such models cannot be studied with conventional density functional theory (DFT) methods. This problem can be solved by recently developed machine learned potentials,[15] which have approximately the same accuracy as the underlying reference method, while reducing the necessary computational effort by orders of magnitude.

In this work, we are interested in the heat-storage ceramic Ti_3O_5, which undergoes an isostructural phase transition from the lower energy β-phase to the higher energy λ-phase at 470 K during heating.[16] When the λ-phase has cooled down to room temperature, it is trapped in a thermodynamically metastable state, and the stored thermal energy can be released on demand by the application of a remarkably small pressure of 60 MPa. It has further been shown that doping can extend the range of application of such heat-storage materials to utilize thermal energy at lower temperatures and lower the pressure for releasing the stored thermal energy.[17−19] The width of the thermal hysteresis loop with a back transition below room temperature and the necessary pressure to induce the $\lambda \rightarrow \beta$ phase transition are linked to crystallite size and morphology. Moreover, λ-Ti_3O_5 was the first metal oxide demonstrated to exhibit a room-temperature photoreversible phase transition.[20] By pump−probe reflectivity measurements, it was recently found that the phase transition pathway is governed by a selection rule, i.e., the phase transition in single crystals of Ti_3O_5 occurs only when the pump pulse is applied on the *ab* plane.[21]

The goal of this study is to elucidate the directionality of the general phase transition process in Ti_3O_5 and the role of pressure. In the first step, we study the pressure effect on both Ti_3O_5 phases using the quasi-harmonic approximation (QHA) and transition state (TS) theory based on conventional unit cells. However, this approach cannot explain the above-mentioned experimental findings. In the second step, we study the β/λ-interfaces parallel to the *bc*, *ac*, and *ab* planes with large supercells (denoted as *interface models*, hereafter). The calculated interface energies during the phase transition process under pressure provide an explanation for the experimental observations.

COMPUTATIONAL DETAILS

Calculations within the QHA framework,[22−25] the simulation of external hydrostatic pressure using the EXTPRESS keyword, TS optimizations using the TSOPT keyword, and the calculation of elastic constants[26,27] were carried out with the CRYSTAL23 v1.0.1 program.[28] We chose the DFT-D3(BJ) dispersion-corrected[29,30] r^{2}SCAN meta-GGA functional[31] (r^{2}SCAN-D3 method) as a reliable, efficient, and accurate method for obtaining structural and thermodynamic properties.[32−35] Calculations using CRYSTAL23 employed the optimized pob-TZVP-rev2 basis sets.[36]

The interface models were calculated with the plane-wave program VASP v6.4.0.[37,38] In these calculations, we applied a kinetic energy cutoff of 700 eV. Core electrons were described by the projector augmented wave (PAW) method.[39,40]

In VASP, partially occupied bands were treated by Gaussian smearing with a width of 0.2 eV. Three-body dispersion terms were included in all CRYSTAL D3 calculations but were neglected by default in VASP. The SCF convergence threshold was set to 10^{-8} a.u. in CRYSTAL23 and 10^{-8} eV in VASP. Recommended integral truncation tolerances of 10^{-7}, 10^{-7}, 10^{-7}, 10^{-7}, and 10^{-14} for mGGA functionals were applied in CRYSTAL23 calculations. We used Γ-centered Monkhorst−Pack meshes with a *k*-point spacing of 0.2 Å^{-1} corresponding to an 8 × 8 × 4 net for primitive cells and a 4 × 8 × 4 net for conventional unit cells. All energies in this work refer to one formula unit of Ti_3O_5.

We previously showed that at a hybrid DFT level, the electronic ground state of β-Ti_3O_5 is antiferromagnetic (AFM) and that of λ-Ti_3O_5 is ferromagnetic (FM).[35] We started all self-consistent field procedures from ferromagnetic initial spin configurations, which relaxed to the correct AFM state for β-Ti_3O_5 and the FM state for λ-Ti_3O_5. In the QHA calculations, it was necessary to lock the summed spin density to 2 *e* per formula unit of λ-Ti_3O_5 to ensure a smooth fit, especially in the compression regime, where the spin density would otherwise converge to closed-shell solutions.

The Gibbs free energy G at a temperature T is calculated from

$$G = H - TS \tag{1}$$

where the enthalpy H and entropy S at a pressure p and volume V

$$H_{\mathrm{vib}} = E_{\mathrm{el}} + \sum_i \frac{1}{2} h\nu_i + \sum_i \frac{h\nu_i}{\exp\left(\frac{h\nu_i}{k_B T}\right) - 1} + pV \tag{2}$$

$$S_{\mathrm{vib}} = \frac{1}{T}\left(\sum_i \frac{1}{2} h\nu_i + \sum_i \frac{h\nu_i}{\exp\left(\frac{h\nu_i}{k_B T} - 1\right)}\right) + k_B \ln\left(\sum_i \frac{\exp\left(\frac{h\nu_i}{2k_B T}\right)}{1 - \exp\left(-\frac{h\nu_i}{k_B T}\right)}\right) \tag{3}$$

are calculated from the vibrational frequencies ν_i, which were obtained from frequency calculations in the harmonic approximation, the Planck constant h, and Boltzmann constant k_B. Translational and rotational contributions are neglected in the solid state.

To incorporate all important geometric degrees of freedom during the phase transition and to minimize artificial interactions between periodic images between phase boundaries, we used supercell models, which are extended along the considered phase transition propagation direction. These large structural models (>3000 atoms) were computed using the machine learned force field (ML-FF) method[41−43] as implemented in VASP. During the active learning procedure, structures obtained from *NpT* molecular dynamics simulations for conventional unit cells of β-Ti_3O_5 and λ-Ti_3O_5 were sampled up to a temperature of 700 K. Structures exceeding a variable Bayesian error estimate threshold (when calculated with the existing force field) were calculated with the r^{2}SCAN-D3 reference method. In this way, a fit set comprising ≈1800 reference structures was compiled.

The interface models used were constructed in the following way. The *ac* interface model with dimensions of ≈20 × 80 × 20 Å^3 is $a \approx 2 \times 20 \times 2$ supercell expansion of the conventional unit cell. For the *bc* and *ab* interface models, we cut a slab containing the conventional unit cell from the respective surface and eliminated the vacuum. Then, supercell expansion yielding models with dimensions of ≈20 × 20 × 100 Å^3 were created

https://doi.org/10.1021/acs.jpcc.3c04986
J. Phys. Chem. C 2023, 127, 20530−20538

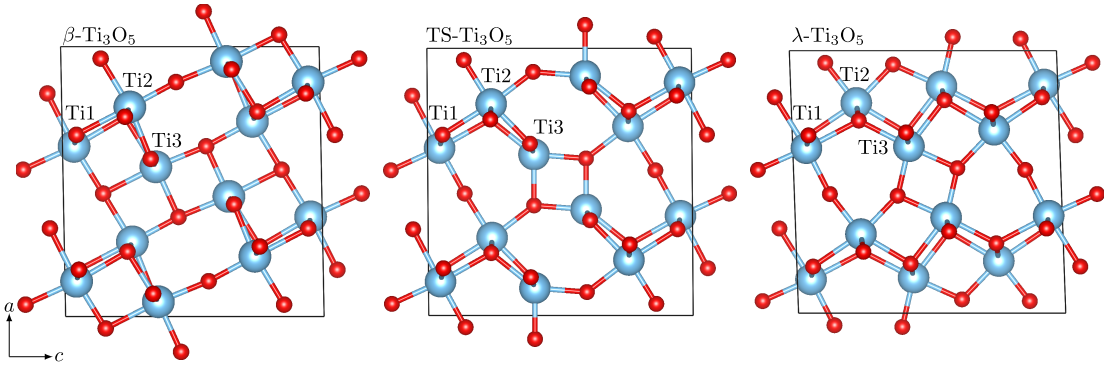

Figure 1. Optimized structures of β-Ti_3O_5 ($C2/m$), the TS ($C2/m$),[35] and λ-Ti_3O_5 ($C2/m$) with symmetry inequivalent Ti atoms indicated in each structure on the r^{2}SCAN-D3/pob-TZVP-rev2 level of theory.

from these respective β- and λ-phases. To simulate the dynamic progression of the phase transition with a specific ratio of β:λ-Ti_3O_5, we used the lattice vectors of the larger unit cell (i.e., the λ-phase) and the fractional coordinates of the β supercell to create the initial model. According to the λ-phase fraction x, the fractional coordinates in the $[0, x]$ interval were substituted by the fractional coordinates of the λ-phase. Both the atomic positions and the lattice vectors of these models were then allowed to relax during optimization of the structure, where we used the conjugate gradient minimizer in VASP, which used the ML-FF energies and forces. In these models, the propagation of the interphase region during phase transition proceeds in the direction of the largest unit cell vector. The unit cell lengths in the other directions normal to the phase transition progression were set to smaller values in order to reduce the computational cost. We verified our choice by carefully converging their lengths toward much larger cells (see the Supporting Information,Figure S1) to ensure that any calculated anisotropy results only from the considered interface and not from the anisotropy of the supercell model. It has to be noted that our monolayer flat models do not capture the complete intricacy of the phase interface; however, it is the most straightforward way to gain insight into the interface structure itself. A more realistic interface could be achieved by performing and analyzing molecular dynamics simulations, which is the topic of future work. Alternatively, nanoparticle surfaces could be considered.

RESULTS AND DISCUSSION

QHA and Elastic Constants. We start to investigate the effect of pressure on the Ti_3O_5 heat-storage system (Figure 1) by calculating the Helmholtz free energy of both phases at several temperatures in the quasi-harmonic approximation (QHA) on the r^{2}SCAN-D3 level of theory (Figure 2). A fit to the Birch–Murnaghan equation of state[44,45] enables us to assign a pressure to a given volume, which we use in other models under simulated pressure.

At ambient conditions, the calculated Helmholtz free energy difference between λ- and β-Ti_3O_5 is ΔF = 7.1 kJ mol^{-1}. The pressure assigned to a λ-Ti_3O_5 volume of ≈362 Å^3 ($\Delta V \approx -0.5\%$), where both curves intersect, is 3.9 GPa. For reference, the experimental enthalpy difference obtained from DSC measurements[16] is $\Delta H = 12 \pm 1$ kJ mol^{-1}, and the pressure for the $\lambda \rightarrow \beta$ -transition ranges from 7 MPa[46] to 500 MPa[47] depending on the particle size and morphology.

The elastic tensors (in Voigt notation), Birch–Murnaghan fit parameters, and the elastic material constants are provided in

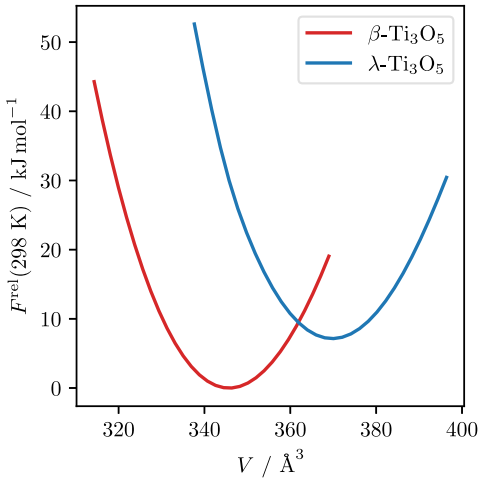

Figure 2. Helmholtz free energy F^{rel} as a function of volume of β-Ti_3O_5 and λ-Ti_3O_5 at 298 K in the quasi-harmonic approximation obtained with r^{2}SCAN-D3 relative to the Helmholtz free energy of equilibrium β-Ti_3O_5. The fit was obtained from 20 points within a ± 8% volume range around the equilibrium structure of each phase.

Table 1. We provide the compliance tensors and seismic velocities for both phases in the Supporting Information, Table S1.

Compared to experimental results for β-Ti_3O_5, $B_0 = 173 \pm 10$ GPa and $B_0' = 7 \pm 1$,[48] our calculated bulk modulus of 185 GPa exceeds the upper experimental error range by only 2 GPa; however, our bulk modulus pressure derivative B_0' is only half the experimental value. The λ-phase bulk modulus with 192 GPa is only ≈3% larger than that of β-Ti_3O_5; however, its bulk modulus pressure derivative is smaller. To the best of the authors' knowledge, no experimental bulk modulus for λ-Ti_3O_5 has been published in the literature. The fitted equilibrium volume V_0 is underestimated by ≈2% for β-Ti_3O_5 and by ≈1% for λ-Ti_3O_5.

Compared to theoretical results obtained with GGA + U,[49] our calculated elastic tensor for λ-Ti_3O_5 is comparable, while our β-Ti_3O_5 elastic tensor shows larger deviations. Also, their shear modulus G and Young's modulus E are much smaller than the present r^{2}SCAN-D3 results. This can be explained by the significant overestimation of the unit cell parameters.

The QHA yields linear thermal expansion predictions of the lattice parameters, which are plotted in the Supporting Information, Figure S2. With expansions of the a and c lattice vectors of approximately 0.45% and 0.35% at T_p = 470 K, respectively, the β-phase structure is more susceptible to

https://doi.org/10.1021/acs.jpcc.3c04986
J. Phys. Chem. C 2023, 127, 20530–20538

Table 1. Elastic Tensors C (in GPa), Birch–Murnaghan Fit Equilibrium Volume V_0 (in Å^3), Bulk Modulus B_0 (in GPa) and Its Pressure Derivative B_0', and Elastic Material Constants Shear Modulus G, Young's Modulus E, and Poisson's Ratio ν (all in GPa) of β-Ti_3O_5 and λ-Ti_3O_5 Obtained with the r^{2}SCAN-D3 Method[a]

phase	C	V_0	B_0	B_0'	G	E	ν
β-Ti_3O_5	$\begin{pmatrix} 247.6 & 150.9 & 113.0 & 0.0 & -6.1 & 0.0 \\ & 454.8 & 157.3 & 0.0 & 14.4 & 0.0 \\ & & 322.7 & 0.0 & 50.0 & 0.0 \\ & & & 76.8 & 0.0 & -5.3 \\ & & & & 98.6 & 0.0 \\ & & & & & 56.3 \end{pmatrix}$	341.93 (349.90[b])	185.46 (173 ± 10[c])	3.78 (7 ± 1[c])	81.88	215.80	0.318
λ-Ti_3O_5	$\begin{pmatrix} 259.9 & 173.6 & 110.0 & 0.0 & -19.9 & 0.0 \\ & 382.9 & 139.7 & 0.0 & -10.3 & 0.0 \\ & & 279.0 & 0.0 & -4.4 & 0.0 \\ & & & 72.5 & 0.0 & -5.2 \\ & & & & 74.3 & 0.0 \\ & & & & & 46.1 \end{pmatrix}$	367.67 (371.21[b])	191.81	2.87	69.22	185.16	0.338

[a]Available experimental values in parentheses. [b]ref 16. [c]ref 48.

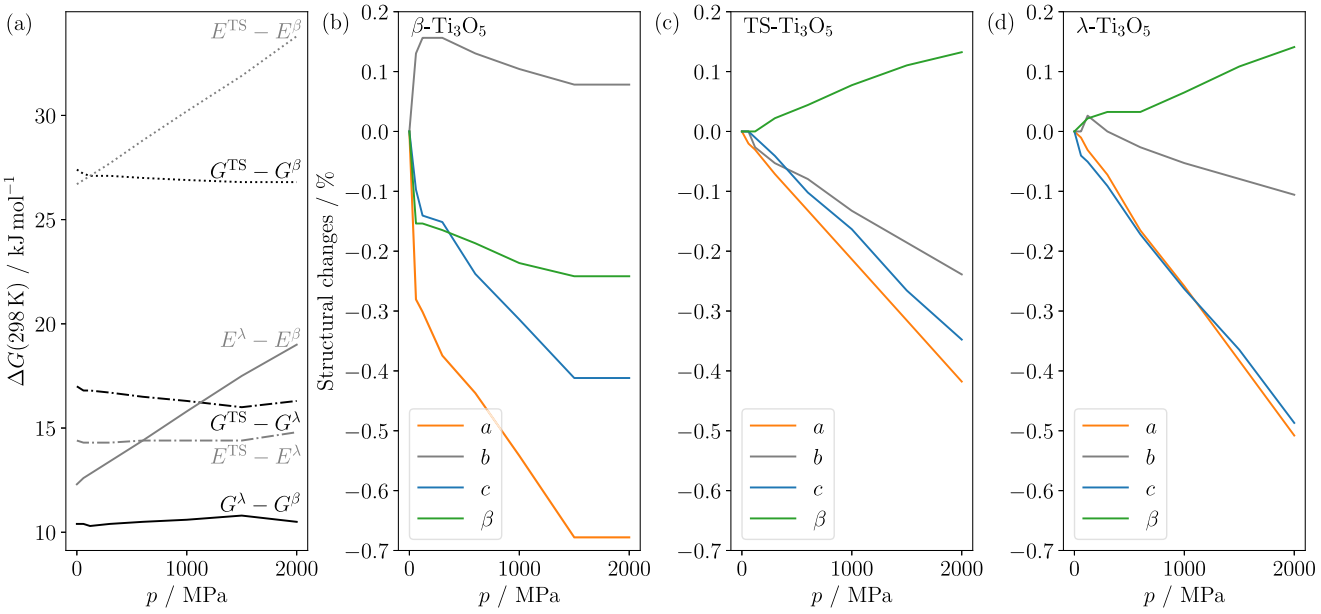

Figure 3. (a) Changes in Gibbs free energy differences ΔG and total electronic energy differences ΔE, (b, c) lattice vectors a, b, c and unique monoclinic angle β as a function of pressure in all three phases on the r^{2}SCAN-D3/pob-TZVP-rev2 level of theory using the CRYSTAL23 program.

temperature than the λ-phase structure, where both lattice vectors exhibit an increase of ≈0.15% at T_p. In contrast, the λ-phase is easier to deform with a Young's modulus ≈15% smaller than for the β-phase. Shear stress and shear strain needed for elastic deformations quantified by the shear modulus G likewise are ≈15% smaller in the λ-phase than in the β-phase. Poisson's ratio of ≈0.3 is nearly the same for both phases. This shows that λ-Ti_3O_5 is more susceptible to pressure compared to the β-phase, which therefore facilitates an efficient reversal of the phase transition.

The elasticity tensor quantifies the stiffness of a material and should be considered in the elastic wave propagation. Strain waves are reported to be a driving force for the phase transition,[47] which motivates the comparison of both phases' elastic tensors. The largest stiffness for both phases is present along the b-axis (C_{22}), with the value of λ-Ti_3O_5 being 15% lower than that of β-Ti_3O_5. In λ-Ti_3O_5, the stiffness of the c-axis is smaller by 14% compared with the β-phase. Along a, the stiffness of λ-Ti_3O_5 is slightly larger than that of β-Ti_3O_5, which explains the major change in the c lattice vector during the phase transition. The C_{35} component of the elasticity tensor changes from 50 in β-Ti_3O_5 to −4.4 in λ-Ti_3O_5, which relates a stress along the c-axis to a strain between a and c, i.e., it relates the compression of c with the change in the unique monoclinic angle β, which increases when pressure is applied to λ-Ti_3O_5.

In summary, the QHA significantly overestimates the experimental transition pressure, and from the elastic constants, a clear anisotropy of the pressure effect is evident. We now study the effect of pressure on the energy and structure of the TS.

Pressure Effect on Bulk Ti_3O_5. We investigated the effect of hydrostatic pressure on bulk Ti_3O_5 by optimizing the unit cells of the β-phase, the TS between the phases, and the λ-phase under several (low) pressures using r^{2}SCAN-D3/CRYSTAL23. The TS is defined as the structure with the highest energy along the minimum energy path connecting λ-Ti_3O_5 and β-Ti_3O_5, which must be overcome to perform the phase transition. The TS was verified by frequency calculations, which showed exactly one imaginary frequency. By inspection of the corresponding normal mode, we verified that it connects β and λ structures. The transition state optimization employed the TSOPT keyword and could be successfully applied up to a pressure of 2000 MPa; however, at higher pressures, it was not possible to optimize the TS, which in all cases relaxed to the β-phase, even under extremely tight accuracy thresholds. We employed closed-shell, AFM, and FM initial spin configurations in all optimizations and found the SCF procedure to converge to FM solutions for the

https://doi.org/10.1021/acs.jpcc.3c04986
J. Phys. Chem. C 2023, 127, 20530−20538

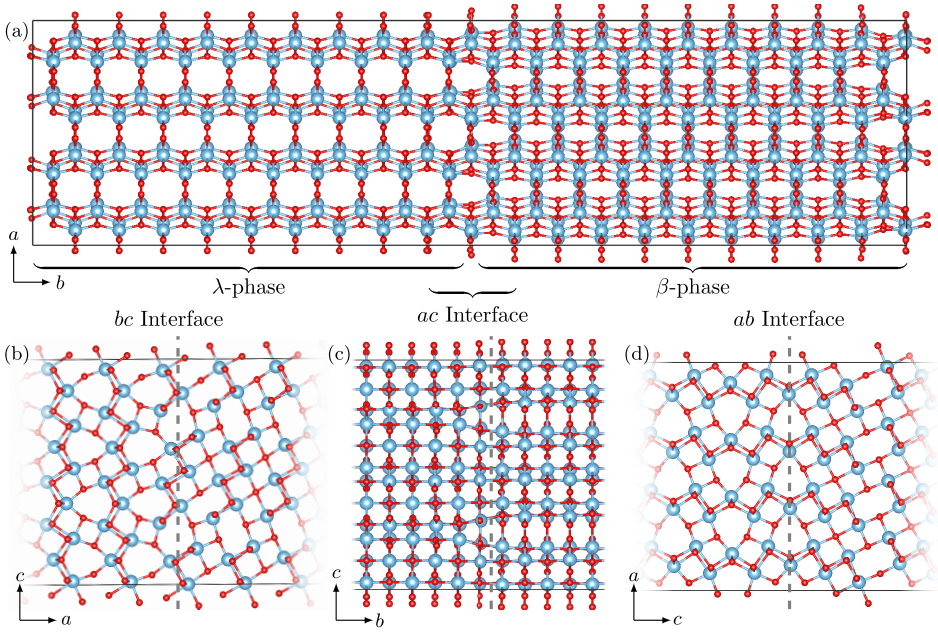

Figure 4. Illustration of the *ac* interface model with a λ-phase fraction of $x = 0.5$ (a) and the optimized *bc*, *ac*, and *ab* interface regions (b–d). In all cases, λ structures are shown on the left, and β structures are shown on the right of the interface (highlighted by a dashed gray line). In panel (c), the *ac* interface is shown from a different perspective compared to panel (a).

TS and λ-phase in all cases; the β-phase remained in the AFM spin configuration when pressure was increased. Within this approximation, the transition pressure would be achieved once the λ-phase becomes less stable than the TS, and the system would spontaneously relax to the TS and eventually to the β-phase.

We present the change in Gibbs free energy differences and total electronic energy differences of β-Ti_3O_5, the TS, and λ-Ti_3O_5 under pressure in Figure 3(a) and list the lattice vectors and unique monoclinic angle as a function of pressure in the Supporting Information, Table S2. Pressures of up to 2000 MPa destabilize all three considered phases; however, the relative electronic energies and free energies show different trends. The difference in total electronic energies of λ-phase and β-phase increases from 12.5 kJ mol^{-1} at ambient pressure up to ≈19 kJ mol^{-1} at 2000 MPa. The electronic energy difference between TS and β-phase (i.e., $E^{TS} - E^{\beta}$) increases from 26.5 to 34.5 kJ mol^{-1}, while the difference between TS and λ-phase electronic energies remains virtually constant. In contrast, the free energy differences among all three phases remain constant as the pressure increases. Since the free energy of activation for the phase transition (i.e., $G^{TS} - G^{\lambda}$) remains unchanged, this approach cannot account for the experimentally observed pressure effect in this material.

We present the change in enthalpy differences and the change in entropy differences between the phases under pressure in the Supporting Information, Figure S3. We observe that already the enthalpy differences are constant with increasing pressure, indicating that destabilization in the electronic energy is offset by a stabilization incurred from the vibrational enthalpy contribution. Interestingly, the entropy also does not change substantially, and the corresponding entropy differences are approximately constant.

We present the change in structural parameters as a function of pressure in Figure 3(b–d). The magnitude of the change relative to zero pressure is most pronounced in the β-phase, where the *a* lattice vector decreases by ≈0.7%. In general, the *a* lattice vector is most affected by the pressure, followed by *c*. The *b* lattice vector changes most in the TS, but only by −0.2%, and is, in general, least sensitive to pressure, as we already observed from the elastic tensors. The monoclinic angle increases under pressure in both TS and λ-phase, which is in accordance with experimental observations,[16] and decreases in the β-phase.

These observations mirror the linear thermal expansion results obtained from our QHA calculations, which show that temperature-induced changes of the lattice vectors are more pronounced in β-Ti_3O_5 than those in λ-Ti_3O_5. This facilitates the temperature-driven phase transition.

To summarize, pressure destabilizes the free energy of all three considered phases uniformly, and therefore, this conventional approach cannot explain the pressure effect in Ti_3O_5. We therefore introduce interface models as an alternative approach to study this phase transition.

Pressure Effect Using Interface Models. Since we demonstrated that the change in lattice parameters is highly anisotropic, it is interesting to consider the effect of pressure on the phase transition separately along the three crystallographic axes. During a phase transition, a phase front of the newly created phase will propagate through the crystal, and the transition will take place at the interface between the new and the host phases. The *ac* interface model and the three interfaces are presented in Figure 4. The corresponding calculations were performed with ML-FF/VASP. Interestingly, the structure of the optimized interface region partly adopts the TS structure that was obtained from solid-state nudged elastic band (ss-NEB) calculations. We provide the 2-layer *ac* interface region in the Supporting Information Figure S4, viewed along the *b* direction. Here, we confirmed the TS structure in every second row by measuring distances and angles and comparing them to our previous results.[35]

We optimized coherent interface models to resolve the phase transition in *a*, *b*, and *c* directions in more detail using the ML-FF

https://doi.org/10.1021/acs.jpcc.3c04986
J. Phys. Chem. C 2023, 127, 20530−20538

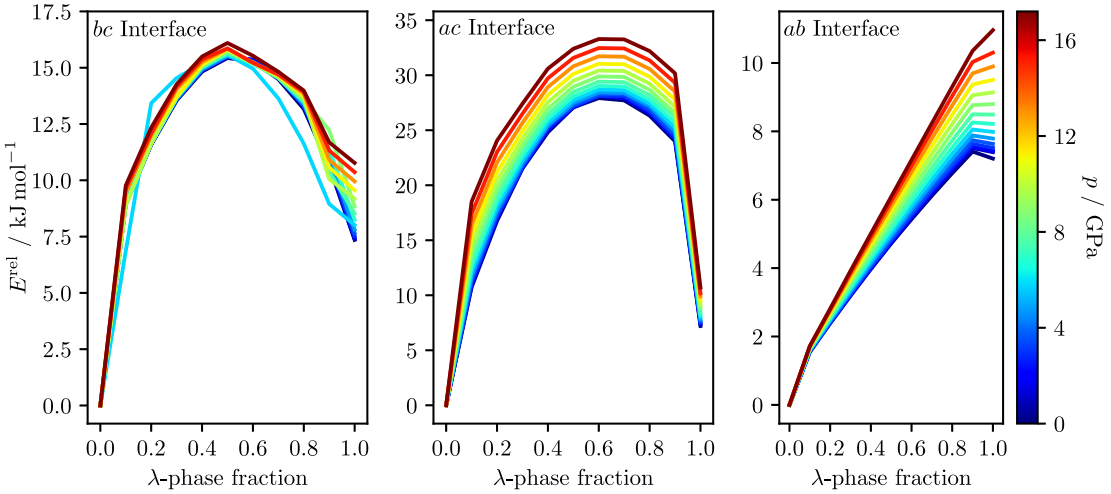

Figure 5. Energy E^{rel} relative to the β-phase for *bc*, *ac*, and *ab* interface models as a function of the λ-phase fraction at pressures corresponding to volume decreases up to 7% (in 0.5% steps).

method (Figure 5). Pressure was simulated by isotropically shrinking the cell volume and performing volume-constrained full optimizations of the interface models with varying ratios of the β:λ-phase. The experimental volume difference between the phases is ΔV = 6.4%, and we thus simulated pressure up to a compression of −7%. To release the stored thermal energy from the heat-storage system, pressure is applied to the λ-phase. We thus assigned pressures to the compressed volumes according to the $P(V)$ relation from our QHA calculations of the λ-phase. This approximation is valid for the pure λ-phase (x = 1.0) and taken only as an approximation for mixed-phase models.

The total energy and the cell volume change with varying ratios of β to λ-phase. The volume increases almost linearly with x, but the structure of the interface region remains virtually unchanged. It is apparent that the potential energy profile of the phase transition depends on the propagation direction through the material (Figure 5). We obtain energetic barriers for conversion of λ-Ti_3O_5 to β-Ti_3O_5 of ≈8 kJ mol^{-1} at x = 0.5 for the *bc*, and ≈25 kJ mol^{-1} at x = 0.6 in the *ac* interface model. In the *ab* interface model, the activation barrier is only ≈1 kJ mol^{-1}. Here, the greatest change in the relative energy is the initial creation of a fraction of β-phase in the λ-matrix from x = 1.0 → x = 0.9 and the vanishing of the last remaining fraction of λ-phase in the system.

The behavior under a simulated external pressure does not change significantly in the *bc* interface model, where only a slight and uniform destabilization of up to ≈2 kJ mol^{-1} is present up to the highest pressure considered here. Pressure affects the structure and stability of models with high fractions of the λ-phase more severely. The *ac* interface model experiences a destabilization of up to ≈4 kJ mol^{-1} with no fundamental change in the shape of the energy profile. In the *ab* interface model, pressure leads to destabilization of all structures along the transition path, but its impact is most pronounced for the pure λ-phase at x = 1. Here, the largest relative change is observed, and the shape of the reaction profile is changed, in that the λ-phase is increasingly destabilized with respect to mixed phases, and eventually, the energy barrier vanishes completely. This behavior, along with the lack of any barrier in the conversion and the previously presented experimental findings, makes this model attractive for further investigation.

Phase Transition along the *c*-Axis. We now focus on the phase transformation along the crystallographic *c*-axis (i.e., the interface is the *ab* plane), which experiences a disproportionate change with respect to the *a* and *b* lattice vectors during the phase transition. Since the enthalpy difference is an important parameter in heat-storage materials, and we already observed in our discussion of the pressure effect on the TS (section pressure effect on Ti_3O_5) that the root cause of the anomalous pressure behavior is the stabilization incurred from the vibrational enthalpy, we present the coherent interface enthalpy change H^{rel} as a function of the λ-phase fraction in Figure 6.

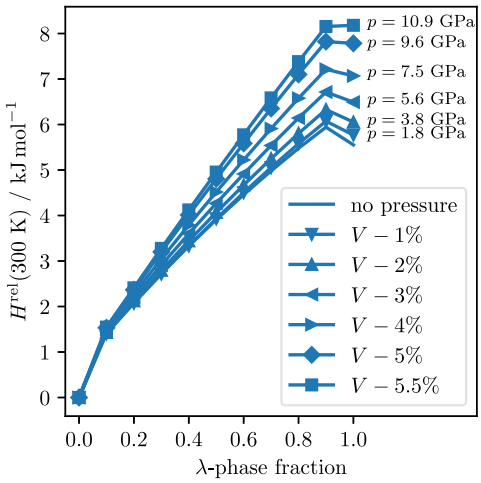

Figure 6. Change in the enthalpy H^{rel} of the *ab* interface model relative to that of the β-phase under pressure. Pressures are converted into reduced volumes according to the QHA calculation on λ-Ti_3O_5.

We first observe that the phase transformation along the *c*-axis is hindered by the formation of the first part of β-phase in the λ host lattice. Increasing the pressure up to 10.9 GPa, which corresponds to a 5.5% decrease in volume, overcomes this enthalpy penalty. In this case, no energetic barrier between the λ-phase and β-phase is present anymore, and λ-Ti_3O_5 readily transforms into β-Ti_3O_5 at room temperature.

The fact that the possible phase transformation pathways along different directions in the crystal differ substantially with

https://doi.org/10.1021/acs.jpcc.3c04986
J. Phys. Chem. C 2023, 127, 20530−20538

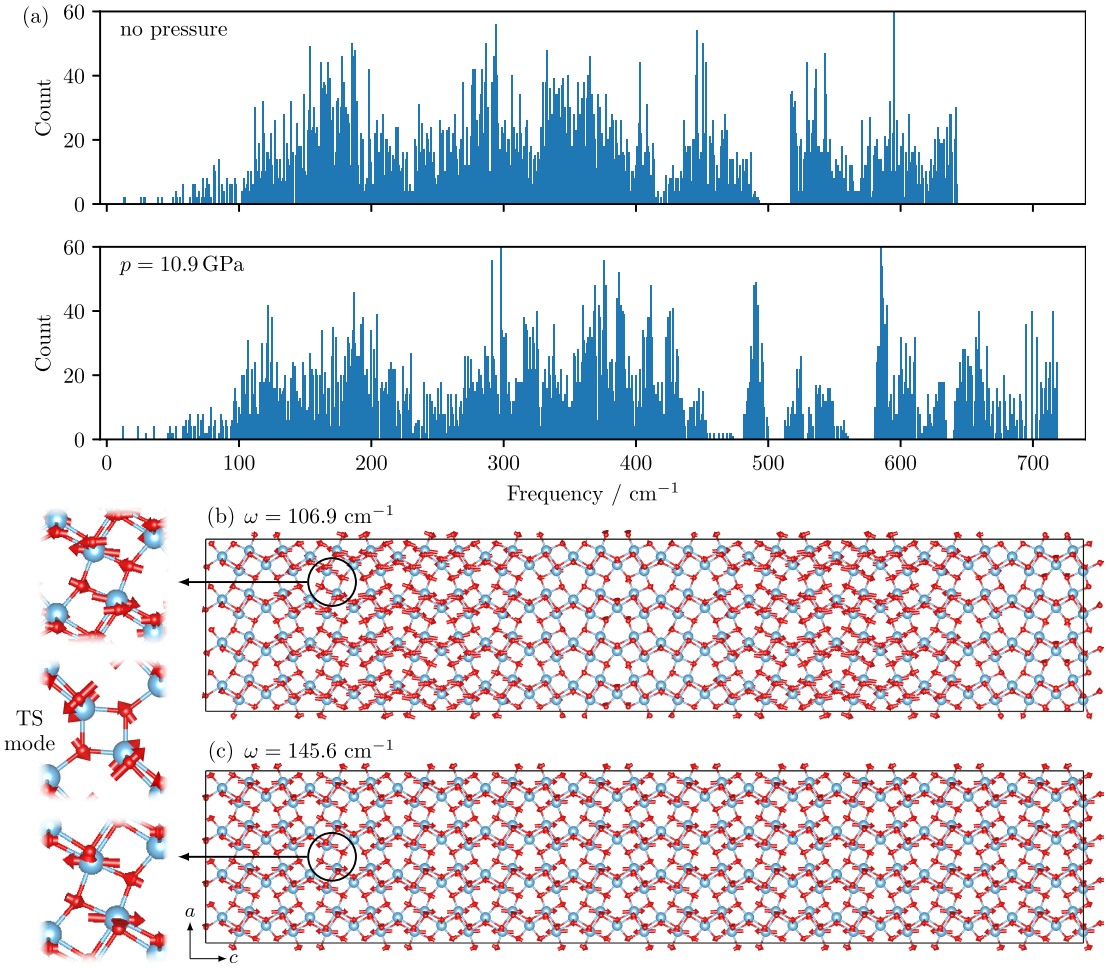

Figure 7. (a) Phonon density of states of the λ-Ti_3O_5 *ab* interface model obtained with the ML-FF method without external pressure and at the transition pressure of 10.9 GPa. (b, c) Phonon modes at 10.9 GPa with a comparison of atomic displacements to the TS mode (taken from ref 35).

respect to energetic barriers confirms the experimentally established anisotropy of the strain associated with the phase transition. In particular, we arrive at the same conclusion that the phase transition will proceed preferentially parallel to the crystallographic *c*-axis.[21] The reason is the lack of any significant activation barrier for conversion along this direction in the crystal, which could also explain the unusually low experimentally observed pressures needed to induce the phase transition.

Our pressures obtained within the QHA framework overestimate the experimental pressures $P_{1/2}$, at which half the material has converted under hydrostatic pressure, i.e., at 0.5 λ-phase fraction.[16] Further, this experimental pressure strongly depends on the crystal morphology.[18,47] We suggest that considering bulk calculations might be insufficient, and certain facets of nanoparticles, for instance, the (001) facet of the λ-phase, might need to be considered to reach more quantitative pressure predictions. Moreover, our simplified models cannot account for elastic interactions between the phases. These have been proposed to decrease the width of the thermal hysteresis loop in thermodynamic mean-field models.[16−18,20,47]

Phonon Density of States. Experimentally, it was observed that the phase transition proceeds at sonic speed as a strain wave similar to an acoustic wavefront.[47] We thus examined the change in acoustic-like phonon modes using our *ab* interface model because this is the energetically preferred pathway for the phase transition. The phonon density of states (pDOS) without pressure and using our proposed phase transition pressure of 10.9 GPa, along with an illustration of the displacements of two exemplary phonon modes, are provided in Figure 7. Acoustic waves along the *c* direction under ambient conditions and under pressure are provided in the Supporting Information, Figure S5.

In the high-frequency regime of the phonon DOS, a shift to higher frequencies is observed as the pressure is increased. We inspected the phonon modes in the 100−200 cm^{-1} interval, which exhibited acoustic phonon characteristics and identified the involvement of Ti_3 displacements along the *c* direction as a common feature. Specifically, these modes displace the Ti_3 atoms in an antiparallel fashion resembling the beginning of a rotation, as it is observed in the transition state mode in the $\beta \rightarrow \lambda$ phase transition, which we first identified recently in pristine and doped Ti_3O_5 as a universal feature of this phase transition.[35,50] These modes soften under pressure by $\Delta\omega \approx 10$ cm^{-1}, which makes these phonon modes easier to populate and, therefore, opens up a more facile phase transition pathway.

It is possible that the wave-like phonons act in particular on specific regions of the interface regions, where we already confirmed alternating domains of TS and λ-phase. Should the 'wavelength' of the phonon coincide with the spacing of the domains, an energy lowering could be achieved by transforming the remaining λ-phase domains into the TS.

https://doi.org/10.1021/acs.jpcc.3c04986
J. Phys. Chem. C 2023, 127, 20530−20538

SUMMARY AND CONCLUSIONS

We studied the effect of pressure on the $\lambda \rightarrow \beta$ phase transition in the Ti_3O_5 heat-storage system from first principles by conventional means (QHA calculations of the conventional unit cell) and by explicitly taking the propagation direction of the phase transition into account in extended supercells. QHA free energy predictions cannot explain the pressure effect, although the λ-phase lattice vectors decrease by up to 0.5% ($\Delta V \approx 1.1\%$). At ambient conditions, QHA calculations predict a phase transition at ≈3.9 GPa, much larger than the experimentally observed transition pressure. Our calculated elastic constants indicate a greater pressure response of the λ-phase, which confirms experimentally observed small transition pressures for the back transition to β-Ti_3O_5 and reveals the anisotropic pressure response of the material. We studied the direction dependency of the phase transition by considering the phase front propagation along the *a*, *b*, and *c* directions with a machine learned potential trained on the r^{2}SCAN-D3 method. We show that the energetic pathway is clearly anisotropic. The $\lambda \rightarrow \beta$ -transition along the *a* and *b* directions must overcome activation barriers of ≈8 and 25 kJ mol^{-1}, respectively, while the transformation along the *c* direction and its associated *ab* interface proceeds gradually and with an activation barrier of only ≈1 kJ mol^{-1}. The application of pressure to the *ab* interface model sufficiently destabilizes high λ-phase fraction systems, such that the $\lambda \rightarrow \beta$ -phase transition is predicted to proceed spontaneously. We propose the small barrier of activation, which vanishes at a pressure of 10.9 GPa, as a rationalization for the surprisingly low experimentally observed transition pressures and the experimentally observed selection rule for this phase transition. This is further explained by a softening of acoustic-like phonon modes under pressure, which displaces the structure of λ-Ti_3O_5 into the structure of the TS, thereby facilitating the conversion to β-Ti_3O_5. The supercell approach resolves the structures of the interface regions, which are largely inaccessible from experiments alone.

Our study highlights intricacies in the phase transition process of the Ti_3O_5 phase change material, which could also be applied in forthcoming studies of other materials (monoclinic crystal systems, in particular). Our results motivated the study of the pressure effect on the surfaces of Ti_3O_5, especially the (001) surface termination. Since doping is known to significantly alter the heat-storage properties and the pressure effect of Ti_3O_5, the structural and energetic influence of dopants at or in the vicinity of the interface should be addressed in the future.

ASSOCIATED CONTENT

Supporting Information

The Supporting Information is available free of charge at https://pubs.acs.org/doi/10.1021/acs.jpcc.3c04986.

Table of pressure dependency of optimized lattice vectors; ML-FF method convergence tests; elastic compliance tensors and seismic wave velocities of both phases; linear thermal expansion plots obtained in the QHA framework; enthalpy and entropy differences between all phases under pressure; *ac* interface region with highlighted λ-phase and TS-like domains; and a comparison of λ-phase acoustic phonons at ambient conditions and under pressure (PDF)

AUTHOR INFORMATION

Corresponding Authors

Stefan Jütten − *Mulliken Center for Theoretical Chemistry, 53115 Bonn, Germany; Max Planck Institute for Chemical Energy Conversion, 45470 Mülheim an der Ruhr, Germany;* orcid.org/0000-0001-8756-7963; Email: juetten@thch.uni-bonn.de

Thomas Bredow − *Mulliken Center for Theoretical Chemistry, 53115 Bonn, Germany*; Email: bredow@thch.uni-bonn.de

Complete contact information is available at: https://pubs.acs.org/10.1021/acs.jpcc.3c04986

Notes

The authors declare no competing financial interest.

ACKNOWLEDGMENTS

This work is supported by the International Max Planck Research School on Reactive Structure Analysis for Chemical Reactions (IMPRS-RECHARGE). The authors thank the Paderborn Center for Parallel Computing (pc^2) for providing computational resources.

REFERENCES

(1) Lencer, D.; Salinga, M.; Wuttig, M. Design rules for phase-change materials in data storage applications. *Adv. Mater.* **2011**, *23*, 2030−2058.

(2) Fallahi, A.; Guldentops, G.; Tao, M.; Granados-Focil, S.; Van Dessel, S. Review on solid-solid phase change materials for thermal energy storage: Molecular structure and thermal properties. *Appl. Therm. Eng.* **2017**, *127*, 1427−1441.

(3) Oxtoby, D. W. Nucleation of first-order phase transitions. *Acc. Chem. Res.* **1998**, *31*, 91−97.

(4) Zacharias, M.; Rosch, A.; Garst, M. Critical elasticity at zero and finite temperature. *Eur. Phys. J.: Spec. Top.* **2015**, *224*, 1021−1040.

(5) Chiara, A.; Giannici, F.; Pipitone, C.; Longo, A.; Aliotta, C.; Gambino, M.; Martorana, A. Solid−solid interfaces in protonic ceramic devices: a critical review. *ACS Appl. Mater. Interfaces* **2020**, *12*, 55537−55553.

(6) Bai, P.; Bazant, M. Z. Charge transfer kinetics at the solid−solid interface in porous electrodes. *Nat. Commun.* **2014**, *5*, No. 3585.

(7) Tu, Z.; Choudhury, S.; Zachman, M. J.; Wei, S.; Zhang, K.; Kourkoutis, L. F.; Archer, L. A. Fast ion transport at solid−solid interfaces in hybrid battery anodes. *Nat. Energy* **2018**, *3*, 310−316.

(8) Zhang, H.; Banfield, J. F. Size dependence of the kinetic rate constant for phase transformation in TiO_2 nanoparticles. *Chem. Mater.* **2005**, *17*, 3421−3425.

(9) Warzoha, R. J.; Fleischer, A. S. Heat flow at nanoparticle interfaces. *Nano Energy* **2014**, *6*, 137−158.

(10) Castro, R. H. R.; Wang, B. The hidden effect of interface energies in the polymorphic stability of nanocrystalline titanium dioxide. *J. Am. Ceram. Soc.* **2011**, *94*, 918−924.

(11) Castro, R. H. R.; Tôrres, R. B.; Pereira, G. J.; Gouvêa, D. Interface energy measurement of MgO and ZnO: understanding the thermodynamic stability of nanoparticles. *Chem. Mater.* **2010**, *22*, 2502−2509.

(12) Wu, X.; Yang, N.; Ji, Y.; He, X.; Li, Q.; Jiang, R.; Lei, Z.; Liu, Z.; Sun, J. Phase Transformation and Interface Crystallography between TiO_2 and Different Ti_nO_{2n-1} Phases. *CrystEngComm* **2023**, *25*, 1146−1158.

(13) Falkowski, M.; Kersch, A. Ab initio interphase characteristics in HfO_2 and ZrO_2 and nucleation of the polar phase. *Appl. Phys. Lett.* **2021**, *118*, No. 032905, DOI: 10.1063/5.0029610.

(14) Lu, S.; Ågren, J.; Vitos, L. Ab initio study of energetics and structures of heterophase interfaces: from coherent to semicoherent interfaces. *Acta Mater.* **2018**, *156*, 20−30.

(15) Friederich, P.; Häse, F.; Proppe, J.; Aspuru-Guzik, A. Machine-learned potentials for next-generation matter simulations. *Nat. Mater.* **2021**, *20*, 750−761.
(16) Tokoro, H.; Yoshikiyo, M.; Imoto, K.; Namai, A.; Nasu, T.; Nakagawa, K.; Ozaki, N.; Hakoe, F.; Tanaka, K.; Chiba, K.; et al. External stimulation-controllable heat-storage ceramics. *Nat. Commun.* **2015**, *6*, No. 7037, DOI: 10.1038/ncomms8037.
(17) Nakamura, Y.; Sakai, Y.; Azuma, M.; Ohkoshi, S.-i. Long-term heat-storage ceramics absorbing thermal energy from hot water. *Sci. Adv.* **2020**, *6*, No. eaaz5264, DOI: 10.1126/sciadv.aaz5264.
(18) Ohkoshi, S.-i.; Jia, F.; Yoshikiyo, M.; Imoto, K.; Tokoro, H.; Nakagawa, K.; Maeno, Y.; Namai, A.; Harada, R.; Hattori, K.; et al. Pressure effect on long-term heat storage ceramics based on Mg-substituted λ-Ti_3O_5. *Mater. Adv.* **2022**, *3*, 4824−4830.
(19) Jia, F.; Yoshikiyo, M.; Makuta, R.; Kawakami, K.; Tokoro, H.; Ohkoshi, S.-i. Observation of a Pressure Effect on an Al-Substituted λ-Ti_3O_5 Heat-Storage Material. *Chem. Lett.* **2023**, *52*, No. 230244, DOI: 10.1246/cl.230244.
(20) Ohkoshi, S.-i.; Tsunobuchi, Y.; Matsuda, T.; Hashimoto, K.; Namai, A.; Hakoe, F.; Tokoro, H. Synthesis of a metal oxide with a room-temperature photoreversible phase transition. *Nat. Chem.* **2010**, *2*, 539−545.
(21) Saiki, T.; Yoshida, T.; Akimoto, K.; Indo, D.; Arizono, M.; Okuda, T.; Katsufuji, T. Selection rule for the photoinduced phase transition dominated by anisotropy of strain in Ti_3O_5. *Phys. Rev. B* **2022**, *105*, No. 075134, DOI: 10.1103/PhysRevB.105.075134.
(22) Erba, A. On combining temperature and pressure effects on structural properties of crystals with standard ab initio techniques. *J. Chem. Phys.* **2014**, *141*, No. 124115, DOI: 10.1063/1.4896228.
(23) Erba, A.; Shahrokhi, M.; Moradian, R.; Dovesi, R. On how differently the quasi-harmonic approximation works for two isostructural crystals: Thermal properties of periclase and lime. *J. Chem. Phys.* **2015**, *142*, No. 044114, DOI: 10.1063/1.4906422.
(24) Erba, A.; Maul, J.; De La Pierre, M.; Dovesi, R. Structural and elastic anisotropy of crystals at high pressures and temperatures from quantum mechanical methods: The case of Mg_2SiO_4 forsterite. *J. Chem. Phys.* **2015**, *142*, No. 204502, DOI: 10.1063/1.4921781.
(25) Erba, A.; Maul, J.; Demichelis, R.; Dovesi, R. Assessing thermochemical properties of materials through ab initio quantum-mechanical methods: the case of α-Al_2O_3. *Phys. Chem. Chem. Phys.* **2015**, *17*, 11670−11677.
(26) Perger, W.; Criswell, J.; Civalleri, B.; Dovesi, R. Ab-initio calculation of elastic constants of crystalline systems with the CRYSTAL code. *Comput. Phys. Commun.* **2009**, *180*, 1753−1759.
(27) Erba, A.; Mahmoud, A.; Orlando, R.; Dovesi, R. Elastic properties of six silicate garnet end members from accurate ab initio simulations. *Phys. Chem. Miner.* **2014**, *41*, 151−160.
(28) Erba, A.; Desmarais, J. K.; Casassa, S.; Civalleri, B.; Donà, L.; Bush, I. J.; Searle, B.; Maschio, L.; Edith-Daga, L.; Cossard, A.et al.CRYSTAL23: A Program for Computational Solid State Physics and Chemistry *J. Chem. Theory Comput.* 2022 DOI: 10.1021/acs.jctc.2c00958.
(29) Grimme, S.; Antony, J.; Ehrlich, S.; Krieg, H. A consistent and accurate ab initio parametrization of density functional dispersion correction (DFT-D) for the 94 elements H-Pu. *J. Chem. Phys.* **2010**, *132*, No. 154104, DOI: 10.1063/1.3382344.
(30) Grimme, S.; Ehrlich, S.; Goerigk, L. Effect of the damping function in dispersion corrected density functional theory. *J. Comput. Chem.* **2011**, *32*, 1456−1465.
(31) Furness, J. W.; Kaplan, A. D.; Ning, J.; Perdew, J. P.; Sun, J. Accurate and Numerically Efficient r2SCAN Meta-Generalized Gradient Approximation. *J. Phys. Chem. Lett.* **2020**, *11*, 8208−8215.
(32) Ehlert, S.; Huniar, U.; Ning, J.; Furness, J. W.; Sun, J.; Kaplan, A. D.; Perdew, J. P.; Brandenburg, J. G. r2SCAN-D4: Dispersion corrected meta-generalized gradient approximation for general chemical applications. *J. Chem. Phys.* **2021**, *154*, No. 061101, DOI: 10.1063/5.0041008.
(33) Grimme, S.; Hansen, A.; Ehlert, S.; Mewes, J.-M. r2SCAN-3c: A "Swiss army knife" composite electronic-structure method. *J. Chem. Phys.* **2021**, *154*, No. 064103, DOI: 10.1063/5.0040021.
(34) Kingsbury, R.; Gupta, A. S.; Bartel, C. J.; Munro, J. M.; Dwaraknath, S.; Horton, M.; Persson, K. A. Performance comparison of r^2SCAN and SCAN metaGGA density functionals for solid materials via an automated, high-throughput computational workflow. *Phys. Rev. Mater.* **2022**, *6*, No. 013801, DOI: 10.1103/PhysRevMaterials.6.013801.
(35) Jütten, S.; Bredow, T. First-Principles Investigation of Electronic Properties and Phase Transition of Ti_3O_5. *J. Phys. Chem. C* **2022**, *126*, 7809−7817.
(36) Oliveira, D. V.; Laun, J.; Peintinger, M. F.; Bredow, T. BSSE-correction scheme for consistent gaussian basis sets of double-and triple-zeta valence with polarization quality for solid-state calculations. *J. Comput. Chem.* **2019**, *40*, 2364−2376, DOI: 10.1002/jcc.26013.
(37) Kresse, G.; Furthmüller, J. Efficient iterative schemes for ab initio total-energy calculations using a plane-wave basis set. *Phys. Rev. B* **1996**, *54*, 11169−11186, DOI: 10.1103/PhysRevB.54.11169.
(38) Kresse, G.; Furthmüller, J. Efficiency of ab-initio total energy calculations for metals and semiconductors using a plane-wave basis set. *Comput. Mater. Sci.* **1996**, *6*, 15−50.
(39) Blöchl, P. E. Projector augmented-wave method. *Phys. Rev. B* **1994**, *50*, 17953−17979, DOI: 10.1103/PhysRevB.50.17953.
(40) Kresse, G.; Joubert, D. From ultrasoft pseudopotentials to the projector augmented-wave method. *Phys. Rev. B* **1999**, *59*, 1758−1775, DOI: 10.1103/PhysRevB.59.1758.
(41) Jinnouchi, R.; Lahnsteiner, J.; Karsai, F.; Kresse, G.; Bokdam, M. Phase transitions of hybrid perovskites simulated by machine-learning force fields trained on the fly with Bayesian inference. *Phys. Rev. Lett.* **2019**, *122*, No. 225701, DOI: 10.1103/PhysRevLett.122.225701.
(42) Jinnouchi, R.; Karsai, F.; Kresse, G. On-the-fly machine learning force field generation: Application to melting points. *Phys. Rev. B* **2019**, *100*, No. 014105, DOI: 10.1103/PhysRevB.100.014105.
(43) Jinnouchi, R.; Karsai, F.; Verdi, C.; Asahi, R.; Kresse, G. Descriptors representing two-and three-body atomic distributions and their effects on the accuracy of machine-learned inter-atomic potentials. *J. Chem. Phys.* **2020**, *152*, No. 234102, DOI: 10.1063/5.0009491.
(44) Murnaghan, F. D. The compressibility of media under extreme pressures. *Proc. Natl. Acad. Sci. U.S.A.* **1944**, *30*, 244−247.
(45) Birch, F. Finite elastic strain of cubic crystals. *Phys. Rev.* **1947**, *71*, No. 809, DOI: 10.1103/PhysRev.71.809.
(46) Ohkoshi, S.-i.; Tokoro, H.; Nakagawa, K.; Yoshikiyo, M.; Jia, F.; Namai, A. Low-pressure-responsive heat-storage ceramics for automobiles. *Sci. Rep.* **2019**, *9*, No. 13203, DOI: 10.1038/s41598-019-49690-0.
(47) Mariette, C.; Lorenc, M.; Cailleau, H.; Collet, E.; Guérin, L.; Volte, A.; Trzop, E.; Bertoni, R.; Dong, X.; Lépine, B.; et al. Strain wave pathway to semiconductor-to-metal transition revealed by time-resolved X-ray powder diffraction. *Nat. Commun.* **2021**, *12*, No. 1239, DOI: 10.1038/s41467-021-21316-y.
(48) Åsbrink, S.; Gerward, L.; Olsen, J. A high-pressure study of Ti_3O_5 by X-ray diffraction and synchrotron radiation. 1. Pressures up to 38.6 GPa. *J. Appl. Crystallogr.* **1989**, *22*, 119−122.
(49) Fu, X.-K.; Chen, W.-Q.; Jiang, Z.-S.; Yang, B.; Zhao, X.; Zuo, L. First-principles investigation on elastic, electronic, and optical properties of Ti_3O_5. *Acta Phys. Sin.* **2019**, *68*, No. 207301, DOI: 10.7498/aps.68.20190664.
(50) Jütten, S.; Bredow, T. Doping Effect on the Electronic Structure and Heat-Storage Properties of Ti_3O_5. *J. Phys. Chem. C* **2023**, *127*, 10445−10452.

APPENDIX D

Effect of Surface Free Energies and Particle Diameter on the Ti_3O_5 $\beta \rightarrow \lambda$ Phase Transition Temperature: A Theoretical Study

THE JOURNAL OF PHYSICAL CHEMISTRY C
A JOURNAL OF THE AMERICAN CHEMICAL SOCIETY

pubs.acs.org/JPCC

Article

Effect of Surface Free Energies and Particle Diameter on the Ti_3O_5 $\beta \rightarrow \lambda$ Phase Transition Temperature: A Theoretical Study

Published as part of The Journal of Physical Chemistry C virtual special issue "Francesc Illas and Gianfranco Pacchioni Festschrift".

Stefan Jütten* and Thomas Bredow*

Cite This: J. Phys. Chem. C 2024, 128, 13402−13409

Read Online

ACCESS | Metrics & More | Article Recommendations | Supporting Information

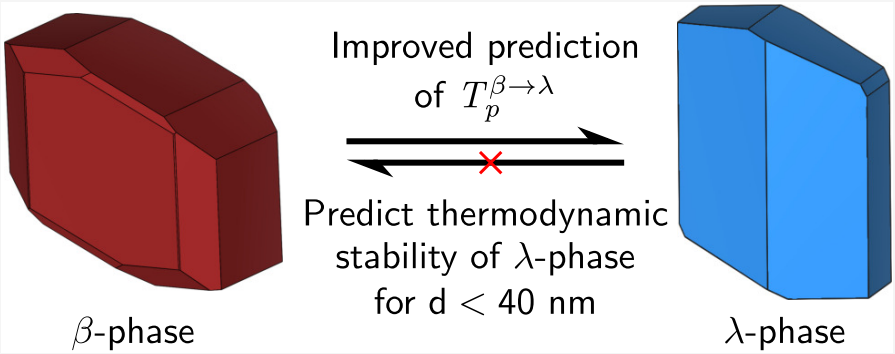

ABSTRACT: The solid−solid heat-storage material Ti_3O_5 is experimentally known to store thermal energy for long time periods and to release the accumulated energy on demand. During the heat-storage process the lower-energy β-phase is transformed into the higher-energy λ-phase, which is retained at ambient conditions, unless external pressure is applied. Therefore, the metastability of the λ-phase is a crucial aspect of the heat-storage system. In previous theoretical studies it was shown that the hysteresis cannot be explained by conventional bulk models. Here, we present a comprehensive theoretical study of the surfaces of both Ti_3O_5 phases in order to demonstrate the effect of the surface energy on the relative phase stability. We apply the r^{2}SCAN-D3 method to the calculation of surface free energies and show that most λ-phase facets are more stable than the corresponding β-phase surfaces. On the basis of calculated surface free energies we predict the temperature dependency of the crystallite morphology and estimate the size-dependent relative free energy of β- and λ-particles. We show that for particles in the experimentally synthesized diameter range the inclusion of surface effects has a substantial effect on the theoretical prediction of phase transition temperatures.

INTRODUCTION

The trititanium-pentoxide (Ti_3O_5) heat-storage system undergoes an isostructural (within space group $C2/m$) solid−solid phase transition from the β-Ti_3O_5 to the λ-Ti_3O_5 polymorph at 470 K.[1,2] λ-Ti_3O_5 is metastable upon cooling down to ambient conditions and the stored thermal energy (ΔH = 12 ± 1 kJ mol^{-1}) can be released on demand by the application of an external pressure of 600 bar.[2] Since the phase transition can also be triggered by irradiation or current, the metastability of λ-Ti_3O_5 could in principle be also exploited in e.g., optical data storage or sensor applications.[3,4]

Experimentally, λ-Ti_3O_5 is usually obtained as a powder consisting of nanoparticles, which agglomerate to microparticles of coral-like shape. The thermodynamic stability of nanoscale λ-Ti_3O_5 has been attributed to surface effects, which suppress the $\lambda \rightarrow \beta$ phase transition and give rise to a broad thermal hysteresis loop spanning from the phase transition temperature to below room temperature.[5] Determination of surface energies is therefore essential for understanding polymorph stability, in addition to the crystallite morphology.[6] In general, the equilibrium shape of crystallites changes with temperature due to the different temperature dependence of the individual surface free energies. This was already observed in the literature for e.g., iron carbide nanoparticles[7] or tungsten surfaces.[8]

Apart from stabilizing the λ-phase at ambient conditions, the surface has important other applications. For instance, the (110) surface of λ-Ti_3O_5 has recently been shown to significantly

Received: June 4, 2024
Revised: July 26, 2024
Accepted: July 29, 2024
Published: August 7, 2024

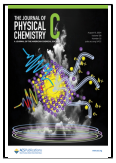

increase the rate of solar steam generation, which can be used for the desalination of seawater.[9]

Experimentally observed Ti_3O_5 particle sizes depend on synthesis conditions such as starting materials, sintering time and reduction agents used. λ-Ti_3O_5 particle diameters between 8 ± 2[10] and 400 nm[11] have been measured experimentally.[2,3,5,12−15] We are interested in the heat-storage aspect of this phase change material and thus focus on the results published in ref 2, where λ-Ti_3O_5 particles with dimensions 200 × 30 × 30 nm^3 were synthesized. This volume equals that of a sphere with a diameter of 70 nm. These nanoparticles agglomerate to microparticles of coral-like morphology with diameter 4 ± 1 μm.

We note that in most experiments a mixture of β-Ti_3O_5 and λ-Ti_3O_5 nanoparticles is obtained. Larger particles have the β-Ti_3O_5 structure while the structure of smaller particles corresponds to the λ-phase.[5] It is therefore reasonable that surface effects play an important role in the relative phase stability.

Nanoparticle size impacts the experimentally observed transition pressure P_{th}, which decreases as the particle size (i.e., particle diameter d) increases.[12] At the same time, the measured phase transition enthalpy ΔH_{trans} decreases as d becomes smaller.[12] While ΔH_{trans} = 13.7 kJ mol^{-1} was observed for d = 400 nm,[11] for d = 70 nm ΔH_{trans} decreases to 12 ± 1 kJ mol^{-1},[2] for d = 57 ± 0.3 nm a ΔH_{trans} of 7.78 ± 0.26 kJ mol^{-1} was measured,[12] for d = 22 ± 8 a further decrease of ΔH_{trans} to 5.5 kJ mol^{-1} is observed,[15] and for particles with d = 25 ± 15 nm ΔH_{trans} is only 4.8 kJ mol^{-1}.[3]

In this study we calculate surface energies of all low-index surfaces of both phases at density-functional theory (DFT) level. For the most stable facets free energy calculations are performed based on phonon calculations employing the harmonic approximation. The Wulff-Gibbs theorem allows the prediction of particle morphology change as a function of temperature. We employ a simple thermodynamic model to estimate the relative stability of λ-Ti_3O_5 and β-Ti_3O_5 nanoparticles depending on the diameter. The stabilization of λ-phase nanoparticles with diameters ≤80 nm is found to significantly lower the calculated $\beta \rightarrow \lambda$-phase transition temperature compared to bulk models.

METHODS

All calculations were performed with the Vienna Ab initio Simulation Package (VASP) v6.3.2[16,17] employing the projector augmented wave (PAW) method[18,19] and a 680 eV plane wave cutoff energy, which is considered as converged for the present purposes. Gaussian smearing with σ = 0.2 eV was used throughout. We used tight SCF convergence thresholds of 10^{-8} eV and a Γ-centered Monkhorst−Pack mesh with a k-point spacing of 0.2 $Å^{-1}$. This spacing was increased to 0.4 $Å^{-1}$ for the calculation of vibrational frequencies to reduce computation time, while largely retaining accuracy. Enhanced integration grids were used to obtain more accurate forces. Accurate total energies on optimized structures were obtained using the tetrahedron method with Blöchl corrections.[20] Structural relaxations were performed until the norm of all forces acting on the ions was smaller than 10^{-4} eV $Å^{-1}$.

We employed the r^{2}SCAN[21] method with the DFT-D3(BJ) dispersion correction,[22,23] which we have already shown to provide accurate relative phase energies, frequencies and structures for Ti_3O_5.[24,25] All calculations used an initial ferromagnetic spin configuration. This is a simplification of the more complicated magnetic ground states of the phases as found previously, which was employed in order to increase symmetry and reduce computational effort. We observed oscillatory convergence behavior of the atomic magnetization during structural optimizations, which could only be fixed by defining a constant net magnetization of 0.5e per formula unit for the β-phase and 1.5e per formula unit for the λ-phase. Those values are obtained after optimizations of both phases without fixing the net magnetization per formula unit in the bulk. Optimized lattice parameters and the energy difference between the phases is largely unaffected by fixing the magnetization in this way. Surface energies were calculated with respect to the corresponding bulk and were converged to 0.02 J m^{-2} employing slab models with increasing number of layers.

Slabs were cut from the optimized bulk phases and only the atomic positions were allowed to relax during optimizations. The selected surface models are symmetric and stoichiometric to avoid artificial dipole moments. One stoichiometric layer always corresponds to four formula units Ti_3O_5, i.e., one conventional cell containing 32 atoms. A vacuum distance of 20 Å was used throughout to minimize interactions between the periodic images of the slab.

Predictions of crystallite shapes used the wulffpack Python module.[26] For visualizations of atomic structures the VESTA program was used.[27]

RESULTS AND DISCUSSION

Surface Models and Surface Energies. We start by fully optimizing the bulk structure of β-Ti_3O_5 and λ-Ti_3O_5 (Figure 1)

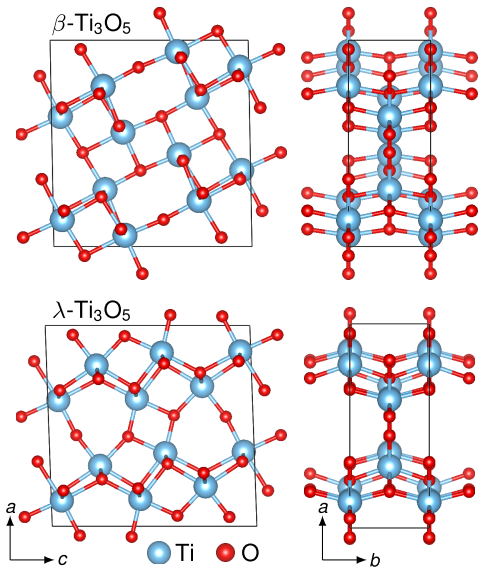

Figure 1. Optimized structures (r^{2}SCAN-D3/680 eV) of bulk β-Ti_3O_5 and λ-Ti_3O_5 shown from two different perspectives.

with the method and settings mentioned above. Deviations from experiment are smaller than 1% as compared to the experimental lattice parameters, except for an underestimation of the c lattice vector in β-Ti_3O_5, see Table 1. This compares well with our previous results, which also included an assessment of the deviation of the atomic positions.[24]

The energy difference between the phases is $\Delta E^{\lambda-\beta} = E^{\lambda} - E^{\beta}$ = 12.3 kJ mol^{-1}, which compares favorably to our previous result of ΔE = 10.6 kJ mol^{-1} obtained without fixing the Ti magnetizations during the geometry optimization.[24]

https://doi.org/10.1021/acs.jpcc.4c03730
J. Phys. Chem. C 2024, 128, 13402−13409

Table 1. Optimized Lattice Parameters (in Å) and Unique Monoclinic Angle β of the $C2/m$ Space Group (in °) of β-Ti_3O_5 and λ-Ti_3O_5 on the r^{2}SCAN-D3/680 eV Level of Theory Compared with Experimental Data[a]

		lattice vectors				
phase	data	a	b	c	β-angle	$\bar{\mu}$
β-Ti_3O_5	opt.	9.70	3.85	9.28	91.10	0.5
	exp.[b]	9.75	3.80	9.44	91.53	
λ-Ti_3O_5	opt.	9.79	3.81	9.92	91.58	1.5
	exp.[b]	9.83	3.79	9.97	91.29	

[a] $\bar{\mu}$ is the Ti magnetization per formula unit. [b] Ref 2.

We computed surface energies for all low-index surfaces of β- and λ-Ti_3O_5. The surface free energy G^{surf}_{hkl} of a slab model cut from the bulk along the Miller indices hkl and containing n formula units is given by eq 1.

$$G^{surf}_{hkl}(n) = \frac{G^{slab}_{hkl}(n) - nG^{bulk}}{2A_{hkl}} \quad (1)$$

where G^{slab}_{hkl} is the free energy of the slab model with n formula units, G^{bulk} is the free energy of the corresponding bulk phase, and A_{hkl} is the surface area of the slab model. To save computational resources we approximate G^{surf}_{hkl} by the electronic surface energy E^{surf}_{hkl} in the screening. E^{surf}_{hkl} of a slab model was converged with the number of layers until the changes were smaller than 0.02 J m^{-2}. For some facets this strict convergence was not achieved for the largest slab models that could be treated with the available computer resources. In these cases we accepted larger changes.

We present our calculated electronic surface energies as a function of the number of stoichiometric layers in Figure 2 and Supporting Information Table S1. Figures of all optimized surfaces of both phases from different perspectives can be found in the Supporting Information. Optimized structures of the converged surface models are attached as an archive in the Supporting Information.

Most surface energies are converged with 3−4 stoichiometric layers. With the exception of the (101) surface, all λ-Ti_3O_5 surface energies for a certain facet are lower than those of the β-phase for the corresponding low-index surface terminations. This trend is found for the higher-index surfaces as well, where the only outlier is the (012) surface. The (101), (010) and (102) surface terminations are the most stable for β-Ti_3O_5, whereas the (110), (100), (010) and (102) surface terminations are most stable for λ-Ti_3O_5.

Surface Free Energies and Wulff Constructions. In a previous study we calculated the phase transition temperature T_p for the $\beta \rightarrow \lambda$ phase transition as 525 K, applying bulk models and the r^{2}SCAN-D3/680 eV level of theory in combination with frequency calculations in the harmonic approximation. This overestimates the experimental value, 470 K,[2] by 55 K. More recently, a similar phase transition temperature of T_p = 535 K

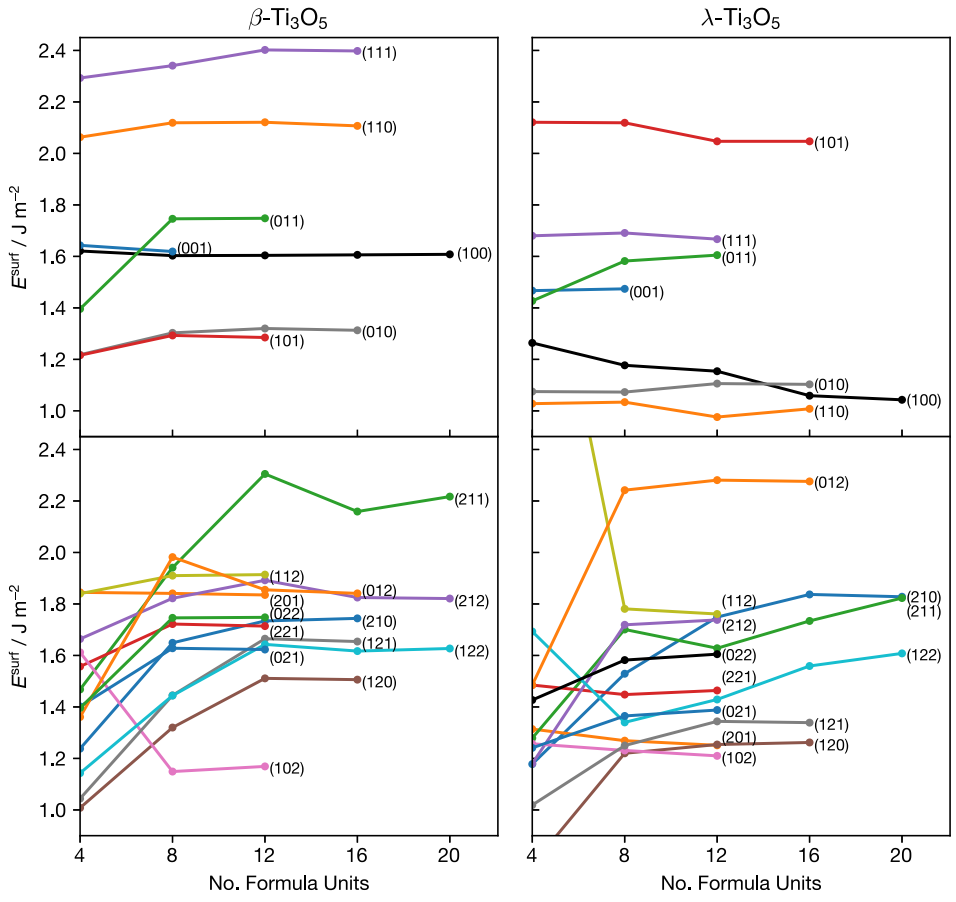

Figure 2. Surface energies E^{surf} of all low-index surface terminations (hkl) of β-Ti_3O_5 and λ-Ti_3O_5 as a function of slab thickness on the r^{2}SCAN-D3/680 eV level of theory. For clarity the top panels show low-index surface terminations and higher index surface terminations are shown in the lower panels.

https://doi.org/10.1021/acs.jpcc.4c03730
J. Phys. Chem. C 2024, 128, 13402−13409

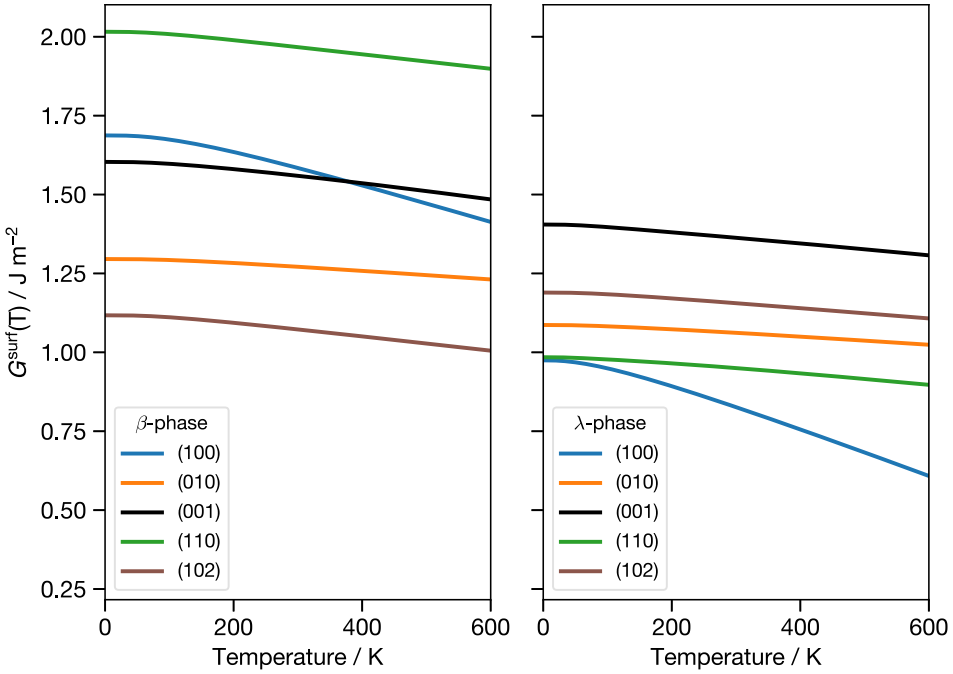

Figure 3. Surface free energies G^{surf} of β-Ti_3O_5 and λ-Ti_3O_5 surfaces that dominate the total surface area of Wulff constructions as a function of temperature.

was calculated by means of well-tempered metadynamics simulations employing the PBE/520 eV method.[28] These simulations were also based on bulk models of Ti_3O_5. Our goal is to improve the theoretical model ansatz by incorporating surface effects. For this purpose we go beyond the above-mentioned approximation where electronic surface energies rather than surface free energies were computed, in order to take temperature effects into account. For a selection of the most stable facets based on E^{surf}_{hkl} we calculate surface free energies for the converged slab models according to eq 1 by performing frequency calculations in the harmonic approximation on the r^{2}SCAN-D3/680 eV level of theory. Using these surface free energies $G^{surf}_{hkl}(T)$ we calculate temperature-dependent Wulff particle shapes applying the Wulff–Gibbs theorem.[29] Figure 3 shows the temperature dependence of the surface free energy of the most relevant facets.

We note that for both phases the (100) surface free energy decreases with a much larger slope compared to all other surfaces, which is an outlier and was therefore carefully checked. The λ-Ti_3O_5 (100) surface free energy is considerably lower (even at 0 K) than that of β-Ti_3O_5 (100), see Table 2. This is caused by the larger zero point energy stabilization of λ-Ti_3O_5 compared to β-Ti_3O_5 which is present in the bulk and in almost every surface. Except the (102) facet, all surface free energies of λ-phase surfaces are smaller than those of their β-phase counterparts. Our predicted ranking of surface energies matches experimentally estimated λ-Ti_3O_5 surface energies from spectroscopic ellipsometry measurements of λ-Ti_3O_5 thin films.[30] These measurements correlated the surface energy with the number of broken bonds per area and gave the following ordering: (100) and (110) 0.11 Å^{-2}, followed by (010) with 0.12 Å^{-2}, (011) with 0.17 Å^{-2}, (101) with 0.19 Å^{-2} and (001) with 0.22 Å^{-2} as the only outlier.

We compare our calculated surface free energies G^{surf}_{hkl} to our electronic surface energies E^{surf}_{hkl} in Table 2 and find that surface free energies are generally lower than electronic surface energies.

Table 2. Comparison of Electronic Surface Energies E^{surf} and Surface Free Energies G^{surf} at T = 0, 300, 600 K (All in J m^{-2}) for β-Ti_3O_5 and λ-Ti_3O_5[a]

phase	surface	E^{surf}	G^{surf} (0 K)	G^{surf} (300 K)	G^{surf} (600 K)
β-Ti_3O_5	(100)	1.61	1.69 (0.08)	1.58 (−0.03)	1.41 (−0.20)
	(010)	1.31	1.30 (−0.01)	1.27 (−0.04)	1.23 (−0.08)
	(001)	1.62	1.60 (−0.02)	1.56 (−0.06)	1.49 (−0.13)
	(110)	2.11	2.02 (−0.09)	1.97 (−0.14)	1.90 (−0.21)
	(102)	1.17	1.12 (−0.05)	1.07 (−0.10)	1.01 (−0.16)
λ-Ti_3O_5	(100)	1.04	0.98 (−0.06)	0.83 (−0.21)	0.61 (−0.43)
	(010)	1.10	1.09 (−0.01)	1.06 (−0.04)	1.02 (−0.08)
	(001)	1.47	1.41 (−0.06)	1.36 (−0.11)	1.31 (−0.16)
	(110)	1.01	0.98 (−0.03)	0.95 (−0.06)	0.90 (−0.11)
	(102)	1.21	1.19 (−0.02)	1.16 (−0.05)	1.11 (−0.10)

[a]The difference $G^{surf}(T) - E^{surf}$ is given in parentheses.

At 0 K the difference is between −0.02 J m^{-2} (β-phase (001) surface) and −0.09 J m^{-2} (β-phase (110) surface). Similarly small differences between surface energies and surface free energies have been reported previously.[31] At higher temperatures, however, the differences are more pronounced and can be as large as −0.21 J m^{-2} (300 K) and −0.43 J m^{-2} (600 K) e.g., for the λ-Ti_3O_5 (100) surface.

Our calculated surface free energies allow us to predict the crystallite shape of both phases as a function of temperature (Figure 4). Supporting Information Figure S21 shows how the Wulff shape relates to the bulk structure of both polymorphs.

With increasing temperature the contributions of the (100) facet and of the (010) facet of β-Ti_3O_5 increase, while the percentages of the (102) and (001) facets remain virtually unchanged. The contributions of the high-energy (012) and (210) surface areas decrease as temperature increases, and the fraction of the (101) facet slightly decreases due to the comparably large increase in surface area of the adjacent (100) facet. In λ-Ti_3O_5 the large decrease of the (100) surface

https://doi.org/10.1021/acs.jpcc.4c03730
J. Phys. Chem. C 2024, 128, 13402−13409

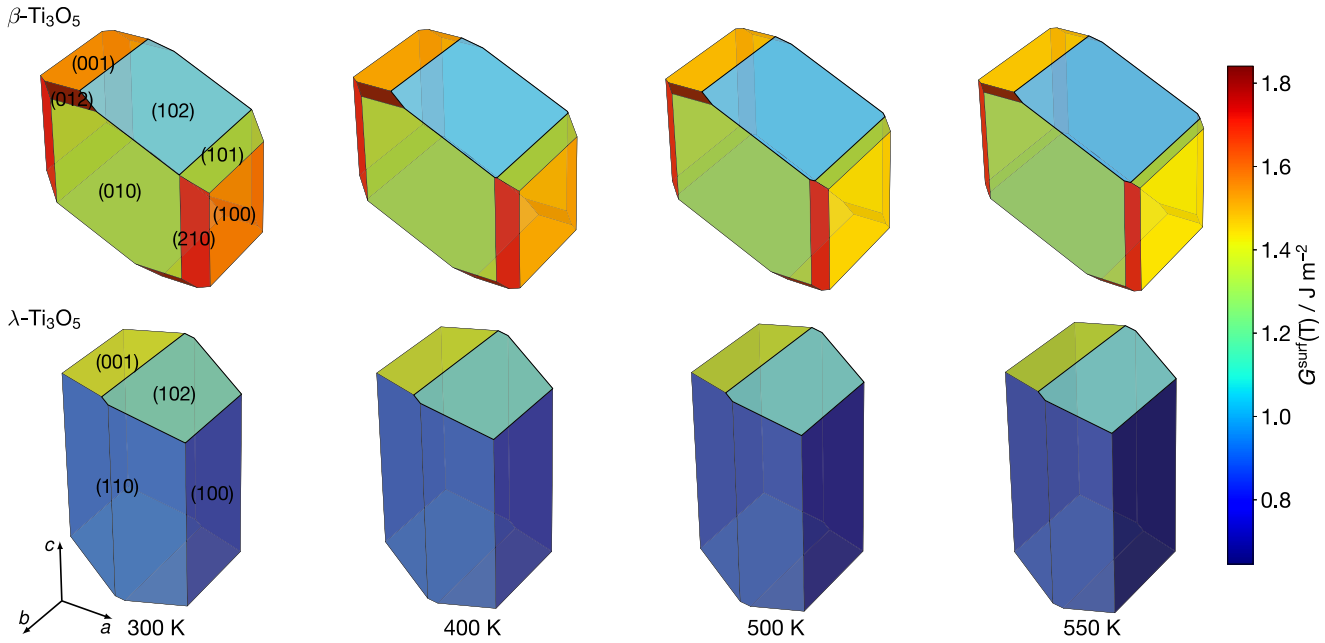

Figure 4. Wulff constructions of β-Ti_3O_5 and λ-Ti_3O_5 particles at several temperatures. Different surface free energies of the individual facets are color-coded according to their surface free energy.

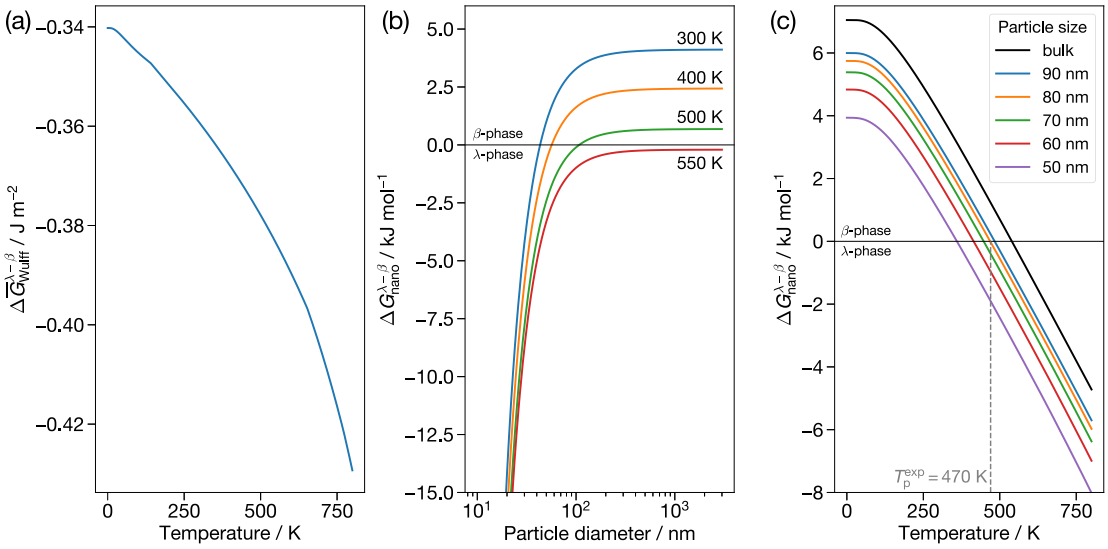

Figure 5. (a) Difference of weighted surface free energies of equilibrium-shape crystallites as a function of temperature, (b) prediction of thermodynamic stability as a function of particle diameter and (c) prediction of phase transition temperatures for particles of different diameter.

free energy results in an elongation of the particle in c direction. The rather uniform decrease of surface free energies of all remaining facets leaves their proportion in the resulting crystallite basically unchanged, only a minor increase in (102) facet surface area is noted. We did not calculate G_{hkl}^{surf} for the (012), (101) and (210) facets of β-Ti_3O_5 since their electronic surface energies are rather high. In these cases $G_{hkl}^{surf}(T)$ was replaced by E_{hkl}^{surf}.

Relative Phase Stability Including Surface Effects. In order to quantify the temperature-dependent stabilization of λ-Ti_3O_5 with respect to β-Ti_3O_5, we consider the weighted surface free energies of the Wulff constructions $\overline{G}_{Wulff}$ taken as

$$\overline{G}_{Wulff}(T) = \frac{1}{A_{tot}} \sum_{hkl} A_{hkl} G_{hkl}(T) \quad (2)$$

where A_{tot} and A_{hkl} are the total surface area of the Wulff construction and the contribution from its (hkl) facet, respectively, and $G_{hkl}(T)$ is the surface free energy at temperature T of the (hkl) surface termination taken from the size-converged surface models.

In Figure 5(a) we present the difference between $\overline{G}_{Wulff}(T)$ of β-Ti_3O_5 and λ-Ti_3O_5 as a function of temperature including the relevant heat-storage temperature range between 300 and 600 K. In this temperature range the weighted surface free energy of a λ-Ti_3O_5 crystallite is significantly smaller than that of a β-Ti_3O_5 particle, for instance $\Delta\overline{G}_{Wulff}^{\lambda-\beta} = -0.36$ J m^{-2} at 300 K. With increasing temperature the difference between the weighted surface free energies of the Wulff constructions becomes more pronounced. We will show the impact of this observation on the phase transition temperature later.

https://doi.org/10.1021/acs.jpcc.4c03730
J. Phys. Chem. C 2024, 128, 13402−13409

We analyze the impact of $\Delta\overline{G}^{\lambda-\beta}_{\mathrm{Wulff}}$ on the relative phase stability of Ti_3O_5 nanoparticles using a thermodynamic model of Navrotsky, which relates phase equilibria of phases of a compound as a function of particle size to their difference in surface free energies.[32] Within this model, the nanoparticle is approximated as a sphere, where the fraction $x_{\mathrm{surf}}(d)$ of atoms within 0.5 nm of the surface (eq 3) are considered as surface atoms. The remaining part $1 - x_{\mathrm{surf}}(d)$ is considered as bulk-like. Here, we adopt a value of 4 Å (or 0.4 nm), which approximates the averaged interlayer distance of all surfaces present in the particles. This selection of surface atoms is reasonable, since only minor deviations of atomic positions from the bulk reference are noted in lower layers during structure relaxation.

$$x_{\mathrm{surf}}(d) = \frac{V(d) - V(d - 0.8\ \mathrm{nm})}{V(d)} \tag{3}$$

Thus, an outer shell of 4 Å depth is defined, with the core of the particle being regarded as perfect bulk. The stabilizing contribution of surfaces to the free energy balance of the system that arises from surface effects is obtained by multiplying the weighted surface free energy difference $\Delta\overline{G}^{\lambda-\beta}_{\mathrm{Wulff}}$ by the molar surface area A_{mol} in eq 4

$$\Delta G^{\mathrm{stabil.}}_{\mathrm{surf}}(d) = A_{\mathrm{mol}}(d)\Delta\overline{G}^{\lambda-\beta}_{\mathrm{Wulff}} \tag{4}$$

Here, the molar surface area A_{mol} ($m^2\ mol^{-1}$) for a particle with diameter d (eq 5) is calculated using the specific surface area $A^{\mathrm{BET}} = 12.82\ m^2\ g^{-1}$ of the experimentally measured particle of diameter $d^{\mathrm{exp.}} = 3000$ nm[13] and the molar mass $M_{Ti_3O_5}$ of Ti_3O_5 (223.6 g mol^{-1})

$$A_{\mathrm{mol}}(d) = \frac{d^{\mathrm{exp.}}}{d} A^{\mathrm{BET}} M_{Ti_3O_5} \tag{5}$$

The prefactor accounts for the decrease of the surface area of a larger particle with respect to the experimental surface area. Thus, the free energy difference $\Delta G^{\lambda-\beta}_{\mathrm{nano}}$ between spherical λ-phase and β-phase particles of diameter d with a bulk fraction of $(1 - x_{\mathrm{surf}}(d))$ is given by eq 6

$$\Delta G^{\lambda-\beta}_{\mathrm{nano}}(d) = (1 - x_{\mathrm{surf}}(d))\Delta G^{\lambda-\beta}_{\mathrm{bulk}} + x_{\mathrm{surf}}(d)\Delta G^{\mathrm{stabil.}}_{\mathrm{surf}}(d) \tag{6}$$

In Figure 5(b) we evaluate $\Delta G^{\lambda-\beta}_{\mathrm{nano}}(d)$ for different temperatures for particles with diameters up to 3 μm. Surface effects start to contribute to the overall free energy difference between the particles below diameters of ≈200 nm. Our calculations predict, that at $T \geq 300$ K the equilibrium structure of Ti_3O_5 nanoparticles with diameter below 43 nm is that of the λ-phase. Stabilization by surface effects overcompensates the bulk free energy difference between the phases. In heat-storage applications nanoparticles with $d < 43$ nm therefore will be trapped in the λ-phase after cooling down, i.e., their thermodynamic stability prevents the $\lambda \rightarrow \beta$ phase transition. At higher temperatures the stabilizing effects are even more pronounced and λ-Ti_3O_5 particles with larger diameters become stable.

The specific surface area of λ-Ti_3O_5 particles is the only experimental variable that enters our model calculations. We show the effect of uncertainties in this crucial parameter in Supporting Information Figure S22 by arbitrarily varying the value of A^{BET}. A variation of $A^{\mathrm{BET}} = 12.82\ m^2\ g^{-1}$ by ±5% leads to changes of ±5 nm for the particle diameter d_{crit} with $\Delta G^{\lambda-\beta}_{\mathrm{nano}}(d_{\mathrm{crit}}) = 0$. Taking these data into account, we predict λ-Ti_3O_5 nanoparticles to be more stable than β-Ti_3O_5 below $d_{\mathrm{crit}} \approx 43 \pm 5$ nm.

Spherical λ-Ti_3O_5 particles published in the literature show diameters of 25 ± 15,[3] 57 ± 0.3,[12] 30−50,[13] 8 ± 2 − 36 ± 15,[10] 40[14] and 22 ± 8 nm[15] at ambient conditions. These diameter ranges compare favorably to our theoretical prediction of thermodynamic stability of λ-Ti_3O_5 nanoparticles below diameters of 50 nm. Discrepancies between our prediction and experiment can be attributed to the idealized assumption of spherical particles, whereas experimentally prepared nanoparticles agglomerate to block, square or nanorod shapes. The specific surface area of λ-Ti_3O_5 was only measured in one instance to the best of the author's knowledge, and could vary depending on the synthesis method. Moreover, we neglect adsorbates (like H_2O) on the surfaces whose interaction with the surfaces could alter their structure and therefore their energetics.

The $\beta \rightarrow \lambda$ phase transition temperature T_p, which was earlier calculated with bulk models,[24,28,33] was recalculated by taking surface effects into account (Figure 5(c)).

The phase transition temperatures for Ti_3O_5 particles of certain diameters are provided in Table 3. Here we compare the calculated results for two values for the surface region of spherical nanoparticles, 4 and 5 Å, respectively. The value of 5 Å was arbitrarily chosen for rutile and anatase in ref 32. Here we propose a value of 4 Å as an average value of the height of the first stoichiometric layer in the considered surfaces, and according to the observed relaxation of atom positions in the slab models.

Table 3. Phase Transition Temperatures T_p (in K) of Particles with Different Diameters (in nm) Compared with the Experimental Phase Transition Temperature[a]

	particle diameter						
surface region	50	60	70	80	90	∞[b]	exp.[c]
4 Å	360	415	448	469	484	525	470
5 Å	314	383	425	451	470		

[a]Results assuming 4 and 5 Å as the depth of surface atoms are provided to showcase the model dependency on this parameter. [b]Ref 24. [c]Ref 2.

The estimated phase transition temperatures T_p show a strong dependence on the surface region. Due to the larger fraction of surface atoms assuming a surface region of 5 Å, T_p is smaller by 14−46 K compared to 4 Å surface depth. The effect decreases with increasing particle diameter. However, both choices lead to similar predictions for the particle diameter, 80−90 nm, that provides best agreement between theoretical and experimental phase transition temperature.

Conclusions. The stability of low-index surfaces of β-Ti_3O_5 and λ-Ti_3O_5 was calculated on the r^{2}SCAN-D3 level of theory. In almost all cases surface energies for λ-Ti_3O_5 are smaller than for the corresponding β-Ti_3O_5 facets. Surface free energies were calculated for the temperature range which is relevant for the $\beta \rightarrow \lambda$ phase transition. At higher temperatures the particle morphology of both Ti_3O_5 phases notably changes. Shapes of β-Ti_3O_5 crystallites are dominated by (010), (100) and (102) facets, while for λ-Ti_3O_5 the (100) and (110) surface terminations are most prominent.

By using a simple thermodynamic model, based on a weighting procedure of bulk and surface free energies,, we derive a particle diameter dependent prediction of the surface stabilization of Ti_3O_5 nanoparticles. Experimental Ti_3O_5

https://doi.org/10.1021/acs.jpcc.4c03730
J. Phys. Chem. C 2024, 128, 13402−13409

powders exhibit a broad variety of different particle diameters. According to our results, particles with diameters smaller than 90 nm will undergo the $\beta \rightarrow \lambda$ phase transition at significantly lower temperatures than larger particles. We predict that particles with diameters $d_{crit} \leq 43 \pm 5$ nm have λ-Ti_3O_5 structure at room temperature. For particle diameters in the range 80−90 nm, the estimated $\beta \rightarrow \lambda$ phase transition temperatures are close to the experimentally measured value of 470 K. For our experimental reference with d = 70 nm, our predictions underestimate T_p by 22 K, whereas our previous bulk calculations overestimate T_p by 55 K.

Based on the present results, we suggest a pressure-induced particle agglomeration as possible explanation for the experimentally observed $\lambda \rightarrow \beta$ phase transition at room temperature under external pressure. The average Ti_3O_5 particle size is increased due to external pressure induced agglomeration and exceeds the limit where λ-Ti_3O_5 is thermodynamically favored. This is in line with experimental observations that a larger particle size lowers the threshold pressure P_{th} for the $\lambda \rightarrow \beta$ phase transition.[12]

■ ASSOCIATED CONTENT

Supporting Information

The Supporting Information is available free of charge at https://pubs.acs.org/doi/10.1021/acs.jpcc.4c03730.

Optimized structures of all converged models in POSCAR format (ZIP)

Surface energies for all surface terminations of both phases; optimized surface structures of all surface terminations from different perspectives (PDF)

■ AUTHOR INFORMATION

Corresponding Authors

Stefan Jütten − *Mulliken Center for Theoretical Chemistry, 53115 Bonn, Germany; Max Planck Institute for Chemical Energy Conversion, 45470 Mülheim an der Ruhr, Germany;* orcid.org/0000-0001-8756-7963; Email: juetten@thch.uni-bonn.de

Thomas Bredow − *Mulliken Center for Theoretical Chemistry, 53115 Bonn, Germany;* orcid.org/0000-0003-4077-5428; Email: bredow@thch.uni-bonn.de

Complete contact information is available at: https://pubs.acs.org/10.1021/acs.jpcc.4c03730

Notes

The authors declare no competing financial interest.

■ ACKNOWLEDGMENTS

This work is supported by the International Max Planck Research School on Reactive Structure Analysis for Chemical Reactions (IMPRS-RECHARGE). The authors gratefully acknowledge the funding of this project by computing time provided by the Paderborn Center for Parallel Computing (PC2).

■ REFERENCES

(1) Ohkoshi, S.-i.; Yoshikiyo, M.; MacDougall, J.; Ikeda, Y.; Tokoro, H. Long-term heat-storage materials based on λ-Ti_3O_5 for green transformation (GX). *Chem. Commun.* **2023**, *59*, 7875−7886.

(2) Tokoro, H.; Yoshikiyo, M.; Imoto, K.; Namai, A.; Nasu, T.; Nakagawa, K.; Ozaki, N.; Hakoe, F.; Tanaka, K.; Chiba, K.; et al. External stimulation-controllable heat-storage ceramics. *Nat. Commun.* **2015**, *6*, No. 7037.

(3) Ohkoshi, S.-i.; Tsunobuchi, Y.; Matsuda, T.; Hashimoto, K.; Namai, A.; Hakoe, F.; Tokoro, H. Synthesis of a metal oxide with a room-temperature photoreversible phase transition. *Nat. Chem.* **2010**, *2*, 539−545.

(4) Zhao, P.-f.; Li, G.-s.; Li, W.-l.; Cheng, P.; Pang, Z.-y.; Xiong, X.-l.; Zou, X.-l.; Qian, X.; Lu, X.-g. Progress in Ti_3O_5: Synthesis, properties and applications. *Trans. Nonferrous Met. Soc. China* **2021**, *31*, 3310−3327.

(5) Makiura, R.; Takabayashi, Y.; Fitch, A. N.; Tokoro, H.; Ohkoshi, S.-i.; Prassides, K. Nanoscale Effects on the Stability of the λ-Ti_3O_5 Polymorph. *Chem. - Asian J.* **2011**, *6*, 1886−1890.

(6) Tran, R.; Xu, Z.; Radhakrishnan, B.; Winston, D.; Sun, W.; Persson, K. A.; Ong, S. P. Surface energies of elemental crystals. *Sci. Data* **2016**, *3*, No. 160080.

(7) Xing, M.; Pathak, A.-D.; Sanyal, S.; Peng, Q.; Liu, X.; Wen, X. Temperature-dependent surface free energy and the Wulff shape of iron and iron carbide nanoparticles: A molecular dynamics study. *Appl. Surf. Sci.* **2020**, *509*, No. 144859.

(8) Scheiber, D.; Renk, O.; Popov, M.; Romaner, L. Temperature dependence of surface and grain boundary energies from first principles. *Phys. Rev. B* **2020**, *101*, No. 174103.

(9) Yang, B.; Zhang, Z.; Liu, P.; Fu, X.; Wang, J.; Cao, Y.; Tang, R.; Du, X.; Chen, W.; Li, S.; et al. Flatband λ-Ti_3O_5 towards extraordinary solar steam generation. *Nature* **2023**, *622*, 499−506.

(10) Nasu, T.; Tokoro, H.; Tanaka, K.; Hakoe, F.; Namai, A.; Ohkoshi, S. In *Sol−Gel Synthesis of Nanosized λ-Ti3O5 Crystals*, IOP Conference Series: Materials Science and Engineering; IOP Publishing, 2014.

(11) Ohkoshi, S.-i.; Tokoro, H.; Nakagawa, K.; Yoshikiyo, M.; Jia, F.; Namai, A. Low-pressure-responsive heat-storage ceramics for automobiles. *Sci. Rep.* **2019**, *9*, No. 13203.

(12) Kubota, T.; Seiki, R.; Fujisawa, A.; Fadilla, A. F.; Jia, F.; Ohkoshi, S.-i.; Tokoro, H. Synthesis of heat storage ceramic λ-Ti_3O_5 using titanium chloride as the starting material. *Mater. Adv.* **2024**, *5*, 3832−3837.

(13) Chai, G.; Huang, W.; Shi, Q.; Zheng, S.; Wei, D. Preparation and characterization of λ-Ti_3O_5 by carbothermal reduction of TiO_2. *J. Alloys Compd.* **2015**, *621*, 404−410.

(14) Cai, Y.; Shi, Q.; Wang, M.; Lv, X.; Cheng, Y.; Huang, W. Synthesis of nanoscale lambda-Ti_3O_5 via a PEG assisted sol-gel method. *J. Alloys Compd.* **2020**, *848*, No. 156585.

(15) Araki, Y.; Ohkoshi, S.; Tokoro, H. Synthesis of λ-Ti_3O_5 nanocrystals using a block copolymer. *Mater. Today Energy* **2020**, *18*, No. 100525.

(16) Kresse, G.; Furthmüller, J. Efficient iterative schemes for ab initio total-energy calculations using a plane-wave basis set. *Phys. Rev. B* **1996**, *54*, No. 11169.

(17) Kresse, G.; Furthmüller, J. Efficiency of ab-initio total energy calculations for metals and semiconductors using a plane-wave basis set. *Comput. Mater. Sci.* **1996**, *6*, 15−50.

(18) Blöchl, P. E. Projector augmented-wave method. *Phys. Rev. B* **1994**, *50*, No. 17953.

(19) Kresse, G.; Joubert, D. From ultrasoft pseudopotentials to the projector augmented-wave method. *Phys. Rev. B* **1999**, *59*, No. 1758.

(20) Blöchl, P. E.; Jepsen, O.; Andersen, O. K. Improved tetrahedron method for Brillouin-zone integrations. *Phys. Rev. B* **1994**, *49*, 16223−16233.

(21) Furness, J. W.; Kaplan, A. D.; Ning, J.; Perdew, J. P.; Sun, J. Accurate and Numerically Efficient r2SCAN Meta-Generalized Gradient Approximation. *J. Phys. Chem. Lett.* **2020**, *11*, 8208−8215.

(22) Grimme, S.; Antony, J.; Ehrlich, S.; Krieg, H. A consistent and accurate ab initio parametrization of density functional dispersion correction (DFT-D) for the 94 elements H-Pu. *J. Chem. Phys.* **2010**, *132*, No. 154104.

(23) Grimme, S.; Ehrlich, S.; Goerigk, L. Effect of the damping function in dispersion corrected density functional theory. *J. Comput. Chem.* **2011**, *32*, 1456−1465.

(24) Jütten, S.; Bredow, T. First-Principles Investigation of Electronic Properties and Phase Transition of Ti_3O_5. *J. Phys. Chem. C* **2022**, *126*, 7809−7817.
(25) Jütten, S.; Bredow, T. Anisotropy of the Pressure Effect in the Ti_3O_5 Phase Transition Process Resolved by Direction-Dependent Interface Propagation. *J. Phys. Chem. C* **2023**, *127*, 20530−20538.
(26) Rahm, J. M.; Erhart, P. WulffPack: A Python package for Wulff constructions. *J. Open Source Software* **2020**, *5*, No. 1944.
(27) Momma, K.; Izumi, F. VESTA: a three-dimensional visualization system for electronic and structural analysis. *J. Appl. Crystallogr.* **2008**, *41*, 653−658.
(28) Liu, M.; Wang, J.; Hu, J.; Liu, P.; Niu, H.; Yan, X.; Li, J.; Yan, H.; Yang, B.; Sun, Y.; et al. Layer-by-layer phase transformation in Ti_3O_5 revealed by machine-learning molecular dynamics simulations. *Nat. Commun.* **2024**, *15*, No. 3079.
(29) Wulff, G. On the question of speed of growth and dissolution of crystal surfaces. *Z. Kristallogr.-Cryst. Mater.* **1901**, *34*, 449−530.
(30) Hakoe, F.; Tokoro, H.; Ohkoshi, S.-i. Dielectric and optical constants of λ-Ti_3O_5 film measured by spectroscopic ellipsometry. *Mater. Lett.* **2017**, *188*, 8−12.
(31) Esch, T. R.; Gadaczek, I.; Bredow, T. Surface structures and thermodynamics of low-index of rutile, brookite and anatase−A comparative DFT study. *Appl. Surf. Sci.* **2014**, *288*, 275−287.
(32) Navrotsky, A. Nanoscale effects on thermodynamics and phase equilibria in oxide systems. *ChemPhysChem* **2011**, *12*, 2207−2215.
(33) Jütten, S.; Bredow, T. Doping Effect on the Electronic Structure and Heat-Storage Properties of Ti_3O_5. *J. Phys. Chem. C* **2023**, *127*, 10445−10452.

https://doi.org/10.1021/acs.jpcc.4c03730
J. Phys. Chem. C 2024, 128, 13402−13409

APPENDIX E

Atomistic Mechanisms of Pressure-Induced Phase Transitions in Heat-Storage Material Ti_3O_5

Atomistic mechanisms of pressure-induced phase transitions in the heat-storage material Ti_3O_5

Stefan Jütten [1,*] Peitao Liu [2,†] Liang Zuo [3] Xing-Qiu Chen,[2] and Thomas Bredow [1]
[1]*Mulliken Center for Theoretical Chemistry, Beringstr. 4, 53115 Bonn, Germany*
[2]*Shenyang National Laboratory for Materials Science, Institute of Metal Research, Chinese Academy of Sciences, Shenyang 110016, China*
[3]*Key Laboratory for Anisotropy and Texture of Materials (Ministry of Education), School of Materials Science and Engineering, Northeastern University, Shenyang 110819, China*

(Received 5 November 2025; revised 3 February 2026; accepted 27 February 2026; published 16 March 2026)

Phase change materials (PCMs) enable the controlled modulation of physical properties through phase transitions induced by external stimuli, including temperature, pressure, irradiation, or electric and magnetic fields. Of particular interest is trititanium pentoxide (Ti_3O_5), a promising PCM for heat storage, which exhibits a low pressure threshold for the λ to β phase transition. Although the phase transitions of bulk Ti_3O_5 have been extensively studied and well understood, research on its surface properties and associated phase transformations remains limited due to the computational challenge of modeling pressure effects on the surface at the atomic scale. Here we introduce a computational framework that combines a machine-learned interatomic potential trained on high-fidelity density functional theory data with explicit pressure simulation via repulsive slab potentials. We identify a hitherto unknown stable surface reconstruction and a kinetically favorable layer-by-layer transition mechanism. On-the-fly probability enhanced sampling simulations reveal that pressure significantly reduces the free energy barrier, predicting a phase transition at only 700 bar, in good agreement with the experimental value. This work presents a feasible and generally applicable protocol for modeling pressure effects in PCMs, paving the way for improved understanding and application of materials under operational conditions.

DOI: 10.1103/1wbw-k4n2

I. INTRODUCTION

Phase change materials (PCMs) allow for the controlled switching between different phases or polymorphs of functional materials, thereby enabling the precise modulation of physical properties [1]. These transitions can be induced by various external stimuli, including temperature, pressure, irradiation, or electric and magnetic fields. Of particular interest are PCMs that enable switching between well-defined and stable phases with low threshold triggers. Their applications span a wide range, from molecular magnets [2] and spin-crossover systems [3] to rewritable data storage [4,5] and heat-storage materials [6].

In the realm of heat-storage materials, trititanium pentoxide (Ti_3O_5) has emerged as a promising candidate [7–12] for efficiently storing waste heat from power generation [9], industrial processes [13], and even excess heat in automobiles [10]. At ambient conditions, the low-temperature semiconducting β-polymorph is the thermodynamically stable ground state, whereas the high-temperature metallic λ-polymorph persists as a metastable phase. The β-to-λ phase transition is of first order, which can be driven by temperature, pressure, and laser pulses [8–12,14,15]. Notably, a large phase transition enthalpy of $\Delta H = 12 \pm 1$ kJ mol^{-1} can be released by applying a modest pressure of just 600 bar to λ-Ti_3O_5 crystallites [9], a remarkably low threshold compared to other metal oxides that typically require several GPa to induce similar changes.

Previous investigations of the phase transition process of Ti_3O_5 highlighted its complexity. Our theoretical studies revealed that a straightforward concerted transition is energetically unfavorable, because of the high free energy barriers of 24 kJ mol^{-1} from β to λ and 14 kJ mol^{-1} from λ to β [16,17]. Experimental observations revealed an even more complicated picture of the phase transition, e.g., with a significant strain anisotropy during the photoinduced phase transition in bulk Ti_3O_5 crystals [14]. Remarkably, the $\lambda \rightarrow \beta$ transformation exhibits a much lower activation barrier when proceeding along the z axis, which was attributed to the favorable stacking at the phase interfaces [18]. This finding was corroborated by subsequent metadynamics and molecular dynamics simulations, which demonstrated a kinetically favorable layer-by-layer transition mechanism [19]. Recent experimental validation of these computational predictions involved aligning Ti_3O_5 crystallites and applying pressure normal to the z axis, resulting in a significantly reduced phase transition pressure [20]. In particular, the theoretically predicted dynamically stable interface structure was confirmed by experiments [20].

While the phase transitions of bulk Ti_3O_5 have been extensively studied and well understood, research on its surface properties and associated phase transitions remains limited. It is important to note that the substantial difference in surface free energies between λ and β phases contributes to the thermodynamic stabilization of λ-Ti_3O_5 nanoparticles at ambient conditions, facilitating its heat-storage application

*Contact author: juetten@thch.uni-bonn.de
†Contact author: ptliu@imr.ac.cn

[21]. Recent experiments have demonstrated that the surface of λ-Ti_3O_5 exhibits exceptional performance in solar steam generation [22]. Given that phase transformations often initiate at the surface, it is essential to investigate the surface structure and the associated phase transitions under pressure.

However, modeling the pressure effect on the surface represents a significant challenge for computational chemistry. Traditional approaches typically model pressure simply by shrinking the lattice vectors of the unit cell. This method has proven inadequate for explaining the pressure effect in Ti_3O_5 using the quasiharmonic approximation at the density functional theory (DFT) level [18]. To overcome this limitation, we introduce an approach that models pressure effects on the slab models of relevant surfaces. Pressure is simulated by applying repulsive potentials to the slab model from both sides, resulting in compression along the surface normal.

We propose a method to correlate this compression with pressure values and calculate via enhanced sampling simulations how the applied pressure influences the free energy barrier for the phase transition and the free energy difference between the phases. This was made possible by training an accurate, efficient, and reliable machine-learned interatomic potential (MLIP) trained on high-fidelity DFT data generated using the dispersion-corrected r^{2}SCAN functional [23,24]. The use of an MLIP significantly extended the spatial and time scales of the simulations. Molecular dynamics (MD) simulations indicate that application of small pressure triggers the λ to β phase transformation of surface models, in good agreement with the experimental observations [20]. This work presents a refined and generally applicable procedure for modeling pressure effects on materials, particularly in scenarios where the directionality of pressure application is critical.

II. METHODS

A. First-principles calculations

First-principles density functional theory (DFT) calculations were performed using the Vienna *Ab Initio* Simulation Package (VASP) [25] within the framework of the projector augmented wave method [26]. The dispersion-corrected r^{2}SCAN (r^{2}SCAN + D3) functional was employed [23,24]. It has been demonstrated that this method yields structures, energies, and phonons in good agreement with experimental results [16,27]. A plane wave cutoff energy of 700 eV and a k-point grid of $6 \times 6 \times 1$ were utilized. To ensure accurate forces, a stringent electronic structure convergence threshold of 10^{-8} eV and augmented integration grids were used. A ferromagnetic state with initially parallel magnetic moments on all Ti atoms was assumed [16].

B. Machine-learning interatomic potential training

For the on-the-fly active learning procedure using the VASP, an MLIP was trained using kernel-based Bayesian regression [28–30]. The cutoff radius for the three-body descriptors and the width of the Gaussian functions used for broadening the atomic distributions of the three-body descriptors were set to 6 Å and 0.4 Å, respectively. The number of radial basis functions and maximum three-body momentum quantum number of the spherical harmonics used to expand the atomic distribution for the three-body descriptors were set to 14 and 4, respectively. The parameters for the two-body descriptors were the same as those for the three-body descriptors. For training the MTP, a cutoff radius of 6.0 Å was used, and the radial basis size was set to be 8. The MTP basis functions were selected such that the level of scalar basis B_α is less than or equal to 26 [31]. The weights expressing the importance of energies and forces were set to 1.0 and 0.05, respectively. The regression coefficients were obtained by a nonlinear least square optimization using the Broyden-Fletcher-Goldfarb-Shanno algorithm.

C. Molecular dynamics calculations

Molecular dynamics calculations were performed employing the MTP using the LAMMPS code [32] patched with the PLUMED code (v2.9) [33] and the MLIP-3 interface [34]. A $2 \times 1 \times 1$ supercell of the primitive (001) Ti_3O_5 surface cell was used in simulations using the NVT ensemble at 300 K. The time step was set to 1 fs. The convergence of on-the-fly probability enhanced sampling (OPES) simulations is determined according to the following criteria [35]: (1) the number of transitions between the metastable states (at least four after the initial phase where the bias is adjusted rapidly), (2) the convergence of the time evolution of the free energy difference between the two basins of interest, and (3) the convergence of the partition function ratio between the biased and unbiased distributions. The repulsive potentials used the "wall/harmonic fix" command in LAMMPS, where the sigma parameter was kept at 0 and the cutoff parameter r_c was set to 80.8 corresponding to 0 Å compression of the slab model centered in the 200 Å long simulation box. The OPES_METAD_EXPLORE simulations up to 1 Å slab compression used a BARRIER of 100 kJ mol^{-1}, which was increased to 170 kJ mol^{-1} for slab compressions up to 3.8 Å due to the much more pronounced free energy difference between the basins.

D. Climbing-image nudged elastic band simulations

Climbing-image nudged elastic band (CI-NEB) simulations were performed with the MTP in LAMMPS and utilized 255 images for slab models with 3–11 layers, and 384 and 512 images for slab models with 12 and 13 layers, respectively. Each layer consists of one conventional unit cell, resulting in model sizes ranging from 128 to 544 atoms. Simulations were considered converged when the maximum force acting on any image was smaller than 0.01 eV Å^{-1}. The CI-NEB simulations of three-layer models enlarged in the x direction (also with defect) used 512 images.

III. RESULTS

A. Machine-learned interatomic potential development

An initial training dataset comprising 2887 slab structures of β-Ti_3O_5 and λ-Ti_3O_5 was generated using the on-the-fly active learning method as implemented in VASP [28–30]. This method allows one to automatically select the representative structures from the *ab initio* MD simulations. All DFT calculations were conducted using the r^{2}SCAN functional [23,24]

with ferromagnetic settings for the spin state of Ti_3O_5 (see Sec. II). Dispersion interaction was taken into account using the Grimme's D3 method [36]. Slab models in the training set contained 64 atoms (i.e., eight formula units), making up two stoichiometric layers, with a 20 Å vacuum between the periodic slabs. The DFT-optimized (001) surface models of both β and λ phases were used as the starting structures, and the NpT ensemble was employed, which allowed for density changes during heating up to 1200 K. Then, a moment tensor potential (MTP) [31] was fitted with optimized basis sets by refining the contraction process of moment tensors [37,38]. This significantly speeds up the calculations without reducing numerical precision. To sample the phase space around the transition state, we performed well-tempered metadynamics (WTMTD) simulations at 600 K and 800 K with the MTP.

The projected y and z components of the Ti_3-Ti_3 dimer rotation vector was used as collective variable (CV) [19] (the Ti_3-Ti_3 dimer rotation is a key feature of the phase transition; see Fig. S1 [39]). All configurations from the WTMTD simulations that exceeded the extrapolation grade threshold of 10 were selected based on the D-optimality criterion [40] for extending the training set, resulting in additional 1026 structures.

The total of 3913 structures were randomly split into the training dataset (3522 structures) and the validation dataset (391 structures). The validation root mean squared errors (RMSEs) are 1.529 meV atom^{-1} for energies, 0.059 eV Å^{-1} for forces, and 0.470 GPa for stress tensors (see Figs. S2 and S3 [39]). To make full use of all the generated structures, the final MTP was fitted on the entire 3913 structures.

To assess the reliability of the MTP, we optimized the atomic positions for the (001) surface slabs of both phases and the lattice parameters of bulk unit cells (Table 1 [39]). Although the bulk structures were not included in the training dataset, the predicted lattice parameters and atomic positions are in good agreement with the DFT results. For bulk λ-Ti_3O_5, the MTP yields a β angle of 90° for the monoclinic $C2/m$ unit cell, resembling the α-Ti_3O_5 phase [41]. The MTP calculated regular (001) surface structures exhibit only small deviations from the DFT reference, whereas the reconstructed surfaces display slightly larger deviations. This is expected, since these reconstructed surface structures were not contained in the training dataset. By recalculating local extrema and intermediate points along the MTP derived NEB phase transition pathway with the reference DFT method (Fig. S4 [39]), close agreement for phase transition barriers and relative energies are confirmed.

The machine-learned potential thus enables rare events sampling in enhanced sampling simulations and molecular dynamics simulations of large systems over hundreds of nanoseconds, timescales which are inaccessible in *ab initio* molecular dynamics simulations, at essentially the same computational accuracy. Slab models and novel structures, such as the reconstructed surfaces in this study, necessitate a custom machine-learned potential. Employing an advanced classical force field fitted explicitly for titanium oxide alloys (2NNMEAM + Qeq [42]) for the prediction of the phase transition pathway or relative energies failed to reproduce DFT data for the relative phase stability, surface energies, and barriers (Table S2 and Fig. S5 [39]), although the evaluation is faster than the MTP (Table S3 [39]).

B. Surface reconstruction of the (001) surface

Our study of the (001) surface termination of λ-Ti_3O_5 starts with the converged surface model from our earlier investigation of the surfaces of Ti_3O_5 polymorphs [21] employing the r^{2}SCAN-D3 method with a plane wave cutoff energy of 680 eV. The calculated surface energy E^{surf} converged at a slab thickness of ∼37 Å for a symmetric surface model containing eight formula units. Reoptimization of this model with r^{2}SCAN + D3 in the present study resulted in a surface energy of 1.474 J m^{-2}.

To assess the dynamic stability of this optimized structure, we conducted simulated annealing MD simulations using the MTP. The temperature was increased from 300 K to 1000 K over 1 ns, followed by cooling to 300 K over 10 ns (Fig. S6 [39]). Intriguingly, the initial surface model—directly cleaved from the bulk and DFT-optimized—was found to be metastable. It undergoes reconstruction via a dynamically stable intermediate (see Fig. 1). This dynamically stable intermediate is formed by migrating the exposed surface Ti atom down into the bulk while the bridging oxygen atom moved upward. This process yields a stabilization of the slab model of −0.085 eV and a reduction in the surface energy of −0.266 J m^{-2} with respect to the DFT-optimized surface model. A subsequent back-rotation of the subsurface Ti_3 atom further lowers the energy by −0.018 eV, resulting in a reduced E^{surf} of 1.074 J m^{-2}. This reconstructed surface ranks among the most stable surface facets of the λ-Ti_3O_5 polymorph (cf. $E^{\text{surf}} = 1.008$ J m^{-2} for the most stable (100) surface [21]). Phonon dispersion calculations confirm the dynamical stability of all structures involved in the reconstruction process (Fig. S7 [39]). The Wulff construction (Fig. S8 [39]) predicts a crystallite shape swaged along the z-axis, reflecting the higher surface area contribution of the (001) facet.

C. Phase transition mechanism

To elucidate the phase transition mechanism, we computed the energy barriers for the most stable reconstructed (001) surface model—a slab with three inner Ti_3-containing layers—using the climbing-image nudged elastic band (CI-NEB) method [43] (Fig. 2). It is observed that the phase transition initiates in the layer below the surface, then proceeds to the innermost bulk-like layer, and finally the other below-surface layer transforms. These transformations occur in a sequential order, i.e., in a layer-by-layer process similar to the pathway observed in the bulk [19] (see the Movie in Supplemental Material [39]). The predicted activation energy $\Delta E^{\ddagger} = E^{I} - E^{\lambda}$ of 0.23 eV is comparable with the value for the bulk (0.26 eV per f.u. [16]). The dynamical stability of the predicted interphase stacking structures in Fig. 2 was confirmed by phonon dispersion calculations (Fig. S9 [39]).

To examine size effects on the phase transition mechanism, we systematically expanded the surface model along the x axis to 2× and 4× the original dimensions. The computed size-dependent activation energies are compiled in Table I. We find

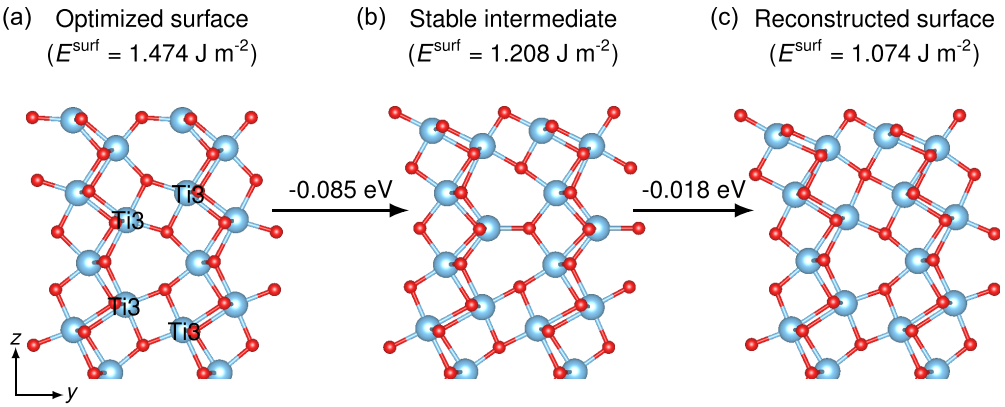

FIG. 1. Surface reconstruction process of the λ-Ti_3O_5 (001) surface. (a) Optimized surface cut from the bulk; (b) stable intermediate structure; (c) reconstructed surface. The surface energies E^{surf} (J m^{-2}) and relative stabilities (eV) are indicated.

that the transformation maintains its characteristic layer-by-layer progression (see the Supplemental Material movie [39]), while consistently initiating in the subsurface layer beneath the reconstructed surface. The activation energy barriers are proportional to the number of broken Ti_3-Ti_3 dimers for the transformation of the first layer. This behavior is reminiscent of a nucleation-like mechanism, where the transformation initiates independently in each layer and the activation barrier depends solely on the dimer-breaking process rather than the total number of atoms in the layer. We therefore normalize all energies to the number of formula units involved in the transformation of a slab layer throughout this work.

Furthermore, we increased the slab thickness along the z axis by incrementally adding one layer at a time and performing CI-NEB simulations after each expansion (see Figs. S10 and S11 [39]). While $\Delta E^{\ddagger}$ decreases with increasing slab thickness, this trend arises purely from the growing number of formula units in the model. When normalized to the transforming four formula units per layer, the activation energy remains constant, indicating that the intrinsic energy barrier for the phase transformation is independent of slab size. Even in the largest simulated system—comprising 16 Ti_3-Ti_3 dimer layers—the normalized energy barrier remains unchanged, suggesting that each layer undergoes independent transformations. These results imply that nucleation events occur in a decoupled manner across different layers.

The nucleation process is also observable in CI-NEB calculations after introducing a defect into the model. To achieve this, one Ti atom was removed from a subsurface Ti_3-Ti_3 dimer, thereby breaking the symmetry. The phase transition initiates at the defect-free surface termination, propagates inward to the interior layers, and finally reaches the defect-containing layer. Within this layer, the transformation occurs sequentially: first in the Ti_3-Ti_3 dimers adjacent to the defect rotate, followed by the defective dimer itself (see Supplemental Material Movie [39]). This progression disrupts the

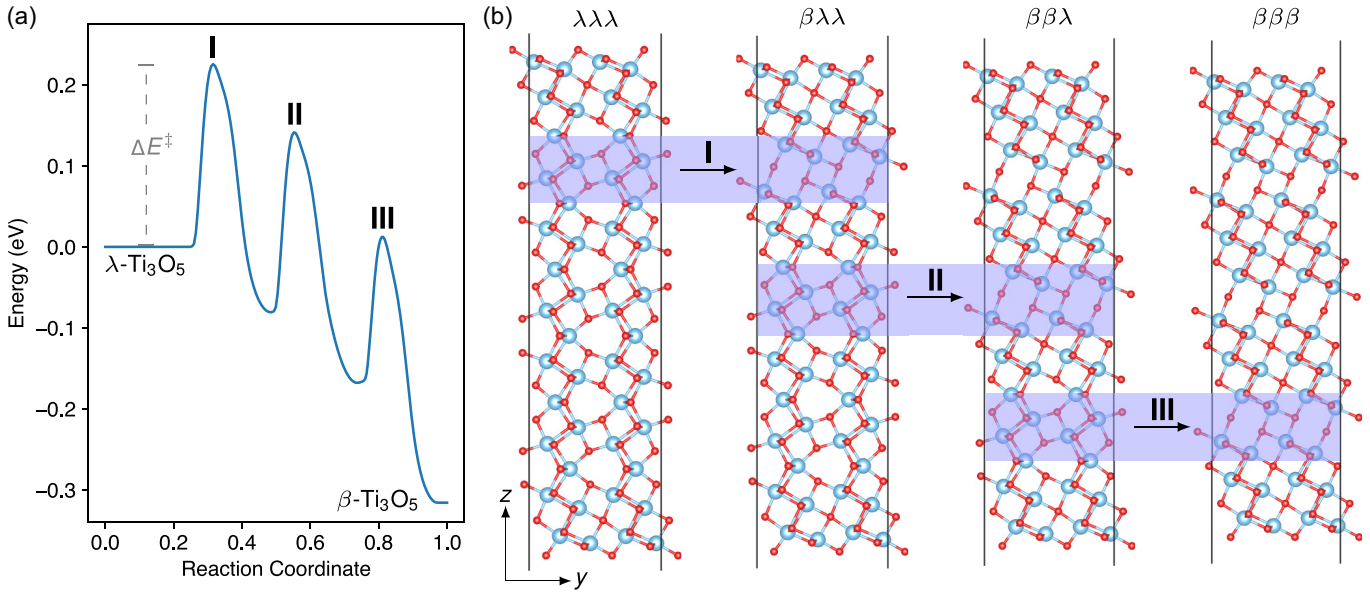

FIG. 2. Energy barriers along the phase transformation pathway. (a) Total energy (in eV) per formula unit (f.u.) of a three-layer (001) slab model as a function of the reaction coordinate during the CI-NEB simulation. (b) Snapshots of structures along the transformation pathway from λ-Ti_3O_5 ($\lambda\lambda\lambda$) to β-Ti_3O_5 ($\beta\beta\beta$), highlighting the sequential transformation of the layers containing Ti_3-Ti_3 dimers.

TABLE I. Activation energy ($\Delta E^{\ddagger}$) and the number of broken Ti_3-Ti_3 dimers (N^{dimers}) for the transformation of the first layer during CI-NEB simulations of supercells with increasing size.

Supercell	N^{dimers}	$\Delta E^{\ddagger}$ (eV)
$1 \times 1 \times 1$	1	0.23
$2 \times 1 \times 1$	2	0.45
$4 \times 1 \times 1$	4	0.90

in-plane collective mechanism, highlighting the defect's role in the nucleation process.

D. Molecular dynamics simulations under pressure

We further investigated the dynamics of the pressure-induced phase transition. The MTP-MD simulations were performed at 300 K with progressive compression, which was obtained by changing the cutoff threshold of a repulsive harmonic potential applied to the top and bottom faces of the simulation cell (see Sec. II). Figure 3(a) shows the potential energy of the slab comprised of 6144 atoms as a function of the compression. After an initial rapid compression, the slab model was given more time to relax under elevated compression levels in the MD simulation to minimize the formation of defects, which have been previously observed in strain-induced $\beta \rightarrow \lambda$ transitions of bulk Ti_3O_5 [19]. In the critical compression regime, the slab was slowly compressed by lowering the cutoff threshold of the repulsive potential on each surface in increments of 0.1 Å. After the slab was compressed by 3.8 Å, the $\lambda \rightarrow \beta$ phase transition was first observed in the layer beneath the reconstructed surface, visible by a sharp drop in potential energy at ≈55 ns. An additional compression of 0.6 Å was required to induce the transition in the next layer below the surface. Finally, when the slab was compressed by another 0.6 Å, the interior layer underwent the transformation. It is noted that the amount of a 0.6 Å compression increment is related to the difference between the c lattice parameters of λ ($c = 9.97$ Å) and β ($c = 9.44$ Å), 0.53 Å [9]. Once the critical compression level was achieved in the MD simulations, each subsequent 0.6 Å compression prompted another layer of the slab to transition from λ to β. Each transformation proceeds rapidly (within a few ps) and immediately after its finalization the compression level was slightly increased. The slab was dynamically stable between individual phase transition events, and no spontaneous phase transitions occurred unless further pressure was applied. Additionally, the present findings reaffirm the characteristic layer-by-layer nature of the phase transition observed previously in bulk phases [18,19].

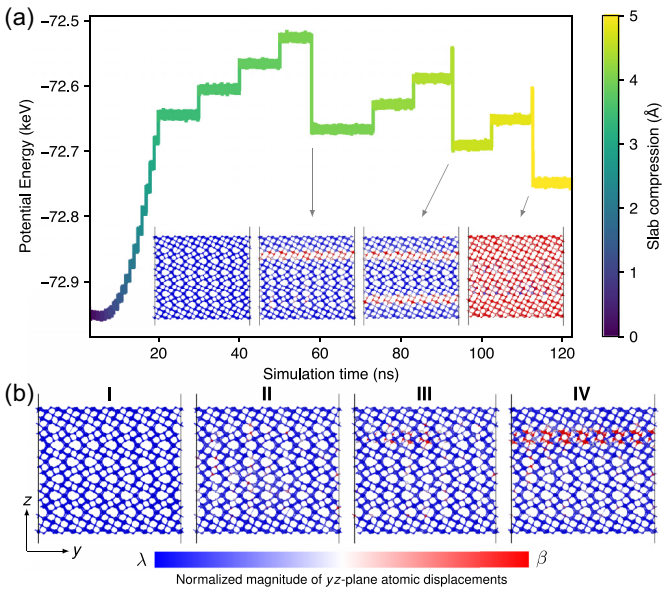

FIG. 3. Pressure-induced phase transitions. (a) Potential energy (eV) as a function of simulation time during a MD simulation at 300 K with increasing slab compressions. The color bar indicates the slab compressions, and the insets show the layer-by-layer progression of the phase transition. (b) Illustration of the nucleation and growth process in the below-surface layer of the slab.

A more detailed examination of the phase transition reveals that it proceeds via an intralayer nucleation event, followed by the complete $\lambda \rightarrow \beta$ transformation of the entire layer, and ultimately the initiation of the phase transition in the adjacent layer. Initially, a nucleus forms within a layer, which triggers the transformation of the entire yz plane within the transforming layer [see Fig. 3(b) and Fig. S12 [39] for a side view along the y axis]. Once this slice is fully transformed, the neighboring yz planes begin to undergo the phase transition, continuing until the entire layer is transformed. Subsequently, the next layer of the slab initiates the phase transition, following the same dynamics as described above.

E. Pressure effect on the phase transition

In this section the pressure effect on the free energy activation barrier ($\Delta G^{\ddagger}$) for the $\lambda \rightarrow \beta$ phase transition is investigated. To study the convergence of the free energy, on-the-fly probability enhanced sampling (OPES) simulations at a temperature of 300 K were performed. During these simulations, a bias was applied to the collective variable that describes the characteristic rotation of the Ti_3-Ti_3 dimer, in either the top or the central layer of the three-layer slab model. To relate a specific compression of the slab model to the corresponding pressure value, the standard definition of pressure p was applied:

$$p = \frac{F}{A}. \tag{1}$$

Since the surface area A of the slab model is known, one only needs to determine the force F acting on this surface area, which can be calculated as the derivative of a repulsive harmonic potential V that acts normal to both vacuum-exposed surfaces of the slab model

$$V = \varepsilon(r - r_{\text{cut}})^2, \quad (r < r_{\text{cut}}), \tag{2}$$

where r_{cut} is the cutoff threshold of the harmonic potential as measured from the unit cell box top and bottom edges. An increase in r_{cut} corresponds to an increased compression of the slab. The force F resulting from this acting potential is then obtained by

$$F = 2\varepsilon(r - r_{\text{cut}}), \tag{3}$$

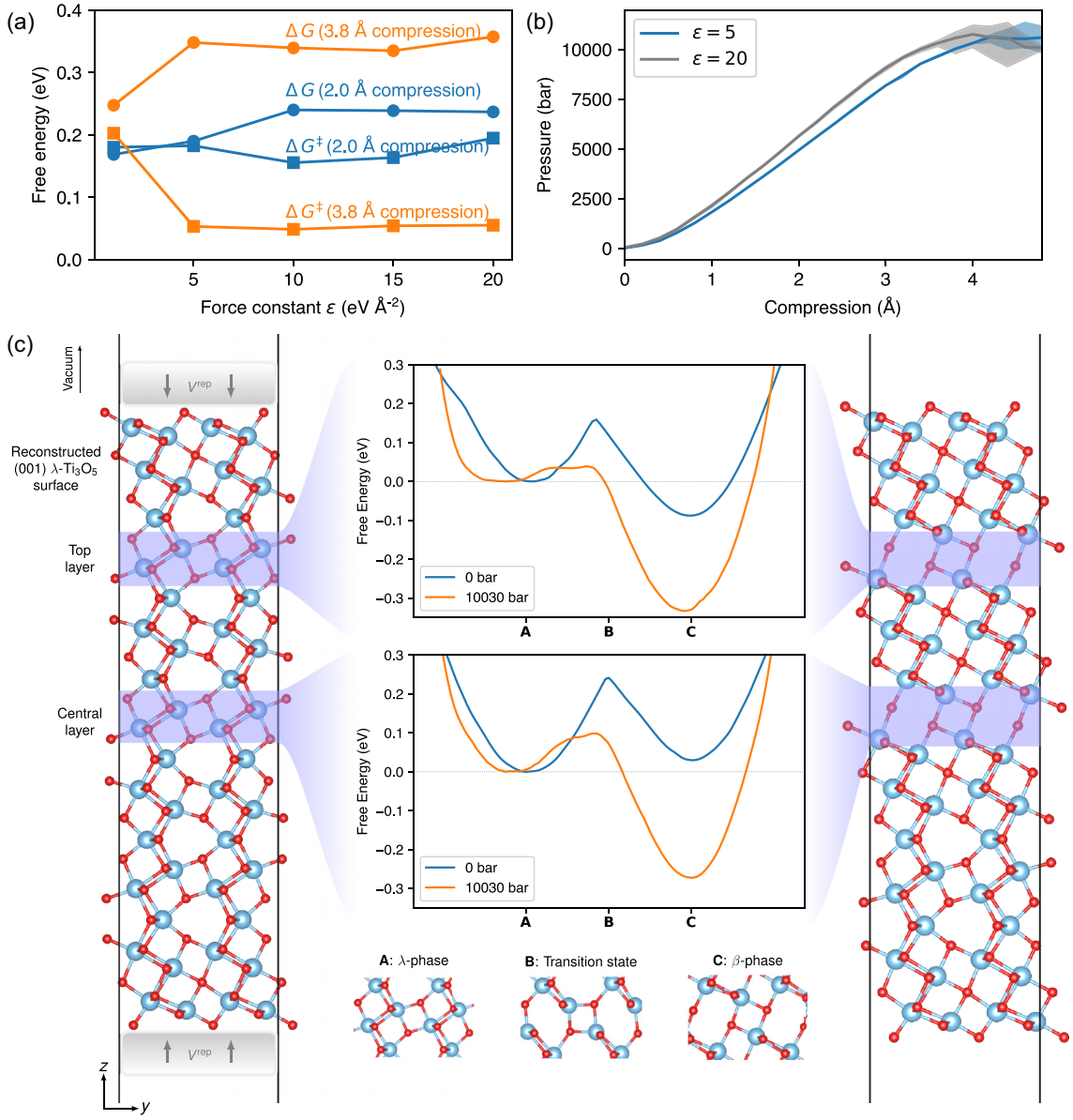

FIG. 4. Pressure effect on the phase transition. (a) Free energy difference (eV) as a function of the force constant ε of the repulsive harmonic potential in OPES simulations for two compression levels. (b) Predicted pressure (bar) as a function of the slab compression for two different ε values. (c) Comparison of the activation free energy $\Delta G^{\ddagger}$ (eV) for the $\lambda \rightarrow \beta$ phase transition obtained from OPES simulations under zero and transition pressures. The structural motifs for the λ, β, and transition state are indicated. The transforming Ti_3O_5 formula units in the slab models and the repulsive potential V^{rep} (eV Å^{-2}) compressing the slab from both z directions are highlighted.

where ε is the force constant.

Analyzing the contributions to the atomic forces during a MD simulation revealed that the force is only applied to the z component of the outermost oxygen atoms of the slab model. This approach necessitates the selection of a force constant ε, which we determine through convergence tests. Figure 4(a) illustrates the values of two types of free energy differences obtained during OPES simulations targeting the $\lambda \rightarrow \beta$ phase transition in the top layer of the slab model under two different slab compressions. The first is the free energy difference $\Delta G^{\lambda-\beta}$ between the λ and β basins, and the second is the activation free energy $\Delta G^{\ddagger}$ for the phase transition starting from the λ basin. For instance, at a slab compression of 3.8 Å, the converged ε is 5 eV Å^{-2}. It is important to note that different compression values of the slab yield different converged values for ε. Specifically, for a slab compression of 2.0 Å, which corresponds to a 0.5 Å compression of the c-lattice vector per unit cell in the slab model, ε converges at 10 eV Å^{-2}. Details on the convergence of the OPES simulations are provided in Figs. S13–S22 [39]. Converged values for ε are applied in all OPES simulations.

Having chosen a converged ε, the pressure p was computed corresponding to a given compression of the slab by sampling along 10 differently initialized MD trajectories of the slab model under that compression over 10 ps. The averaged force F acting on each surface over the simulation duration, which is due to the repulsive potential, is then used to calculate p using Eq. (1). Figure 4(b) shows the predicted pressure as a

TABLE II. Comparison of phase transition pressure thresholds p_{thresh} (in GPa) obtained within the quasi-harmonic approximation in the bulk, and the harmonic approximation and OPES simulations for slab models with the experimental value (see Fig. 5).

	QHA (bulk)	Harm. approx.	OPES	Experiment
p_{thresh}	3–4[a]	0.03	0.07	0.06[b]

[a]References [18,19].
[b]Reference [9].

function of the slab compression, comparing two different values of ε. At a compression of 3.8 Å and using $\varepsilon = 5$ eV Å^{-2}, the pressure threshold needed to induce the $\lambda \rightarrow \beta$ phase transition was determined as $p_{\text{thresh}} = 10\,030$ bar. The predicted pressure does not strongly depend on ε, e.g., for a slab compression of 1 Å it changes from 1828 bar at $\varepsilon = 5$ eV Å^{-2} to 2147 bar at $\varepsilon = 20$ eV Å^{-2}. Accordingly the uncertainty in the calculated pressure is low for all but the highest compression levels, where the curve flattens and the variance in the prediction increases. The latter observation can be explained by the fact that at these compression levels the phase transition should have already occurred, but the simulation time is not long enough.

In Fig. 4(c) the free energy surface under zero pressure and the transition pressure determined above are compared. For the top layer of the slab model, the application of pressure reduces $\Delta G^{\ddagger}$ from 0.16 eV to 0.05 eV and ΔG from −0.09 eV to −0.35 eV. For the central layer, increased pressure lowers $\Delta G^{\ddagger}$ from 0.24 eV to 0.11 eV and ΔG from 0.03 eV to −0.28 eV. Therefore the pressure effect on the free activation energy is most pronounced in the below-surface layer with a reduction of $\Delta G^{\ddagger}$ by 0.11 eV, such that the system may spontaneously undergo the phase transition under moderate temperatures. In contrast, the central layer experiences roughly a halving of its $\Delta G^{\ddagger}$ under pressure (see Fig. S23 [39]). Without the application of pressure the λ-like orientation of the Ti_3-Ti_3 dimer is thermodynamically slightly favored in the more bulklike central layer, while the β-like structural motif is favored in the top layer. The thermodynamic instability of the λ-phase in the top layer facilitates its transformation due to increased pressure. Stabilization due to the lower surface free energy of the (001) λ phase compared to β can explain the observed metastability of this surface termination in nanoparticles.

Finally, the effect of pressure on the small free energy difference between the basins in the central layer is examined (Fig. 5). Here, the compression of the slab was increased in 0.1 Å increments (see Fig. S24 [39]) and the bias was applied to the Ti_3-Ti_3 dimer in the central layer of the slab during OPES simulations (see Figs. S25–S37 [39]). With increasing pressure, the λ phase is progressively destabilized, and the free energy difference $\Delta G^{\lambda-\beta}$ vanishes at ≈700 bar. This result is in very good agreement with the experimental XRD measurements (see Table II), which show that half of the experimental samples were converted from the λ phase to the β phase at 600 bar [9].

By contrast, employing the harmonic approximation to calculate the free energy differences yields a phase transition

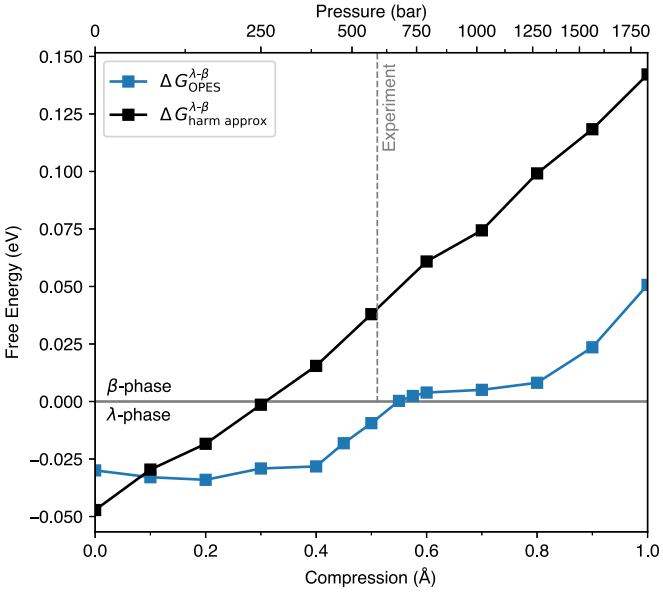

FIG. 5. Pressure dependence of the free energy difference. Free energy difference $\Delta G^{\lambda-\beta}$ at 300 K as a function of pressure (i.e., slab compression) for the central layer of the slab model. Results from OPES simulations are compared with those from the harmonic approximation. A 8 × 3 × 1 (≈30 Å × 30 Å × 37 Å) supercell was used.

pressure of ≈250 bar, far below the experimental value. This underlines the importance of enhanced sampling techniques for accurately calculating thermodynamic properties of the phase transition process.

IV. DISCUSSION

Accelerated by the MLIP trained on r^{2}SCAN + D3 DFT data, our large-scale MD simulations combined with enhanced sampling approach provide insights into the pressure-induced $\lambda \rightarrow \beta$ phase transition at the (001) surface of Ti_3O_5. The discovery of a stable surface reconstruction and a layer-by-layer transition mechanism underscores the critical role of surface effects in PCMs, particularly for heat-storage applications.

The proposed approach of applying repulsive harmonic potentials to simulate pressure on slab models overcomes the limitations of established methods typically for bulk systems, such as the quasiharmonic approximation, which significantly overestimates the transition pressure (3–4 GPa [18,19]). Our predicted transition pressure of 700 bar aligns well with the experimental value (e.g., 600 bar for stripe-type particles [9]), highlighting the importance of surface-specific modeling. The reconstructed (001) surface, with a reduced surface energy of 1.074 J m^{-2}, stabilizes the λ phase, facilitating its metastability in nanoparticles [21]. The OPES simulations reveal a significant reduction in the free activation energy barrier and the free energy difference between the phases under pressure, consistent with the low pressure threshold observed experimentally. Employing standard thermostatistics based on the harmonic approximation for computing free energies greatly underestimates the phase transition pressure,

emphasizing the need for advanced sampling methods such as OPES.

The discrepancy between our calculated transition pressure and the experimental values (e.g., 60 bar for block-type [10]) likely stems from simplifications in our model, which neglects real-world factors such as surface adsorbates and atomic-scale defects, both known to influence phase stability. This simplification points to a clear path for future work, such as modeling adsorbate coverage or different surface facets to better match experimental conditions. The layer-by-layer transformation mechanism, initiated in the subsurface layer via intralayer nucleation, reflects bulk behavior [19] but exhibits enhanced sensitivity to pressure at the surface, offering opportunities to tailor transition thresholds through surface engineering.

In conclusion, we have introduced a method to simulate external pressure on surfaces using a repulsive harmonic potential on slab models, enabling a direct connection between compression and pressure. When applied to Ti_3O_5 using MLIP-accelerated MD and enhanced sampling simulations, this approach successfully predicted a $\lambda \rightarrow \beta$ transition pressure of 700 bar for a surface layer, aligning with the experimental value of 600 bar. Furthermore, it uncovered a surface reconstruction and a kinetically favorable layer-by-layer transformation mechanism. Our work establishes a transferable framework for modeling anisotropic pressure responses in PCMs over large length and time scales, addressing a critical gap in computational materials science. By revealing the critical role of surfaces in phase transitions, our method paves the way for the rational design of PCMs with enhanced performance for energy storage applications.

ACKNOWLEDGMENTS

S.J. and T.B. gratefully acknowledge the access to the Marvin cluster of the University of Bonn. P.L. thanks Dr. J. Wang and Dr. M. Liu for useful discussions. S.J. and T.B. conceived the project. T.B. supervised the project. S.J. and P.L. conducted the calculations. X.-Q.C. and L.Z. participated in discussions. S.J. drafted the manuscript. P.L. and T.B. edited the manuscript. All authors commented on the manuscript. P.L. acknowledges funding from the National Natural Science Foundation of China (Grants No. 52422112 and No. 52188101) and the Science and Technology Major Project of Liaoning province (2024JH1/11700032).

The authors declare no competing interests.

DATA AVAILABILITY

The data that support the findings of this article are openly available [44].

[1] S. Raoux, Phase change materials, Annu. Rev. Mater. Res. **39**, 25 (2009).

[2] E. Coronado, Molecular magnetism: From chemical design to spin control in molecules, materials and devices, Nat. Rev. Mater. **5**, 87 (2020).

[3] J. Tao, R.-J. Wei, R.-B. Huang, and L.-S. Zheng, Polymorphism in spin-crossover systems, Chem. Soc. Rev. **41**, 703 (2012).

[4] M. Wuttig and N. Yamada, Phase-change materials for rewriteable data storage, Nat. Mater. **6**, 824 (2007).

[5] S. Raoux, W. Wełnic, and D. Ielmini, Phase change materials and their application to nonvolatile memories, Chem. Rev. **110**, 240 (2010).

[6] H. Nazir, M. Batool, F. J. B. Osorio, M. Isaza-Ruiz, X. Xu, K. Vignarooban, P. Phelan, A. M. Kannan, *et al.*, Recent developments in phase change materials for energy storage applications: A review, Int. J. Heat Mass Transf. **129**, 491 (2019).

[7] S.-i. Ohkoshi, M. Yoshikiyo, J. MacDougall, Y. Ikeda, and H. Tokoro, Long-term heat-storage materials based on λ-Ti_3O_5 for green transformation (GX), Chem. Commun. **59**, 7875 (2023).

[8] S.-i. Ohkoshi, Y. Tsunobuchi, T. Matsuda, K. Hashimoto, A. Namai, F. Hakoe, and H. Tokoro, Synthesis of a metal oxide with a room-temperature photoreversible phase transition, Nat. Chem. **2**, 539 (2010).

[9] H. Tokoro, M. Yoshikiyo, K. Imoto, A. Namai, T. Nasu, K. Nakagawa, N. Ozaki, F. Hakoe, K. Tanaka, K. Chiba, *et al.*, External stimulation-controllable heat-storage ceramics, Nat. Commun. **6**, 7037 (2015).

[10] S.-i. Ohkoshi, H. Tokoro, K. Nakagawa, M. Yoshikiyo, F. Jia, and A. Namai, Low-pressure-responsive heat-storage ceramics for automobiles, Sci. Rep. **9**, 13203 (2019).

[11] C. Mariette, M. Lorenc, H. Cailleau, E. Collet, L. Guérin, A. Volte, E. Trzop, R. Bertoni, X. Dong, B. Lépine, *et al.*, Strain wave pathway to semiconductor-to-metal transition revealed by time-resolved X-ray powder diffraction, Nat. Commun. **12**, 1239 (2021).

[12] P.-f. Zhao, G.-s. Li, W.-l. Li, P. Cheng, Z.-y. Pang, X.-l. Xiong, X.-l. Zou, Q. Xu, and X.-g. Lu, Progress in Ti_3O_5: Synthesis, properties and applications, Trans. Nonferrous Met. Soc. China **31**, 3310 (2021).

[13] Y. Nakamura, Y. Sakai, M. Azuma, and S.-i. Ohkoshi, Long-term heat-storage ceramics absorbing thermal energy from hot water, Sci. Adv. **6**, eaaz5264 (2020).

[14] T. Saiki, T. Yoshida, K. Akimoto, D. Indo, M. Arizono, T. Okuda, and T. Katsufuji, Selection rule for the photoinduced phase transition dominated by anisotropy of strain in Ti_3O_5, Phys. Rev. B **105**, 075134 (2022).

[15] R. Mandal, M. Lorenc, M. Cammarata, M. Levantino, S. Zerdane, É. Janod, L. Cario, H. Tokoro, S.-i. Ohkoshi, E. Trzop, *et al.*, Picosecond anisotropic phase separation governing photoinduced phase stability in submicron Ti_3O_5 crystals, Commun. Mater. **6**, 209 (2025).

[16] S. Jütten and T. Bredow, First-principles investigation of electronic properties and phase transition of Ti_3O_5, J. Phys. Chem. C **126**, 7809 (2022).

[17] S. Jütten and T. Bredow, Doping effect on the electronic structure and heat-storage properties of Ti_3O_5, J. Phys. Chem. C **127**, 10445 (2023).

[18] S. Jütten and T. Bredow, Anisotropy of the pressure effect in the Ti_3O_5 phase transition process resolved by direction-dependent interface propagation, J. Phys. Chem. C **127**, 20530 (2023).

[19] M. Liu, J. Wang, J. Hu, P. Liu, H. Niu, X. Yan, J. Li, H. Yan, B. Yang, Y. Sun, *et al.*, Layer-by-layer phase transformation in Ti_3O_5 revealed by machine-learning molecular dynamics simulations, Nat. Commun. **15**, 3079 (2024).

[20] P. Zhao, G. Li, X. Xiong, P. Cheng, Z. Pang, C. Sun, H. Cheng, C. Shi, X. Yu, Q. Xu, *et al.*, Sub-minute synthesis and modulation of β/λ-$M_xTi_{3-x}O_5$ ceramics towards accessible heat storage, Nat. Commun. **16**, 2443 (2025).

[21] S. Jütten and T. Bredow, Effect of surface free energies and particle diameter on the Ti_3O_5 $\beta \rightarrow \lambda$ phase transition temperature: A theoretical study, J. Phys. Chem. C **128**, 13402 (2024).

[22] B. Yang, Z. Zhang, P. Liu, X. Fu, J. Wang, Y. Cao, R. Tang, X. Du, W. Chen, S. Li, *et al.*, Flatband λ-Ti_3O_5 towards extraordinary solar steam generation, Nature (London) **622**, 499 (2023).

[23] J. W. Furness, A. D. Kaplan, J. Ning, J. P. Perdew, and J. Sun, Accurate and numerically efficient r^2SCAN meta-generalized gradient approximation, J. Phys. Chem. Lett. **11**, 8208 (2020).

[24] S. Ehlert, U. Huniar, J. Ning, J. W. Furness, J. Sun, A. D. Kaplan, J. P. Perdew, and J. G. Brandenburg, r^2SCAN-D4: Dispersion corrected meta-generalized gradient approximation for general chemical applications, J. Chem. Phys. **154**, 061101 (2021).

[25] G. Kresse and J. Furthmüller, Efficient iterative schemes for *ab initio* total-energy calculations using a plane-wave basis set, Phys. Rev. B **54**, 11169 (1996).

[26] G. Kresse and D. Joubert, From ultrasoft pseudopotentials to the projector augmented-wave method, Phys. Rev. B **59**, 1758 (1999).

[27] R. Kingsbury, A. S. Gupta, C. J. Bartel, J. M. Munro, S. Dwaraknath, M. Horton, and K. A. Persson, Performance comparison of r^2SCAN and SCAN metaGGA density functionals for solid materials via an automated, high-throughput computational workflow, Phys. Rev. Mater. **6**, 013801 (2022).

[28] R. Jinnouchi, J. Lahnsteiner, F. Karsai, G. Kresse, and M. Bokdam, Phase transitions of hybrid perovskites simulated by machine-learning force fields trained on the fly with Bayesian inference, Phys. Rev. Lett. **122**, 225701 (2019).

[29] R. Jinnouchi, F. Karsai, and G. Kresse, On-the-fly machine learning force field generation: Application to melting points, Phys. Rev. B **100**, 014105 (2019).

[30] R. Jinnouchi, F. Karsai, C. Verdi, R. Asahi, and G. Kresse, Descriptors representing two-and three-body atomic distributions and their effects on the accuracy of machine-learned interatomic potentials, J. Chem. Phys. **152**, 234102 (2020).

[31] A. V. Shapeev, Moment tensor potentials: A class of systematically improvable interatomic potentials, Multiscale Model. Simul. **14**, 1153 (2016).

[32] A. P. Thompson, H. M. Aktulga, R. Berger, D. S. Bolintineanu, W. M. Brown, P. S. Crozier, P. J. In't Veld, A. Kohlmeyer, S. G. Moore, T. D. Nguyen, *et al.*, LAMMPS-a flexible simulation tool for particle-based materials modeling at the atomic, meso, and continuum scales, Comput. Phys. Commun. **271**, 108171 (2022).

[33] G. A. Tribello, M. Bonomi, D. Branduardi, C. Camilloni, and G. Bussi, PLUMED 2: New feathers for an old bird, Comput. Phys. Commun. **185**, 604 (2014).

[34] E. Podryabinkin, K. Garifullin, A. Shapeev, and I. Novikov, MLIP-3: Active learning on atomic environments with moment tensor potentials, J.Chem. Phys. **159**, 084112 (2023).

[35] E. Trizio, A. Rizzi, P. M. Piaggi, M. Invernizzi, and L. Bonati, Advanced simulations with PLUMED: OPES and machine learning collective variables, arXiv:2410.18019.

[36] S. Grimme, J. Antony, S. Ehrlich, and H. Krieg, A consistent and accurate *ab initio* parametrization of density functional dispersion correction (DFT-D) for the 94 elements H-Pu, J. Chem. Phys. **132**, 154104 (2010).

[37] J. Wang, P. Liu, H. Zhu, M. Liu, H. Ma, Y. Chen, Y. Sun, and X.-Q. Chen, Efficient moment tensor machine-learning interatomic potential for accurate description of defects in Ni-Al alloys, Phys. Rev. Mater. **9**, 053805 (2025).

[38] Y. Cao, J. Wang, M. Liu, Y. Liu, H. Ma, C. Franchini, Y. Sun, G. Kresse, X.-Q. Chen, and P. Liu, Quantum delocalization enables water dissociation on Ru(0001), Phys. Rev. Lett. **134**, 178001 (2025).

[39] See Supplemental Material at http://link.aps.org/supplemental/10.1103/1wbw-k4n2 for the definition of the employed collective variable, fitset visualization and correlation plots, validation of the MTP on structures and relative energies, simulated annealing plot and phonon dispersions of the surface reconstruction process, Wulff constructions of the λ-Ti_3O_5 crystallite, phonon dispersions of NEB intermediate structues, NEB activation energy barriers and plots for increasing number of layers, rotated view of the nucleation event, OPES force constant convergence results, pressure vs compression error visualization, and OPES simulation convergence results.

[40] E. V. Podryabinkin and A. V. Shapeev, Active learning of linearly parametrized interatomic potentials, Comput. Mater. Sci. **140**, 171 (2017).

[41] M. Onoda, Phase transitions of Ti_3O_5, J. Solid State Chem. **136**, 67 (1998).

[42] E. Lee, K.-R. Lee, M. I. Baskes, and B.-J. Lee, A modified embedded-atom method interatomic potential for ionic systems: 2 NNMEAM + Qeq, Phys. Rev. B **93**, 144110 (2016).

[43] G. A. Henkelman, B. P. Uberuaga, and H. Jónsson, A climbing image nudged elastic band method for finding saddle points and minimum energy paths, J. Chem. Phys. **113**, 9901 (2000).

[44] S. Jütten, Data associated with the paper "Atomistic mechanisms of pressure-induced phase transitions in heat-storage material Ti_3O_5" (2025), https://doi.org/10.6084/m9.figshare.30541151.